



Universiteit
Leiden
The Netherlands

Development of novel anti-cancer strategies utilizing the zebrafish xenograft model

Chen, Q.

Citation

Chen, Q. (2020, September 1). *Development of novel anti-cancer strategies utilizing the zebrafish xenograft model*. Retrieved from <https://hdl.handle.net/1887/136271>

Version: Publisher's Version

License: [Licence agreement concerning inclusion of doctoral thesis in the Institutional Repository of the University of Leiden](#)

Downloaded from: <https://hdl.handle.net/1887/136271>

Note: To cite this publication please use the final published version (if applicable).

Cover Page



Universiteit Leiden



The handle <http://hdl.handle.net/1887/136271> holds various files of this Leiden University dissertation.

Author: Chen, Q.

Title: Development of novel anti-cancer strategies utilizing the zebrafish xenograft model

Issue Date: 2020-09-01

**Development of novel anti-cancer strategies
utilizing the zebrafish xenograft model**

Quanchi Chen

ISBN: 978-94-92597-49-6

Thesis layout & cover designed by Quanchi Chen

Printed by Boekendeal.nl

©2020 Quanchi Chen, Leiden, the Netherlands

All rights reserved. No part of this publication may be reproduced or transmitted in any form or by any means, electronic or mechanical, including photocopying, recording, or any information storage and retrieval system, without permission in writing from the copyright owner.

Development of novel anti-cancer strategies utilizing the zebrafish xenograft model

Proefschrift

ter verkrijging van
de graad van Doctor aan de Universiteit Leiden,
op gezag van Rector Magnificus prof.mr. C.J.J.M. Stolker,
volgens besluit van het College voor Promoties
te verdedigen op dinsdag 1 september 2020
klokke 12:30 uur

door

Quanchi Chen

Geboren te Yancheng, China
in 1990

Promotores: Prof. dr. B. Ewa Snaar-Jagalska and
Prof. dr. Sylvestre Bonnet

Promotiecommissie: Prof. dr. Gilles P. van Wezel
Prof. dr. Annemarie H. Meijer
Prof. dr. Alexander Kros
Prof. dr. Peter ten Dijke (Leiden University Medical Center)
Prof. dr. Martine Jager (Leiden University Medical Center)

Table of contents

Chapter 1	Introduction and thesis outline	1
Chapter 2	Lactic acid secreted by glycolytic B16.F10 melanoma cells attracts macrophages to drive angiogenesis	19
Chapter 3	TLD1433 photosensitizer inhibits conjunctival melanoma cell growth in zebrafish ectopic and orthotopic tumour models	45
Chapter 4	New ruthenium-based photoactivated chemotherapy compound is cytotoxic for various tumour cells in culture and conjunctival melanoma cells in a zebrafish orthotopic xenograft model	77
Chapter 5	Light-triggered cancer cell-specific targeting and liposomal drug delivery in a zebrafish xenograft model	111
Chapter 6	Summary	141
	Nederlandse Samenvatting	139
	Abbreviations	143
	Publication list	146
	Curriculum vitae	147

Chapter 1

Introduction and thesis outline

Cancer is one of the main causes of morbidity and mortality, being responsible for an estimated 18.1 million new cancer cases, and 9.6 million cancer deaths per year [1]. One in five men and one in six women worldwide will develop cancer during their lifetime, and one in eight men, and one in eleven women die from the disease. The majority of cancers, 90%-95% of cases, are induced by environmental and lifestyle factors, which may include smoking, diet, alcohol, sun exposure, environmental pollutants, infections, stress, obesity, and physical inactivity. About 5-10% of cases are due to inherited genetic aberrations. Carcinogenesis is a complex multi-step process that usually proceeds over several years and starts from one single cell. Endogenous and exogenous agents can lead to DNA damage, epigenetic defects and gene mutations. A series of mutations in cancer known as “driver genes” (oncogenes and tumour suppressors) as well as other “passenger genes” initiate the transformation from a normal cell to a cancer cell, which results in aberrant cell behaviour, such as cell migration, growth, differentiation and failure of apoptosis. These events are part of a multistep process and contribute progressively to the generation and development of cancer. The different characteristics of cancer pathogenesis and disease progression have been outlined by Hanahan and Weinberg as “Hallmarks of cancer” [2]. However, the biology of tumours should be investigated not only by focusing on the traits of single cancer cells, but should also consider the contributions of the tumour microenvironment, the interactions between tumour cells and the supportive stroma, the role of the immune system and the preferential tropism of spreading tumour cells to specific metastatic sites [3].

The clinical diagnosis of cancer is based on medical tests, including blood tests, X-rays, CT scans, endoscopy and MRI. Current treatments include surgery, chemotherapy, radiation therapy, hormonal therapy, targeted therapy and palliative care, depending on the type, location and grade of the tumour. There are two main reasons restricting the efficacy of existing treatments: one is the observation of heterogeneity, as based on a patients’ genetic background, gene mutations, lifestyle, tumour size and tumor metabolism. All of these may affect treatment results. Therefore, a deeper understanding of inter- and intratumoral heterogeneity of tumours is needed for personalized interventions. A second problem is cancer cell resistance to the currently used therapeutics. Common targeting strategies aimed at inhibiting specific molecular pathways often have only a temporary success and are followed by a tumour relapse. The use of a combined approach with several drugs can give rise to higher efficiency and avoidance of chemoresistance but so far, the results have not achieved the required efficacy in all malignancies. Therefore, there is still an unmet clinical need to develop new drugs and cancer models for testing the anti-cancer efficacy of targeted drug delivery to avoid adverse side effects and increase the success rate of treatments. In this thesis, we are going to discuss the development of novel anti-cancer strategies utilizing zebrafish xenograft models.

Cancer development

Tumour clonality is one of the fundamental features of cancer and describes the development of tumours from a single cell. The accumulation of gene mutations leading to abnormal cell proliferation can be thought of as tumour initiation [4] (Figure 1). The outgrowth of a population of clonally-derived tumour cells into adjacent tissues will form a tumour microenvironment (TME), which supports tumour cell growth. The abilities to sustain proliferative signalling [5], evade growth suppressors [6], resist cell death [7], enable replicative immortality [8], induce angiogenesis [9], and activate invasion and metastasis [10] sustain tumour cell proliferation [2]. During tumour progression, further gene mutations keep occurring. Similar to a microevolutionary process, the stepwise progress of cancer consists of a stage I, which is the evolution of tumours from normal tissues and stage II, which represents the evolution within tumours [11]. Tumor progression drives intratumor diversity and heterogeneity. At the primary site, the tumour cells can grow thanks to enough nutrition and oxygen derived from the surrounding normal tissue. When the nutrition and oxygen become limited, the tumour center often transforms to a necrotic core. The term Oxidative Stress refers to elevated intracellular levels of reactive oxygen species (ROS) and oxygen limitation initiates tumour angiogenesis after the so-called “angiogenic switch”, which causes the normal quiescent vasculature to sprout and produce new branches (neovascularization) [12]. The new vessels in the tumour have an aberrant morphology and are characterized by abnormal level of endothelial cell proliferation and apoptosis. In addition, leakiness of tumour vessels is one of the major reasons for the low efficiency in the delivery of therapies specifically to tumour lesions [13].

It takes time for the tumour cells to grow at the primary site and develop the capacity to invade and metastasize. In this context, transformed epithelial cells acquire a motile mesenchymal phenotype in a process referred to as “epithelial-to-mesenchymal transition” (EMT) [14]. This invasive phenotype is generally associated with an increased migratory capacity of the tumour cells. Both blood and lymphatic vessels provide an escape route by which tumour cells can leave the primary site, through a process called intravasation. After tumour cells have invaded the circulatory system, they have to survive in the circulation and resist necrosis, until the tumour cells adhere to the vascular wall and extravasate [15].

Most circulating tumour cells will die, only a few tumour cells go into an anchorage-independent survival. Once tumour cells have extravasated, they can invade the distant tissue and organ and undergo mesenchymal-to-epithelial transition, which allows the tumour cells to switch back to their epithelial and proliferative state. Once micrometastases are formed, sustained growth and angiogenesis allow them to grow out into secondary tumours. Additionally, tumour cells can also remain dormant for several years and then suddenly re-initiate proliferation and form a metastatic lesion. Metastasis is the final stage of tumour progression and is the main cause of mortality.

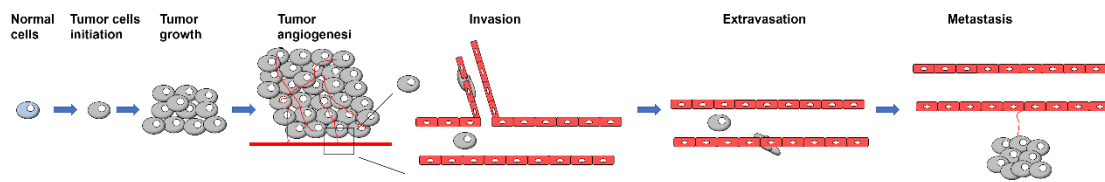


Fig. 1 Scheme of tumour cell growth, angiogenesis, invasion and the metastasis process.

Metabolic reprogramming in cancer

In addition to the above mentioned specific hallmarks, tumour cells can also adapt their metabolism and switch to the so-called “aerobic glycolysis”, converting their metabolism largely to glycolysis and lactate production (i.e. Warburg-effect) [16]. This is one of the bases of the non-invasive visualization of tumour-dependent positron emission tomography (PET) with a radiolabelled analogue of glucose as reporter. In proliferating cancer cells, the mitochondrial oxidative phosphorylation (OXPHOS) is reprogrammed towards a macromolecular synthesis to sustain multiple cell divisions [17]. The advantage of such a deregulated metabolism is to favour the accumulation of glycolytic intermediates, fuelling derivative anabolic pathways, such as the pentose phosphate pathway, the hexosamine pathway, and amino acid synthesis, thereby sustaining cell proliferation [18]. However, recent advances have highlighted substantial intratumoral metabolic heterogeneity and even metabolic plasticity, depending on the tissue context, tumour stage, TME, that regulate the metabolic strategies in tumour cells, leading, for example, to concurrent glycolysis and glucose oxidation in the same tissue [19]. Nevertheless, the majority of cancer cells enhance glucose and glutamine consumption to satisfy their requirements for rapid proliferation. In aerobic glycolysis in tumour cells, glucose is partially oxidized into pyruvate, which is subsequently reduced to lactate, that is then extruded into the extracellular space. Emerging evidence now argues that lactate plays a role in regulating different signalling pathways and the behaviour of malignant and non-malignant cells. Lactate can affect multiple biological processes during tumour progression, plays roles in the immune and inflammatory responses in TME, and also influences proliferation, metastasis and angiogenesis [20].

Moreover, oncogenic mutations in metabolic enzymes such as the cytosolic NADP⁺-dependent isocitrate dehydrogenase 1 gene (IDH1) and the mitochondrial homolog IDH2, responsible for converting α -ketoglutarate to 2-hydroglutarate (2HG), a metabolite found only in reduced amounts in mammalian cells under normal conditions, have been reported [21]. Interestingly this has also an effect on epigenetic mechanisms, resulting in altered histone methylation marks, hypermethylation at CpG islands and dysregulated cell differentiation [21].

The function of macrophages in the tumour microenvironment

More knowledge now starts to elucidate the role of the TME and immune system during tumour initiation, growth and progression. Importantly, TME also shapes therapeutic responses and resistance [22,23].

During cancer progression, the stroma co-evolves with the tumour and creates a dynamic signaling network of paracrine signals that promotes cancer progression. The different stromal components of TME include cancer-associated fibroblasts (CAFs), pericytes, and immune cells, which surround blood vessels and are present in the extracellular matrix (ECM) [24,25]. These stromal cells are recruited to the tumour, and need to adapt to their new environment to allow them to survive. The immune system has evolved to discriminate between normal and malignant cells. It launches immune responses to eliminate damaged or malignant cells and protects the host [26]. Growing evidence suggests that cancer immunosurveillance not only protects the host against the development of primary cancer, but also shapes the immunogenicity of tumours [27,28]. However, upon cancer initiation and formation, tumour cells activate tolerogenic signalling pathways, resulting in cancer immune tolerance and escape from classical immune attack [28,29]. The first generation of antibody-based immunotherapies against so-called immune-checkpoints (Immune-checkpoint blockade or ICB), works by blocking the receptor and/or ligand interactions of molecules, such as CTLA-4 and PD-1, which are involved in dampening T cell activation or function [30]. Unfortunately, ICB therapies have shown significant clinical benefit for only a minority of patients and there is still need to search for novel therapeutic targets.

Within the TME, cancer cells release soluble molecules to activate their own oncogenic signalling for growth and metastasis, and alter the surrounding cells to enhance tumour progression [31]. Macrophages, a major cell population in the TME, play an essential role in immune homeostasis. They are activated and polarized by signals from the TME to become classically-activated (M1) or alternatively-activated (M2) phenotypes [32,33]. A large body of evidence suggests that macrophages within the TME are activated by tumour-derived cytokines into M2-polarized tumour-associated macrophages (TAM), which promote tumour progression and suppress anti-tumour responses [34]. Importantly, therapeutic targeting of macrophages enhances chemotherapy efficacy of platinum-based chemotherapeutics by unleashing type I interferon responses [23].

TAM are either derived from tissue residence, or peripheral reservoirs such as the bone marrow (BM) and spleen [35]. Transcriptome profiling of freshly-isolated TAM suggests that they are similar to those that are involved in development [36]. TAM can contribute to many aspects of cancer development. In particular, they can regulate senescence, interact with and modulate the

extracellular matrix [37,38], promote cancer cell proliferation, invasion and metastasis [39,40] and promote tumor angiogenesis [41,42]. TAMs regulate tumor angiogenesis largely through production of vascular endothelial growth factor (VEGF-A) [43]. Genetic deletion of the VEGF-A gene in macrophages attenuates tumor angiogenesis and results in a morphologically more physiological vasculature [44]. Colegio et al discovered that lactate, as a by-product of aerobic or anaerobic glycolysis, has a critical function in signalling, by inducing the expression of VEGF and the arginase 1 dependent M2-like polarization of TAMs [45]. They demonstrated that lactate-induced VEGF expression in macrophages is mediated by hypoxia-inducible factor 1 α (HIF-1 α). Recently, metabolic analysis coupled with enzyme activity assays, identified that cancer-derived succinate promotes macrophages polarization to M2-like TAMs via the succinate receptor-triggered PI3K-hypoxia-HIF-1 α axis and increases macrophage migration and lung cancer metastasis [46].

In a zebrafish tumour model, innate immune cells (neutrophils and macrophages) were thought to contribute to different steps of tumour progression, including the formation of tumour vasculature and metastasis [47]. In zebrafish embryos, the caudal haematopoietic tissue (CHT) is known as a transient site of haematopoiesis and leukocyte differentiation [48]. The macrophage population of zebrafish embryos has been studied in detail and similarities with human macrophage functions have been reported [49,50]. Therefore, the transparent zebrafish embryonic tumour model is very suitable to dissect how macrophages respond to tumour environmental factors and contribute to angiogenesis.

Zebrafish embryonic tumour xenografts: a model for cancer research

In the last decades, zebrafish (*Danio rerio*) have been applied to the cancer research field, due to several advantages [51]. Benefits include the relatively short generation time of three months, cost-effective maintenance, *ex utero* development, temporal separation between innate and adaptive immunity, transparency and easy manipulation of embryos [52]. Human and zebrafish share a high grade of similarity: 71% of human proteins and 82% of disease-causing human proteins have an orthologue in zebrafish [53]. There is a high conservation of oncogenes and tumour-suppressor genes between zebrafish and humans [54], and various oncogenic transgenic zebrafish lines have been developed [55,56]. The histology of zebrafish tumours has been shown to be highly similar to tumours found in humans [57]. The adaptive immune system in zebrafish does not reach maturity until four weeks post fertilization [58], allowing circumvention of graft rejection by using early stage zebrafish for human or murine cancer cell engraftment. Zebrafish embryos can absorb various small molecular weight compounds from water, allowing easy drug administration, which is advantageous when screening for anti-cancer compounds [59]. Use of transgenic lines with fluorescent vasculature or granulocytes [60] allows live imaging of cancer development and interaction with the microenvironment.

There are several approaches to generate human cancers in zebrafish, such as the development of mutant and transgenic zebrafish lines, and transplantation of tumour cells [51]. Chemical mutagenesis, irradiation mutagenesis, or viral vector mutagenesis as well microinjection of exogenous DNA into one-cell-stage zebrafish embryos can induce transgenic cancer models. Currently, zebrafish genetic cancer models have been developed for many types of cancer e.g. cutaneous melanoma [61], neuroblastoma [62], rhabdomyosarcoma [55], leukaemia (specifically T-ALL) [63] and liver cancer [56,64].

Another approach to generate cancer in zebrafish is the transplantation of tumour cells. The engraftment of murine or human cancer cells into a zebrafish embryo is a fast way to build a new *in vivo* model. The injection site for transplantation can vary, depending on the research purpose. These sites include the Yolk sac, the Duct of Cuvier, the perivitelline space, the hindbrain ventricle, the swimming bladder, and the retro-orbital space [65-76]. This model helps us to understand the processes of angiogenesis, tumour cell extravasation, invasion, metastasis onset as well as interactions with the microenvironment [77]. Interactions between human cancer cells and the zebrafish microenvironment have been extensively described [78-80]. Yi Feng et al observed that H₂O₂ production in oncogene-transformed cells led to leukocyte recruitment and a host inflammatory response that contributes to increased growth of the transformed cells [81]. He et al found that zebrafish neutrophils guide human cancer cell extravasation and invasion by reorganizing the extracellular matrix at the metastatic site at caudal hematopoietic tissue (CHT), the transient site of haematopoiesis and leukocyte differentiation [47,48]. The motility and adhesion of zebrafish neutrophils during metastatic niche preparation is orchestrated by the CXCR4 receptor, which is expressed on zebrafish neutrophils [47]. Next, Tulotta et al proved that engrafted human cancer cells expressing the CXCR4 receptor can sense the host's (zebrafish) CXCL-12 ligand, which is produced by mesenchymal stem cells in zebrafish CHT [82], inducing metastatic colonization [29,30]. Targeting of either CXCR-4 (the CXCL-12 receptor) in breast human cancer cells and zebrafish neutrophils or CXCL-12 in zebrafish significantly inhibited extravasation and metastatic tumour growth at the CHT area. Britto et al used an embryonic zebrafish xenograft model to show that zebrafish macrophages can enhance VEGF-A-driven tumour angiogenesis [83]. Moreover, human cancer cells can comparably respond to the microenvironment of zebrafish and mice, by inducing activation of the NF-κB–Activin A signalling axis, which drives the metastatic cancer stem cell (CSC)-like phenotype of prostate cancer cells [84]. Transplantation of zebrafish BRAFV600E-driven melanoma cells into *casper* fish showed that the degree of pigmentation is a key feature defining cells with metastatic capability [85]. De Sousa Pontes et al used (fli:GFP) *Casper* zebrafish embryos to establish a model for human conjunctival melanoma [86]. Heilmann et al used transparent *Casper* zebrafish to generate single-cell resolution of the metastatic process to evaluate the tumour cell's metastatic ability [85]. Importantly, several groups described successful xenotransplantation of human patient samples into zebrafish larvae for phenotypic testing of drug responses [87].

Zebrafish embryonic tumour xenograft model for drug discovery

Perhaps the most promising application of the zebrafish xenograft model is the ability to perform high-throughput drug screening on human cancer cells and samples in a way that is not possible using any other model organism. Larvae absorb drugs from the water through the skin and oral, enhancing the simplicity of drug administration [88]. Because embryos are maintained in 96-well plates, typically in 100–300 μL of water, screens require smaller drug quantities compared to mice. The efficacy of drugs can be quantified by live imaging of the tumour burden by fluorescence microscope [89,90]. Several research groups have also applied xenotransplantation methods to zebrafish, for the study of human cancer cell behavior, responses to therapy, within the context of the whole organism [91]. The different cell lines so far tested in xenotransplantation are cutaneous melanoma [92], conjunctival and uveal melanoma, colorectal cancer [93], breast cancer [87], leukemia [94], ovarian cancer [95], neuroblastoma [96], pancreatic cancer [97], prostate cancer [51], and sarcoma [92]. Typically, cells are dye labeled to allow their identification within the living host and their growth, and to follow their infiltration into host tissues, monitored over two to five days. Treatment of engrafted embryos with drugs can result in graft stasis or regression, mirroring outcomes that can be observed in more costly and lengthier mouse xenograft experiments [98].

The technique of xenotransplantation into zebrafish can also be used with patient-derived tissues, which has been demonstrated previously for pancreatic adenocarcinoma, prostate cancer, and leukemia [87,99,100]. The total sample needed for this approach could be as little as 100 cells. The time for engraftment is between two and three days after fertilization. Given these characteristics, patient-derived xenografts (PDX) in zebrafish (zPDX) could be tools to predict patient responses to drug treatments. The valuable biopsy tissue from a patient could be injected into scores of zebrafish embryos potentially with different reporter constructs in the background and different treatments applied to select the most suitable clinical intervention. However, more proof-of-principle studies are needed to fully evaluate the value of zebrafish PDX models. Recently, development of immunodeficient zebrafish enabled the development of zPDX in adult zebrafish [100]. This approach is probably the most relevant when looking at it from a translational perspective and may in the near future provide fast and reliable assessments for personalized treatments and precision cancer therapy. Today, eight small molecules identified from zebrafish studies have been advanced into clinical trials, illustrating the ability to move fundamental discoveries from zebrafish to human [101].

Zebrafish embryonic tumour xenograft model for photodynamic dynamic therapy (PDT) and photoactivated chemotherapy (PACT) testing

Another approach to treat cancer is to accumulate photosensitizers (PSs) in tumour tissue followed by the light-induced generation of cytotoxic reactive oxygen species (ROS) to kill the tumour cells.

Photodynamic therapy (PDT) is a clinically-approved treatment in which the drugs only work after they have been “activated” or “switched on” by light. There are several types of PDT. Type II PDT is

oxygen-dependent meaning that the energy of the excited photosensitizer PS* could be transferred into the O₂ molecules in the irradiated tissues. Such energy transfer produces the excited state of O₂ called “singlet oxygen”, which is highly oxidative and leads to cell death via damage of DNA, proteins, and lipids (Fig. 2). Thus, PDT type II relies not only on light irradiation, but also on the local presence of dioxygen in the irradiated tumour tissue. Usually PDT type II ceases to work when the oxygen supply to the irradiated tissues is too low, for example in hypoxic tumours, or when the light intensity is too high [102].

Type I PDT consists of the generation of radical species via electron transfer from the excited photosensitizer PS* to O₂, which typically generates the superoxide radical O₂^{•-} and, by cascade reactions, other types of radical oxygen species (Fig. 2). Usually PDT type I is therefore also oxygen-dependent, but in some cases electron transfer can happen directly from PS* to DNA or proteins to create radicals, without the involvement of dioxygen. In this case, PDT type I can also work in hypoxic conditions [103].

Photoactivated chemotherapy (PACT) relies on the oxygen-independent activation by light of a pro-drug, turning a poorly toxic molecule into a much more toxic species. Metal-based PACT compounds are based on a heavy metal centre such as ruthenium (II) [82,104]. In some aspects, ruthenium (II) is similar to platinum (II), found for example in cisplatin, but it has photochemical properties: when coordinated to an appropriate ligand set, it can photosubstitute some of the ligands bound to it, i.e. replace them by water molecules, as shown in the figure below. Water is poorly bound to heavy metal ions, so that biological molecules such as DNA, lipids, or proteins can bind to the aqua metal photoproduct, thereby creating metallated DNA or inhibiting proteins, which kill cancer cells. This metal binding of biomolecules cannot occur in the dark because the ligands protect the metal ion. Thus, the molecule is more toxic after light irradiation. A second form of PACT consists of using photo-substitutional active ruthenium compounds where the liberated ligands bear the toxicity, rather than the metal-based photoproduct. This second form of PACT is sometimes called “photocaging”: the ruthenium complex appears as a “caging group”, and the ruthenium-ligand prodrug is called a “ruthenium-caged” cytotoxin [82].

In PACT, whether the toxicity after light activation is due to the metal-containing photoproduct or to the ligand, the activation mechanism does not involve O₂. Thus, PACT should be suitable for phototherapy of hypoxic tumours, where PDT usually fails. This idea has been demonstrated *in vitro* by the Bonnet group [105].

For light-activated compounds (whether PDT or PACT) the photoindex, defined as $PI = EC_{50(\text{dark})}/EC_{50(\text{light})}$, characterizes the enhanced toxicity upon irradiation in a given set of conditions (and with a given cell testing protocol). $EC_{50(\text{dark})}$ and $EC_{50(\text{light})}$ are cell growth inhibition effective

concentration values, ie concentrations that prevent 50% of cancer cell growth, compared to drug-free control.

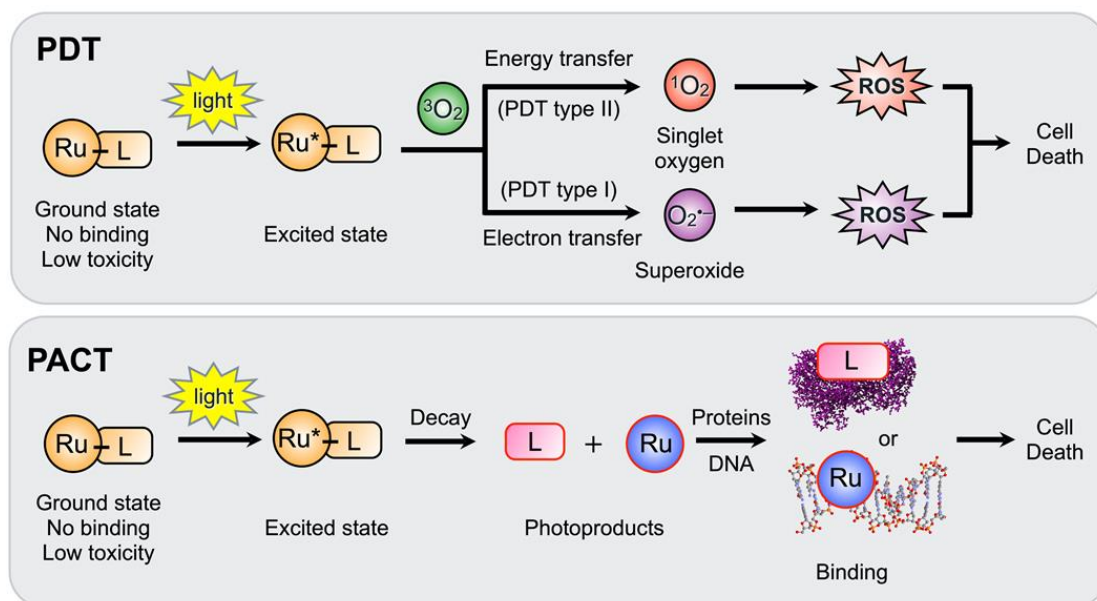


Fig. 2 Scheme of PDT and PACT compound mechanisms.

The zebrafish liver tumour model was used as an *in vivo* platform to investigate the biodistribution of fluorescent PS and the therapeutic efficiency of theranostic polymer-encapsulated nanoparticles to carry out PDT [106]. The first photoswitchable inhibitor of human dihydrofolate reductase (DHFR) has been developed as a potent chemotherapy drug as determined in a zebrafish model [107]. In addition, this animal model has been increasingly utilized to assess the toxicity of nanoparticles. The acute and chronic toxic effects of metal nanoparticles, including Au, Ag, Cu, and metal oxide nanoparticles, such as TiO_2 , Al_2O_3 , CuO, NiO and ZnO were measured [108]. Moreover, this model allowed assessment of off-target organ toxicities including immunotoxicity, developmental toxicity, neurotoxicity, reproductive toxicity, cardiovascular toxicity and hepatotoxicity [109]. Wehmas et al used embryonic zebrafish to investigate the toxicity of engineered metal oxide nanoparticles [110].

A Zebrafish embryonic tumour xenograft model for nanomedicine optimization and delivery

Recently, zebrafish stood out as a tool to develop and test new drug administration strategies of nanomedicines. Nanomedicine toxicity, biodistribution and systemic circulation, stability, functionality and targeting efficiency have all been successfully assessed within the complex biological, *in vivo* environment of living zebrafish larvae. The potential value of the zebrafish model for anti-cancer nanomedicine development has been demonstrated by many studies [111-113]. Most studies measured the toxicity and safety of blank nanoparticles (mostly liposomes) prior to drug incorporation. Taking advantage of the embryo's transparency, biodistribution studies have also been performed to determine the ability of the nanocarriers to reach the target site, and to even pass the blood-brain barrier [114]. Apart from determining these critical parameters, the zebrafish xenograft

model has also been proven useful in the study of the interaction between drug-loaded nanocarriers and xenografted cells. For example, Yang and collaborators described the application of coiled coil peptides in liposomal anticancer drug delivery using the zebrafish xenograft model [111]. The work of Evensen and collaborators addressed the ability of PEGylated nanocarriers to avoid uptake by macrophages, a fact that translates in improved circulation time and increased accumulation into tumours [112]. The ultimate goal of nano-delivery methodologies is cell-specific targeting, yet on-target uptake is approximately 1% of all injected nanoparticles [115] due to off-target interaction in the liver [116] and scavenger endothelial cells (SECs) of various tissues (e.g. kidney, heart and gills). Zebrafish whole-body 4D intravital imaging was applied to monitor the distribution of fluorescent liposomes with cellular resolution in near real-time [117]. The tested liposomes accumulated on endothelial cells. Dextran sulphate (a competitive inhibitor of stab-2 scavenger receptors) and *stab2* mutants led to a dramatic increase in the concentration of freely-circulating liposomes due to diminished stab-2 scavenger receptor binding. This study provided evidence that anionic liposomes are an ideal delivery system for targeting cells overexpressing stab-2 (such as SECs) and that inhibiting nanoparticles-SEC interactions may serve to enhance bioavailability of numerous nanocarrier classes.

Thesis outline

In this thesis, we will utilize embryonic zebrafish tumour models to understand the interaction between engrafted human cancer cells and macrophages from the host, test drug administration modalities and anti-cancer efficacies of newly-developed PDT and PACT compounds, and test a light-triggered liposomal system for targeted drug delivery specifically to cancer cells *in vivo*.

In **chapter 2**, we investigate the role of macrophages in tumour-induced angiogenesis. We show that macrophage-dependent angiogenesis is driven by macrophage recruitment to lactic acid secreted by glycolytic B16 melanoma cells. Chemical inhibition of macrophages and glycolysis blocks the initiation of angiogenesis in these models, suggesting that macrophages attracted to glycolytic melanoma cells contribute to the tumour-induced angiogenesis process.

In **chapters 3 and 4**, we explore novel PDT and PACT compounds, respectively, for treatment of conjunctival melanoma in zebrafish. We inject conjunctival melanoma cells into the retro-orbital site to establish an orthotopic model and into the Duct of Cuvier to generate an ectopic model. Our results prove that zebrafish provides a fast vertebrate cancer model to test the optimal administration regimen of drugs, conditions of light irradiation, host toxicity and anti-cancer efficacy of PDT and PACT drugs against conjunctival melanoma.

In **chapter 5**, we focus on modifying liposomes to be light triggered in order to deliver drugs specifically to cancer cells. We inject MDA231 breast cancer cells into the Duct of Cuvier at 2 days

post fertilization (dpf) to initiate metastasis to the CHT. We successfully demonstrate that light-triggered, cell-specific delivery of liposome-encapsulated doxorubicin reduces the xenograft cancer cell burden without enhanced cytotoxicity of the zebrafish embryos.

In **chapter 6**, we summarize the novel anti-cancer strategies, which we have developed using zebrafish xenograft models. In the same chapter, we frame our findings in the current scientific landscape and discuss future perspectives.

References

1. Bray, F.; Ferlay, J.; Soerjomataram, I.; Siegel, R.L.; Torre, L.A.; Jemal, A. Global cancer statistics 2018: GLOBOCAN estimates of incidence and mortality worldwide for 36 cancers in 185 countries. *CA: a cancer journal for clinicians* **2018**, *68*, 394-424, doi:10.3322/caac.21492.
2. Hanahan, D.; Weinberg, R.A. Hallmarks of cancer: the next generation. *Cell* **2011**, *144*, 646-674, doi:10.1016/j.cell.2011.02.013.
3. Valkenburg, K.C.; de Groot, A.E.; Pienta, K.J. Targeting the tumour stroma to improve cancer therapy. *Nature reviews. Clinical oncology* **2018**, *15*, 366-381, doi:10.1038/s41571-018-0007-1.
4. Lord, C.J.; Ashworth, A. The DNA damage response and cancer therapy. *Nature* **2012**, *481*, 287-294, doi:10.1038/nature10760.
5. Cheng, N.; Chytil, A.; Shyr, Y.; Joly, A.; Moses, H.L. Transforming growth factor-beta signaling-deficient fibroblasts enhance hepatocyte growth factor signaling in mammary carcinoma cells to promote scattering and invasion. *Molecular cancer research : MCR* **2008**, *6*, 1521-1533, doi:10.1158/1541-7786.mcr-07-2203.
6. Burkhart, D.L.; Sage, J. Cellular mechanisms of tumour suppression by the retinoblastoma gene. *Nature reviews. Cancer* **2008**, *8*, 671-682, doi:10.1038/nrc2399.
7. Adams, J.M.; Cory, S. The Bcl-2 apoptotic switch in cancer development and therapy. *Oncogene* **2007**, *26*, 1324-1337, doi:10.1038/sj.onc.1210220.
8. Blasco, M.A. Telomeres and human disease: ageing, cancer and beyond. *Nature reviews. Genetics* **2005**, *6*, 611-622, doi:10.1038/nrg1656.
9. Li, T.; Kang, G.; Wang, T.; Huang, H. Tumor angiogenesis and anti-angiogenic gene therapy for cancer. *Oncology letters* **2018**, *16*, 687-702, doi:10.3892/ol.2018.8733.
10. Valastyan, S.; Weinberg, R.A. Tumor metastasis: molecular insights and evolving paradigms. *Cell* **2011**, *147*, 275-292, doi:10.1016/j.cell.2011.09.024.
11. Wu, C.I.; Wang, H.Y.; Ling, S.; Lu, X. The Ecology and Evolution of Cancer: The Ultra-Microevolutionary Process. *Annu Rev Genet* **2016**, *50*, 347-369, doi:10.1146/annurev-genet-112414-054842.
12. Bergers, G.; Benjamin, L.E. Tumorigenesis and the angiogenic switch. *Nat Rev Cancer* **2003**, *3*, 401-410, doi:10.1038/nrc1093.
13. Jayson, G.C.; Kerbel, R.; Ellis, L.M.; Harris, A.L. Antiangiogenic therapy in oncology: current status and future directions. *Lancet (London, England)* **2016**, *388*, 518-529, doi:10.1016/s0140-6736(15)01088-0.
14. Zhang, Y.; Weinberg, R.A. Epithelial-to-mesenchymal transition in cancer: complexity and opportunities. *Frontiers of medicine* **2018**, *12*, 361-373, doi:10.1007/s11684-018-0656-6.
15. Massagué, J.; Obenauf, A.C. Metastatic colonization by circulating tumour cells. *Nature* **2016**, *529*, 298-306, doi:10.1038/nature17038.
16. Warburg, O. On the origin of cancer cells. *Science (New York, N.Y.)* **1956**, *123*, 309-314, doi:10.1126/science.123.3191.309.
17. Ward, P.S.; Thompson, C.B. Metabolic reprogramming: a cancer hallmark even warburg did not anticipate. *Cancer Cell* **2012**, *21*, 297-308, doi:10.1016/j.ccr.2012.02.014.
18. Vander Heiden, M.G.; Cantley, L.C.; Thompson, C.B. Understanding the Warburg effect: the metabolic requirements of cell proliferation. *Science (New York, N.Y.)* **2009**, *324*, 1029-1033,

- doi:10.1126/science.1160809.
19. Hensley, C.T.; Faubert, B.; Yuan, Q.; Lev-Cohain, N.; Jin, E.; Kim, J.; Jiang, L.; Ko, B.; Skelton, R.; Loudat, L., et al. Metabolic Heterogeneity in Human Lung Tumors. *Cell* **2016**, *164*, 681-694, doi:10.1016/j.cell.2015.12.034.
 20. Colegio, O.R.; Chu, N.Q.; Szabo, A.L.; Chu, T.; Rhebergen, A.M.; Jairam, V.; Cyrus, N.; Brokowski, C.E.; Eisenbarth, S.C.; Phillips, G.M., et al. Functional polarization of tumour-associated macrophages by tumour-derived lactic acid. *Nature* **2014**, *513*, 559-563, doi:10.1038/nature13490.
 21. Dang, L.; White, D.W.; Gross, S.; Bennett, B.D.; Bittinger, M.A.; Driggers, E.M.; Fantin, V.R.; Jang, H.G.; Jin, S.; Keenan, M.C., et al. Cancer-associated IDH1 mutations produce 2-hydroxyglutarate. *Nature* **2010**, *465*, 966, doi:10.1038/nature09132.
 22. Binnewies, M.; Roberts, E.W.; Kersten, K.; Chan, V.; Fearon, D.F.; Merad, M.; Coussens, L.M.; Gabrilovich, D.I.; Ostrand-Rosenberg, S.; Hedrick, C.C., et al. Understanding the tumor immune microenvironment (TIME) for effective therapy. *Nature medicine* **2018**, *24*, 541-550, doi:10.1038/s41591-018-0014-x.
 23. Salvagno, C.; Ciampricotti, M.; Tuit, S.; Hau, C.S.; van Weverwijk, A.; Coffelt, S.B.; Kersten, K.; Vrijland, K.; Kos, K.; Ulas, T., et al. Therapeutic targeting of macrophages enhances chemotherapy efficacy by unleashing type I interferon response. *Nature cell biology* **2019**, *21*, 511-521, doi:10.1038/s41556-019-0298-1.
 24. Grivennikov, S.I.; Greten, F.R.; Karin, M. Immunity, inflammation, and cancer. *Cell* **2010**, *140*, 883-899, doi:10.1016/j.cell.2010.01.025.
 25. Ridnour, L.A.; Cheng, R.Y.; Switzer, C.H.; Heinecke, J.L.; Ambbs, S.; Glynn, S.; Young, H.A.; Trinchieri, G.; Wink, D.A. Molecular pathways: toll-like receptors in the tumor microenvironment--poor prognosis or new therapeutic opportunity. *Clinical cancer research : an official journal of the American Association for Cancer Research* **2013**, *19*, 1340-1346, doi:10.1158/1078-0432.ccr-12-0408.
 26. Murray, P.J.; Smale, S.T. Restraint of inflammatory signaling by interdependent strata of negative regulatory pathways. *Nature immunology* **2012**, *13*, 916-924, doi:10.1038/ni.2391.
 27. de Visser, K.E.; Eichten, A.; Coussens, L.M. Paradoxical roles of the immune system during cancer development. *Nat Rev Cancer* **2006**, *6*, 24-37, doi:10.1038/nrc1782.
 28. Dunn, G.P.; Old, L.J.; Schreiber, R.D. The immunobiology of cancer immunosurveillance and immunoediting. *Immunity* **2004**, *21*, 137-148, doi:10.1016/j.immuni.2004.07.017.
 29. Yu, J.; Vodyanik, M.A.; Smuga-Otto, K.; Antosiewicz-Bourget, J.; Frane, J.L.; Tian, S.; Nie, J.; Jonsdottir, G.A.; Ruotti, V.; Stewart, R., et al. Induced pluripotent stem cell lines derived from human somatic cells. *Science (New York, N.Y.)* **2007**, *318*, 1917-1920, doi:10.1126/science.1151526.
 30. Topalian, S.L.; Drake, C.G.; Pardoll, D.M. Immune checkpoint blockade: a common denominator approach to cancer therapy. *Cancer Cell* **2015**, *27*, 450-461, doi:10.1016/j.ccell.2015.03.001.
 31. Singh, R.; Mishra, M.K.; Aggarwal, H. Inflammation, Immunity, and Cancer. *Mediators of inflammation* **2017**, *2017*, 6027305, doi:10.1155/2017/6027305.
 32. Biswas, S.K.; Mantovani, A. Orchestration of metabolism by macrophages. *Cell metabolism* **2012**, *15*, 432-437, doi:10.1016/j.cmet.2011.11.013.
 33. Biswas, S.K.; Allavena, P.; Mantovani, A. Tumor-associated macrophages: functional diversity, clinical significance, and open questions. *Seminars in immunopathology* **2013**, *35*, 585-600, doi:10.1007/s00281-013-0367-7.
 34. Chanmee, T.; Ontong, P.; Konno, K.; Itano, N. Tumor-associated macrophages as major players in the tumor microenvironment. *Cancers* **2014**, *6*, 1670-1690, doi:10.3390/cancers6031670.
 35. Quail, D.F.; Joyce, J.A. Microenvironmental regulation of tumor progression and metastasis. *Nat Med* **2013**, *19*, 1423-1437, doi:10.1038/nm.3394.
 36. Ojalvo, L.S.; King, W.; Cox, D.; Pollard, J.W. High-density gene expression analysis of tumor-associated macrophages from mouse mammary tumors. *Am J Pathol* **2009**, *174*, 1048-1064, doi:10.2353/ajpath.2009.080676.
 37. Mantovani, A.; Allavena, P.; Sica, A.; Balkwill, F. Cancer-related inflammation. *Nature* **2008**, *454*, 436-444, doi:10.1038/nature07205.
 38. Pickup, M.W.; Mouw, J.K.; Weaver, V.M. The extracellular matrix modulates the hallmarks of

- cancer. *EMBO reports* **2014**, *15*, 1243-1253, doi:10.15252/embr.201439246.
39. Lin, J.Y.; Li, X.Y.; Tadashi, N.; Dong, P. Clinical significance of tumor-associated macrophage infiltration in supraglottic laryngeal carcinoma. *Chinese journal of cancer* **2011**, *30*, 280-286, doi:10.5732/cjc.010.10336.
 40. Roh-Johnson, M.; Shah, A.N.; Stonick, J.A.; Poudel, K.R.; Kargl, J.; Yang, G.H.; di Martino, J.; Hernandez, R.E.; Gast, C.E.; Zarour, L.R., et al. Macrophage-Dependent Cytoplasmic Transfer during Melanoma Invasion In Vivo. *Dev Cell* **2017**, *43*, 549-562 e546, doi:10.1016/j.devcel.2017.11.003.
 41. Clear, A.J.; Lee, A.M.; Calaminici, M.; Ramsay, A.G.; Morris, K.J.; Hallam, S.; Kelly, G.; Macdougall, F.; Lister, T.A.; Gribben, J.G. Increased angiogenic sprouting in poor prognosis FL is associated with elevated numbers of CD163+ macrophages within the immediate sprouting microenvironment. *Blood* **2010**, *115*, 5053-5056, doi:10.1182/blood-2009-11-253260.
 42. Lin, E.Y.; Li, J.F.; Gnatovskiy, L.; Deng, Y.; Zhu, L.; Grzesik, D.A.; Qian, H.; Xue, X.N.; Pollard, J.W. Macrophages regulate the angiogenic switch in a mouse model of breast cancer. *Cancer Res* **2006**, *66*, 11238-11246, doi:10.1158/0008-5472.CAN-06-1278.
 43. Lin, E.Y.; Li, J.F.; Bricard, G.; Wang, W.; Deng, Y.; Sellers, R.; Porcelli, S.A.; Pollard, J.W. Vascular endothelial growth factor restores delayed tumor progression in tumors depleted of macrophages. *Mol Oncol* **2007**, *1*, 288-302, doi:10.1016/j.molonc.2007.10.003.
 44. Stockmann, C.; Doedens, A.; Weidemann, A.; Zhang, N.; Takeda, N.; Greenberg, J.I.; Cheresch, D.A.; Johnson, R.S. Deletion of vascular endothelial growth factor in myeloid cells accelerates tumorigenesis. *Nature* **2008**, *456*, 814-818, doi:10.1038/nature07445.
 45. Mu, X.; Shi, W.; Xu, Y.; Xu, C.; Zhao, T.; Geng, B.; Yang, J.; Pan, J.; Hu, S.; Zhang, C., et al. Tumor-derived lactate induces M2 macrophage polarization via the activation of the ERK/STAT3 signaling pathway in breast cancer. *Cell cycle (Georgetown, Tex.)* **2018**, *17*, 428-438, doi:10.1080/15384101.2018.1444305.
 46. Wu, J.Y.; Huang, T.W.; Hsieh, Y.T.; Wang, Y.F.; Yen, C.C.; Lee, G.L.; Yeh, C.C.; Peng, Y.J.; Kuo, Y.Y.; Wen, H.T., et al. Cancer-Derived Succinate Promotes Macrophage Polarization and Cancer Metastasis via Succinate Receptor. *Molecular cell* **2020**, *77*, 213-227.e215, doi:10.1016/j.molcel.2019.10.023.
 47. He, S.; Lamers, G.E.; Beenakker, J.W.; Cui, C.; Ghotra, V.P.; Danen, E.H.; Meijer, A.H.; Spaink, H.P.; Snaar-Jagalska, B.E. Neutrophil-mediated experimental metastasis is enhanced by VEGFR inhibition in a zebrafish xenograft model. *The Journal of pathology* **2012**, *227*, 431-445, doi:10.1002/path.4013.
 48. Chen, A.T.; Zon, L.I. Zebrafish blood stem cells. *Journal of cellular biochemistry* **2009**, *108*, 35-42, doi:10.1002/jcb.22251.
 49. Kissa, K.; Herbomel, P. Blood stem cells emerge from aortic endothelium by a novel type of cell transition. *Nature* **2010**, *464*, 112-115, doi:10.1038/nature08761.
 50. Bertrand, J.Y.; Chi, N.C.; Santoso, B.; Teng, S.; Stainier, D.Y.; Traver, D. Haematopoietic stem cells derive directly from aortic endothelium during development. *Nature* **2010**, *464*, 108-111, doi:10.1038/nature08738.
 51. Letrado, P.; de Miguel, I.; Lamberto, I.; Díez-Martínez, R.; Oyarzabal, J. Zebrafish: Speeding Up the Cancer Drug Discovery Process. *Cancer Res* **2018**, *78*, 6048-6058, doi:10.1158/0008-5472.can-18-1029.
 52. Berghmans, S.; Jette, C.; Langenau, D.; Hsu, K.; Stewart, R.; Look, T.; Kanki, J.P. Making waves in cancer research: new models in the zebrafish. *BioTechniques* **2005**, *39*, 227-237, doi:10.2144/05392rv02.
 53. Lam, S.H.; Wu, Y.L.; Vega, V.B.; Miller, L.D.; Spitsbergen, J.; Tong, Y.; Zhan, H.; Govindarajan, K.R.; Lee, S.; Mathavan, S., et al. Conservation of gene expression signatures between zebrafish and human liver tumors and tumor progression. *Nature biotechnology* **2006**, *24*, 73-75, doi:10.1038/nbt1169.
 54. White, R.; Rose, K.; Zon, L. Zebrafish cancer: the state of the art and the path forward. *Nat Rev Cancer* **2013**, *13*, 624-636, doi:10.1038/nrc3589.
 55. Kendall, G.C.; Watson, S.; Xu, L.; LaVigne, C.A.; Murchison, W.; Rakheja, D.; Skapek, S.X.; Tirode, F.; Delattre, O.; Amatruda, J.F. PAX3-FOXO1 transgenic zebrafish models identify HES3 as a mediator of rhabdomyosarcoma tumorigenesis. *eLife* **2018**, *7*, doi:10.7554/eLife.33800.

56. Li, Y.; Agrawal, I.; Gong, Z. Reversion of tumor hepatocytes to normal hepatocytes during liver tumor regression in an oncogene-expressing transgenic zebrafish model. *Disease models & mechanisms* **2019**, *12*, doi:10.1242/dmm.039578.
57. Etchin, J.; Kanki, J.P.; Look, A.T. Zebrafish as a model for the study of human cancer. *Methods in cell biology* **2011**, *105*, 309-337, doi:10.1016/b978-0-12-381320-6.00013-8.
58. Novoa, B.; Figueras, A. Zebrafish: model for the study of inflammation and the innate immune response to infectious diseases. *Advances in experimental medicine and biology* **2012**, *946*, 253-275, doi:10.1007/978-1-4614-0106-3_15.
59. Huiting, L.N.; Laroche, F.; Feng, H. The Zebrafish as a Tool to Cancer Drug Discovery. *Austin journal of pharmacology and therapeutics* **2015**, *3*, 1069.
60. Proulx, K.; Lu, A.; Sumanas, S. Cranial vasculature in zebrafish forms by angioblast cluster-derived angiogenesis. *Dev Biol* **2010**, *348*, 34-46, doi:10.1016/j.ydbio.2010.08.036.
61. Kaufman, C.K.; Mosimann, C.; Fan, Z.P.; Yang, S.; Thomas, A.J.; Ablain, J.; Tan, J.L.; Fogley, R.D.; van Rooijen, E.; Hagedorn, E.J., et al. A zebrafish melanoma model reveals emergence of neural crest identity during melanoma initiation. *Science (New York, N.Y.)* **2016**, *351*, aad2197, doi:10.1126/science.aad2197.
62. Zhu, S.; Thomas Look, A. Neuroblastoma and Its Zebrafish Model. *Advances in experimental medicine and biology* **2016**, *916*, 451-478, doi:10.1007/978-3-319-30654-4_20.
63. Burns, M.A.; Liao, Z.W.; Yamagata, N.; Pouliot, G.P.; Stevenson, K.E.; Neuberger, D.S.; Thorner, A.R.; Ducar, M.; Silverman, E.A.; Hunger, S.P., et al. Hedgehog pathway mutations drive oncogenic transformation in high-risk T-cell acute lymphoblastic leukemia. *Leukemia* **2018**, *32*, 2126-2137, doi:10.1038/s41375-018-0097-x.
64. Yang, Q.; Salim, L.; Yan, C.; Gong, Z. Rapid Analysis of Effects of Environmental Toxicants on Tumorigenesis and Inflammation Using a Transgenic Zebrafish Model for Liver Cancer. *Marine biotechnology (New York, N.Y.)* **2019**, *21*, 396-405, doi:10.1007/s10126-019-09889-8.
65. Drabsch, Y.; ten Dijke, P. TGF-beta signalling and its role in cancer progression and metastasis. *Cancer metastasis reviews* **2012**, *31*, 553-568, doi:10.1007/s10555-012-9375-7.
66. Haldi, M.; Ton, C.; Seng, W.L.; McGrath, P. Human melanoma cells transplanted into zebrafish proliferate, migrate, produce melanin, form masses and stimulate angiogenesis in zebrafish. *Angiogenesis* **2006**, *9*, 139-151, doi:10.1007/s10456-006-9040-2.
67. Naber, H.P.; Drabsch, Y.; Snaar-Jagalska, B.E.; ten Dijke, P.; van Laar, T. Snail and Slug, key regulators of TGF-beta-induced EMT, are sufficient for the induction of single-cell invasion. *Biochemical and biophysical research communications* **2013**, *435*, 58-63, doi:10.1016/j.bbrc.2013.04.037.
68. Navis, A.; Bagnat, M. Loss of cfr function leads to pancreatic destruction in larval zebrafish. *Dev Biol* **2015**, *399*, 237-248, doi:10.1016/j.ydbio.2014.12.034.
69. Nicoli, S.; Presta, M. The zebrafish/tumor xenograft angiogenesis assay. *Nature protocols* **2007**, *2*, 2918-2923, doi:10.1038/nprot.2007.412.
70. Nicoli, S.; Ribatti, D.; Cotelli, F.; Presta, M. Mammalian tumor xenografts induce neovascularization in zebrafish embryos. *Cancer Res* **2007**, *67*, 2927-2931, doi:10.1158/0008-5472.can-06-4268.
71. Tobia, C.; De Sena, G.; Presta, M. Zebrafish embryo, a tool to study tumor angiogenesis. *The International journal of developmental biology* **2011**, *55*, 505-509, doi:10.1387/ijdb.103238ct.
72. van der Ent, W.; Burrello, C.; Teunisse, A.F.; Ksander, B.R.; van der Velden, P.A.; Jager, M.J.; Jochemsen, A.G.; Snaar-Jagalska, B.E. Modeling of human uveal melanoma in zebrafish xenograft embryos. *Investigative ophthalmology & visual science* **2014**, *55*, 6612-6622, doi:10.1167/iovs.14-15202.
73. van der Ent, W.; Jochemsen, A.G.; Teunisse, A.F.; Krens, S.F.; Szuhai, K.; Spaink, H.P.; Hogendoorn, P.C.; Snaar-Jagalska, B.E. Ewing sarcoma inhibition by disruption of EWSR1-FLI1 transcriptional activity and reactivation of p53. *J Pathol* **2014**, *233*, 415-424, doi:10.1002/path.4378.
74. Wang, J.; Cao, Z.; Zhang, X.M.; Nakamura, M.; Sun, M.; Hartman, J.; Harris, R.A.; Sun, Y.; Cao, Y. Novel mechanism of macrophage-mediated metastasis revealed in a zebrafish model of tumor development. *Cancer Res* **2015**, *75*, 306-315, doi:10.1158/0008-5472.can-14-2819.
75. Wehmas, L.C.; Tanguay, R.L.; Punnoose, A.; Greenwood, J.A. Developing a Novel Embryo-Larval Zebrafish Xenograft Assay to Prioritize Human Glioblastoma Therapeutics. *Zebrafish*

- 2016**, *13*, 317-329, doi:10.1089/zeb.2015.1170.
76. Tang, Q.; Moore, J.C.; Ignatius, M.S.; Tenente, I.M.; Hayes, M.N.; Garcia, E.G.; Torres Yordan, N.; Bourque, C.; He, S.; Blackburn, J.S., et al. Imaging tumour cell heterogeneity following cell transplantation into optically clear immune-deficient zebrafish. *Nat Commun* **2016**, *7*, 10358, doi:10.1038/ncomms10358.
 77. Hill, D.; Chen, L.; Snaar-Jagalska, E.; Chaudhry, B. Embryonic zebrafish xenograft assay of human cancer metastasis. *F1000Research* **2018**, *7*, 1682, doi:10.12688/f1000research.16659.2.
 78. Astell, K.R.; Sieger, D. Zebrafish In Vivo Models of Cancer and Metastasis. *Cold Spring Harbor perspectives in medicine* **2019**, 10.1101/cshperspect.a037077, doi:10.1101/cshperspect.a037077.
 79. Chen, L.; Groenewoud, A.; Tulotta, C.; Zoni, E.; Kruihof-de Julio, M.; van der Horst, G.; van der Pluijm, G.; Ewa Snaar-Jagalska, B. A zebrafish xenograft model for studying human cancer stem cells in distant metastasis and therapy response. *Methods in cell biology* **2017**, *138*, 471-496, doi:10.1016/bs.mcb.2016.10.009.
 80. Kim, I.S.; Heilmann, S.; Kansler, E.R.; Zhang, Y.; Zimmer, M.; Ratnakumar, K.; Bowman, R.L.; Simon-Vermot, T.; Fennell, M.; Garippa, R., et al. Microenvironment-derived factors driving metastatic plasticity in melanoma. *Nature communications* **2017**, *8*, 14343, doi:10.1038/ncomms14343.
 81. Feng, Y.; Santoriello, C.; Mione, M.; Hurlstone, A.; Martin, P. Live imaging of innate immune cell sensing of transformed cells in zebrafish larvae: parallels between tumor initiation and wound inflammation. *PLoS Biol* **2010**, *8*, e1000562, doi:10.1371/journal.pbio.1000562.
 82. Bonnet, S. Why develop photoactivated chemotherapy? *Dalton transactions (Cambridge, England : 2003)* **2018**, *47*, 10330-10343, doi:10.1039/c8dt01585f.
 83. Britto, D.D.; Wyroba, B.; Chen, W.; Lockwood, R.A.; Tran, K.B.; Shepherd, P.R.; Hall, C.J.; Crosier, K.E.; Crosier, P.S.; Astin, J.W. Macrophages enhance Vegfa-driven angiogenesis in an embryonic zebrafish tumour xenograft model. *Disease models & mechanisms* **2018**, *11*, doi:10.1242/dmm.035998.
 84. Chen, L.; De Menna, M.; Groenewoud, A.; Thalmann, G.N.; Kruihof-de Julio, M.; Snaar-Jagalska, B.E. A NF- κ B-Activin A signaling axis enhances prostate cancer metastasis. *Oncogene* **2020**, *39*, 1634-1651, doi:10.1038/s41388-019-1103-0.
 85. Heilmann, S.; Ratnakumar, K.; Langdon, E.; Kansler, E.; Kim, I.; Campbell, N.R.; Perry, E.; McMahon, A.; Kaufman, C.; van Rooijen, E., et al. A Quantitative System for Studying Metastasis Using Transparent Zebrafish. *Cancer Res* **2015**, *75*, 4272-4282, doi:10.1158/0008-5472.can-14-3319.
 86. Pontes, K.C.S.; Groenewoud, A.; Cao, J.; Ataide, L.M.S.; Snaar-Jagalska, E.; Jager, M.J. Evaluation of (fli:GFP) Casper Zebrafish Embryos as a Model for Human Conjunctival Melanoma. *Invest Ophthalmol Vis Sci* **2017**, *58*, 6065-6071, doi:10.1167/iovs.17-22023.
 87. Mercatali, L.; La Manna, F.; Groenewoud, A.; Casadei, R.; Recine, F.; Miseroocchi, G.; Pieri, F.; Liverani, C.; Bongiovanni, A.; Spadazzi, C., et al. Development of a Patient-Derived Xenograft (PDX) of Breast Cancer Bone Metastasis in a Zebrafish Model. *International journal of molecular sciences* **2016**, *17*, doi:10.3390/ijms17081375.
 88. Kirla, K.T.; Groh, K.J.; Poetzsch, M.; Banote, R.K.; Stadnicka-Michalak, J.; Eggen, R.I.L.; Schirmer, K.; Kraemer, T. Importance of Toxicokinetics to Assess the Utility of Zebrafish Larvae as Model for Psychoactive Drug Screening Using Meta-Chlorophenylpiperazine (mCPP) as Example. *Frontiers in pharmacology* **2018**, *9*, 414, doi:10.3389/fphar.2018.00414.
 89. Chen, Q.; Ramu, V.; Aydar, Y.; Groenewoud, A.; Zhou, X.Q.; Jager, M.J.; Cole, H.; Cameron, C.G.; McFarland, S.A.; Bonnet, S., et al. TLD1433 Photosensitizer Inhibits Conjunctival Melanoma Cells in Zebrafish Ectopic and Orthotopic Tumour Models. *Cancers* **2020**, *12*, doi:10.3390/cancers12030587.
 90. Tulotta, C.; He, S.; Chen, L.; Groenewoud, A.; van der Ent, W.; Meijer, A.H.; Spaik, H.P.; Snaar-Jagalska, B.E. Imaging of Human Cancer Cell Proliferation, Invasion, and Micrometastasis in a Zebrafish Xenogeneic Engraftment Model. *Methods in molecular biology (Clifton, N.J.)* **2016**, *1451*, 155-169, doi:10.1007/978-1-4939-3771-4_11.
 91. Wu, J.Q.; Zhai, J.; Li, C.Y.; Tan, A.M.; Wei, P.; Shen, L.Z.; He, M.F. Patient-derived xenograft in zebrafish embryos: a new platform for translational research in gastric cancer. *Journal of experimental & clinical cancer research : CR* **2017**, *36*, 160, doi:10.1186/s13046-017-0631-0.

92. Barriuso, J.; Nagaraju, R.; Hurlstone, A. Zebrafish: a new companion for translational research in oncology. *Clinical cancer research : an official journal of the American Association for Cancer Research* **2015**, *21*, 969-975, doi:10.1158/1078-0432.ccr-14-2921.
93. Fior, R.; Póvoa, V.; Mendes, R.V.; Carvalho, T.; Gomes, A.; Figueiredo, N.; Ferreira, M.G. Single-cell functional and chemosensitive profiling of combinatorial colorectal therapy in zebrafish xenografts. *Proceedings of the National Academy of Sciences of the United States of America* **2017**, *114*, E8234-e8243, doi:10.1073/pnas.1618389114.
94. Khan, N.; Mahajan, N.K.; Sinha, P.; Jayandharan, G.R. An efficient method to generate xenograft tumor models of acute myeloid leukemia and hepatocellular carcinoma in adult zebrafish. *Blood cells, molecules & diseases* **2019**, *75*, 48-55, doi:10.1016/j.bcmd.2018.12.007.
95. Liu, J.F.; Palakurthi, S.; Zeng, Q.; Zhou, S.; Ivanova, E.; Huang, W.; Zervantonakis, I.K.; Selfors, L.M.; Shen, Y.; Pritchard, C.C., et al. Establishment of Patient-Derived Tumor Xenograft Models of Epithelial Ovarian Cancer for Preclinical Evaluation of Novel Therapeutics. *Clinical cancer research : an official journal of the American Association for Cancer Research* **2017**, *23*, 1263-1273, doi:10.1158/1078-0432.ccr-16-1237.
96. Casey, M.J.; Stewart, R.A. Zebrafish as a model to study neuroblastoma development. *Cell and tissue research* **2018**, *372*, 223-232, doi:10.1007/s00441-017-2702-0.
97. Wang, L.; Chen, H.; Fei, F.; He, X.; Sun, S.; Lv, K.; Yu, B.; Long, J.; Wang, X. Patient-derived Heterogeneous Xenograft Model of Pancreatic Cancer Using Zebrafish Larvae as Hosts for Comparative Drug Assessment. *Journal of visualized experiments : JoVE* **2019**, 10.3791/59507, doi:10.3791/59507.
98. Yan, C.; Yang, Q.; Do, D.; Brunson, D.C.; Langenau, D.M. Adult immune compromised zebrafish for xenograft cell transplantation studies. *EBioMedicine* **2019**, *47*, 24-26, doi:10.1016/j.ebiom.2019.08.016.
99. Hason, M.; Bartůněk, P. Zebrafish Models of Cancer-New Insights on Modeling Human Cancer in a Non-Mammalian Vertebrate. *Genes* **2019**, *10*, doi:10.3390/genes10110935.
100. Yan, C.; Brunson, D.C.; Tang, Q.; Do, D.; Iftimia, N.A.; Moore, J.C.; Hayes, M.N.; Welker, A.M.; Garcia, E.G.; Dubash, T.D., et al. Visualizing Engrafted Human Cancer and Therapy Responses in Immunodeficient Zebrafish. *Cell* **2019**, *177*, 1903-1914.e1914, doi:10.1016/j.cell.2019.04.004.
101. Cassar, S.; Adatto, I.; Freeman, J.L.; Gamse, J.T.; Iturria, I.; Lawrence, C.; Muriana, A.; Peterson, R.T.; Van Cruchten, S.; Zon, L.I. Use of Zebrafish in Drug Discovery Toxicology. *Chemical research in toxicology* **2020**, *33*, 95-118, doi:10.1021/acs.chemrestox.9b00335.
102. Agostinis, P.; Berg, K.; Cengel, K.A.; Foster, T.H.; Girotti, A.W.; Gollnick, S.O.; Hahn, S.M.; Hamblin, M.R.; Juzeniene, A.; Kessel, D., et al. Photodynamic therapy of cancer: an update. *CA: a cancer journal for clinicians* **2011**, *61*, 250-281, doi:10.3322/caac.20114.
103. Sengar, P.; Garcia-Tapia, K.; Chauhan, K.; Jain, A.; Juarez-Moreno, K.; Borbón-Nuñez, H.A.; Tiznado, H.; Contreras, O.E.; Hirata, G.A. Dual-photosensitizer coupled nanoscintillator capable of producing type I and type II ROS for next generation photodynamic therapy. *Journal of colloid and interface science* **2019**, *536*, 586-597, doi:10.1016/j.jcis.2018.10.090.
104. Farrer, N.J.; Salassa, L.; Sadler, P.J. Photoactivated chemotherapy (PACT): the potential of excited-state d-block metals in medicine. *Dalton transactions (Cambridge, England : 2003)* **2009**, 10.1039/b917753a, 10690-10701, doi:10.1039/b917753a.
105. Lameijer, L.N.; Ernst, D.; Hopkins, S.L.; Meijer, M.S.; Askes, S.H.C.; Le Dévédec, S.E.; Bonnet, S. A Red-Light-Activated Ruthenium-Caged NAMPT Inhibitor Remains Phototoxic in Hypoxic Cancer Cells. *Angewandte Chemie (International ed. in English)* **2017**, *56*, 11549-11553, doi:10.1002/anie.201703890.
106. Manghnani, P.N.; Wu, W.; Xu, S.; Hu, F.; Teh, C.; Liu, B. Visualizing Photodynamic Therapy in Transgenic Zebrafish Using Organic Nanoparticles with Aggregation-Induced Emission. *Nano-micro letters* **2018**, *10*, 61, doi:10.1007/s40820-018-0214-4.
107. Matera, C.; Gomila, A.M.J.; Camarero, N.; Libergoli, M.; Soler, C.; Gorostiza, P. Photoswitchable Antimetabolite for Targeted Photoactivated Chemotherapy. *Journal of the American Chemical Society* **2018**, *140*, 15764-15773, doi:10.1021/jacs.8b08249.
108. Shaw, B.J.; Handy, R.D. Physiological effects of nanoparticles on fish: a comparison of nanometals versus metal ions. *Environment international* **2011**, *37*, 1083-1097, doi:10.1016/j.envint.2011.03.009.

109. Bai, C.; Tang, M. Toxicological study of metal and metal oxide nanoparticles in zebrafish. *Journal of applied toxicology : JAT* **2020**, *40*, 37-63, doi:10.1002/jat.3910.
110. Wehmas, L.C.; Anders, C.; Chess, J.; Punnoose, A.; Pereira, C.B.; Greenwood, J.A.; Tanguay, R.L. Comparative Metal Oxide Nanoparticle Toxicity Using Embryonic Zebrafish. *Toxicology reports* **2015**, *2*, 702-715, doi:10.1016/j.toxrep.2015.03.015.
111. Gutiérrez-Lovera, C.; Vázquez-Ríos, A.J.; Guerra-Varela, J.; Sánchez, L.; de la Fuente, M. The Potential of Zebrafish as a Model Organism for Improving the Translation of Genetic Anticancer Nanomedicines. *Genes* **2017**, *8*, doi:10.3390/genes8120349.
112. Evensen, L.; Johansen, P.L.; Koster, G.; Zhu, K.; Herfindal, L.; Speth, M.; Fenaroli, F.; Hildahl, J.; Bagherifam, S.; Tulotta, C., et al. Zebrafish as a model system for characterization of nanoparticles against cancer. *Nanoscale* **2016**, *8*, 862-877, doi:10.1039/c5nr07289a.
113. Lee, K.Y.; Jang, G.H.; Byun, C.H.; Jeun, M.; Searson, P.C.; Lee, K.H. Zebrafish models for functional and toxicological screening of nanoscale drug delivery systems: promoting preclinical applications. *Bioscience reports* **2017**, *37*, doi:10.1042/bsr20170199.
114. Yang, T.; Martin, P.; Fogarty, B.; Brown, A.; Schurman, K.; Phipps, R.; Yin, V.P.; Lockman, P.; Bai, S. Exosome delivered anticancer drugs across the blood-brain barrier for brain cancer therapy in *Danio rerio*. *Pharmaceutical research* **2015**, *32*, 2003-2014, doi:10.1007/s11095-014-1593-y.
115. Wilhelm, S.; Tavares, A.J.; Dai, Q.; Ohta, S.; Audet, J.; Dvorak, H.F.; Chan, W.C.W. Analysis of nanoparticle delivery to tumours. *Nature Reviews Materials* **2016**, *1*, 16014, doi:10.1038/natrevmats.2016.14.
116. Zhang, Y.N.; Poon, W.; Tavares, A.J.; McGilvray, I.D.; Chan, W.C.W. Nanoparticle-liver interactions: Cellular uptake and hepatobiliary elimination. *Journal of controlled release : official journal of the Controlled Release Society* **2016**, *240*, 332-348, doi:10.1016/j.jconrel.2016.01.020.
117. Campbell, F.; Bos, F.L.; Sieber, S.; Arias-Alpizar, G.; Koch, B.E.; Huwyler, J.; Kros, A.; Bussmann, J. Directing Nanoparticle Biodistribution through Evasion and Exploitation of Stab2-Dependent Nanoparticle Uptake. *ACS nano* **2018**, *12*, 2138-2150, doi:10.1021/acsnano.7b06995.

Chapter 2

Lactic acid secreted by glycolytic B16.F10 melanoma cells attracts macrophages to drive angiogenesis

Quanchi Chen ¹, Xiaobing Zhang ², Daan Kloosterman ¹, Sylvia Le Dévédec ², B. Ewa Snaar-Jagalska ^{1*}

1 Institute of Biology, Leiden University, Leiden, The Netherlands

2 Institute of Drug Discovery & Safety division, Leiden University, Leiden, The Netherlands

* Correspondence: b.e.snaar-jagalska@biology.leidenuniv.nl; Tel.: +31-71-527-4980 (E.S.J.)

Manuscript in preparation

Keywords: melanoma, macrophages, angiogenesis, lactic acid, zebrafish xenograft

Abstract

Malignant melanoma is often linked to increased angiogenesis and a high infiltration with tumor-associated macrophages (TAMs). TAMs influence various processes during tumor development, including immune responses, tumor growth, metastasis and angiogenesis. These immune cells may act as a local source of Vascular endothelial growth factor (VEGF), thereby stimulating neo-vascularization. However, the dynamic interactions between macrophages and the tumor environment, including melanoma and endothelial cells, remain elusive. We utilized a zebrafish allo- and xenograft model to understand the role of macrophages during melanoma progression and tumor-induced angiogenesis. Three red fluorescence-labeled melanoma cell lines (zebrafish ZMEL1, human SK-MEL28 and mouse B16.F10) were injected into transgenic reporter *Tg(mpeg:GAL4:UAS:lifeact:GFP)* embryos with green fluorescent macrophages to study the interaction between melanoma cells and host macrophages. First, we compared the interactions between xeno- and allografted melanoma cells with macrophages, to ensure the response is not due to cross-species immune recognition. Next, the recruitment of macrophages to the primary tumor was analyzed. Additionally, the functional significance of these immune cells was studied by chemical ablation of macrophages in *Tg(mpeg:GAL4:UAS:NTR:mCherry)* embryos, using metronidazole (MTZ). The growth kinetics and angiogenic activity of each engrafted cell line were quantified in the presence and absence of macrophages. Finally, the function of lactic acid secreted by glycolytic B16.F10 melanoma cells was investigated after chemical inhibition of glycolysis. We observed that macrophages are attracted to lactic acid, secreted by glycolytic B16.F10 cells and subsequently promote their angiogenic potential.

Introduction

Cutaneous melanoma is an aggressive type of skin cancer which arises when pigment-producing skin cells, called melanocytes, become cancerous. Whereas healthy melanocytes respond properly to growth signals, melanoma cells proliferate, form blood vessels, invade the circulatory system and spread to distant tissues and organs. A high ability to metastasize makes melanoma one of the deadliest forms of cancers. Unfortunately, melanoma is becoming more common every year and is now the second most common cancer type in young people [1].

The progression of cutaneous melanoma can be defined by a multi-phase model, from benign nevus, dysplastic nevus, radial growth phase, to vertical growth phase and metastatic melanoma [2]. The key driver behind its development is the accumulation of mutations in crucial genes which regulate cell growth, differentiation and survival. Mutations are primarily due to prolonged ultra-violet radiation (UVR) exposure. In the benign nevus stage, oncogenic mutations in the BRAF and N-RAS genes pave the way for melanoma development. After acquiring these mutations, a dysplastic nevus is shaped, which is characterized by molecular abnormalities that affect cell growth, DNA repair and survival. In this stage, loss of function mutations in tumor suppressor genes CDKN2A or PTEN are crucial for initiating the highly proliferative radial growth phase (RGP) and, henceforth, the migratory vertical growth phase

(VGP) [3]. In the VGP, melanoma cells lose cell-cell contact and undergo epithelial to mesenchymal transition (EMT). Finally, vertical growth of the tumor through the basement membrane of the dermis is followed by periods of increased angiogenesis. As the tumor continues to expand into the dermis, the need for nutrients and oxygen increases. Through angiogenesis, the tumor stimulates the development of new blood vessels from existing ones. Additionally, these vessels provide a transportation route for nutrients and oxygen but also a route for the melanoma cells to the circulatory system [4]. Before homing of the disseminated melanoma cells (DMCs) at a secondary site, a pre-metastatic niche is formed as a result of the accumulation of lysosomal oxidase, placental growth factor (PIGF) and exosomes derived from the primary tumor. The pre-metastatic niche promotes metastatic colonization upon arrival of the DMCs [5]. The DMCs extravasate from the circulatory system into the tissue and begin to proliferate, resulting in the formation of a secondary tumor.

It is generally accepted that the tumor microenvironment (TME) is an important factor in tumorigenesis. The TME is highly heterogeneous and is composed of various cell types which can either enhance or inhibit tumor growth [6]. Among these are immune cells such as macrophages, neutrophils, natural killer cells and T cells. During development, cancers acquire hundreds or even thousands of mutations in coding exons, promoting the production of tumor specific- and tumor-associated proteins. These proteins, respectively, may serve as tumor-specific-antigens (TSAs) and tumor-associated-antigens (TAAs) for recognition by the immune system [7,8]. Upon recognition of these antigens, attracted immune cells provide immunosurveillance and destroy malignant cells [9].

In contrast, the host's immune system can also promote tumor survival, growth and metastasis [10]. Some malignant cells are able to secrete molecules which change the cellular composition and function of the TME, thereby evading immunosurveillance [11]. The established TME shares many similar features with a chronic wound, inducing a wound-healing-like immune response. When immune cells are recruited to the TME, they secrete inflammatory cytokines, growth factors and chemokines, which in turn stimulate tumor growth, angiogenesis and migration [12].

One of the most abundant immune cells in the melanoma TME are macrophages, which are characterized by their plasticity and flexibility. Owing to their plasticity, macrophages alter their phenotype continuously, following environmental cues and intercellular interactions [13]. Conventionally, macrophage phenotypes have been classified in two main groups, namely the pro-inflammatory type I macrophages (M1) and the anti-inflammatory type II macrophages (M2) [14]. However, these phenotypes should not be seen as binary, but as a spectrum where M1 and M2 macrophages are at the opposite end [15,16]. M1 polarization is promoted by pro-inflammatory stimuli such as interferon gamma (IFN γ), tumor necrosis factor alpha (TNF- α) and toll-like receptor (TLRs) ligands. Many pro-inflammatory cytokines are secreted by M1 macrophages, including IL-1 β , TNF- α , TNF- β and IL-6. Whereas M1 macrophages are involved in the initial tissue damage response, M2 macrophages dominate later in repair [17,18]. Polarization towards an M2 phenotype is induced by IL-

4, IL-13, the immune complex or glucocorticoids. M2 macrophages are characterized by their secretion of TGF- β , IL-10, VEGF and matrix metalloproteinases (MMPs), thereby assisting in the resolution of inflammation, and the promotion of tissue remodeling and repair [19].

Melanoma cells secrete several factors that attract monocytes, including lactic acid, VEGF, and colony-stimulating factor (CSF-1). Upon arrival at the tumor site, monocytes may differentiate into tumor-associated macrophages (TAMs). In cutaneous melanoma, TAMs exhibit heterogeneous responses which can be pro- and antitumoral. It has been found that the function and phenotype of macrophages changes during melanoma progression. During the early neoplastic phase, macrophages play a proinflammatory role and provide immune surveillance, whereas macrophages in a malignant melanoma environment can promote angiogenesis and enhance tumor cell dissemination [20,21]. Therefore, pharmacological targeting of the macrophage activity depends on the stage of the disease.

In melanoma, neovascularization is linked to high malignancy and metastasis, and is a crucial predictive factor in melanoma tumorigenesis [22]. Toriso H. et al. found that the number of infiltrating macrophages and blood vessels positively correlated with the depth of melanoma invasion. They suggest that activated macrophages are a local source of VEGF and that these immune cells upregulate pro-angiogenic factors IL-8 and VEGF in melanoma cells through secreting TNF- α and IL-1 β [23]. How activated macrophages dynamically interact with melanoma cells and vascular endothelial cells remains unknown. However, using zebrafish as a model organism makes it possible to study these dynamic interactions *in vivo*. Over the last decade, zebrafish have emerged as a convenient *in vivo* model for cancer, immune and stem cell research. More than 70% of all human disease genes have a functional homolog in zebrafish [24]. Another advantage of this model is breeding efficiency. One zebrafish pair can produce up to 200 embryos per week, which develop *ex vivo* and are transparent, making them easy to study [25]. Additionally, the adaptive immune system is absent in early stage embryos, allowing tolerance for human tumor cell engraftment and exclusive study of the innate immune system [26]. In this research we aimed to microscopically trace macrophages in an allo- and xenograft zebrafish models and dissect their role in the tumor induced angiogenesis. The transgenic line, *Tg(kdlr:GFP/mpeg:NTR:mCherry)* with fluorescent blood vessels (green) and macrophages (red) was employed here to study the interaction between macrophages, vessels and engrafted melanoma cells (red and far red). Importantly, this transgenic line made possible to deplete macrophages in live embryos in the inducible fashion by adding metronidazol (MTZ) to the medium, which in turn was broken down by nitroreductase (NTR) enzyme to toxic compound, ablating macrophages [27]. Melanoma cells were engrafted into the Duct in Cuvier (DOC) or within the perivital space of two days old embryos, where they settled, formed a primary tumor and induced angiogenesis. Using these models, we observed attraction of macrophages to engrafted melanoma cells of different origin. Restrictively, macrophages attracted to lactic acid, secreted by glycolytic B16.F10 cells elevated their angiogenic response.

Methods

Transgenic Fish Lines

The transgenic lines *Tg(kdlr:GFP/mpeg:NTR:mCherry)* and *Tg(mpeg:GAL4:UAS:lifect:GFP)* were used in this study and were handled in compliance with local animal welfare regulations and maintained according to standard protocols (www.ZFIN.org). Zebrafish embryos were collected and treated with 0.2 mM *N*-phenylthiourea at 24 hours post fertilization (hpf) to prevent melanization. To deplete macrophages, *Tg(mpeg:GAL4:UAS:NTR:mCherry)* fish were exposed to 2.5 mM metronidazol (MTZ) at 48 hpf. The medium of 2.5 mM MTZ treated embryos was refreshed every two days.

Melanoma Cell Lines

Cell lines ZMEL1, a zebrafish melanoma cell line, kindly provided by dr. Richard M. White [28], SK-MEL28, a human- cutaneous melanoma cell line, and B16.F10, a mouse melanoma cell line from the ATTC, were used. The cell lines were cultured in DMEM/F12 10% Fetal Calf Serum (FBS; Gibco). Stable fluorescent cell lines were created using lentiviral vectors expressing GFP or far red.

Cell proliferation assay

Sulforhodamine B (SRB) colorimetric assay was used to evaluate cell proliferation as described previously [29]. B16.F10 cells were seeded in a 96-well plate and left overnight. Cells were treated with different doses of 2-Deoxyglucose (2DG) for different times as indicated and then were fixed with 30 μ L 50% trichloroacetic acid (TCA, Sigma-Aldrich) for 1 h at 4 °C. Cellular proteins were stained with 60 μ L 0.4% SRB (Sigma-Aldrich) for 30 min and unbound SRB was removed by washing with 1% acetic acid 5 times (VWR, Amsterdam, The Netherlands). Protein-bound SRB was dissolved in 200 μ L 10 mM unbuffered Tris (Thermo Fisher) and solution absorbance was measured at 540 nm on an Infinite M1000 microplate reader (Tecan, Giessen, The Netherlands). Dose response curves and IC50 values were made in GraphPad Prism (version 8.1.1).

ATP luciferase assay

Following the manual's instructions of the ATPlite 1 step Kit (PerkinElmer, the Netherlands), optimized number of cells were seeded on the black screen-star plate (Greiner, the Netherlands) and attached overnight in the incubator. After staining with Cells Hoechst for 45 mins, cells were treated with exposure medium. Prior to assay, the images of nuclei were captured on a Nikon Eclipse Ti microscope using a Plan Fluor 10 objective with 37 °C 5% CO₂ incubator chamber, automated stage and perfect focus. At indicated measurement time, each plate well was replaced with 50 μ L fresh medium and then 50 μ L of ATP substrate was added. After 2 mins mixture on the shaker, luminescence was measured with FLUO star plate reader (BMG Labtech, the Netherlands). All graphs were plotted in Graphpad Prism. The numbers of cells were calculated by custom-made ImagePro macro. All values were normalized to cell numbers.

Lactate assay

Cells were cultured and treated with 100 μ L indicated compound medium in 96 well plate. At collection time, cells were removed by spinning down and supernatants were collected to a new 96-well plate. 10 μ L of supernatant was mixed with ... of lactate assay reagent (including 108 mM Triethanolamine HCl, 10.7 mM EDTA.Na₂, 42 mM MgCl₂). After 7 mins incubation in the dark, absorbance was measured at wavelength of 490 nm on FLUO star plate reader (BMG Labtech, the Netherlands). Meantime, cells were stained with Hoechst and the images of nuclei were captured on a Nikon Eclipse Ti microscope using a Plan Fluor 10 objective with 37 °C 5% CO₂ incubator chamber, automated stage and perfect focus. All graphs were plotted in Graphpad Prism. The numbers of cells were calculated by custom-made ImagePro macro. All values were normalized to cell numbers.

Embryo Preparation and Tumor Injection

Zebrafish embryos at 2 days post fertilization (dpf) were anaesthetized with tricaine and translocated to a Petri dish coated with 1% agarose. Melanoma cells were trypsinized and collected as a single cell suspension in a 15ml collection tube. After 5 minutes centrifuging at 1200 rpm the supernatant was removed and the pellet was resuspended in phosphate-buffered saline (PBS). After second centrifugation the supernatant was removed, pellet was resuspended in 10 μ l 2% PVP and kept at room temperature before implantation. The cell suspension was transferred into glass capillary needles (nr 99.) and the injections were performed with a Pneumatic Pico pump with a manipulator (WPI) within 2 hours. ~50 ZMEL1 cells, ~300 SK-MEL28 or ~300 B16.F10 cells were injected above the ventral end of the Duct of Cuvier or within the perivital space [30,31]. As a negative control, 2% PVP was injected instead. ZMEL1 injected fish were maintained at 28°C, whereas SK-MEL28 and B16.F10 injected fish were kept at 34°C.

Macrophages attraction assay

1 nL of purified CCL₂ protein (R&D Systems, The Netherlands) or lactic acid (Sigma Aldrich, The Netherlands) (10 ng/ml) were injected into the hindbrain ventricle of *Tg(kdlr:GFP/mpeg:NTR:mCherry)* larvae at 48 hpf [32]. 1 nL of PBS injected embryos were set as an injected control group. Samples were fixed with 4% PFA at 3 hours post injection (hpi), and macrophages were counted within the hindbrain ventricle under a Zeiss Observer 6.5.32 laser scanning confocal microscope (Carl Zeiss) by going through the z-stacks, comprising the whole hindbrain ventricle.

Microscopy and Analysis

Before confocal live imaging, larvae were anaesthetized with tricaine and positioned on a glass cover plate before embedding them in 0.5% low melting agarose. The position of larvae was corrected after embedding with a toothpick to obtain a uniform view of all samples for confocal imaging. For stereo live imaging, anaesthetized larvae were positioned on a 1% agarose covered Petri dish. After stereo imaging, embryos were translocated to a 48-wells plate, and were subjected to confocal imaging to

monitor tumor growth in each embryo at higher magnification. A Leica TCS SPE confocal microscope and a Leica stereo microscope were used to acquire fluorescent images. Time-lapse movies and three-dimensional images were reconstructed using ImageJ. The stereo *xy* and confocal *xyz* images were analyzed in ImageJ. The data generated in ImageJ was transferred to excel and Prism 6 software (GraphPad) for further analysis.

Statistical Analysis

The statistical analysis was performed using Prism 6 software. Comparisons between two groups were calculated with one-tailed non-parametric unpaired t-tests. Comparisons between more than two groups were performed with a multi-way ANOVA. Not significant ($p > 0.05$), $*0.01 < p < 0.05$, $**0.001 < p < 0.01$, $*** p < 0.001$.

Results

Zebrafish model to study melanoma growth and angiogenesis formation

To study the interactions between macrophages and melanoma cells, we took advantage of the allo- and xenograft zebrafish model. Injecting fluorescence-labeled tumor cells into the Duct of Cuvier (DOC) of two-day old transgenic embryos allowed us to follow the growth kinetics of these cells in the presence of a microenvironment [30]. The head and tail, representing the primary tumor and the extravasation site, respectively, were imaged at various time points (Figure 1A). We tested three melanoma cell lines with BRAF^{V600E} and p53^{-/-} mutations, including zebrafish melanoma cell line ZMEL1, human cutaneous melanoma cell line SK-MEL28 and mouse melanoma cell line B16.F10. The number of melanoma cells that were injected was optimized by taking into account the survival of the embryos and tumor cells. We found that all cell lines formed a tumor at the injection site and migrated to the caudal hematopoietic tissue (CHT) (Figure 1B). ZMEL1 cells were highly proliferative at the injection site and formed a solid primary tumor surrounding the skin of the embryo at 6dpi. These cells showed low single cell extravasation from the vessel at the CHT without establishing a secondary tumor in the tail fin. We found that SK-MEL28 cells induced high extravasation and were more invasive, however they did not establish a solid primary tumor at the injection site. In contrast, these cells did form a secondary tumor at the CHT. B16.F10 cells induced a compact primary tumor on the skin, induced angiogenesis and established a secondary tumor, while SK-MEL28 induced a primary tumor without clear angiogenesis (Figure 2C). All cell lines were able to form primary tumors in the embryos, which allowed us to study the role of macrophages during the tumor growth of these cell lines after transplantation.

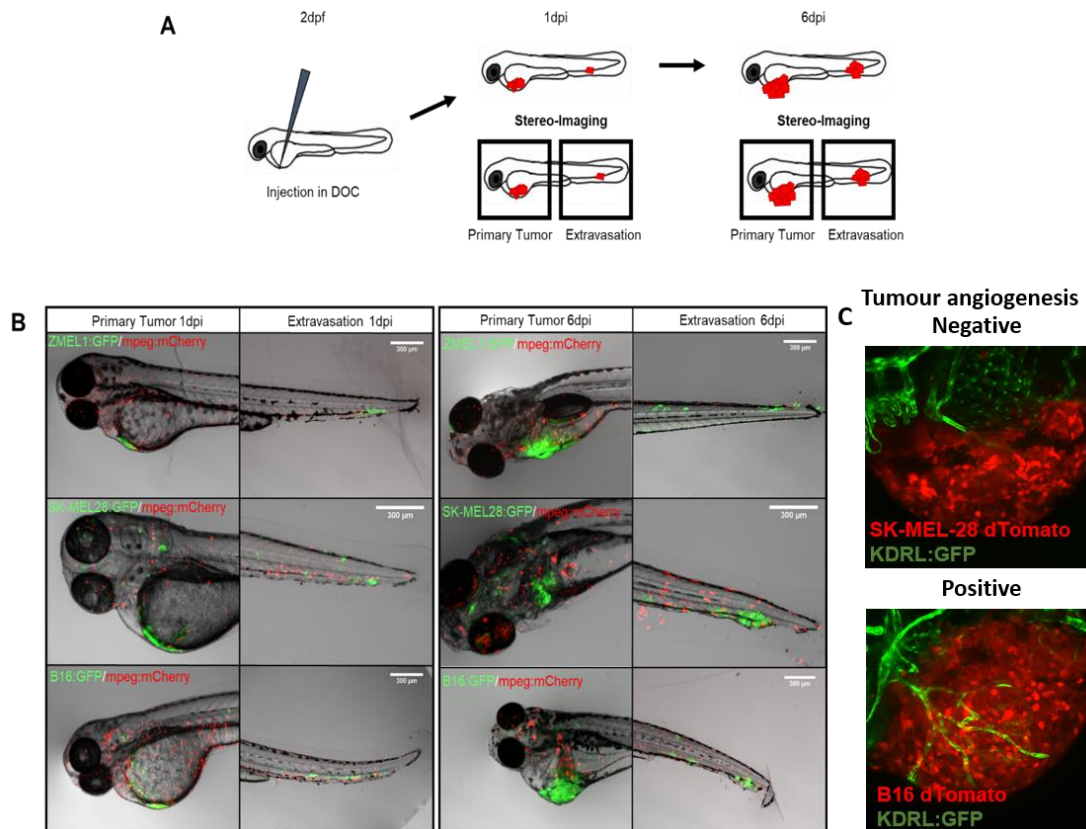


Figure 1 Experimental setup and melanoma growth dynamics in zebrafish embryos. An allo- and xenograft zebrafish model was used to study the role of macrophages on engrafted melanoma development. Around 300 tumor cells were injected into the Duct of Cuvier at 2 dpf. After injection of fluorescence-labeled tumor cells in the DOC, stereo and confocal images were taken at various time points of the head and tail respectively (A). Representative images show the ZMEL1, SK-MEL28 and B16.F10 primary tumor site and extravasation. The mCherry labeled macrophages are located throughout the entire embryo (B). Negative tumor angiogenesis formation (SK-MEL-28) and positive tumor angiogenesis formation (B16) at the primary site (C).

Host macrophages recruited to injection site and interact with engrafted melanoma cells

We next asked if host macrophages respond to engrafting of melanoma cells and whether interaction occurs between these cells. Injecting dTomato-labeled tumor cells into transgenic embryos with GFP-labeled macrophages allowed us to trace the migration and behavior of the tumor cells and macrophages for 10 hpi by using time lapse imaging (Figure 2A). The mock injection procedure induced accumulation of macrophages near the injection site. The macrophage population surrounding the 2% PVP injection resolved between 3-6hpi, indicating a resolution of inflammation. However, the macrophage population at the tumor injection site remained high and gradually increased until the termination of the experiment, suggesting that macrophages are attracted to the primary tumor and not the injection wound (Figure 2B). To ensure that there were close interactions between these cells, we reconstructed three-dimensional images of confocal z-stacks from the primary tumor. These images reveal that macrophages interacted closely with tumor cells and quickly infiltrated the engrafted tumor (Figure 2C).

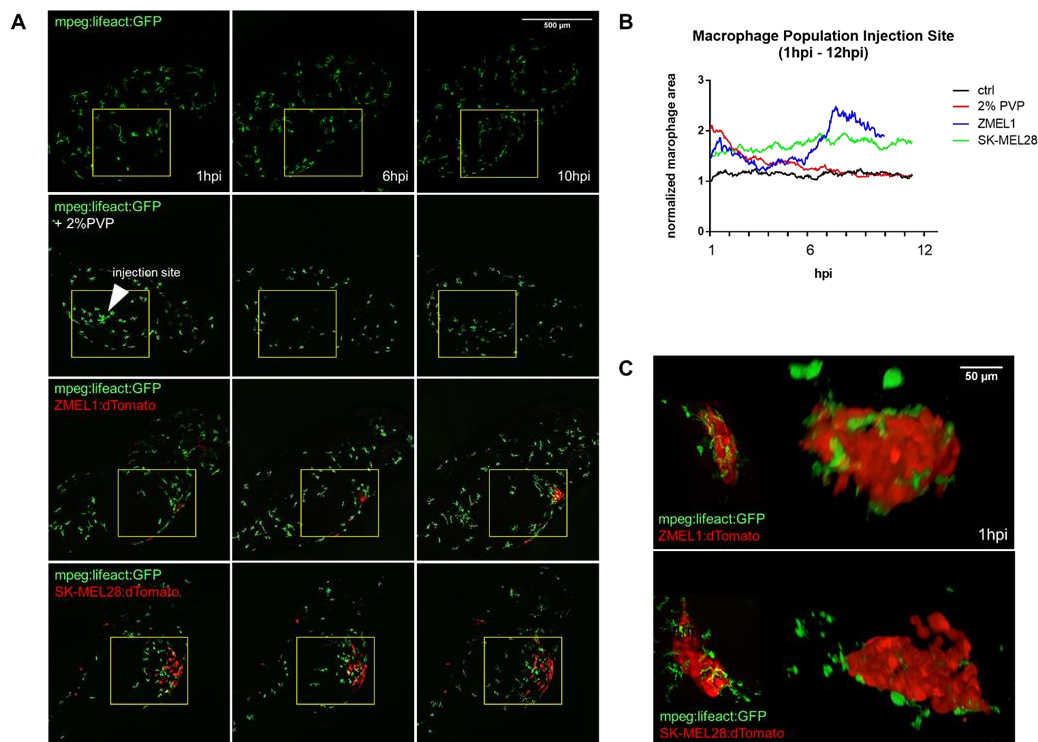


Figure 2 Tracking macrophage migration and their interactions with melanoma cells. Still images from the time lapse at 1hpi, 6hpi and 10hpi. Each row represents a single embryo, either non-injected or injected with 2% PVP, ZMEL1 or SK-MEL28. Images were taken with a 10x magnification. Macrophages accumulated near the injection site, which is marked in yellow (A). Quantification of the macrophage area at the injection site of each frame within the time lapse. A 175x175 pixels ROI was used to represent the injection site. The fluorescent signal in this ROI was normalized by dividing it by the total fluorescent expression in the same channel. Macrophages quickly respond to the injection, but only continued to accumulate near the injection site when tumor cells were present (B). 2D/3D reconstructed confocal z-stacks of the ZMEL1 and SK-MEL28 primary tumor at 1hpi, obtained with a 40x magnification. Right, the 3D image is shown of the 2D images, which is visualized on the left. Macrophages infiltrated the engrafted tumor at 1hpi (C).

Macrophages continue to accumulate at the primary tumor site

To verify whether engrafted melanoma cells continue to recruit macrophages during the timespan of our experiments, we analyzed and quantified three-dimensional images of the primary tumor at 1hpi, 1dpi and 4dpi (Figure 3A). At 1hpi and 1dpi, SK-MEL28 had a significantly-larger tumor area than ZMEL1. However, ZMEL1 showed a trend to have a larger tumor area at 4dpi compared to SK-MEL28, suggesting that ZMEL1 proliferated more effectively. The number of macrophages in the field of view (FOV) of the injection site was similar between 2% PVP and tumor-injected embryos at 1hpi. The number of macrophages in the FOV of the primary tumor induced by ZMEL1 and SK-MEL28 injection gradually increased at 1dpi and 4dpi, whereas the population of macrophages at the 2% PVP injection site remained constantly small throughout the experiment (Figure 3B and 3C). The macrophages in proximity of the tumor showed a more rounded morphology, characterizing an inflammatory

phenotype. Occasionally, macrophages and melanoma cells showed overlap between their fluorescence signal, indicating that macrophages phagocytose tumor cells or debris (Figure 3D). These results suggest that macrophages are recruited to the engrafted tumor throughout and that these cells continuously interact with one another during the timespan of our experiments.

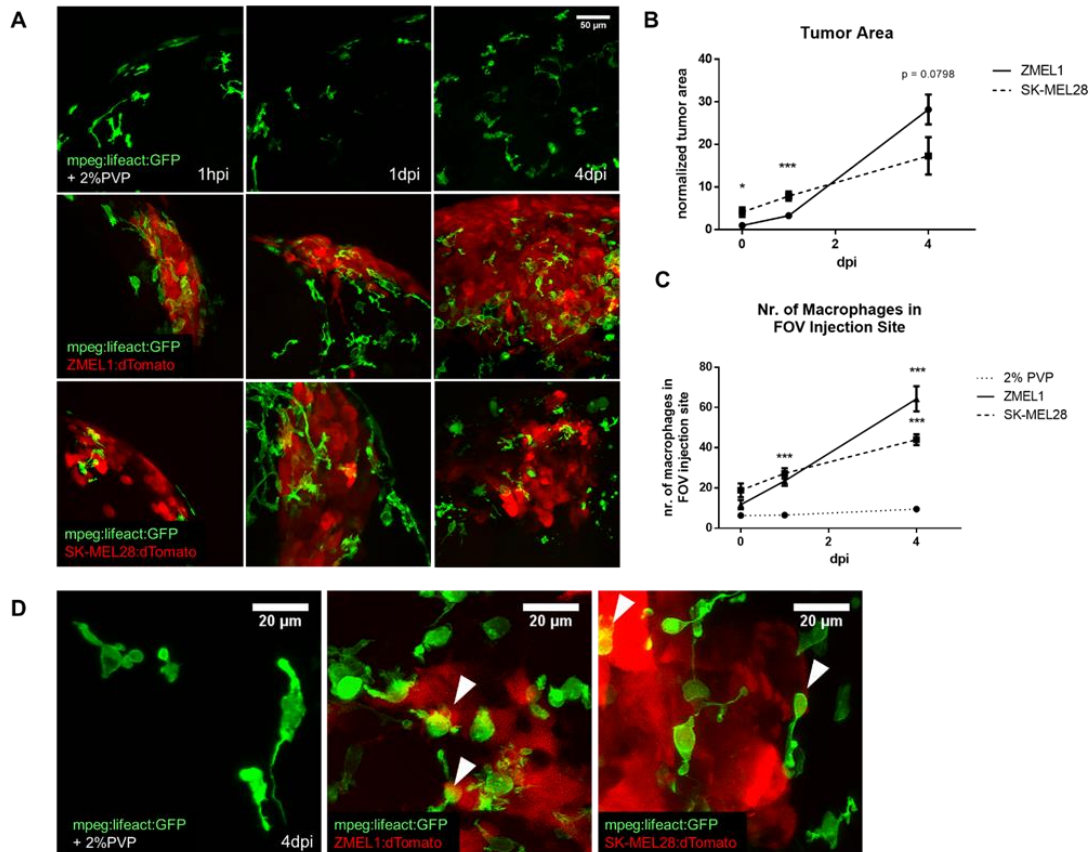


Figure 3 Macrophages accumulate at the primary tumor site. Representative confocal images from the injection site of 2% PVP, ZMEL1 and SK-MEL28 injected embryos at 1hpi, 1dpi and 4dpi, obtained with a 40x magnification. Macrophages are labelled with lifect:GFP and melanoma cells with dTomato (A). Quantification of the area of the ZMEL1 and SK-MEL28 primary tumor. The tumor area represents the z-stacked 2D area of each tumor. Each data point represents the average area at that time point. The error bars represent the \pm SD. Non-parametric unpaired t-test was performed between each group (B). Quantification of the number of macrophages in the field of view (FOV) of the 2% PVP, ZMEL1 and SK-MEL28 injection site. An object larger than 10.000 voxels within the field of view (FOV) of the injection site was identified as a macrophage. Each point represents an average of 10 observations (n=10) and the error bars correspond to the mean \pm SD. Non-parametric unpaired t-test was performed between each group. The number of macrophages gradually increased at the tumor site (3C). The characteristic morphology of macrophages at 4dpi under different circumstances was imaged. The macrophages outside tumor were more elongated, directional comparing to rounded macrophages inside the tumor. The white arrows mark macrophages phagocytose tumor cells (3D).

Metronidazol (MTZ) effectively depletes macrophages in *Tg(mpeg:GAL4:UAS:NTR:mCherry)* embryos

To study the functional significance of macrophages during melanoma development, we utilized the NTR/MTZ ablation system to deplete macrophages [33,34]. Embryos from 2dpf until 8dpf were exposed to various concentrations of MTZ to optimize the efficiency of the macrophage's ablation without sign of toxicity. We observed that all MTZ concentrations successfully depleted macrophages in embryos from 3dpf until the termination of the experiment at 8dpf (Figure 4A). Furthermore, treatment with 2.5mM, 5mM and 7.5mM MTZ had no effect on the survival of embryos. Embryos treated with 10mM MTZ showed enhanced lethality, indicating that MTZ is toxic at higher concentrations (Figure 4B). Increasing the concentration affected the development of the embryos, as embryos treated with a higher concentration were significantly shorter (Figure 4C). Based on these findings, a concentration of 2.5mM MTZ was used throughout this study to successfully deplete macrophages.

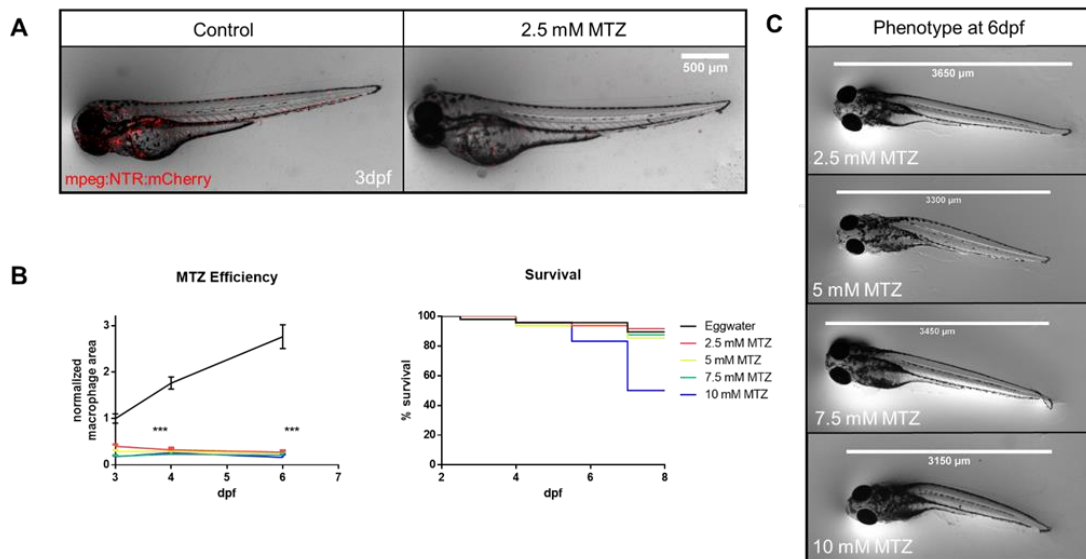


Figure 4 Efficiency and toxicity of NTR/MTZ Ablation System. We treated *Tg(mpeg:NTR:mCherry)* embryos with MTZ at 2dpf to deplete macrophages. Representative images of the macrophage population of untreated and 2.5mM MTZ treated embryos at 3dpf. Macrophages are labeled in mCherry (A). The macrophage area and survival rate of various treatments, including 2.5mM, 5mM, 7.5mM and 10mM were quantified. MTZ successfully depletes macrophages and is lethal at a concentration of 10mM (B). The effect of different MTZ concentrations on the length of the embryos. Increasing the concentration negatively correlated with the embryo length (C).

B16.F10 ells rely on macrophages for tumor angiogenesis

As macrophages are known to be crucial in angiogenesis, we asked whether macrophage depletion indirectly inhibits primary tumor growth through impairing neo-angiogenesis. To investigate the effect of macrophage ablation on vascularization induction by each engrafted cell line, we imaged the primary tumor and their vascular network at various time points in *Tg(kdlr:GFP/mpeg:NTR:mCherry)* embryos in the presence and absence of macrophages. After injection in the DOC, ZMEL1 and B16.F10 formed solid tumors at 6dpi. In line with previous data, SK-MEL28 cells formed no solid tumor, but invaded the

tissue where blood vessels were already located (Figure 5A). The neo-angiogenesis was quantified by calculating the percentage of embryos with a positive phenotype, which is characterized by having a solid primary tumor with a neo-vascular network. All SK-MEL28 injected embryos had a negative phenotype, as SK-MEL28 cells were unable to form a solid primary tumor. At 3dpi, all B16.F10 primary tumors induced neo-vascularization, whereas only 40% of ZMEL1 injected embryos had a positive phenotype. At 6dpi, B16.F10 had a higher percentage of neo-vascularized tumors compared to ZMEL1. We observed that macrophage ablation by MTZ severely lowered the percentage of neo-vascularized B16.F10 tumors at both timepoints. However, the percentage of positive phenotype of ZMEL1 injected embryos was not affected by macrophage depletion (Figure 5B). This data implies that B16.F10 angiogenesis is macrophage dependent, while ZMEL1 cells initiate angiogenesis in the absence of macrophages (Figure 5B-D).

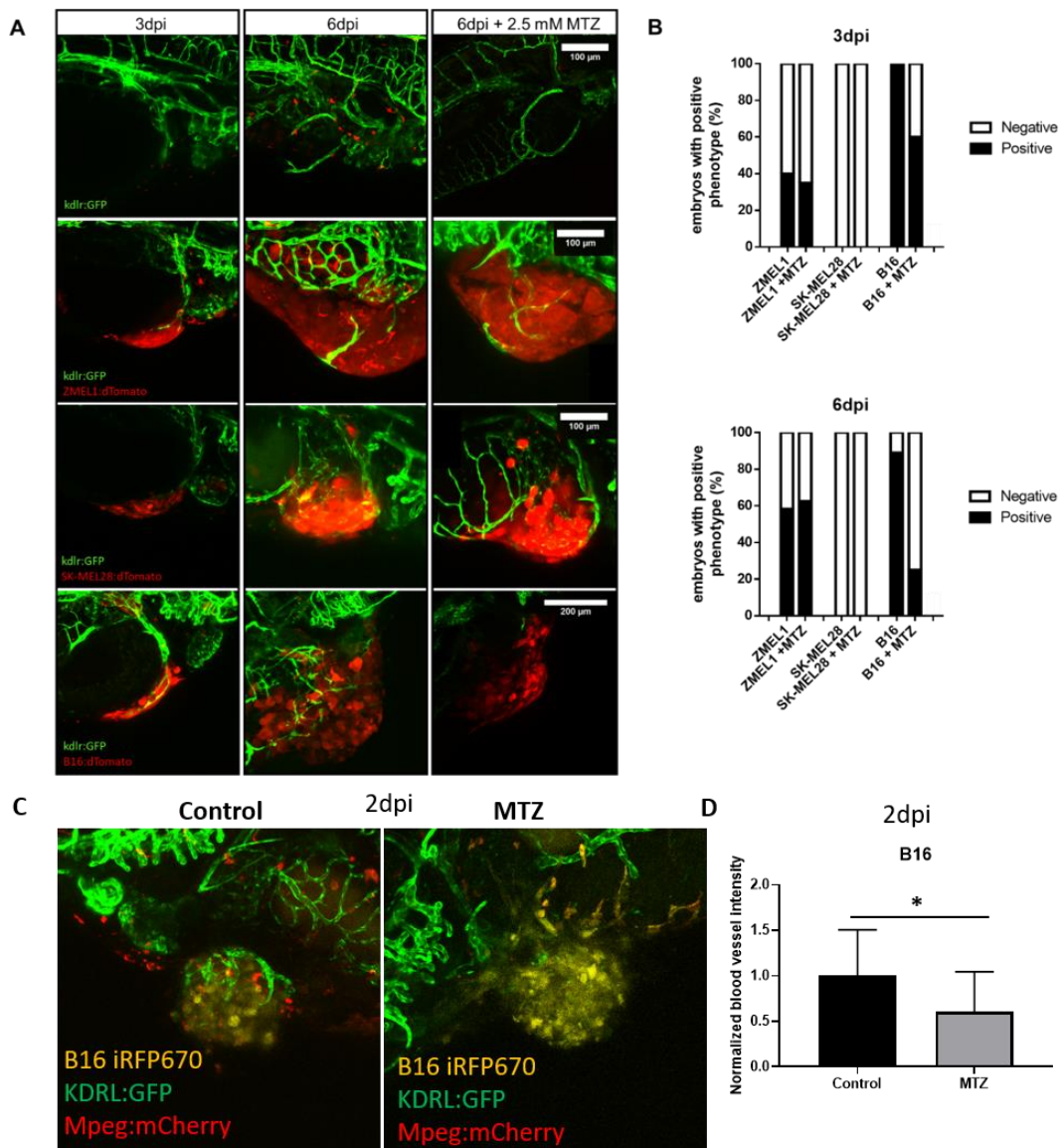


Figure 5 B16.F10 primary tumor relies on macrophages for neo-vascularization. The angiogenesis of the primary tumor was visualized to investigate the effect of macrophage depletion on the vascular network. Representative images are shown of each group at 3dpi and 6dpi, and 6dpi in combination with 2.5mM MTZ treatment (n=10).

The control group, *kdlr:GFP*, represents the vascular network in the absence of melanoma engraftment (A). The percentage of embryos with a solid primary tumor with a neo-vascular network. B16.F10 had the highest angiogenic activity. SK-MEL28 did not form a solid tumor, but invaded the surrounding tissue and nearby blood vessels. ZMEL1 neo-angiogenesis was not affected by macrophages depletion, whereas ablation of macrophages did inhibit neo-angiogenesis in B16.F10 primary tumors (B). Unfortunately, in the images depicted in B we are not able to distinguish macrophages from cancer cells as there were both labelled with red fluorescent marker, therefore we additionally conducted three colour experiments to confirm these results, using B16 iRFP670 cells expressing far- red fluorescence (C). The analysis was done by normalizing the blood vessel fluorescent intensity by tumor size at 2 dpi (D).

Angiogenic activity of B16.F10 is macrophage dependent

To further prove that B16.F10 induced angiogenesis is macrophage dependent, we performed another *in vivo* angiogenesis assay, which is used to measure the angiogenic activity of tumor cells in 18hpi [31]. In this assay, the growth of the blood vessels from the sub-intestinal vein plexus (SIV) is analyzed in the presence of tumor cells. Angiogenic cells are able to induce sprouting or remodel the SIV complex [31]. ZMEL1, SK-MEL28 and B16.F10 cells were injected in the perivitelline space of 48hpf *Tg(kdlr:GFP/mpeg:NTR:mCherry)* and macrophage-depleted embryos. Growth of the blood vessels from the sub-intestinal vein (SIV) was imaged at 1 dpi (Figure 6A). The percentage of positive SIV phenotypes, which is characterized by tumor induced sprouting or complete remodeling of the complex, was calculated for each cell line. B16.F10 had the highest percentage of positive phenotypes, followed by SK-MEL28 and thereafter ZMEL1. Injection of 2% PVP induced no sprouting. The number of positive phenotypes induced by B16.F10 cells was severely decreased in macrophage depleted embryos (Figure 6B, 6C). The elongation of the SIV was quantified by dividing the length of the SIV by the width of the SIV. This parameter gives information about the attraction and sprouting of the SIV, as both increase the length of the SIV. B16.F10 significantly enhanced elongation of the SIV complex, whereas ZMEL1 and SK-MEL28 did not. Macrophage ablation significantly reduced the B16.F10 induced elongated phenotype of the SIV complex (Figure 6D). Additionally, we found that macrophage depletion overall inhibited the formation of the SIV complex, implying that macrophages are essential in the establishment of this complex (Figure 6E). In conclusion, these results suggest that B16.F10 has the highest angiogenic activity and that this activity is macrophage dependent.

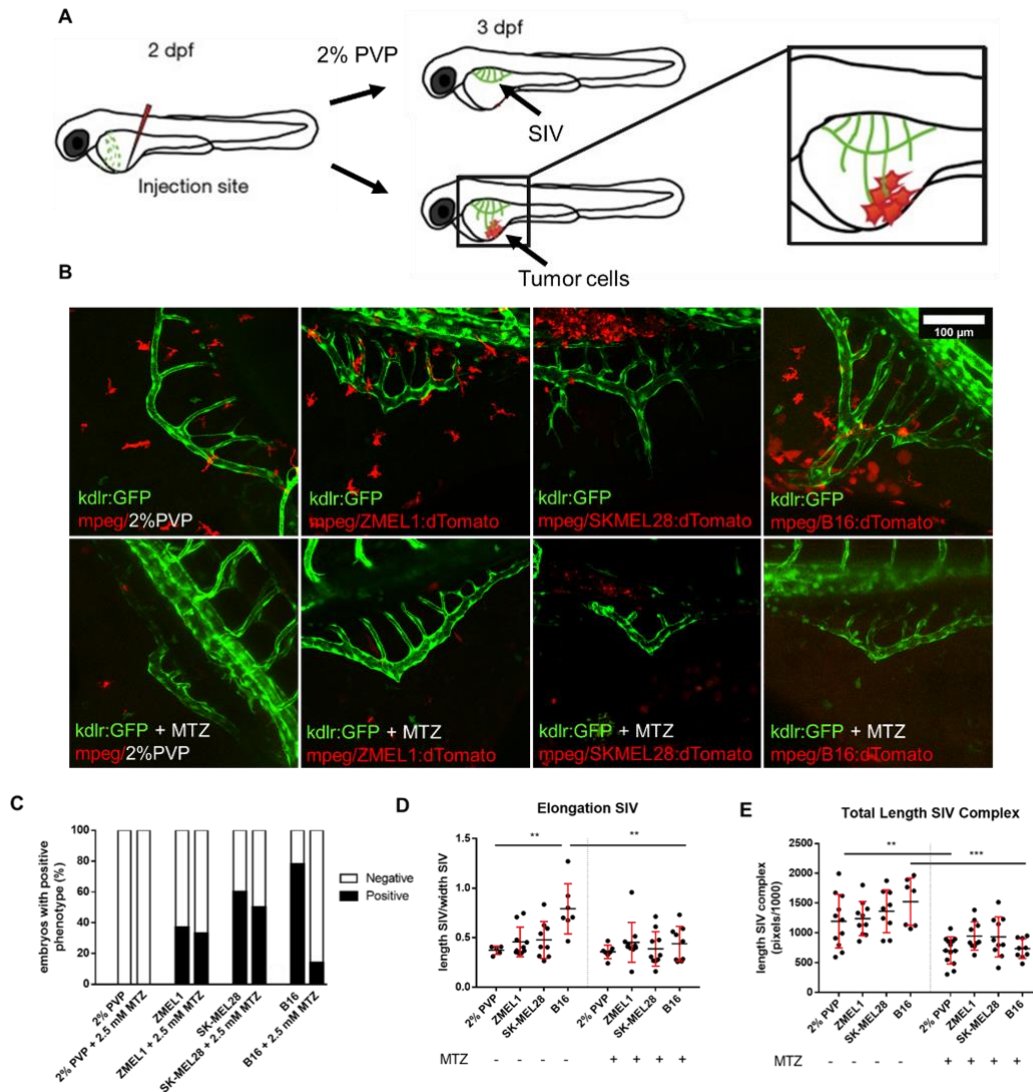


Figure 6 Macrophage ablation inhibits tumor-induced angiogenesis. An angiogenesis assay was performed to study the angiogenic activity of tumor cells. Tumor cells were injected in the perivitelline space of two-days old *Tg(kdlr:GFP/mpeg:NTR:mCherry)* embryos. 2% PVP was injected as a negative control. The SIV complex was imaged between 24-30hpi (A). Representative images of each injection and treatment groups. Blood vessels are labelled with GFP, macrophages and tumor cells lines with mCherry and dTomato therefore in these images we are not able to distinguish macrophages from cancer cells as there both are labelled with red fluorescent markers (B). The percentage of embryos with a positive phenotype, which is characterized by either attraction of the SIV or the formation of sprouts (C). Quantification angiogenic capability of tumor cells with (- MTZ) and without macrophages (+ MTZ). The elongation of the SIV complex was calculated by dividing the length by the width of the SIV complex. B16.F10, not ZMEL1 and SK-MEL28, induced elongation of the SIV complex towards the tumor, which was partly rescued through macrophage depletion (D). The total length of the SIV complex represents the total pixels of the skeletonized SIV complex. The error bars represent the standard error of each group (n=10). Macrophage depletion impaired SIV development in the presence of the tumor (E).

Lactic acid secreted by B16.F10 melanoma cells recruit macrophages to drive angiogenesis

To address why macrophages are attracted to the tumor induced by engraftment of high glycolytic B16.F10 cells, we tested if lactic acid, product of glycolysis can attract macrophages in zebrafish model [35]. The lactic acid (10 μ M) was injected into the zebrafish hindbrain at 2 dpf, which is free of macrophages at this developmental stage (Figure 7A). As positive control we used human cytokine hCCL2, as well known chemoattractant of macrophages in zebrafish [36]. To estimate macrophages response to the local inflammation generated by wound we injected PVP solvent and compared to un injected control (Figure 7B). At 3hpi, the number of macrophages inside hindbrain was imaged and quantified (Figure 7B). Injection of hCCL2 and lactic acid significantly increased number of accumulated macrophages in the hindbrain comparing to number of macrophages in the same area of control and PVP injected embryos (Figure 7C). In order to verify if lactic acid is secreted by tumor cells to attract macrophages, B16.F10 cells were pre-treated with glycolysis inhibitor 2-deoxyglucose (2DG). The 24h treatment of cells with 10 mM 2DG sufficiently inhibited lactic acid secretion, without influencing cell proliferation and cellular ATP production (Figure 7D). After 24h of 10 mM 2DG treatment, around 300 far-red B16 cells were injected into DOC of 2 dpf embryos. Tumor size, macrophages infiltration, and blood vessels density inside tumor were analyzed at 2 dpi. The relative tumor area in 2DG group was not statistically reduced comparing to control group (Figure 7E). The fluorescence of macrophages and blood vessels was normalized by fluorescent tumor area in corresponding embryos and revealed that 2DG treatment impaired the macrophages accumulation and blood vessel intensity (Figure 7F) suggesting that indeed lactic acid secreted by B16.F10 cells contributes to macrophages accumulation and tumor blood vessels formation in zebrafish xenograft model.

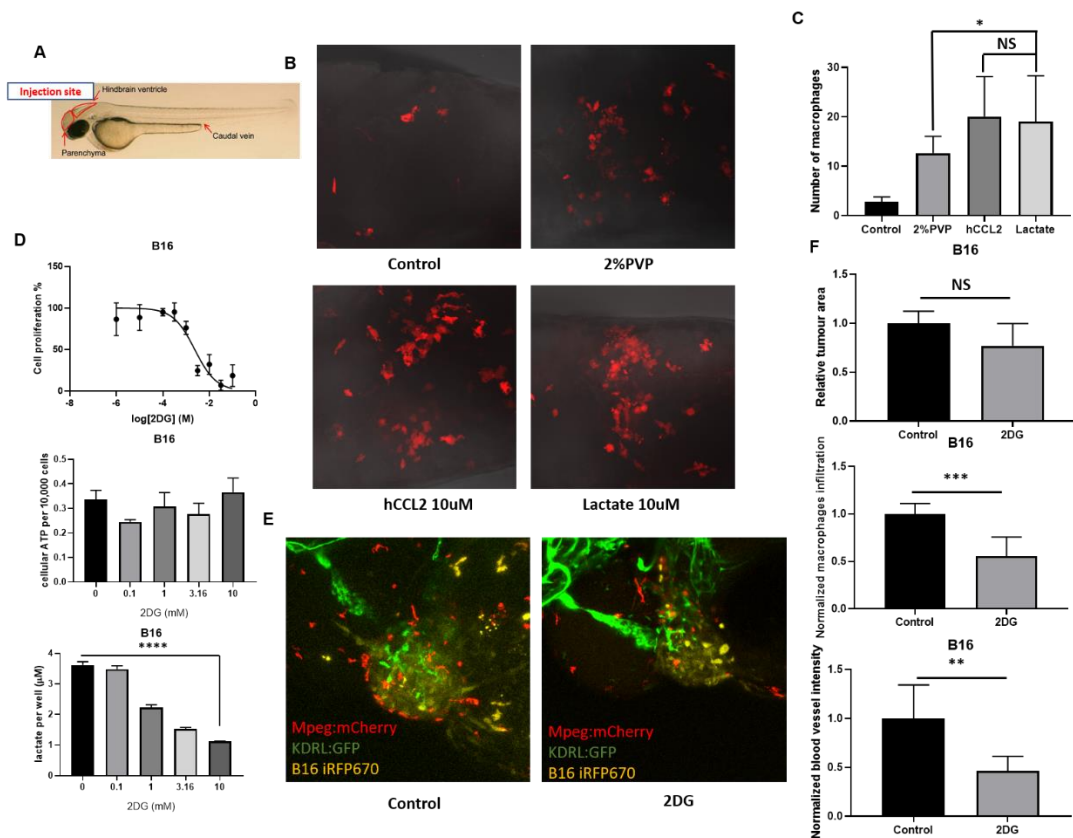


Figure 9 Lactic acid inhibition by 2DG in B16 tumor cells impairs macrophages accumulation and tumor angiogenesis formation. The macrophages attraction assay was performed here. 1 nL of lactic acid (10 μ M), 2% PVP and hCCL2 (negative and positive controls) were injected into hindbrain of zebrafish at 2 dpf (A). After 3h, the images of macrophages in the hindbrain were taken by fluorescent microscope (B). The number of macrophages was calculated (C). B16 cells were treated with 2DG (0.1, 2, 3.16, 10 mM) for 24 h. After treatment, the cell proliferation, cellular ATP per 10000 cells and lactate per well were measured (D). Around 300 B16 cells treated with 10 mM 2DG for 24 h were injected into Duct of Cuvier of 2dpf embryos. After 2 dpi, the fluorescent images were taken (E) and relative tumor area, normalized macrophages infiltration and normalized blood vessel intensity were quantified (E, F).

Discussion

The malignancy of melanoma is often linked to increased angiogenesis and a high number of infiltrating TAMs [22,23]. Currently, many studies are aimed to understand the interplay between TAMs, melanoma and endothelial cells. However, the majority of these studies are conducted *in vitro* or *in vivo* using mouse models, which require complicated and invasive procedures to visualize dynamic interactions between tumor cells and their microenvironment. In contrast, the zebrafish xenograft model is a powerful platform to investigate dynamic cellular interactions within the tumor microenvironment, due to its transparency [25]. Injecting fluorescently labeled tumor cells into transgenic embryos with mCherry labeled macrophages allows us to study their interactions and behavior. In this work, we elucidated the functional significance of macrophages in primary tumor growth and neo-angiogenesis. We provided evidence that macrophages can enhance melanoma

growth by promoting neo-angiogenesis. Thus, we put forth a model which serves as the foundation for further research aimed to discover the exact molecular mechanism by which macrophages enhance neo-angiogenesis in melanoma, and thereby contribute to its malignancy. Initially, we asked if macrophages interact and respond to engrafted tumor cells. Through time lapse imaging and confocal analysis of the primary tumor, we found no differences between the first response of macrophages to 2%PVP and tumor injections. Within six hours, we observed a gradual decrease of macrophages surrounding the 2% PVP injection site, which suggests that resolution of inflammation occurred after the wound was repaired. Inflammatory responses associated with wound healing and tumors are remarkably similar. Tumors have been found to behave as wounds that do not heal, in order to establish a favorable microenvironment [37]. Accordingly, in the presence of melanoma cells, no resolution phase was observed. Additionally, macrophages continued to accumulate at the primary tumor until four days after injection. These results suggest that the engrafted melanoma cells continuously induce an inflammatory response, thereby recruiting macrophages. This response was not simply due to cross-species immune recognition, as we observed similar inflammatory responses towards allografted zebrafish ZMEL1 and xenografted human SK-MEL28 cells. The tumor fluorescent signals in macrophages suggest that these immune cells phagocytose components of the tumor. These components could be from alive tumor cells or from debris from dead tumor cells, as a result of phagocytosis. To further evaluate the function of macrophages during primary tumor growth, we depleted the entire macrophage population in embryos by utilizing the MTZ/NTR ablation system [33,34].

By comparing the growth kinetics of various melanoma cell lines in normal and macrophage depleted embryos, we found that macrophages promoted murine B16.F10 primary tumor growth, while inhibiting this process in ZMEL1 and SK-MEL28 tumors. We do not ignore the fact that macrophages could perform an anti-tumoral role during B16.F10 development at 6dpi. Hence, this could explain the marginal effect of macrophage depletion, as both the positive and negative functions of macrophages are abolished. The origin of each cell line was studied to find an explanation for the cell line dependent effect of macrophage depletion. The ZMEL1 cell line was obtained by Heilman S. et al. by harvesting *in situ* melanoma from transgenic *mitfa*-*BRAF*^{V600E}; *p53*^{-/-} zebrafish [38]. ZMEL1 cells are known to take advantage of the growth-promoting effect of the embryonic microenvironment, since these cells and the recipient are of the same species [28,39]. The xenografted cell line, SK-MEL28, was isolated from an axillary lymph node of a patient [40]. Involvement of the lymph nodes suggest that this melanoma has advanced to Stage III, implying that this cell line is highly malignant [41]. B16 cells were harvested from a tumor which developed naturally surrounding the ear of a C57BL/6 mouse. In this study we used the highly metastatic and aggressive variant B16.F10, which has classically been described as a non- or low-immunogenic tumor cell line [42]. No correlations were drawn between the origin of the cell line, its stage and the response to macrophage depletion, as we found that the *in situ* melanoma ZMEL1 and the highly malignant melanoma SK-MEL28 both progressed better in the

absence of macrophages, while a similar malignant melanoma B16.F10 showed impaired growth under the same circumstances. These results imply that only xenografted B16.F10 tumors profit from macrophages during development. Considering that B16.F10 is a low-immunogenic cell line, we decided not to focus on the immunosuppressive function of macrophages, but on their ability to promote angiogenesis.

To assess the importance of macrophages in tumor-induced angiogenesis, we firstly proved that ZMEL1 and B16.F10 cells were able to form a solid tumor with neo-vascularization. Macrophage depletion severely impaired the neo-vascularization of the B16.F10 tumor. In previous research, it was found that the presence of pro-inflammatory macrophages leads to a significant increase in the amount and complexity of blood vessels. Pro-inflammatory macrophages, which can act as a local source of VEGF, are often associated with the vessel tips, thereby inducing vessel sprouting. Another mechanism by which macrophages support angiogenesis is through dislodging neutrophils from the vessel tips. Neutrophils were found to exhibit inhibitory angiogenic influences, and therefore require dislodging to promote angiogenesis [43]. Possibly, due to macrophage ablation, the angiogenic switch of the B16.F10 tumor is tilted towards an anti-angiogenic outcome, resulting in severely impaired tumor vascularization, which in turn inhibited tumor growth [44]. In contrast, ZMEL1 neo-angiogenesis was not affected by macrophage depletion. The ability of ZMEL1 to produce zebrafish VEGFA could explain why this tumor is capable of inducing angiogenesis in the absence of macrophages. Possibly, ZMEL1 tumors rely on their own production of VEGFA to tilt the angiogenic switch to a pro-angiogenic outcome. To strengthen this hypothesis, we assessed the ability of tumor cells to induce sprouting or attract blood vessels from the SIV. Consistent with our previous findings, B16.F10 showed the highest angiogenic activity. Ablation of macrophages impaired this activity, whereas ZMEL1 induced angiogenesis was not affected. These results strongly imply that the mechanism behind vascularization varies between each cell line. However, we found that cell lines which rely on macrophages for angiogenesis, also showed impaired growth in the absence of macrophages at 6dpi.

In the end, we used zebrafish macrophages attraction assays to prove that lactic acid function as chemoattractant to recruit macrophages comparing to well-known cytokine, hCCL2. After chemical inhibition of glycolysis hence lactic acid secretion, less macrophages were attracted to the tumor site and tumor angiogenesis was impaired. Surprisingly the tumor burden at 2dpi was not significantly influenced by 2DG treatment presumably due to a short duration of the experiment. In future, genetic interference approach is required to further prove that angiogenesis induction by high glycolytic cells is indeed control by lactic acid dependent macrophages attraction.

In summary, our findings demonstrate that macrophages can promote melanoma growth by inducing angiogenesis in the zebrafish xenograft model. Our results show that there is no universal mechanism

by which melanoma cell lines induce and rely on angiogenesis, but that this is cell line specific. We found that the growth of melanoma, which is able to induce angiogenesis in the absence of macrophages, was not promoted by macrophages. Similarly, macrophages did not promote growth of melanoma which did not induce neo-angiogenesis. Importantly, we found that macrophages are attracted by lactic acid to promote tumor angiogenesis in B16.F10 cells.

In conclusion, this study has aided in the understanding of the interactions between macrophages and melanoma cells, and serves as a foundation for further research aimed to discover the exact mechanism by which macrophages induce neo-angiogenesis in melanoma with high glycolytic index.

Reference

1. Ossio, R.; Roldán-Marín, R.; Martínez-Said, H.; Adams, D.J.; Robles-Espinoza, C.D. Melanoma: a global perspective. *Nat Rev Cancer* **2017**, *17*, 393-394, doi:10.1038/nrc.2017.43.
2. Leonardi, G.C.; Falzone, L.; Salemi, R.; Zanghi, A.; Spandidos, D.A.; McCubrey, J.A.; Candido, S.; Libra, M. Cutaneous melanoma: From pathogenesis to therapy (Review). *Int J Oncol* **2018**, *52*, 1071-1080, doi:10.3892/ijo.2018.4287.
3. Prasad, C.P.; Mohapatra, P.; Andersson, T. Therapy for BRAFi-Resistant Melanomas: Is WNT5A the Answer? *Cancers* **2015**, *7*, 1900-1924, doi:10.3390/cancers7030868.
4. Nishida, N.; Yano, H.; Nishida, T.; Kamura, T.; Kojiro, M. Angiogenesis in cancer. *Vascular health and risk management* **2006**, *2*, 213-219, doi:10.2147/vhrm.2006.2.3.213.
5. Sceneay, J.; Smyth, M.J.; Möller, A. The pre-metastatic niche: finding common ground. *Cancer metastasis reviews* **2013**, *32*, 449-464, doi:10.1007/s10555-013-9420-1.
6. Maman, S.; Witz, I.P. A history of exploring cancer in context. *Nat Rev Cancer* **2018**, *18*, 359-376, doi:10.1038/s41568-018-0006-7.
7. Gajewski, T.F.; Schreiber, H.; Fu, Y.X. Innate and adaptive immune cells in the tumor microenvironment. *Nature immunology* **2013**, *14*, 1014-1022, doi:10.1038/ni.2703.
8. Criscitiello, C. Tumor-associated antigens in breast cancer. *Breast care (Basel, Switzerland)* **2012**, *7*, 262-266, doi:10.1159/000342164.
9. Kroemer, G.; Senovilla, L.; Galluzzi, L.; André, F.; Zitvogel, L. Natural and therapy-induced immunosurveillance in breast cancer. *Nature medicine* **2015**, *21*, 1128-1138, doi:10.1038/nm.3944.
10. Gao, F.; Liang, B.; Reddy, S.T.; Farias-Eisner, R.; Su, X. Role of inflammation-associated microenvironment in tumorigenesis and metastasis. *Current cancer drug targets* **2014**, *14*, 30-45, doi:10.2174/15680096113136660107.
11. Criscitiello, C.; Esposito, A.; Curigliano, G. Tumor-stroma crosstalk: targeting stroma in breast cancer. *Current opinion in oncology* **2014**, *26*, 551-555, doi:10.1097/cco.000000000000122.
12. Arnold, K.M.; Opdenaker, L.M.; Flynn, D.; Sims-Mourtada, J. Wound healing and cancer stem cells: inflammation as a driver of treatment resistance in breast cancer. *Cancer growth and metastasis* **2015**, *8*, 1-13, doi:10.4137/cgm.s11286.
13. Gazzaniga, S.; Bravo, A.I.; Guglielmotti, A.; van Rooijen, N.; Maschi, F.; Vecchi, A.; Mantovani, A.; Mordoh, J.; Wainstok, R. Targeting tumor-associated macrophages and inhibition of MCP-1 reduce angiogenesis and tumor growth in a human melanoma xenograft. *The Journal of investigative dermatology* **2007**, *127*, 2031-2041, doi:10.1038/sj.jid.5700827.
14. Das, A.; Sinha, M.; Datta, S.; Abas, M.; Chaffee, S.; Sen, C.K.; Roy, S. Monocyte and macrophage plasticity in tissue repair and regeneration. *The American journal of pathology* **2015**, *185*, 2596-2606, doi:10.1016/j.ajpath.2015.06.001.
15. Williams, C.B.; Yeh, E.S.; Soloff, A.C. Tumor-associated macrophages: unwitting accomplices in breast cancer malignancy. *NPJ breast cancer* **2016**, *2*, 15025-, doi:10.1038/npjbcancer.2015.25.
16. Biswas, S.K.; Mantovani, A. Macrophage plasticity and interaction with lymphocyte subsets: cancer as a paradigm. *Nature immunology* **2010**, *11*, 889-896, doi:10.1038/ni.1937.
17. Geeraerts, X.; Bolli, E.; Fendt, S.M.; Van Ginderachter, J.A. Macrophage Metabolism As Therapeutic Target for Cancer, Atherosclerosis, and Obesity. *Frontiers in immunology* **2017**,

- 8, 289, doi:10.3389/fimmu.2017.00289.
18. Mantovani, A.; Sica, A. Macrophages, innate immunity and cancer: balance, tolerance, and diversity. *Current opinion in immunology* **2010**, *22*, 231-237, doi:10.1016/j.coi.2010.01.009.
 19. Ohtsuki, T.; Kimura, K.; Tokunaga, Y.; Tsukiyama-Kohara, K.; Tateno, C.; Hayashi, Y.; Hishima, T.; Kohara, M. M2 Macrophages Play Critical Roles in Progression of Inflammatory Liver Disease in Hepatitis C Virus Transgenic Mice. *Journal of virology* **2016**, *90*, 300-307, doi:10.1128/jvi.02293-15.
 20. Hao, N.B.; Lü, M.H.; Fan, Y.H.; Cao, Y.L.; Zhang, Z.R.; Yang, S.M. Macrophages in tumor microenvironments and the progression of tumors. *Clinical & developmental immunology* **2012**, *2012*, 948098, doi:10.1155/2012/948098.
 21. Panni, R.Z.; Linehan, D.C.; DeNardo, D.G. Targeting tumor-infiltrating macrophages to combat cancer. *Immunotherapy* **2013**, *5*, 1075-1087, doi:10.2217/imt.13.102.
 22. Hussein, M.R. Tumour-associated macrophages and melanoma tumourigenesis: integrating the complexity. *International journal of experimental pathology* **2006**, *87*, 163-176, doi:10.1111/j.1365-2613.2006.00478.x.
 23. Torisu, H.; Ono, M.; Kiryu, H.; Furue, M.; Ohmoto, Y.; Nakayama, J.; Nishioka, Y.; Sone, S.; Kuwano, M. Macrophage infiltration correlates with tumor stage and angiogenesis in human malignant melanoma: possible involvement of TNFalpha and IL-1alpha. *International journal of cancer* **2000**, *85*, 182-188.
 24. Howe, K.; Clark, M.D.; Torroja, C.F.; Torrance, J.; Berthelot, C.; Muffato, M.; Collins, J.E.; Humphray, S.; McLaren, K.; Matthews, L., et al. The zebrafish reference genome sequence and its relationship to the human genome. *Nature* **2013**, *496*, 498-503, doi:10.1038/nature12111.
 25. Zhao, S.; Huang, J.; Ye, J. A fresh look at zebrafish from the perspective of cancer research. *Journal of experimental & clinical cancer research : CR* **2015**, *34*, 80, doi:10.1186/s13046-015-0196-8.
 26. Ellett, F.; Lieschke, G.J. Zebrafish as a model for vertebrate hematopoiesis. *Current opinion in pharmacology* **2010**, *10*, 563-570, doi:10.1016/j.coph.2010.05.004.
 27. Mesureur, J.; Feliciano, J.R.; Wagner, N.; Gomes, M.C.; Zhang, L.; Blanco-Gonzalez, M.; van der Vaart, M.; O'Callaghan, D.; Meijer, A.H.; Vergunst, A.C. Macrophages, but not neutrophils, are critical for proliferation of *Burkholderia cenocepacia* and ensuing host-damaging inflammation. *PLoS Pathog* **2017**, *13*, e1006437-e1006437, doi:10.1371/journal.ppat.1006437.
 28. Heilmann, S.; Ratnakumar, K.; Langdon, E.; Kansler, E.; Kim, I.; Campbell, N.R.; Perry, E.; McMahon, A.; Kaufman, C.; van Rooijen, E., et al. A Quantitative System for Studying Metastasis Using Transparent Zebrafish. *Cancer Res* **2015**, *75*, 4272-4282, doi:10.1158/0008-5472.can-14-3319.
 29. Chen, Q.; Ramu, V.; Aydar, Y.; Groenewoud, A.; Zhou, X.Q.; Jager, M.J.; Cole, H.; Cameron, C.G.; McFarland, S.A.; Bonnet, S., et al. TLD1433 Photosensitizer Inhibits Conjunctival Melanoma Cells in Zebrafish Ectopic and Orthotopic Tumour Models. *Cancers* **2020**, *12*, doi:10.3390/cancers12030587.
 30. He, S.; Lamers, G.E.; Beenakker, J.W.; Cui, C.; Ghotra, V.P.; Danen, E.H.; Meijer, A.H.; Spaink, H.P.; Snaar-Jagalska, B.E. Neutrophil-mediated experimental metastasis is enhanced by VEGFR inhibition in a zebrafish xenograft model. *J Pathol* **2012**, *227*, 431-445, doi:10.1002/path.4013.
 31. Nicoli, S.; Presta, M. The zebrafish/tumor xenograft angiogenesis assay. *Nature protocols* **2007**, *2*, 2918-2923, doi:10.1038/nprot.2007.412.
 32. Li, Y.J.; Hu, B. Establishment of multi-site infection model in zebrafish larvae for studying *Staphylococcus aureus* infectious disease. *Journal of genetics and genomics = Yi chuan xue bao* **2012**, *39*, 521-534, doi:10.1016/j.jgg.2012.07.006.
 33. Ellett, F.; Pase, L.; Hayman, J.W.; Andrianopoulos, A.; Lieschke, G.J. mpeg1 promoter transgenes direct macrophage-lineage expression in zebrafish. *Blood* **2011**, *117*, e49-56, doi:10.1182/blood-2010-10-314120.
 34. Gray, C.; Loynes, C.A.; Whyte, M.K.; Crossman, D.C.; Renshaw, S.A.; Chico, T.J. Simultaneous intravital imaging of macrophage and neutrophil behaviour during inflammation using a novel transgenic zebrafish. *Thrombosis and haemostasis* **2011**, *105*, 811-819, doi:10.1160/th10-08-0525.

35. Colegio, O.R.; Chu, N.Q.; Szabo, A.L.; Chu, T.; Rhebergen, A.M.; Jairam, V.; Cyrus, N.; Brokowski, C.E.; Eisenbarth, S.C.; Phillips, G.M., et al. Functional polarization of tumour-associated macrophages by tumour-derived lactic acid. *Nature* **2014**, *513*, 559-563, doi:10.1038/nature13490.
36. Cambier, C.J.; Takaki, K.K.; Larson, R.P.; Hernandez, R.E.; Tobin, D.M.; Urdahl, K.B.; Cosma, C.L.; Ramakrishnan, L. Mycobacteria manipulate macrophage recruitment through coordinated use of membrane lipids. *Nature* **2014**, *505*, 218-222, doi:10.1038/nature12799.
37. Dvorak, H.F. Tumors: wounds that do not heal-redux. *Cancer immunology research* **2015**, *3*, 1-11, doi:10.1158/2326-6066.cir-14-0209.
38. Heilmann, S.; Ratnakumar, K.; Langdon, E.; Kansler, E.; Kim, I.; Campbell, N.R.; Perry, E.; McMahon, A.; Kaufman, C.; van Rooijen, E., et al. A Quantitative System for Studying Metastasis Using Transparent Zebrafish. *Cancer Res* **2015**, *75*, 4272-4282, doi:10.1158/0008-5472.CAN-14-3319.
39. Kansler, E.R.; Verma, A.; Langdon, E.M.; Simon-Vermot, T.; Yin, A.; Lee, W.; Attiyeh, M.; Elemento, O.; White, R.M. Melanoma genome evolution across species. *BMC Genomics* **2017**, *18*, 136-136, doi:10.1186/s12864-017-3518-8.
40. Carey, T.E.; Takahashi, T.; Resnick, L.A.; Oettgen, H.F.; Old, L.J. Cell surface antigens of human malignant melanoma: mixed hemadsorption assays for humoral immunity to cultured autologous melanoma cells. *Proceedings of the National Academy of Sciences of the United States of America* **1976**, *73*, 3278-3282, doi:10.1073/pnas.73.9.3278.
41. Bevilacqua, R.G.; Coit, D.G.; Rogatko, A.; Younes, R.N.; Brennan, M.F. Axillary dissection in melanoma. Prognostic variables in node-positive patients. *Annals of surgery* **1990**, *212*, 125-131, doi:10.1097/0000658-199008000-00002.
42. Overwijk, W.W.; Restifo, N.P. B16 as a mouse model for human melanoma. *Current protocols in immunology* **2001**, *Chapter 20*, Unit 20.21, doi:10.1002/0471142735.im2001s39.
43. Gurevich, D.B.; Severn, C.E.; Twomey, C.; Greenhough, A.; Cash, J.; Toye, A.M.; Mellor, H.; Martin, P. Live imaging of wound angiogenesis reveals macrophage orchestrated vessel sprouting and regression. *The EMBO journal* **2018**, *37*, doi:10.15252/embj.201797786.
44. Baeriswyl, V.; Christofori, G. The angiogenic switch in carcinogenesis. *Seminars in cancer biology* **2009**, *19*, 329-337, doi:10.1016/j.semcancer.2009.05.003.
45. Wong, J.R.; Nanji, A.A.; Galor, A.; Karp, C.L. Management of conjunctival malignant melanoma: a review and update. *Expert Rev Ophthalmol* **2014**, *9*, 185-204, doi:10.1586/17469899.2014.921119.
46. Eskandarpour, M.; Huang, F.; Reeves, K.A.; Clark, E.; Hansson, J. Oncogenic NRAS has multiple effects on the malignant phenotype of human melanoma cells cultured in vitro. *Int J Cancer* **2009**, *124*, 16-26, doi:10.1002/ijc.23876.
47. Larsen, A.C. Conjunctival malignant melanoma in Denmark: epidemiology, treatment and prognosis with special emphasis on tumorigenesis and genetic profile. *Acta ophthalmologica* **2016**, *94 Thesis 1*, 1-27, doi:10.1111/aos.13100.
48. Missotten, G.S.; Keijser, S.; De Keizer, R.J.; De Wolff-Rouendaal, D. Conjunctival melanoma in the Netherlands: a nationwide study. *Invest Ophthalmol Vis Sci* **2005**, *46*, 75-82, doi:10.1167/iovs.04-0344.
49. Brouwer, N.J.; Marinkovic, M.; van Duinen, S.G.; Bleeker, J.C.; Jager, M.J.; Luyten, G.P.M. Treatment of conjunctival melanoma in a Dutch referral centre. *The British journal of ophthalmology* **2018**, *102*, 1277-1282, doi:10.1136/bjophthalmol-2017-311082.
50. Esmaeli, B.; Rubin, M.L.; Xu, S.; Goepfert, R.P.; Curry, J.L.; Prieto, V.G.; Ning, J.; Tetzlaff, M.T. Greater Tumor Thickness, Ulceration, and Positive Sentinel Lymph Node Are Associated With Worse Prognosis in Patients With Conjunctival Melanoma: Implications for Future AJCC Classifications. *The American journal of surgical pathology* **2019**, *43*, 1701-1710, doi:10.1097/pas.0000000000001344.
51. Cao, J.; Heijkants, R.C.; Jochemsen, A.G.; Dogrusoz, M.; de Lange, M.J.; van der Velden, P.A.; van der Burg, S.H.; Jager, M.J.; Verdijk, R.M. Targeting of the MAPK and AKT pathways in conjunctival melanoma shows potential synergy. *Oncotarget* **2017**, *8*, 58021-58036, doi:10.18632/oncotarget.10770.
52. Griewank, K.G.; Westekemper, H.; Murali, R.; Mach, M.; Schilling, B.; Wiesner, T.; Schimming, T.; Livingstone, E.; Sucker, A.; Grabellus, F., et al. Conjunctival melanomas harbor BRAF and NRAS mutations and copy number changes similar to cutaneous and mucosal melanomas.

- Clin Cancer Res* **2013**, *19*, 3143-3152, doi:10.1158/1078-0432.ccr-13-0163.
53. Larsen, A.C.; Dahmcke, C.M.; Dahl, C.; Siersma, V.D.; Toft, P.B.; Coupland, S.E.; Prause, J.U.; Guldberg, P.; Heegaard, S. A Retrospective Review of Conjunctival Melanoma Presentation, Treatment, and Outcome and an Investigation of Features Associated With BRAF Mutations. *JAMA ophthalmology* **2015**, *133*, 1295-1303, doi:10.1001/jamaophthalmol.2015.3200.
54. Cao, J.; Pontes, K.C.; Heijkants, R.C.; Brouwer, N.J.; Groenewoud, A.; Jordanova, E.S.; Marinkovic, M.; van Duinen, S.; Teunisse, A.F.; Verdijk, R.M., et al. Overexpression of EZH2 in conjunctival melanoma offers a new therapeutic target. *J Pathol* **2018**, *245*, 433-444, doi:10.1002/path.5094.
55. Pontes, K.C.S.; Groenewoud, A.; Cao, J.; Ataide, L.M.S.; Snaar-Jagalska, E.; Jager, M.J. Evaluation of (fli:GFP) Casper Zebrafish Embryos as a Model for Human Conjunctival Melanoma. *Invest Ophthalmol Vis Sci* **2017**, *58*, 6065-6071, doi:10.1167/iovs.17-22023.
56. Banerji, U.; Affolter, A.; Judson, I.; Marais, R.; Workman, P. BRAF and NRAS mutations in melanoma: potential relationships to clinical response to HSP90 inhibitors. *Molecular cancer therapeutics* **2008**, *7*, 737-739, doi:10.1158/1535-7163.mct-08-0145.
57. McCain, J. The MAPK (ERK) Pathway: Investigational Combinations for the Treatment Of BRAF-Mutated Metastatic Melanoma. *P & T: a peer-reviewed journal for formulary management* **2013**, *38*, 96-108.
58. Scholz, S.L.; Cosgarea, I.; Susskind, D.; Murali, R.; Moller, I.; Reis, H.; Leonardelli, S.; Schilling, B.; Schimming, T.; Hadaschik, E., et al. NF1 mutations in conjunctival melanoma. *Br J Cancer* **2018**, *118*, 1243-1247, doi:10.1038/s41416-018-0046-5.
59. Dos Santos, A.I.F.; De Almeida, D.R.Q.; Terra, L.F.; Baptista, M.c.S.; Labriola, L. Photodynamic therapy in cancer treatment - an update review. *Journal of Cancer Metastasis and Treatment* **2019**, *2019*, doi:10.20517/2394-4722.2018.83.
60. Triesscheijn, M.; Baas, P.; Schellens, J.H.; Stewart, F.A. Photodynamic therapy in oncology. *Oncologist* **2006**, *11*, 1034-1044, doi:10.1634/theoncologist.11-9-1034.
61. Dolmans, D.E.; Fukumura, D.; Jain, R.K. Photodynamic therapy for cancer. *Nature reviews. Cancer* **2003**, *3*, 380-387, doi:10.1038/nrc1071.
62. Frochot, C.; Mordon, S. Update of the situation of clinical photodynamic therapy in Europe in the 2003–2018 period. *Journal of Porphyrins and Phthalocyanines* **2019**, *23*, 347-357, doi:10.1142/s1088424619300027.
63. Monro, S.; Colón, K.L.; Yin, H.; Roque, J.; Konda, P.; Gujar, S.; Thummel, R.P.; Lilge, L.; Cameron, C.G.; McFarland, S.A. Transition Metal Complexes and Photodynamic Therapy from a Tumor-Centered Approach: Challenges, Opportunities, and Highlights from the Development of TLD1433. *Chemical Reviews* **2019**, *119*, 797-828, doi:10.1021/acs.chemrev.8b00211.
64. Chibazakura, T.; Toriyabe, Y.; Fujii, H.; Takahashi, K.; Kawakami, M.; Kuwamura, H.; Haga, H.; Ogura, S.; Abe, F.; Nakajima, M., et al. 5-Aminolevulinic acid enhances cell death under thermal stress in certain cancer cell lines. *Bioscience, biotechnology, and biochemistry* **2015**, *79*, 422-431, doi:10.1080/09168451.2014.975186.
65. Kennedy, J.C.; Pottier, R.H.; Pross, D.C. Photodynamic therapy with endogenous protoporphyrin IX: basic principles and present clinical experience. *Journal of photochemistry and photobiology. B, Biology* **1990**, *6*, 143-148, doi:10.1016/1011-1344(90)85083-9.
66. Kaspler, P.; Lazic, S.; Forward, S.; Arenas, Y.; Mandel, A.; Lilge, L. A ruthenium(ii) based photosensitizer and transferrin complexes enhance photo-physical properties, cell uptake, and photodynamic therapy safety and efficacy. *Photochemical & photobiological sciences: Official journal of the European Photochemistry Association and the European Society for Photobiology* **2016**, *15*, 481-495, doi:10.1039/c5pp00450k.
67. Molpus, K.L.; Kato, D.; Hamblin, M.R.; Lilge, L.; Bamberg, M.; Hasan, T. Intraperitoneal photodynamic therapy of human epithelial ovarian carcinomatosis in a xenograft murine model. *Cancer Res* **1996**, *56*, 1075-1082.
68. Elliott, J.T.; Samkoe, K.S.; Gunn, J.R.; Stewart, E.E.; Gardner, T.B.; Tichauer, K.M.; Lee, T.Y.; Hoopes, P.J.; Pereira, S.P.; Hasan, T., et al. Perfusion CT estimates photosensitizer uptake and biodistribution in a rabbit orthotopic pancreatic cancer model: a pilot study. *Academic radiology* **2015**, *22*, 572-579, doi:10.1016/j.acra.2014.12.014.
69. Engbrecht, B.W.; Menon, C.; Kachur, A.V.; Hahn, S.M.; Fraker, D.L. Photofrin-mediated photodynamic therapy induces vascular occlusion and apoptosis in a human sarcoma

- xenograft model. *Cancer Res* **1999**, *59*, 4334-4342.
70. McFarland, S.A.; Mandel, A.; Dumoulin-White, R.; Gasser, G. Metal-based photosensitizers for photodynamic therapy: the future of multimodal oncology? *Curr Opin Chem Biol* **2019**, *56*, 23-27, doi:10.1016/j.cbpa.2019.10.004.
 71. Ramu, V.; Aute, S.; Taye, N.; Guha, R.; Walker, M.G.; Mogare, D.; Parulekar, A.; Thomas, J.A.; Chattopadhyay, S.; Das, A. Photo-induced cytotoxicity and anti-metastatic activity of ruthenium(ii)-polypyridyl complexes functionalized with tyrosine or tryptophan. *Dalton transactions (Cambridge, England : 2003)* **2017**, *46*, 6634-6644, doi:10.1039/c7dt00670e.
 72. Heinemann, F.; Karges, J.; Gasser, G. Critical Overview of the Use of Ru(II) Polypyridyl Complexes as Photosensitizers in One-Photon and Two-Photon Photodynamic Therapy. *Accounts of chemical research* **2017**, *50*, 2727-2736, doi:10.1021/acs.accounts.7b00180.
 73. Fong, J.; Kasimova, K.; Arenas, Y.; Kaspler, P.; Lazic, S.; Mandel, A.; Lilge, L. A novel class of ruthenium-based photosensitizers effectively kills in vitro cancer cells and in vivo tumors. *Photochemical & photobiological sciences : Official journal of the European Photochemistry Association and the European Society for Photobiology* **2015**, *14*, 2014-2023, doi:10.1039/c4pp00438h.
 74. Liu, S.; Leach, S.D. Zebrafish models for cancer. *Annual review of pathology* **2011**, *6*, 71-93, doi:10.1146/annurev-pathol-011110-130330.
 75. Goessling, W.; North, T.E.; Zon, L.I. New waves of discovery: modeling cancer in zebrafish. *Journal of clinical oncology : official journal of the American Society of Clinical Oncology* **2007**, *25*, 2473-2479, doi:10.1200/jco.2006.08.9821.
 76. Howe, K.; Clark, M.D.; Torroja, C.F.; Torrance, J.; Berthelot, C.; Muffato, M.; Collins, J.E.; Humphray, S.; McLaren, K.; Matthews, L., et al. The zebrafish reference genome sequence and its relationship to the human genome. *Nature* **2013**, *496*, 498-503, doi:10.1038/nature12111.
 77. Amatruda, J.F.; Shepard, J.L.; Stern, H.M.; Zon, L.I. Zebrafish as a cancer model system. *Cancer cell* **2002**, *1*, 229-231, doi:10.1016/s1535-6108(02)00052-1.
 78. Lam, S.H.; Chua, H.L.; Gong, Z.; Lam, T.J.; Sin, Y.M. Development and maturation of the immune system in zebrafish, *Danio rerio*: a gene expression profiling, in situ hybridization and immunological study. *Developmental and comparative immunology* **2004**, *28*, 9-28, doi:10.1016/s0145-305x(03)00103-4.
 79. Zon, L.I.; Peterson, R.T. In vivo drug discovery in the zebrafish. *Nature reviews. Drug discovery* **2005**, *4*, 35-44, doi:10.1038/nrd1606.
 80. Lawson, N.D.; Weinstein, B.M. In vivo imaging of embryonic vascular development using transgenic zebrafish. *Dev Biol* **2002**, *248*, 307-318, doi:10.1006/dbio.2002.0711.
 81. Renshaw, S.A.; Loynes, C.A.; Trushell, D.M.; Elworthy, S.; Ingham, P.W.; Whyte, M.K. A transgenic zebrafish model of neutrophilic inflammation. *Blood* **2006**, *108*, 3976-3978, doi:10.1182/blood-2006-05-024075.
 82. Manghnani, P.N.; Wu, W.; Xu, S.; Hu, F.; Teh, C.; Liu, B. Visualizing Photodynamic Therapy in Transgenic Zebrafish Using Organic Nanoparticles with Aggregation-Induced Emission. *Nano-micro letters* **2018**, *10*, 61, doi:10.1007/s40820-018-0214-4.
 83. Wang, C.; Qian, Y. A water soluble carbazolyl-BODIPY photosensitizer with an orthogonal D-A structure for photodynamic therapy in living cells and zebrafish. *Biomaterials science* **2019**, *10.1039/c9bm01709g*, doi:10.1039/c9bm01709g.
 84. Hanson, K.; Robinson, S.D.; Al-Yousuf, K.; Hendry, A.E.; Sexton, D.W.; Sherwood, V.; Wheeler, G.N. The anti-rheumatic drug, leflunomide, synergizes with MEK inhibition to suppress melanoma growth. *Oncotarget* **2018**, *9*, 3815-3829, doi:10.18632/oncotarget.23378.
 85. van der Ent, W.; Burrello, C.; Teunisse, A.F.; Ksander, B.R.; van der Velden, P.A.; Jager, M.J.; Jochemsen, A.G.; Snaar-Jagalska, B.E. Modeling of human uveal melanoma in zebrafish xenograft embryos. *Investigative ophthalmology & visual science* **2014**, *55*, 6612-6622, doi:10.1167/iovs.14-15202.
 86. Chapman, A.; Fernandez del Ama, L.; Ferguson, J.; Kamarashev, J.; Wellbrock, C.; Hurlstone, A. Heterogeneous tumor subpopulations cooperate to drive invasion. *Cell Rep* **2014**, *8*, 688-695, doi:10.1016/j.celrep.2014.06.045.
 87. Nicoli, S.; Ribatti, D.; Cotelli, F.; Presta, M. Mammalian tumor xenografts induce neovascularization in zebrafish embryos. *Cancer Res* **2007**, *67*, 2927-2931, doi:10.1158/0008-5472.CAN-06-4268.

88. Wang, J.; Cao, Z.; Zhang, X.M.; Nakamura, M.; Sun, M.; Hartman, J.; Harris, R.A.; Sun, Y.; Cao, Y. Novel mechanism of macrophage-mediated metastasis revealed in a zebrafish model of tumor development. *Cancer Res* **2015**, *75*, 306-315, doi:10.1158/0008-5472.CAN-14-2819.
89. Wehmas, L.C.; Tanguay, R.L.; Punnoose, A.; Greenwood, J.A. Developing a Novel Embryo-Larval Zebrafish Xenograft Assay to Prioritize Human Glioblastoma Therapeutics. *Zebrafish* **2016**, *13*, 317-329, doi:10.1089/zeb.2015.1170.
90. Nareyeck, G.; Wuestemeyer, H.; von der Haar, D.; Anastassiou, G. Establishment of two cell lines derived from conjunctival melanomas. *Experimental eye research* **2005**, *81*, 361-362, doi:10.1016/j.exer.2005.04.018.
91. Keijser, S.; Maat, W.; Missotten, G.S.; de Keizer, R.J. A new cell line from a recurrent conjunctival melanoma. *The British journal of ophthalmology* **2007**, *91*, 1566-1567, doi:10.1136/bjo.2006.110841.
92. Luyten, G.P.; Naus, N.C.; Mooy, C.M.; Hagemeyer, A.; Kan-Mitchell, J.; Van Drunen, E.; Vuzevski, V.; De Jong, P.T.; Luiders, T.M. Establishment and characterization of primary and metastatic uveal melanoma cell lines. *International journal of cancer* **1996**, *66*, 380-387, doi:10.1002/(sici)1097-0215(19960503)66:3<380::aid-ijc19>3.0.co;2-f.
93. Chen, P.W.; Murray, T.G.; Uno, T.; Salgaller, M.L.; Reddy, R.; Ksander, B.R. Expression of MAGE genes in ocular melanoma during progression from primary to metastatic disease. *Clinical & experimental metastasis* **1997**, *15*, 509-518, doi:10.1023/a:1018479011340.
94. Carlotti, F.; Bazuine, M.; Kekarainen, T.; Seppen, J.; Pognonec, P.; Maassen, J.A.; Hoeben, R.C. Lentiviral vectors efficiently transduce quiescent mature 3T3-L1 adipocytes. *Molecular therapy : the journal of the American Society of Gene Therapy* **2004**, *9*, 209-217, doi:10.1016/j.ymthe.2003.11.021.
95. Hopkins, S.L.; Siewert, B.; Askes, S.H.; Veldhuizen, P.; Zwier, R.; Heger, M.; Bonnet, S. An in vitro cell irradiation protocol for testing photopharmaceuticals and the effect of blue, green, and red light on human cancer cell lines. *Photochemical & photobiological sciences : Official journal of the European Photochemistry Association and the European Society for Photobiology* **2016**, *15*, 644-653, doi:10.1039/c5pp00424a.
96. Hopkins, S.L.; Siewert, B.; Askes, S.H.C.; Veldhuizen, P.; Zwier, R.; Heger, M.; Bonnet, S. An in vitro cell irradiation protocol for testing photopharmaceuticals and the effect of blue, green, and red light on human cancer cell lines. *Photochemical & photobiological sciences : Official journal of the European Photochemistry Association and the European Society for Photobiology* **2016**, *15*, 644-653, doi:10.1039/c5pp00424a.
97. Cuello-Garibo, J.-A.; Meijer, M.S.; Bonnet, S. To cage or to be caged? The cytotoxic species in ruthenium-based photoactivated chemotherapy is not always the metal. *Chem Commun (Camb)* **2017**, *53*, 6768-6771, doi:10.1039/c7cc03469e.
98. Monro, S.; Colón, K.L.; Yin, H.; Roque, J., 3rd; Konda, P.; Gujar, S.; Thummel, R.P.; Lilge, L.; Cameron, C.G.; McFarland, S.A. Transition Metal Complexes and Photodynamic Therapy from a Tumor-Centered Approach: Challenges, Opportunities, and Highlights from the Development of TLD1433. *Chemical reviews* **2019**, *119*, 797-828, doi:10.1021/acs.chemrev.8b00211.
99. Galluzzi, L.; Vitale, I.; Aaronson, S.A.; Abrams, J.M.; Adam, D.; Agostinis, P.; Alnemri, E.S.; Altucci, L.; Amelio, I.; Andrews, D.W., et al. Molecular mechanisms of cell death: recommendations of the Nomenclature Committee on Cell Death 2018. *Cell Death Differ* **2018**, *25*, 486-541, doi:10.1038/s41418-017-0012-4.
100. Mishra, R.R.; Kneitz, S.; Scharl, M. Comparative analysis of melanoma deregulated miRNAs in the medaka and Xiphophorus pigment cell cancer models. *Comparative biochemistry and physiology. Toxicology & pharmacology : CBP* **2014**, *163*, 64-76, doi:10.1016/j.cbpc.2014.01.002.
101. Li, H.; Qian, Z.M. Transferrin/transferrin receptor-mediated drug delivery. *Medicinal research reviews* **2002**, *22*, 225-250, doi:10.1002/med.10008.
102. Qian, Z.M.; Li, H.; Sun, H.; Ho, K. Targeted drug delivery via the transferrin receptor-mediated endocytosis pathway. *Pharmacological reviews* **2002**, *54*, 561-587, doi:10.1124/pr.54.4.561.
103. Johnsen, K.B.; Burkhart, A.; Thomsen, L.B.; Andresen, T.L.; Moos, T. Targeting the transferrin receptor for brain drug delivery. *Progress in neurobiology* **2019**, *181*, 101665, doi:10.1016/j.pneurobio.2019.101665.

Chapter 3

TLD1433 photosensitizer inhibits conjunctival melanoma cells in zebrafish ectopic and orthotopic tumour models

Quanchi Chen¹, Vadde Ramu², Yasmin Aydar¹, Arwin Groenewoud¹, Xuequan Zhou², Martine J. Jager³, Houston Cole⁴, Colin G. Cameron⁴, Sherri A. McFarland^{4*}, Sylvestre Bonnet^{2*}, B. Ewa Snaar-Jagalska^{1*}

¹ Institute of Biology, Leiden University, Leiden, The Netherlands.

² Leiden Institute of Chemistry, Leiden University, P.O. Box 9502, 2300 RA Leiden, The Netherlands.

³ Department of Ophthalmology, Leiden University Medical Center, Leiden, The Netherlands

⁴ Department of Chemistry and Biochemistry, The University of Texas at Arlington, Arlington, Texas 76019, United States

* Correspondence:

Prof. B. Ewa Snaar-Jagalska, b.e.snaar-jagalska@biology.leidenuniv.nl; Tel : +31-71-527-4980

Dr. Sylvestre Bonnet, bonnet@chem.leidenuniv.nl; Tel : +31-71-527-4260

Prof. Sherri A. McFarland, sherri.mcfarland@uta.edu; Tel: 1-817-272-6072

Published in: Cancers 2020, 12, 578; doi: 10.3390

Keywords: Photodynamic therapy; conjunctival melanoma; in vitro and in vivo models; application in cancer; zebrafish tumour model

Abstract

The ruthenium-based photosensitizer (PS) TLD1433 has completed a phase I clinical trial for photodynamic therapy (PDT) treatment of bladder cancer. Here, we investigated a possible repurposing of this drug for treatment of conjunctival melanoma (CM). CM is a rare but often deadly ocular cancer. The efficacy of TLD1433 was tested on several cell lines from CM (CRMM1, CRMM2 and CM2005), Uveal Melanoma (OMM1, OMM2.5, MEL270), epidermoid carcinoma (A431) and cutaneous melanoma (A375). Using 15 minutes green light irradiation (21 mW/cm², 19 J.cm⁻², 520 nm), the highest phototherapeutic index (PI) was reached in CM cells, with cell death occurring via apoptosis and necrosis. The therapeutic potential of TLD1433 was hence further validated in zebrafish ectopic and newly-developed orthotopic CM models. Fluorescent CRMM1 and CRMM2 cells were injected into the circulation of zebrafish (ectopic model) or behind the eye (orthotopic model) and 24 hours later, the engrafted embryos were treated with the maximally-tolerated dose of TLD1433. The drug was administered in three ways, either by i) incubating the fish in drug-containing water (WA), or ii) injecting the drug intravenously into the fish (IV), or iii) injecting the drug retro-orbitally (RO) into the fish. Optimally, four consecutive PDT treatments were performed on engrafted embryos using 60 min drug-to-light intervals and 90 min green light irradiation (21 mW/cm², 19 J.cm⁻², 520 nm). This PDT protocol was not toxic to the fish. In the ectopic tumour model, both systemic administration by IV injection and RO injection of TLD1433 significantly inhibited growth of engrafted CRMM1 and CRMM2 cells. However, in the orthotopic model, tumour growth was only attenuated by localized RO injection of TLD1433. These data unequivocally prove that the zebrafish provides a fast vertebrate cancer model that can be used to test the administration regimen, host toxicity and anti-cancer efficacy of PDT drugs against CM. Based on our results, we suggest repurposing of TLD1433 for treatment of incurable CM and further testing in alternative pre-clinical models.

Introduction

Conjunctival melanoma (CM) is a rare but often deadly ocular disease that arises from mutated melanocytes, the melanin-producing cells in the conjunctiva [45]. Despite its rare occurrence, conjunctival melanoma is increasing [46]. Current treatment for CM is surgery combined with cryotherapy, brachytherapy, and/or topical chemotherapy. However, efficient treatment for this disease has not yet been developed and the side-effects caused by present treatments are severe [47]. Furthermore, lymph node metastases often develop in spite of a seemingly effective treatment of the local tumor, and may lead to further spreading [48-50]. Mutations in BRAF and NRAS genes lead to constitutive activation of the MAPK/ERK signalling pathway, which promotes CM proliferation and survival [50-53].

New treatments for CM are being actively looked for, for example by knocking down the over-expressed gene EZH2 in CM cell lines [54], using e.g. zebrafish xenograft models for faster and more predictive

drug testing [55], and by CM-specific gene discovery for targeted therapy [56]. However, cross-talk between different signalling pathways makes specific gene targeting approaches quite challenging [57,58]. In addition, cancer cells proliferate and mutate under single-treatment, often creating resistance against the common cancer drugs or gene-targeting therapies. Considering the superficial growth of CM and the widespread use of laser technology for curing eye diseases, photodynamic therapy (PDT), i.e. tumour ablation through visible light irradiation of a PS located inside the tumour [59-62], offers an interesting opportunity.

PDT is used for a wide range of dermatological conditions, and for Barrett's esophagus, bladder and prostate cancer [63]. Compared to surgery, PDT is less invasive, as tumour eradication can be obtained without creating a wound. PDT uses a PS molecule as a prodrug that under light irradiation generates an intense blast of reactive oxygen species (ROS) such as superoxides (O_2^-), hydroxyl radicals (HO^\cdot), and/or singlet oxygen 1O_2 , which eventually cause cytotoxic damage to biomolecules adjacent to the PS. ROS generation inside a malignant tissue may directly destroy cancer cells via ROS-induced cell death, as demonstrated with 5-aminolevulinic acid (5-ALA)-derived protoporphyrin IX (PpIX) [64]. However, indirect anti-tumour effects can also occur via ROS-induced damage to the tumour vasculature, as seen with TOOKAD[®], mTHPC, or Photofrin[®] [65-69]. Besides tetrapyrrole compounds and their precursors (5-ALA), the metal-based PDT PS, in particular those containing ruthenium(II) (Ru), show a high potential for generating intracellular ROS [70]. These PS absorb in the visible region of the spectrum, which is critical for *in vivo* activation [71], and suffer less from photobleaching compared to many tetrapyrrole compounds [72,73].

Recently, the McFarland and Lilje research groups have actively developed TLD1433 (Figure 1, left), a Ru-based PS. A phase Ib clinical trial for intravesical PDT treatment of non-muscle invasive bladder tumours using this PS was successfully completed in 2018, [66,73] and a much larger Phase 2 study is underway. The compound has a low cytotoxicity in the dark and an exceptionally high phototoxicity with light activation when tested on a wide range of human cancer cells [73]. Its activation in cells is optimal in the green domain of the spectrum (520 nm), and although the mechanism of cell death by light-activated TLD1433 is not completely clear, this PS generates 1O_2 with near-to-unity quantum efficacy [66]. The outstanding type-II PDT properties of this compound involve initial population of metal-to-ligand charge transfer excited states, which, after intersystem crossing, lead to triplet intra-ligand (3IL) or intra-ligand charge-transfer excited states (3ILCT , Figure 1, right) that are very sensitive to oxygen and other excited state quenchers. These remarkable results led us to investigate a possible repurposing of TLD1433 for the PDT treatment of conjunctival melanoma (CM). We analysed the *in vitro* and *in vivo* efficacy of this compound in different CM cells lines and zebrafish embryonic xenograft CM models using green light irradiation ($\lambda = 520$ nm).

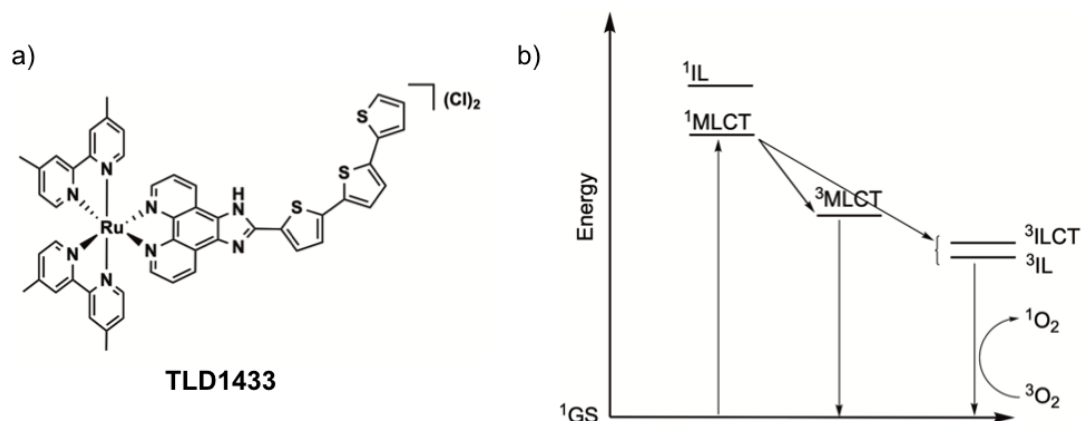


Figure 1 a) Chemical structure of the PDT photosensitizer TLD1433. b) Jablonski diagram showing the formation of singlet oxygen ($^1\text{O}_2$) by irradiation of TLD1433 via initial population of metal-to-ligand charge transfer (MLCT) states and intersystem crossing to intra-ligand (IL, ILCT) states.

Zebrafish (*Danio rerio*) are indeed increasingly used as an *in vivo* model to study cancer [74]. Benefits include large clutch size, *ex utero* development and easy manipulability of larvae [75]. Because there is high conservation of genes between zebrafish (ZF) and human, data collected in ZF are relevant for humans [76]. Notably, the histology of ZF tumours has been shown to be highly similar to tumours found in human cancers [77]. The adaptive immune system in ZF does not reach maturity until 4 weeks post-fertilization, allowing circumvention of cell graft-host rejection by using ZF in early stages [78]. ZF larvae can absorb various small molecular weight compounds from the water they swim in, which is advantageous when screening for anti-cancer compounds. When assessing drug efficacy, ZF experiments require much less material than mouse models [79]. Routinely 1 mL (1 nM to 20 μM) of drug solution is enough for testing drug efficacy in 6 individual ZF embryos. Alternatively, (pro)drugs can also be injected in the animal in nL quantities, which further minimizes the amount of compound required for testing. Importantly, the use of transgenic lines with fluorescent vasculature, neutrophil granulocytes or macrophages, allows live, non-invasive imaging of proliferation, migration and tumour-associated neo-angiogenesis, and interaction with the microenvironment at the single cell resolution in the entire organism within 1 week [80,81]. For PDT, the transparency of the animals allows for activating a PS in the entire organism by simple light irradiation. Overall, these combined advantages account for the increased experimental use of zebrafish cancer models in drug discovery during the last two decades [82,83].

For cutaneous melanoma, a current phase I/II clinical trial of leflunomide combined with vemurafenib is the first to arise from initial screens in zebrafish [84]. Many ZF xenograft models have been established, and the choice of the best ZF model depends on the type of disease, but also on the type of treatment. Human tumour cells can be injected for example into the yolk sac [85], the Duct of Cuvier [30], the pericardial cavity [86], the perivitelline space [87], the swimming bladder [88], or the hindbrain [89]. Here, we aimed to engage different CM xenograft models for testing the TLD1433 PS as a potential new

PDT treatment strategy to combat CM growth. We hence developed a new orthotopic model for CM by RO injection of CM cells, mimicking primary tumour spread. We also investigated a previously-developed ectopic model, generated by intravenous cell injection: circulating cancer cells usually form tumour lesions in the tail of the embryo [30,55]. Using three different treatment modalities of TLD1433 in two different tumour models, we established a testing platform in which the anti-tumour efficacy of this PS can be observed.

Materials and methods

Photosensitizers

For *in vitro* studies, TLD1433 was firstly diluted to 2 mM in autoclaved PBS and further diluted in media as required. For the *in vivo* studies, TLD1433 was directly diluted to autoclaved 2%PVP as required.

Culturing Cell lines

Human conjunctival malignant melanoma cell lines CRMM1 and CRMM2, isolated by Nareyeck et al [90], were cultured in F12 Kaighn's modified medium (Hyclone, cat# SH30526.01) supplemented with 10% fetal bovine serum (FBS; Gibco, location). CM2005.1 established by Keijser et al [91] was cultured in RPMI 1640, Dutch Modified (Life Technologies, cat# 22409-015), supplemented with 10% fetal bovine serum (FBS; Gibco), 3 mM L-glutamine (1%, Life Technologies cat# 35050-038). Human uveal melanoma cell lines OMM1 (provided by Prof. Dr. G.P.M Luyten) [92], OMM2.5, MEL270 (provided by Dr. B.R. Ksander BR) [93]) were cultured in Ham's F12 medium (Sigma-Aldrich, cat# N3790) supplemented with 10% FCS. Stable fluorescent CRMM1 and CRMM2 cell lines were generated using lentivirus expressing both tandem dimer (td)Tomato and Blastocidin-S, as previously described [94]. Human cancer cell lines A431 and A375 were distributed by the European Collection of Cell Cultures (ECACC), and purchased through Sigma Aldrich (Zwijndrecht). A375 and A431 cells were thawed and at least passaged twice before starting cytotoxicity and uptake experiments. A375 and A431 cells were cultured in Dulbecco's Modified Eagle Medium with phenol red, supplemented with 10.0% v/v FCS, 0.2% v/v penicillin/streptomycin (P/S), and 0.9% v/v Glutamine-S (GM). Cells were cultured in either 25 cm² or 75 cm² flasks and split at 70-80% confluence. The flasks were incubated in a normoxic incubator at 37 °C at 5.0% CO₂ in a PHCbi O₂/CO₂ incubator, MCO-170M). The medium was refreshed twice a week. Cells used in all biological experiments were cultured for not more than eight weeks. Dulbecco's Minimal Essential Medium (DMEM, high glucose, without glutamine), 200 mM Glutamine-S (GM), trichloroacetic acid (TCA), glacial acetic acid, sulforhodamine B (SRB), tris (hydroxymethyl) aminomethane (tris base), and cis-diamineplatinum (II) dichloride (cisplatin) were purchased from Sigma Aldrich. (2R,3R,4R,5R)-hexan-1,2,3,4,5,6-hexol (D-mannitol) was purchased from Santa Cruz Biotechnology via Bio-Connect. FCS was purchased from Hyclone. Penicillin and streptomycin were purchased from Duchefa and were diluted to a 100 mg/mL penicillin/streptomycin solution (P/S). Trypsin and Opti-MEM® (without phenol red) were purchased from Gibco® Life Technologies. Trypan blue (0.4% in 0.81% sodium chloride and

0.06% potassium phosphate dibasic solution) was purchased from Bio-Rad. Plastic disposable flasks and 96-well plates were obtained from Sarstedt. Cells were counted using a Bio-Rad TC10 automated cell counter with Bio-Rad Cell Counting Slides.

Cytotoxicity (SRB) assay

At day 0, cells were detached using 1mL of trypsin, resuspended in 4 mL of media and transferred to a 15 mL corning falcon tube. Cells were counted using trypan blue and BioRad® TC20™ automated cell counter (Figure 11). Dilutions of 6000 (CRMM1), 6000 (CRMM2), 8000 (CM2005.1), 6000 (OMM1), 6000 (OMM2.5), 6000 (MEL270) 8000 (A431), and 4000 (A375) cells/well were calculated from each cell suspension at a final volume of 6 mL using the following formula:

$$Vc = (Vt \times 10C) / Lc$$

Vc = volume of cell suspension to be diluted (mL)

Vt = total volume of solution

C = number of cells per well/per 100 μ L

Lc = live cell count (cells/mL)

The cell suspensions were transferred to a 50 mL reservoir and 100 μ l of each cell line was seeded at the aforementioned cell densities in triplicate in six 96-well plates. Boarder wells were intentionally filled with PBS media to avoid boarder effects. After 24 h, the cells were treated with TLD1433 with six different concentrations ranging from 0.025 μ M to 3.0 μ M, followed by incubation in a normoxic incubator. After 24 h of post treatment the cells were exposed to the green light for 15 min (520 nm, 21 mW/cm², 19J/cm²). The dark control plate was kept under dark conditions. Cisplatin was used as a positive control in all cell types. Then cells were incubated for another 48 h before fixing them with trichloroacetic acid (10% w/w) solution. The fixed cells were kept at 4°C for 48hrs, when TCA was washed out with distilled water before adding the sulphorhodamin B (SRB) (0.6 % SRB) dye. The SRB dye was washed out after 30 minutes and plates were air dried for overnight. Next day, the dye was dissolved using Tri-base (0.25%) and absorbance of SRB at 510 nm was recorded from each well using a Tecan plate reader. The SRB absorbance data was used to calculate the fraction of viable cells in each well (Excel and GraphPad Prism software). The absorbance data were averaged from triplicate wells per concentration. Relative cell viabilities were calculated by dividing the average absorbance of the treated wells by the average absorbance of the untreated wells. Three independent biological replicates were completed for each cell line (three different passage numbers per cell line). The average cell viability of the three biological replicates was plotted versus log(concentration) [μ M], with the SD error of each point. By using the dose–response curve for each cell line under dark- and irradiated conditions, the effective concentration (EC₅₀) was calculated by fitting the curves to a non-linear regression function with a fixed maximum (100 %) and minimum (0 %) (relative cell viability) and a variable Hill slope, which resulted in the simplified two-parameter Hill-slope equation [Eq. (1)]:

$$100/(1+10((\log_{10}EC_{50}-X) \cdot \text{Hillslope}))\dots\dots\dots(1)$$

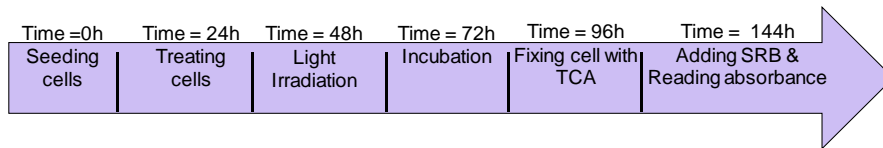


Figure 2 Time line for the SRB assay.

Cell irradiation setup

The cell irradiation system consisted of a Databis thermostat (980923001) fitted with two flat-bottomed microplate thermoblocks (800010600) and a 96-LED array fitted to a standard 96-well plate. The $\lambda=520$ nm LED (OVL3324), fans (40 mm, 24 V DC, 9714839), and power supply (EA PS 2042-06B) were obtained from Farnell as reported in our previous publication [95].

Flow Cytometry

CRMM1 (10000/well) and CRMM2 (10000/well) cells were seeded into an 8-well chamber in Opti-MEM™ (Gibco, Reduced Serum Medium, no phenol red) with 2.5% FBS (Gibco). After 24 h incubation, TLD1433 (0.0059 μM for CRMM1, 0.0048 μM for CRMM2) was added into the medium. 24h later, wells were washed and new drug-free medium was added. The cells were exposed to green light (520 nm, 21 mW/cm^2 , 19 J/cm^2) for 15 min and incubated for 48h. Medium of all wells was collected and wells were washed with PBS and lysed by 500 μl trypsin for 3 min. Collected medium was added to the wells with lysed cells, mixed and centrifuged for 2000 rpm, 3min. After washing, cells were resuspended in 200 μl of 1X binding buffer. Next, 5 μl of Annexin-V-FITC and 5 μl of Propidium Iodide was added to each well and incubated for 15 min at room temperature. 200 μl of sample was added to 96-well plate, and used for FACS measurement.

Zebrafish maintenance, tumour cells implantation and tumour analysis

The Zebrafish (ZF) *Tg(fli1: GFP/Casper)* [80] were handled in compliance with local animal welfare regulations and maintained according to standard protocols (www.ZFIN.org).

For cancer cell injection, two days post-fertilization (dpf), dechorionated zebrafish embryos were anaesthetized with 0.003% tricaine (Sigma) and plated on a 10cm Petri dish covered with 1.5% of solidified agarose. CRMM1 and CRMM2 cells were suspended in PBS containing 2% polyvinylpyrrolidone (PVP; Sigma-Aldrich) with a concentration of 50,000 cells/ μl and loaded into borosilicate glass capillary needles (1 mm O.D. \times 0.78 mm I.D.; Harvard Apparatus). In the ectopic model, 200 (td)Tomato fluorescent CM cells were injected into the Duct of Cuvier or at 2 dpf, which led to dissemination through the blood circulation and outgrowth in the head and tail. In orthotopic tumour model, 100 (td)Tomato fluorescent CRMM1 or CRMM2 cells were injected RO in 2 dpf embryos using a Pneumatic Picopump and a manipulator (WPI). After injection, the embryos were incubated in a 34 $^{\circ}\text{C}$ incubator. Images were

acquired at 1-, 2-, 4- and 6-days post injection (dpi) with a Leica M165 FC stereo fluorescence microscope. Tumor growth was quantified by calculating the total fluorescence intensity and area with the ZF4 pixel counting program (Leiden). Each experiment was performed at least 3 times with a group size of >30 embryos.

Light Toxicity assay for zebrafish embryos

2 dpf embryos were transferred into 6-well plates (10 embryos/well). The embryos were exposed to green light (520 nm, 9.82 J.cm⁻²) for 0, 3, 6, 12 h. After irradiation, images were taken using a DFC420C camera coupled to a Leica MZ16FA fluorescence microscope.

Maximum tolerated dose (MTD) for wild type zebrafish and tumour cells injected zebrafish

For determining the MTD of the WA of the TLD1433 solution in wild type zebrafish, solutions of 2.3 nM, 4.6 nM, 9.2 nM, 11.5 nM, 23 nM were made before the experiment. At 2.5, 3.5, 4.5, 5.5 dpf, TLD1433 was added to the fish water and maintained for 12 h. At 3, 4, 5, 6 dpf, the fish water was refreshed and after 1 h, embryos were exposed to the green light for 90 min (520 nm, 21 mW/cm², 19J/cm²). For the IV and RO administration, TLD1433 solution (1.15 mM, 2.3 mM, 4.6 mM, 9.2 mM, 11.5 mM) was made before the experiment. At 3, 4, 5, 6 dpf, 1nl of TLD1433 was injected via the dorsal vein or the RO site and maintained for 1 h. Embryos were exposed to the green light for 90 min (520 nm, 21 mW/cm², 19J/cm²). The images of treated and wild type embryos at 6dpf were taken using a DFC420C camera coupled to a Leica MZ16FA fluorescence microscope. In order to determine the The MTD of tumour cell bearing zebrafish, was performed according to the same procedure, after TLD1433 was delivered by WA, IV and RA administration as described above for the wild type embryos.

TUNEL assay

The zebrafish larvae were fixed overnight with 4% PFA at 4 °C. Embryos were washed in PBST for five minutes and dehydrated by a graded methanol series until reaching 100% methanol. Embryos were stored at -20 °C for further use. Embryos were gradually rehydrated in PBST (25%, 50%, 75%), washed twice for 10 minutes with PBST and digested by proteinase K (Roche) solution in PBST (10 µg/mL) at 37 °C for 40 minutes. After two washes in PBST, embryos were post-fixed in 4% PFA for 20 minutes. After twice washing in PBST for 10 minutes, 50 µl of TdT reaction mix (Roche) was added to the embryos. Embryos were overnight incubated with the TdT at 37 °C (in the dark). The reaction was stopped by three 15 min washes with PBST at room temperature and embryos were used for high-resolution imaging. Embryos were placed on glass-bottom petri dishes and covered with 1% low melting agarose containing 0.003% tricaine (Sigma). Imaging was performed using the Leica SP8 confocal microscope. The images were processed with ImageJ software. Each experiment was performed 3 times with a group size of 10 embryos.

Statistical analysis

Determination of the EC₅₀ concentrations in vitro was based on a non-linear regression analysis performed using GraphPad Prism Software. Results are presented as means ± SD from three independent experiments. Significant differences were detected by one-way ANOVA followed by Dunnett's multiple comparisons test implemented by Prism 8 (GraphPad Software, La Jolla, CA, USA). A p-value < 0.05 was considered statistically significant (*p≤0.05, **p≤0.01, ***p≤0.001, ****p≤0.0001).

Results

TLD1433 is phototoxic in six eye melanoma cell lines

TLD1433 is known to generate reactive oxygen species (ROS) with high quantum efficacy in many cancer cell lines. However, there is no report of the in vitro toxicity of this compound in eye melanoma cell lines. We determined the cell viability of three conjunctival melanoma cell lines (CRMM1, CRMM2 and CM2005.1), and three uveal melanoma cell lines (OMM1, OMM2.5, MEL270) in the presence of TLD1433, both in the dark or under green light irradiation (21 mW/cm², 19 J/cm², 520 nm, 15 min), and compared this viability to epidermoid carcinoma A431 and cutaneous melanoma A375 cell lines under the same conditions. The protocol used was based on previous work from the Bonnet group [96,97], and differed slightly from recommendations from McFarland et al [98]. Notably, the cell seeding time was 24 h instead of 3 h, and the drug-to-light interval (DLI) was 24 h instead of 16 h. The effective concentration (EC₅₀) values, i.e. the concentration required to reduce cell viability by 50% compared to untreated wells, were assessed by fitting the dose-response curves with a Hill equation. The phototoxicity index (PI), defined as the ratio of the dark EC₅₀ to the light EC₅₀, was also calculated and represents the amplification of TLD1433 activity with a light trigger. In control A375 and A431 cells, the dark toxicity of TLD1433 was very low, with EC₅₀ values higher than the highest concentration used in that assay (5 μM). PIs greater than 100, as previously reported for other cell lines [66], were observed. In eye melanoma cells, the dark toxicity of TLD1433 was relatively high, with EC₅₀ values around 1 μM. Upon light activation, TLD1433 became significantly more potent (as observed with the A375 and A431 cell lines), with EC₅₀ values in the nanomolar regime. The lowest EC₅₀ values were measured for CM cells, where the PI values were also the highest (>140). Due to the higher PI values for CM cells compared to uveal or cutaneous cancer cells, CM cells were chosen for later in vivo experiments (Figure 3, Table1). It should be noted that the PIs determined were somewhat lower than those reported for TLD1433 with other cell lines (>1000), which could be due either to a preferential toxicity toward uveal and CM melanoma lines or a difference in the in vitro PDT protocol used or both. Under the selected conditions, the dark toxicity observed for both uveal and CM cell lines was relatively high [73], which reduced the maximum PIs that can be obtained. In addition, the slightly lower PI could be due to the low light dose that we used, compared to other studies: typically, 100 J.cm⁻² has been proposed by McFarland et al [98]. Regardless, we chose CM cells for further studies given that TLD1433 had the largest PI and was most phototoxic toward this particular cell line.

Table 1 Three conjunctival melanoma cell lines, three uveal melanoma cell lines and two control cell lines were tested in an SRB cell viability assay, after exposure to TLD1433 with or without 19 J.cm⁻² green light exposure for 15 minutes (21 mW/cm², 19 J.cm⁻²). Cell growth inhibition effective concentrations (EC₅₀, in μM) and 95% confidence intervals (95% CI, in μM) were obtained. The photo index (PI) was calculated as EC₅₀, light divided by EC₅₀, dark.

	CRMM1	CRMM2	CM2005.1	OMM1	OMM2.5	MEL270	A431	A375
EC _{50,dark} (μM)	0.84	1.0	1.1	1.4	0.64	1.1	>5	>5
95% CI (μM)	-0.23 +0.27	-0.17 +0.19	-0.22 +0.25	-0.48 +0.95	-0.16 +0.19	-0.092 +0.097	n.a	-0.020 +0.020
EC _{50,light} (μM)	0.0059	0.0048	0.0058	0.014	0.013	0.010	0.049	0.050
95% CI (μM)	0.00099 +0.0012	-0.00050 +0.00055	-0.00061 +0.00066	-0.0016 +0.0019	-0.0011 +0.0013	-0.0012 +0.0013	-0.025 n.a	n.a n.a
PI	140	210	190	100	49	110	>102	>100

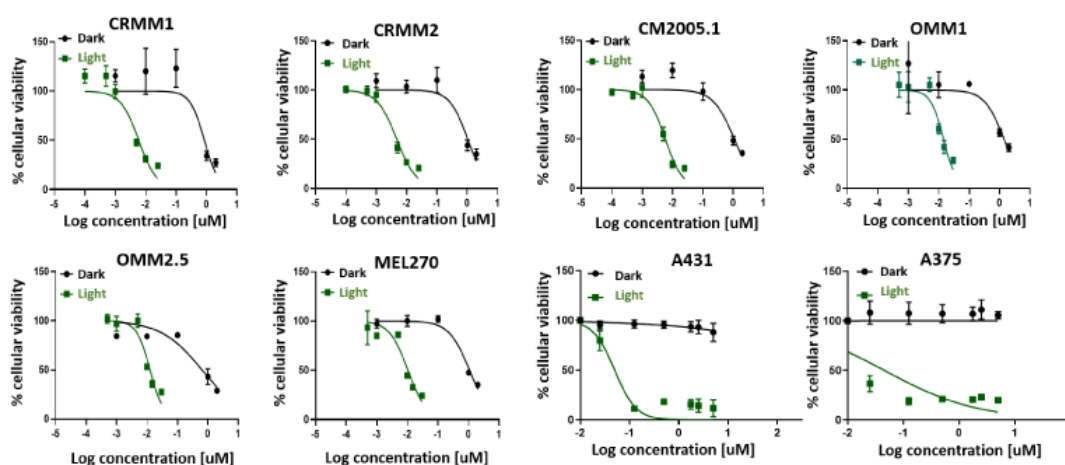


Figure 3 Cell viability after TLD1433 treatment of eight tumour cell lines (CRMM1, CRMM2, CM2005.1, OMM1, OMM2.5, MEL270, A431, A375). The green line shows TLD1433 activated by 520 nm light, 21 mW/cm², 19 J.cm² (light-induced toxicity). The dark line shows TLD1433 treatment without light irradiation (dark toxicity). The tumour cells were treated with TLD1433 for 24 hours with concentrations ranging from 0.001 μM to 5 μM and kept in the dark, or ranging from 0.0001 μM to 0.025 μM and illuminated with a light dose of 21 mW/cm², 19 J/cm². SRB assay was carried out at 48 hours after light irradiation. The absorbance of Sulforhodamine B in solution was measured at 520 nm. Results are presented as means ± SD from three independent experiments with 95% confidence intervals.

TLD1433 induces apoptosis and necrosis in CRMM1 and CRMM2 cells

Depending on the nature and intracellular localization of a PS, the light dose, and the cell type, PDT is known to provoke either necrosis, apoptosis, or autophagy [99]. In order to investigate the death mechanism induced by green light-activated TLD1433 in CRMM1 and CRMM2 cells, the cells were stained with Annexin V and Propidium Iodide, and further analysed by fluorescence-activated cell sorting (FACS). In both the vehicle control and the dark TLD1433 groups, most cells were found alive. In

the light-activated TLD1433 group, about half of the cells were found dead, either in the late apoptotic or necrotic quadrant (Figure 4A, 4B, 4C, 4D), but most importantly, very few early apoptotic cells were found. Overall, these results suggest that the CM cells treated with TLD1433 and light did not die via apoptosis, but probably by necrosis.

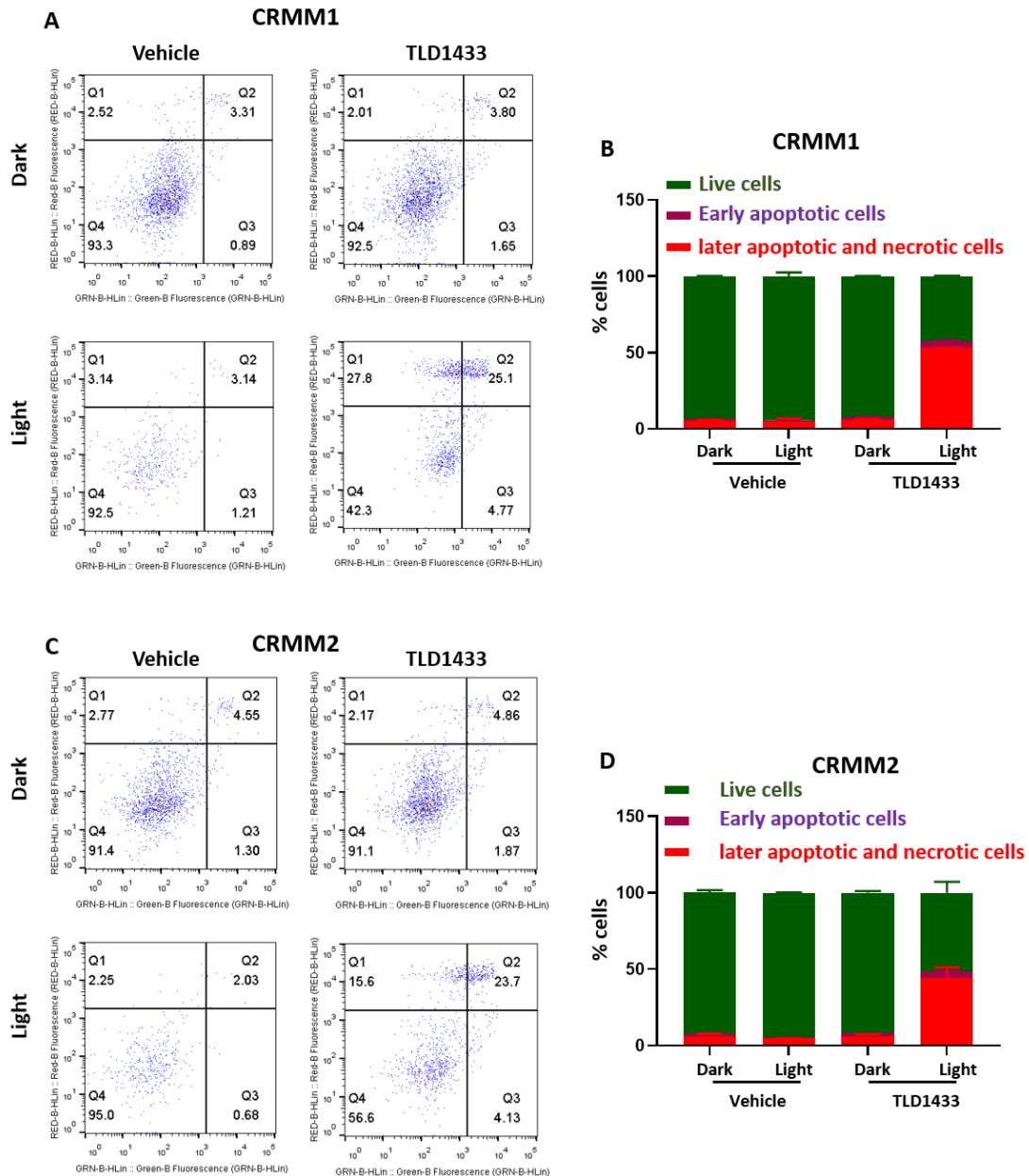


Figure 4 Green light irradiation of TLD1433 induces apoptosis and necrosis in CRMM1 and CRMM2 cells. (A) CRMM1 and (C) CRMM2 were stained with Annexin-V-FITC and Propidium Iodide. The percentages of live, early apoptotic, later apoptotic and necrotic cells in CRMM1 (B) and CRMM2 (D) were counted by FACS. Results are presented as means \pm SD from three independent experiments.

Light toxicity and the maximum tolerated dose of TLD1433 by water, intra-venous and RO administration in zebrafish embryos

In order to test the effectiveness of TLD1433-induced PDT in zebrafish CM cancer models, we first examined the effect of light irradiation on wild type, non-injected embryos. 2 days post fertilization (dpf) embryos (30 embryos per group) were exposed continuously to green light (21 mW/cm², 520 nm) for 0, 3, 6, and 12 h and cytotoxicity symptoms were monitored by stereomicroscope. Green light irradiation for 6h did not induce any toxicity or developmental defects in zebrafish embryos; the percentage of mortality, malformation (i.e. bent spine and pericardial edema) and fish length were the same as in the control group (Figure 5), indicating that green light is not toxic to ZF until at least 6 h of continued exposure.

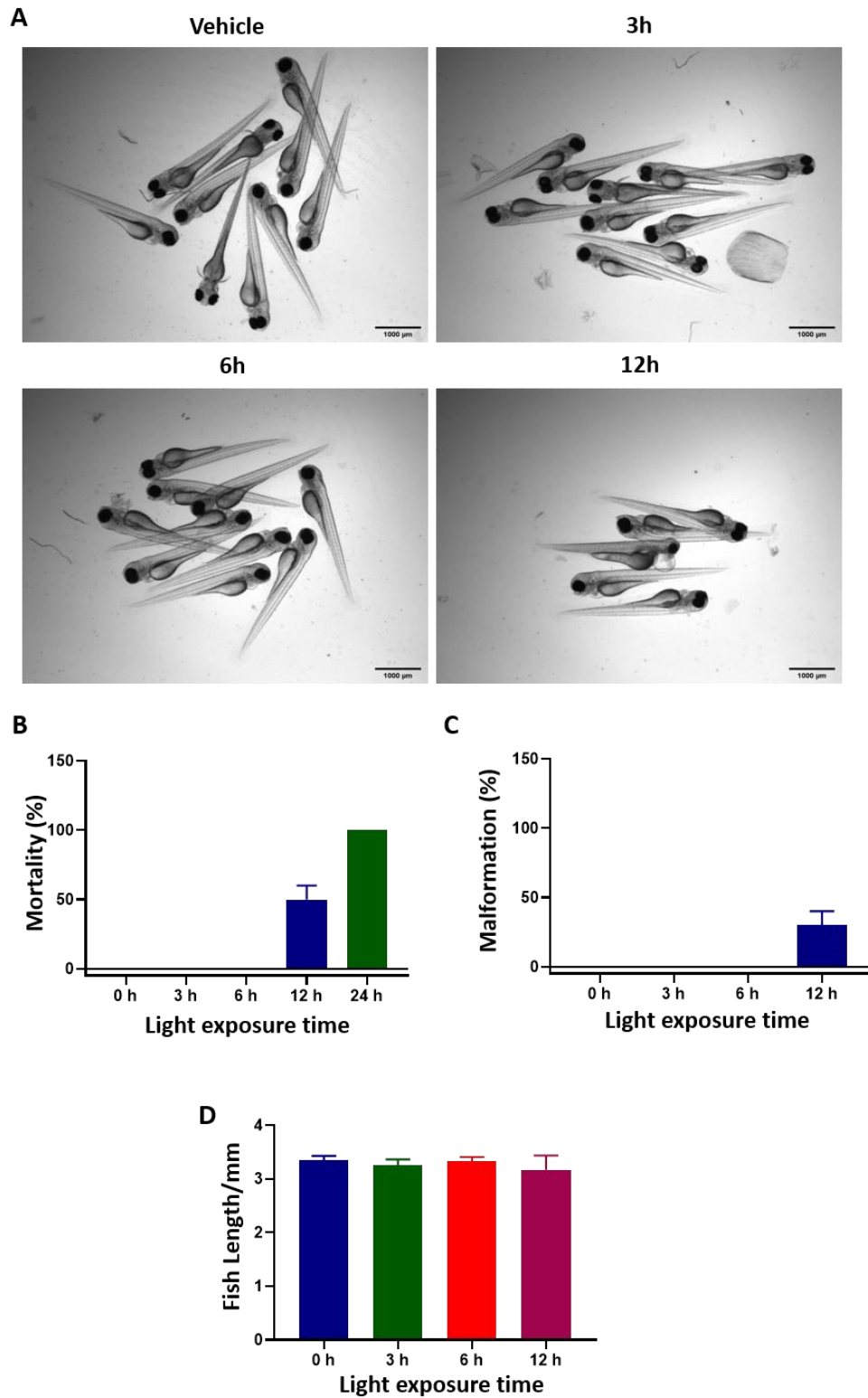


Figure 5 Light toxicity in zebrafish embryos. 2 dpf embryos (n=30) were exposed to green light (21 mW/cm², 520 nm) for 0, 3, 6, or 12 h. (A) Transmitted light images of the embryos after light irradiation. (B-D) The percentage of mortality, malformation and fish length after various time of light exposure. Results represents the means \pm SD from three independent experiments.

Next, we tried three different regimens of drug administration into zebrafish larvae and determined the maximum tolerated dose (MTD) of TLD1433 in dark and after light activation (Figure 6 and Table 2). Water administration (WA) of drugs by skin epithelial cell absorption and drinking is commonly used in zebrafish drug experiments [79]. Hence, different concentrations of TLD1433 were added into the egg water at 2.5, 3.5, 4.5, and 5.5 dpf embryos, followed by 12 h DLI and 90 min green light irradiation (21 mW/cm², 112.9 J.cm⁻², 520 nm). In addition, we also tested IV of TLD1433 by direct injection into the dorsal vein, as well behind the eye injections for RO administration [41]. For IV and RO administration, the compound was injected four times into the embryos at 3, 4, 5 and 6dpf, followed by 60 min drug-to-light interval and the same kinetic and irradiation regime as for the WA administration (Figure 6A). Zebrafish embryos tolerated light-activated TLD1433 without any effect on the mortality, malformation and fish length at an MTD of 9.2nM when delivered by WA administration and an MTD of 4.6mM when delivered by IV and RO administration, respectively (Figure 6 B-D). Considering that in the dark, even higher concentrations of TLD1433 (23 nM by WA, 11.5 mM by IV and RO) were not toxic to embryos, we conclude that this compound is activated by green light irradiation and very effective at low concentrations *in vivo*.

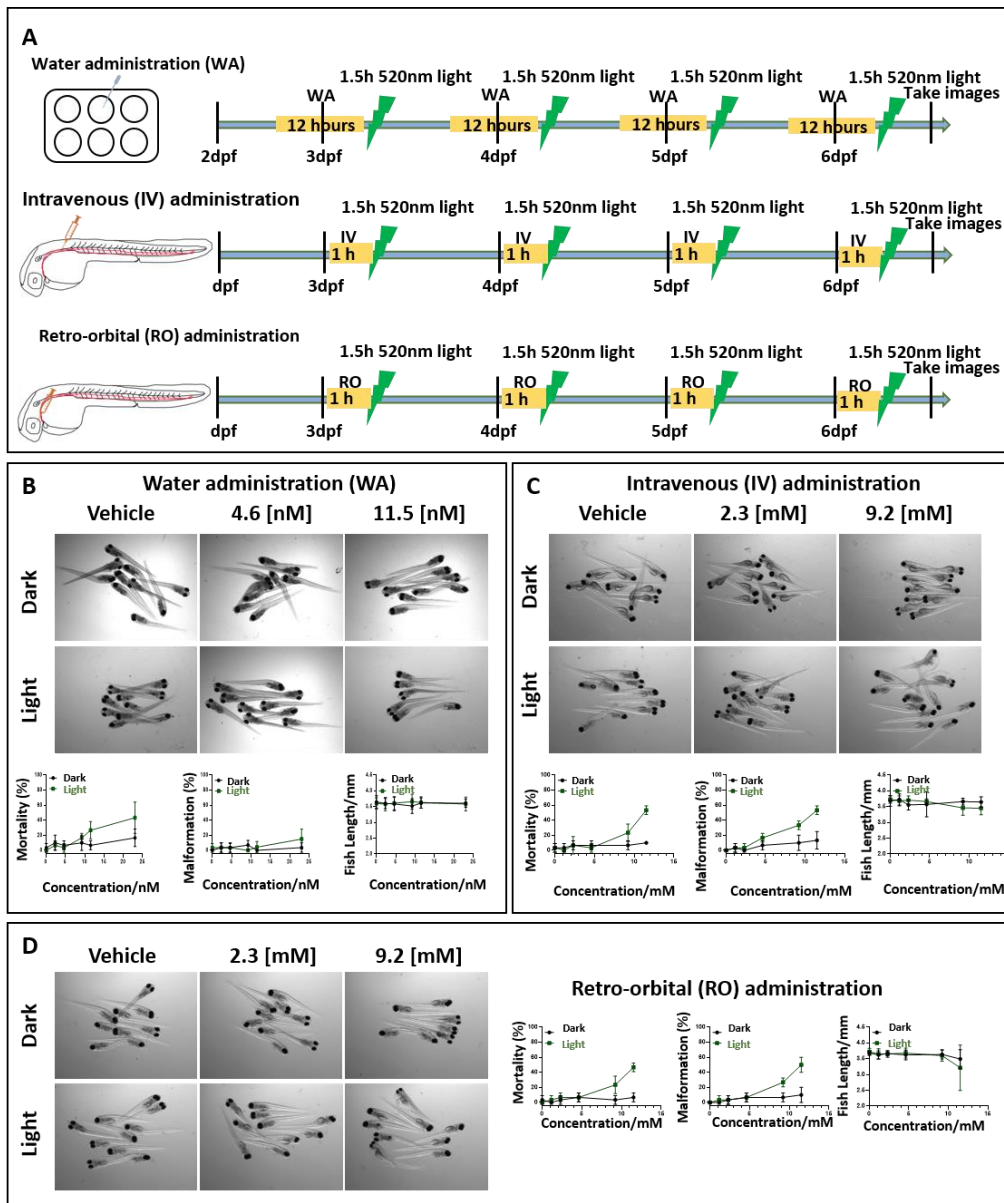


Figure 6 The maximum tolerated dose of TLD1433 in wild type zebrafish embryos administered through three different routes. (A) Schedule of TLD1433 treatment in wild type zebrafish. WA: TLD1433 (2.3nM, 4.6 nM, 9.2 nM, 11.5 nM, 23 nM) were added to the water containing 10 embryos per well at 2.5, 3.5, 4.5, 5.5 dpf, for 12h (yellow box). After these treatments, the drug was removed and replaced by egg water followed by 90 min green light irradiation (21 mW/cm^2 , $112.9 \text{ J}\cdot\text{cm}^{-2}$, 520 nm), depicted as a green lightning bolt. IV or RO: 1 nl of TLD1433 (1.15 mM, 2.3 mM, 4.6 mM, 9.2 mM, 11.5 mM) were injected into the embryos at 3dpf to 6dpf every morning, followed by 60 min drug-to-light interval (yellow box) and 90 min green light irradiation (21 mW/cm^2 , $112.9 \text{ J}\cdot\text{cm}^{-2}$, 520 nm), depicted as a green lightning bolt. (B) WA, (C) IV, (D) RO. (B-D) Images were made of irradiated (light) and non-irradiated (dark) embryos ($n=30$) at 6dpf and the percentages of mortality, malformation and fish length were calculated (shown as means \pm SD from three independent experiments). Representative images of embryos under dark and light conditions are shown.

The treatment of TLD1433 by WA, IV and RO in a zebrafish ectopic and orthotopic tumour model

The zebrafish ectopic conjunctival melanoma tumour model has been described previously [30]. In this model, around 200 fluorescent CM cells are injected into the Duct of Cuvier at 2 dpf, and then disseminate through the blood circulation and grow in the head and tail. To establish the orthotopic tumour model, around 100 red, (td)Tomato fluorescent CRMM1 or CRMM2 cells were injected RO at 2dpf into *Tg(Fli:GFP/Casper)*, endothelial reporter transgenic zebrafish with green fluorescent vasculature and examined by fluorescent microscopy at day 1 and 4 after engraftment (Figure 7A). Tumour expansion at the injection site was measured as fluorescence intensity and tumour area. Figure 6B shows that RO-engrafted CRMM1 and CRMM2 significantly proliferated at the site of injection and formed primary tumour lesions (Figure 7B, C).

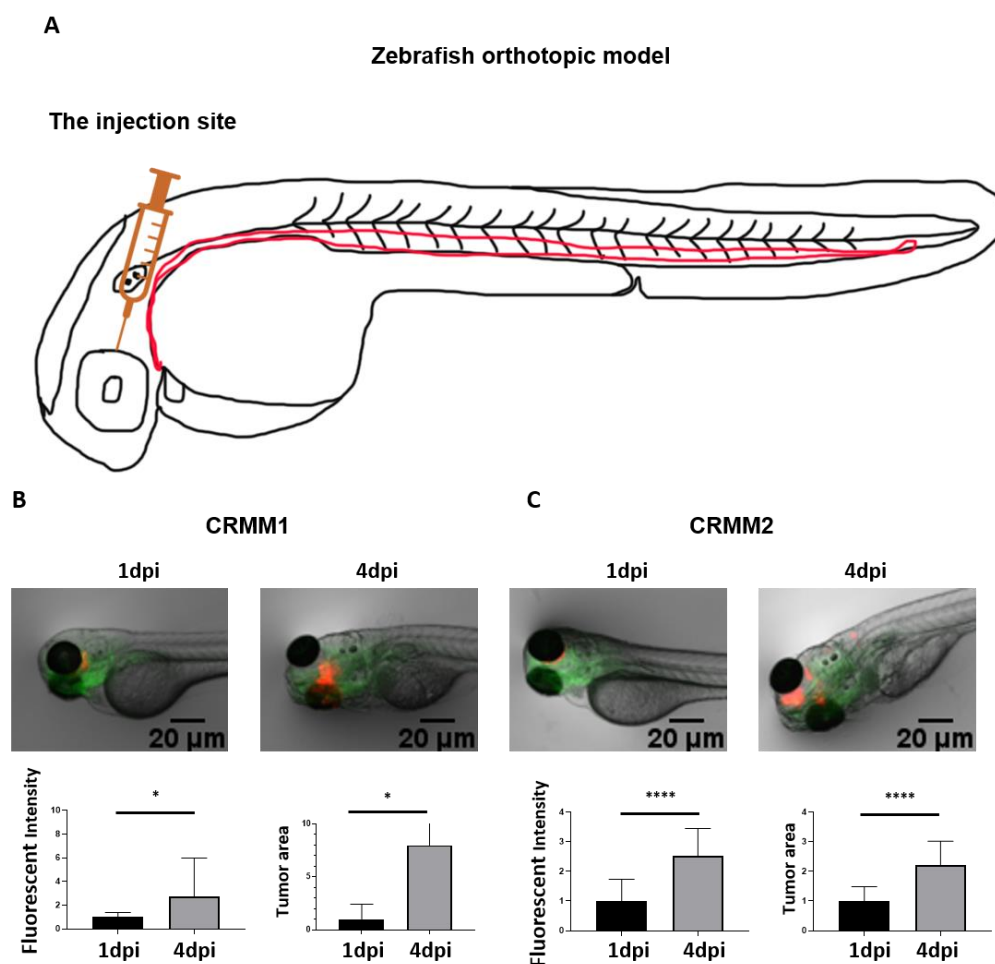


Figure 7 Development of a new conjunctival melanoma orthotopic tumour model in ZF. (A) Location of CM cell injection, (B) red fluorescent CRMM1 and (C) CRMM2 cells were injected RO into 2 dpf *Tg(Fli:GFP/Casper)* (n=10) and imaged by fluorescence microscopy at 1 and 4 days post injection (dpi). Relative tumour burden was calculated as fluorescent intensity and area of tumour cells by Image J. Results are means \pm SD of three independent experiments.

To engage both CM models for testing the efficacy of TLD1433 as a potential new PDT treatment strategy to combat CM growth, first, the MTD of TLD1433 delivered into zebrafish embryos engrafted with CM cells was measured (Table 2) following the same procedure as already described for wild type embryos (Figure 8 and Table 2). Engrafted embryos were more sensitive to light-activated TLD1433 than non-engrafted embryos (Table 2). MTD concentrations of 4.6 nM and 2.3 mM were delivered by WA, IV and RO administration. Delivery of TLD1433 at the MTD by WA did not inhibit tumour burden in the ectopic or orthotopic tumour model after engraftment of CRMM1 and CRMM2 cells (Figure 8). Relative tumour burden, estimated as fluorescence intensity and tumour area, was not significantly different between the dark and light treatments, indicating that the low concentrations of TLD1433 added to the water of engrafted embryos were not sufficient to attenuate CM growth in either model (Table 3, 4). The TLD1433 concentration in these experiments was not increased further as the initial treatment was already at the pre-determined MTD.

Table 2 The maximum tolerated dose (MTD) of TLD1433 in wild type zebrafish embryos and in the ectopic and orthotopic CM tumour model.

TLD1433 administration type	Maximum tolerated dose (MTD)	
	Wild type embryos	CM engrafted embryos Ectopic and orthotopic model
Water	9.2 nM	4.6 nM
Intravenous	4.6 mM	2.3 mM
Retro-orbital	4.6 mM	2.3 mM

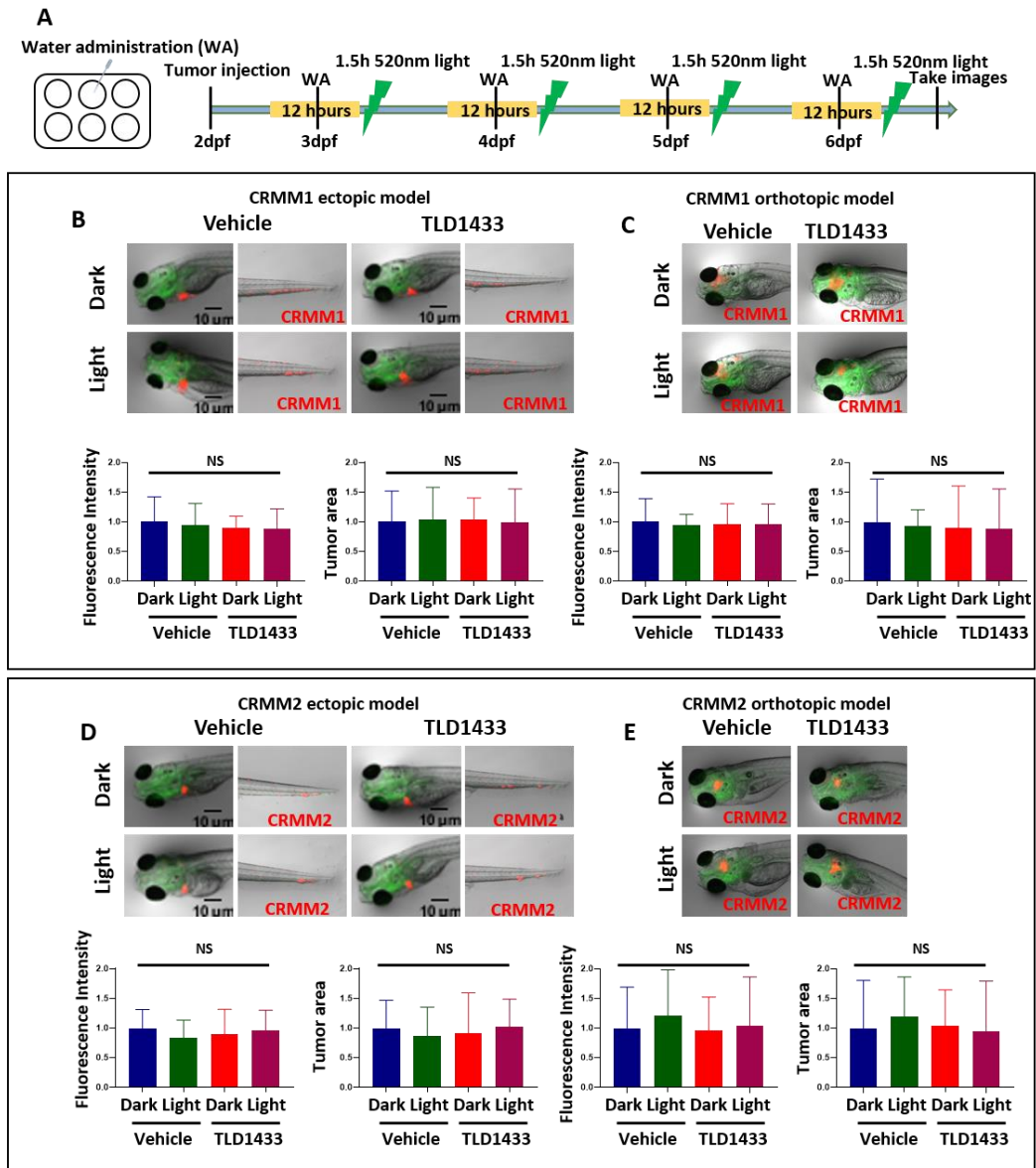


Figure 8 Treatment of zebrafish ectopic and orthotopic CM models with TLD1433 through WA. (A) Schedule of tumour injection and TLD1433 administration in zebrafish embryos. Fluorescent CRMM1 and CRMM2 cells were injected at 2 dpf into the Duct of Cuvier (ectopic model) and behind the eye (orthotopic model) and TLD1433 was administered with or without a light treatment following the schedule presented in A. Relative tumour burden estimated as fluorescence intensity and tumour area was calculated by Image J. (B) CRMM1 tumour burden in ectopic model ($n \approx 30$). (C) CRMM1 tumour burden in orthotopic model ($n \approx 15$). (D) CRMM2 tumour burden in ectopic model ($n \approx 30$). (E) CRMM2 tumour burden in orthotopic model ($n \approx 15$). Results are presented as means \pm SD from three independent experiments. Representative images show CM tumour burden in the head and tail regions in the ectopic model and a localised tumour in the orthotopic model.

Next, the effect of IV administration of TLD1433 was determined in both CM models. Figure 9 indicates that light activation of TLD1433 significantly reduced the tumour burden in the CRMM1 and CRMM2 ectopic model but not in the orthotopic model. In the ectopic model, light activation with the MTD (2.3 mM) of TLD1433 inhibited the CRMM1 and CRMM2 tumour fluorescence intensity as well as tumour

area (41%, 31%, 54%, and 50%) (Figure 9 B, D and Table 3, 4). The CRMM1 and CRMM2 tumour burden was not changed in the orthotopic model (Figure 9 C, E and Table 3, 4). This clearly shows that CRMM1 and CRMM2 tumour cells received a sufficient amount of activated TLD1433 in the ectopic model but not in the orthotopic model, suggesting that IV administration allows the compound to reach and inhibit CM cells in the ectopic model but is not effective to attenuate localized CM growth behind the eye in orthotopic model.

In contrast, delivery of the same concentration of TLD1433 (2.3 mM) by RO administration toward CRMM1 and CRMM2-induced tumours diminished the fluorescence intensity and tumour area in both ectopic (47%, 40%, 64%, 52%) and orthotopic models (35%, 55%, 69%, 71%) upon green light activation (58.3 J.cm⁻², 520 nm) (Figure 10 and Table 3, 4). We propose that TLD1433 remained longer in the interstitial fluid at the injection site after RO injection, reaching a higher effective concentration to inhibit CM cells grown in the same area.

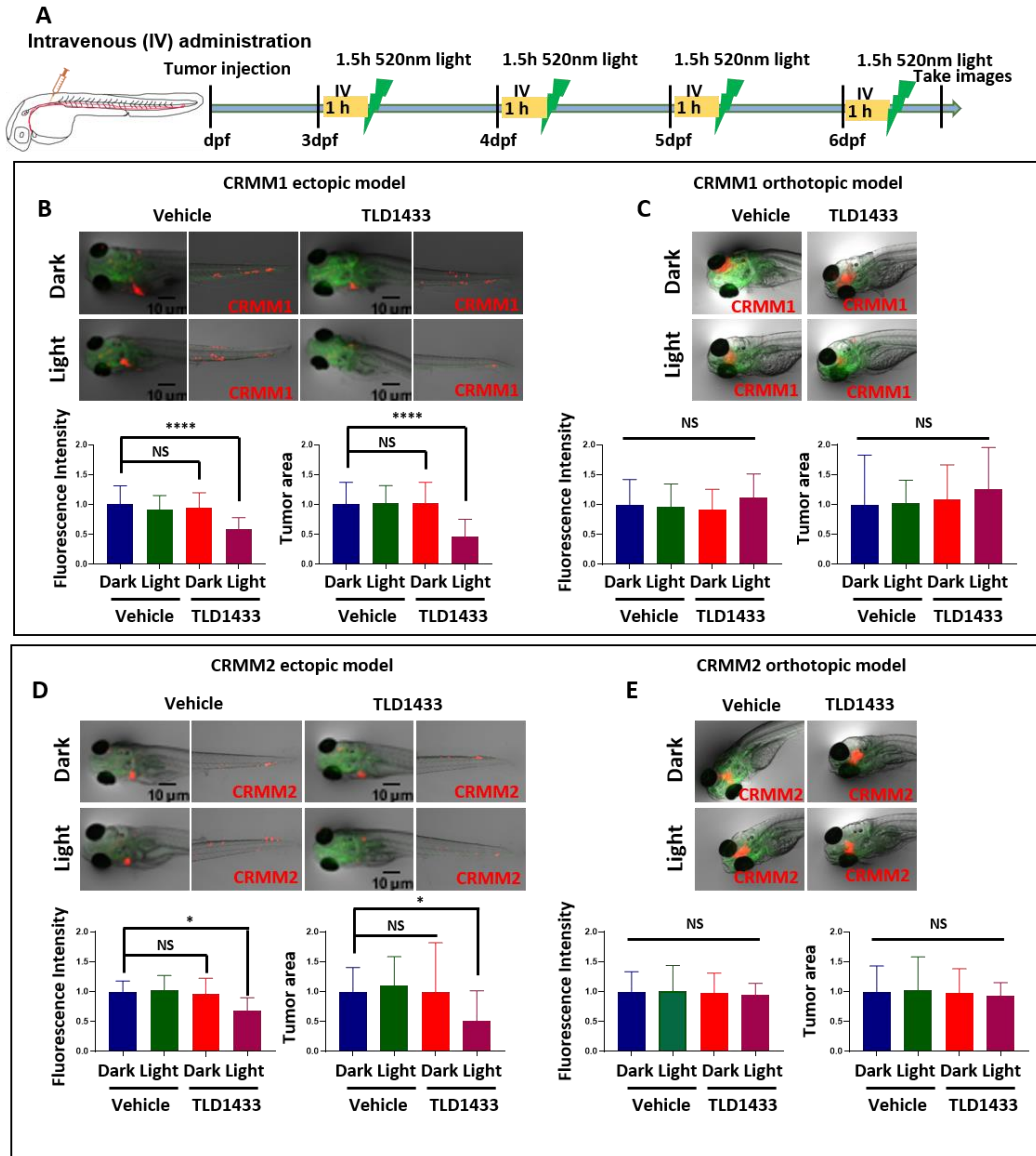


Figure 9 TLD1433 treatments by IV administration in the zebrafish ectopic and orthotopic CM model. (A) Schedule of tumour injection and TLD1433 administration in zebrafish embryos. Relative tumour burden was calculated as described in Figure 7. (B) CRMM1 tumour burden in the ectopic model ($n \approx 30$). (C) CRMM1 tumour burden in the orthotopic model ($n \approx 15$). (D) CRMM2 tumour burden in the ectopic model ($n \approx 30$). (E) CRMM2 tumour burden in the orthotopic model ($n \approx 15$). Results are presented as means \pm SD from three independent experiments. Representative images show CM tumour burden in the head and tail regions in ectopic model and localised tumours in the orthotopic model.

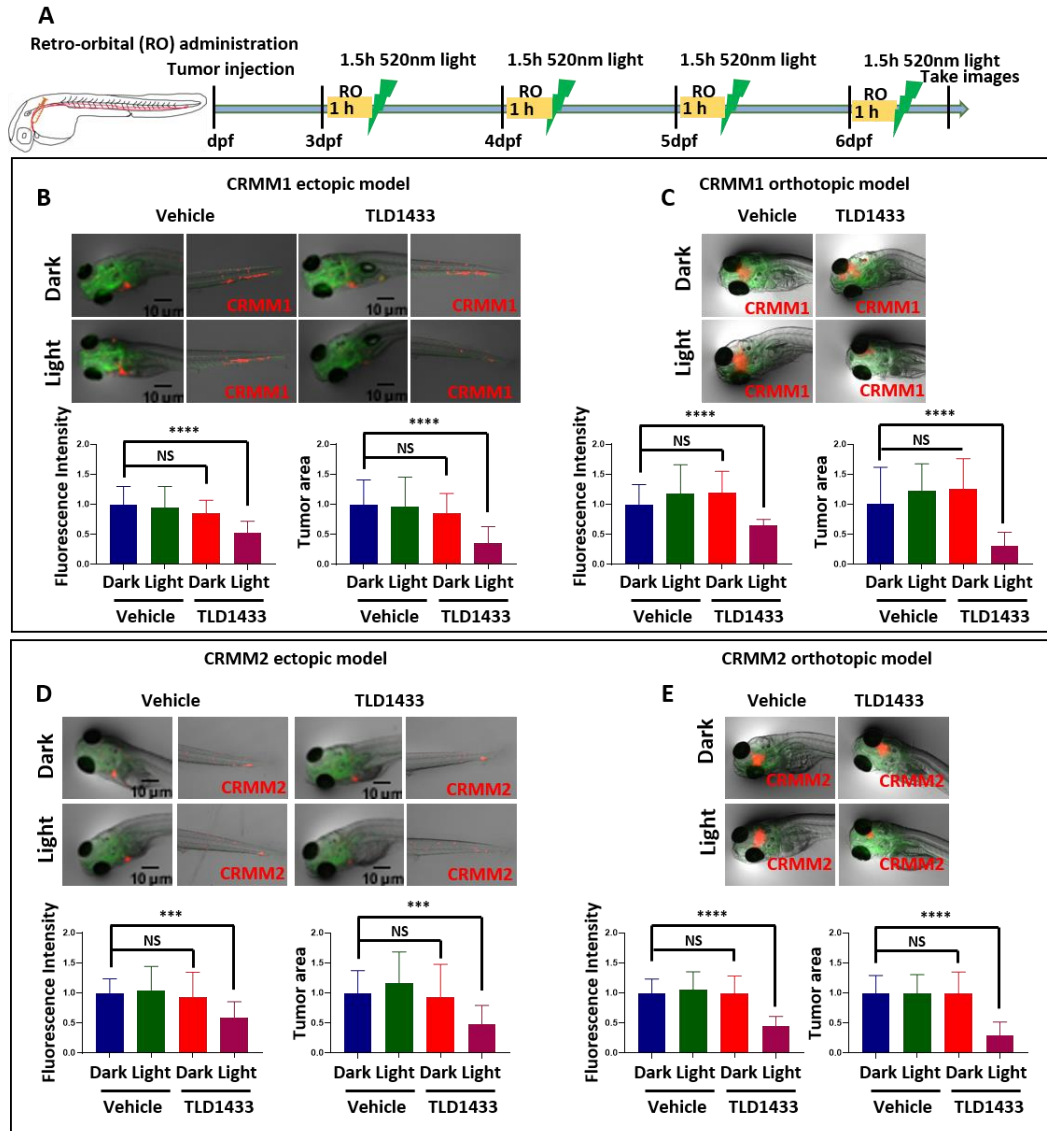


Figure 10 TLD1433 treatments by RO administration in the zebrafish ectopic and orthotopic CM model. (A) Schedule of tumour injection and TLD1433 administration in zebrafish embryos. Relative tumour burdens were calculated as described in Figure 7. (B) CRMM1 tumour burden in the ectopic model ($n \approx 30$). (C) CRMM1 tumour burden in the orthotopic model ($n \approx 15$). (D) CRMM2 tumour burden in the ectopic model ($n \approx 30$). (E) CRMM2 tumour burden in the orthotopic model ($n \approx 15$). Results are presented as means \pm SD from three independent experiments. Representative images show CM tumour burden in the head and tail regions in ectopic model and localised tumour in orthotopic model.

Table 3 Relative tumour burden quantified by fluorescence intensity in zebrafish embryonic models after treatment with TLD1433, delivered by three different administration routes. The fluorescence intensity is calculated as percentage, compared to the control dark group (100%).

		Relative tumour burden as measured by Fluorescence Intensity					
Route of TLD1433 administration		Ectopic Model			Orthotopic Model		
		Light dose (J.cm ⁻²)		PI	Light dose (J.cm ⁻²)		PI
		0	19		0	19	
CRMM1	Water	91%	89%	1.0	96%	96%	1.0
	Intravenous	94%	59%	1.6	91%	111%	0.82
	Retro-orbital	85%	53%	1.6	120%	65%	1.8
CRMM2	Water	90%	96%	0.93	96%	104%	0.92
	Intravenous	97%	69%	1.4	98%	95%	1.0
	Retro-orbital	93%	60%	1.6	100%	45%	2.2

Table 4 The relative tumour burden quantified by tumour area in zebrafish embryonic models after treatment with TLD1433 delivered by three different administration routes. The tumour area is calculated as percentage, compared to the control dark group (100%).

		Tumour area					
Route of TLD1433 administration		Ectopic Model			Orthotopic Model		
		Light dose (J.cm ⁻²)		PI	Light dose (J.cm ⁻²)		PI
		0	19		0	19	
CRMM1	Water	103%	99%	1.0	90%	89%	1.0
	Intra venous	102%	46%	2.2	109%	126%	0.87
	Retro orbital	85%	36%	2.4	125%	31%	4.1
CRMM2	Water	92%	102%	0.90	104%	95%	1.1
	Intra venous	99%	50%	2.0	97%	93%	1.1
	Retro orbital	94%	48%	2.0	99%	29%	3.4

TLD1433 by retro orbital administration induces apoptosis of CRMM1 and CRMM2 cells in zebrafish orthotopic model

In situ TUNEL assay on fixed embryos was used to detect TLD1433 induced apoptosis in zebrafish CRMM1 and CRMM2 orthotopic tumour models at 4 dpi after light activation of 2.3 mM TLD1433, administrated by retro orbital injection. The DNA strand breaks in apoptotic tumour cells were stained with fluorescein and visualized as a green signal. In control dark, control light, TLD1433 dark groups there was no positive green signal detected, which co-localized with red signal of CRMM1 and CRMM2 engrafted cells (Figure 11). In contrast, light activation of TLD1433, as described before (Figure 11C, E),

induced CRMM1 and CRMM2 cell apoptosis in the zebrafish orthotopic model. After light irradiation, the red signal representing engrafted CM cells was reduced, however some of the remaining cells stained positive for apoptotic cells and turned green (yellow in overlay), indicating that PDT-driven anti-tumour efficacy of TLD1433 in this PDT regimen is partially apoptosis-dependent.

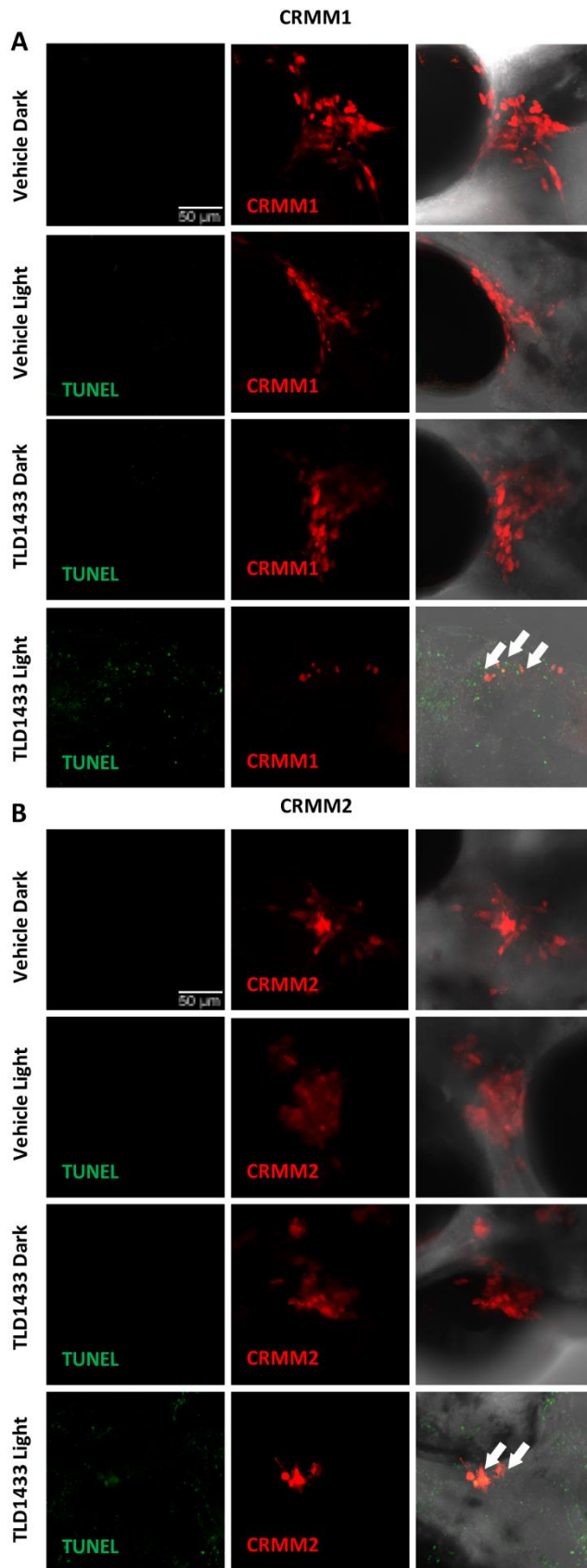


Figure 11 TUNEL assay of in CRMM1 and CRMM2 orthotopic model after RO of TLD1433. Red fluorescent CRMM1 (A) and CRMM2 (B) cells were injected at 2dpf behind the ZF eye and divided into four groups for drug treatment. RO administration of vehicle control and TLD1433 was

performed as described in Figure 10C, E. After dark or light exposure embryos were fixed and TUNEL staining was performed. Representative images of embryos are shown in this figure. (A, B) In TLD1433 light groups nuclear DNA fragmentation by nucleases is detected by co-localization of green (DNA fragments) and red signal of engrafted CM cells, depicted as yellow signal and marked by white arrows. In control dark, control light, TLD1433 dark, there are no positive green apoptotic tumour cells observed. Background green signal in TLD1433 light groups, does not co-localized with cytosolic red signal, which is diminished in degraded cells and TUNEL stains only the DNA breaks in these CM apoptotic cells. Experiment was performed 3 times with a group size of 10 embryos.

Discussion

Developing new ocular PDT treatments often depends on a limited number of rabbit studies, due to lack of other animal models. To overcome this, we previously generated an ectopic CM model, and now developed an orthotopic CM model in zebrafish. Zebrafish xenograft models are particularly straightforward for testing compound toxicity and efficacy *in vivo*, as one can examine on the one hand adverse effects on developing phenotypes or animal survival, and on the other hand tumour burden by fluorescence microscopy. For PDT in zebrafish, one should note that the PI can either be defined as the total tumour fluorescence or the total tumour area (as detected in confocal microscopy) in the light-activated group, divided by the tumour fluorescence or tumour area in the dark group. These definitions are quite different from the definition of the PI *in vitro*, where it is usually defined as the ratio between the EC₅₀ values in the dark and in light-irradiated conditions. As a consequence, *in vitro* and *in vivo* PIs cannot be directly compared. For example, the PI obtained by fluorescence spectroscopy in the orthotopic CRMM1 model and using RO injection of TLD1433 was 1.85, while that obtained by measuring the tumour area was 4.1; the PI measured by the ratio of EC₅₀ values *in vitro* was 140. The only PIs that can be compared are the ones defined identically in the same cancer model.

Here, our results demonstrate not only activity of TLD1433 in a broad range of different CM and UM cells *in vitro*, but also anti-tumour activity in a zebrafish embryo tumour models of CM. Interestingly, the *in vitro* results on 6 different eye melanoma cell lines are not significantly different, which means that TLD1433 shows a broad range of photoactivity, independently of the genetic background of the different cell lines. For the *in vivo* part of this work, we focussed on CM because TLD1433 induced the highest PIs in these cell lines. However, future experiments may further analyse UM, as good activity was also observed in the UM cell lines. Clearly, the excellent photodynamic properties of the Ru-based TLD1433 sensitizer make it phototoxic in most cell lines, including cutaneous melanoma and non-melanoma cell lines. When testing it *in vivo*, it is hence particularly important to optimise the mode of administration, compound dose, and light dose, in order to minimise side effects.

The main limitation for PDT of the zebrafish embryo tumour model is that due to the small size of the animal, light irradiation occurs on the whole organism, while in mice (or patients) prodrug activation occurs locally by light irradiation of the tumour. Global toxicity after local light activation in larger

animals is less likely to occur than upon full-body activation of a sensitizer in a small zebrafish embryo. Hence, higher toxicity is expected in zebrafish models, compared to mice models, which is why our results included an MTD study. On the other hand, zebrafish embryos are transparent and the engrafted CM cells are fluorescent, which allows for following in time and space the outcome of anti-tumour treatment, particularly in the primary tumour.

Despite such advantages, the relationship between the method of implanting the tumour and the mode of administration of the compound has to be established for each particular disease. For CM, our results clearly demonstrate that when the route of administration did not fit with the chosen tumour model, the activity in zebrafish was abrogated. This result is very important considering the notoriously excellent ROS generation properties of TLD1433 and its excellent PDT properties in mice tumour models [98]. In other words, activity in fish only appeared when the proper administration route was used. Clearly, the best model for tumor growth and drug testing was the orthotopic one, combined with local injection of TLD1433, i.e. injection behind the eye. Such a mode of administration turns out to be reminiscent of that used in bladder cancer patients, where TLD1433 is injected in the bladder and taken up very selectively by the tumour cells. Our results open the door for further zebrafish testing of not only TLD1433 (to assess on its toxicity, activity, and mode of action), but also of other phototherapeutic compounds, for which no activity *in vivo* has ever been reported.

Last but not least, clinical PDT in intraocular melanoma has up to now been limited not only by the lack of clinically approved PS, but also by interferences by the ocular and tumour pigment with light absorption. Most approved PDT sensitizers are porphyrin compounds, which offer a quite narrow (~20 nm) excitation wavelength range. If the pigment of the tumour absorbs too much of that light, PDT activity may be compromised. TLD1433, like most Ru polypyridyl compounds, shows broad absorption bands ($\Delta\lambda \sim 150$ nm) between the blue and red regions of the spectrum, thereby allowing to fine-tune the excitation wavelength and optimise light absorption by the sensitizer vs light absorption by the pigment [100]. These effects could not be tested here, as the CM and uveal melanoma cell lines have lost their pigments. Rutherrin, a new formulation of TLD1433 and transferrin, is now being proposed to improve the target specificity and water solubility of the PS [101-103]. Rutherrin was proven to cross the blood brain barrier (BBB) and is now under clinical investigation for glioblastoma multiforme (GBM) and non-small-cell lung cancer (NSCLC) [98]. However, this obstacle should be taken into account in any further *in vivo* testing of Ru-based sensitizers for PDT.

Conclusion

Our work supports three main conclusions. First, the Ru-based PDT sensitizer TLD1433 is very active in eye melanoma cell lines, where green light activation provokes cell death via apoptosis and necrosis. Second, this paper is one of the rare examples of testing PDT in a zebrafish tumour model. It could hence act as a basis for future PDT sensitizer screening *in vivo*, somewhere between *in vitro* and mice studies.

Due to the excellent ROS generation properties of this PDT sensitizer, it appears of utmost importance to fine-tune the way of administration of the prodrug to the tumour model. For two different models of conjunctive melanoma, i.e. an ectopic and an orthotopic model, we have tested three ways of administration of TLD1433. The WA, which is often chosen to test compounds in zebrafish, did not give good results: the phototoxicity to the zebrafish was high, and the anti-tumour efficacy low. When the compound was injected IV or RO, however, the toxicity became much lower and, when injected IV or RO, excellent anti-tumour properties were observed. We hence propose, as a third and last conclusion of this work, that TLD1433 can be repurposed as a treatment against conjunctival melanoma.

Author Contributions: Project administration, S.B. (Sylvestre Bonnet), and E.S.J. (Ewa Snaar-Jagalska); Investigation, Q.C. (Quanchi Chen), V.R. (Vadde Ramu), Y.A. (Yasmin Aydar), A.G. (Arwin Groenewoud) and X.Z. (Xuequan Zhou); Writing—original draft, Q.C. (Quanchi Chen), and V.R. (Vadde Ramu); Writing—review and editing, S.B. (Sylvestre Bonnet), E.S.J. (Ewa Snaar-Jagalska), M.J.J. (Martine J. Jager) and S.M. (Sherri McFarland).

Funding: This work was funded through Chinese Scholarship Council grants (QC) and TLD1433 compound was kindly provided by Theralase (Canada).

Conflicts of Interest: The authors declare no conflicts of interest.

References

1. Wong, J.R.; Nanji, A.A.; Galor, A.; Karp, C.L. Management of conjunctival malignant melanoma: a review and update. *Expert Rev Ophthalmol* **2014**, *9*, 185-204, doi:10.1586/17469899.2014.921119.
2. Eskandarpour, M.; Huang, F.; Reeves, K.A.; Clark, E.; Hansson, J. Oncogenic NRAS has multiple effects on the malignant phenotype of human melanoma cells cultured in vitro. *Int J Cancer* **2009**, *124*, 16-26, doi:10.1002/ijc.23876.
3. Larsen, A.C. Conjunctival malignant melanoma in Denmark: epidemiology, treatment and prognosis with special emphasis on tumorigenesis and genetic profile. *Acta ophthalmologica* **2016**, *94 Thesis 1*, 1-27, doi:10.1111/aos.13100.
4. Missotten, G.S.; Keijsers, S.; De Keizer, R.J.; De Wolff-Rouendaal, D. Conjunctival melanoma in the Netherlands: a nationwide study. *Invest Ophthalmol Vis Sci* **2005**, *46*, 75-82, doi:10.1167/iovs.04-0344.
5. Brouwer, N.J.; Marinkovic, M.; van Duinen, S.G.; Bleeker, J.C.; Jager, M.J.; Luyten, G.P.M. Treatment of conjunctival melanoma in a Dutch referral centre. *The British journal of ophthalmology* **2018**, *102*, 1277-1282, doi:10.1136/bjophthalmol-2017-311082.
6. Esmaeli, B.; Rubin, M.L.; Xu, S.; Goepfert, R.P.; Curry, J.L.; Prieto, V.G.; Ning, J.; Tetzlaff, M.T. Greater Tumor Thickness, Ulceration, and Positive Sentinel Lymph Node Are Associated With Worse Prognosis in Patients With Conjunctival Melanoma: Implications for Future AJCC Classifications. *The American journal of surgical pathology* **2019**, *43*, 1701-1710, doi:10.1097/pas.0000000000001344.
7. Cao, J.; Heijkants, R.C.; Jochemsen, A.G.; Dogrusoz, M.; de Lange, M.J.; van der Velden, P.A.; van der Burg, S.H.; Jager, M.J.; Verdijk, R.M. Targeting of the MAPK and AKT pathways in conjunctival melanoma shows potential synergy. *Oncotarget* **2017**, *8*, 58021-58036, doi:10.18632/oncotarget.10770.
8. Griewank, K.G.; Westekemper, H.; Murali, R.; Mach, M.; Schilling, B.; Wiesner, T.; Schimming, T.; Livingstone, E.; Sucker, A.; Grabellus, F., et al. Conjunctival melanomas harbor BRAF and NRAS mutations and copy number changes similar to cutaneous and mucosal melanomas.

Clin Cancer Res **2013**, *19*, 3143-3152, doi:10.1158/1078-0432.ccr-13-0163.

9. Larsen, A.C.; Dahmcke, C.M.; Dahl, C.; Siersma, V.D.; Toft, P.B.; Coupland, S.E.; Prause, J.U.; Guldberg, P.; Heegaard, S. A Retrospective Review of Conjunctival Melanoma Presentation, Treatment, and Outcome and an Investigation of Features Associated With BRAF Mutations. *JAMA ophthalmology* **2015**, *133*, 1295-1303, doi:10.1001/jamaophthalmol.2015.3200.
10. Cao, J.; Pontes, K.C.; Heijkants, R.C.; Brouwer, N.J.; Groenewoud, A.; Jordanova, E.S.; Marinkovic, M.; van Duinen, S.; Teunisse, A.F.; Verdijk, R.M., et al. Overexpression of EZH2 in conjunctival melanoma offers a new therapeutic target. *J Pathol* **2018**, *245*, 433-444, doi:10.1002/path.5094.
11. Pontes, K.C.S.; Groenewoud, A.; Cao, J.; Ataide, L.M.S.; Snaar-Jagalska, E.; Jager, M.J. Evaluation of (fli:GFP) Casper Zebrafish Embryos as a Model for Human Conjunctival Melanoma. *Invest Ophthalmol Vis Sci* **2017**, *58*, 6065-6071, doi:10.1167/iovs.17-22023.
12. Banerji, U.; Affolter, A.; Judson, I.; Marais, R.; Workman, P. BRAF and NRAS mutations in melanoma: potential relationships to clinical response to HSP90 inhibitors. *Molecular cancer therapeutics* **2008**, *7*, 737-739, doi:10.1158/1535-7163.mct-08-0145.
13. McCain, J. The MAPK (ERK) Pathway: Investigational Combinations for the Treatment Of BRAF-Mutated Metastatic Melanoma. *P & T: a peer-reviewed journal for formulary management* **2013**, *38*, 96-108.
14. Scholz, S.L.; Cosgarea, I.; Susskind, D.; Murali, R.; Moller, I.; Reis, H.; Leonardelli, S.; Schilling, B.; Schimming, T.; Hadaschik, E., et al. NF1 mutations in conjunctival melanoma. *Br J Cancer* **2018**, *118*, 1243-1247, doi:10.1038/s41416-018-0046-5.
15. Dos Santos, A.I.F.; De Almeida, D.R.Q.; Terra, L.F.; Baptista, M.c.S.; Labriola, L. Photodynamic therapy in cancer treatment - an update review. *Journal of Cancer Metastasis and Treatment* **2019**, *2019*, doi:10.20517/2394-4722.2018.83.
16. Triesscheijn, M.; Baas, P.; Schellens, J.H.; Stewart, F.A. Photodynamic therapy in oncology. *Oncologist* **2006**, *11*, 1034-1044, doi:10.1634/theoncologist.11-9-1034.
17. Dolmans, D.E.; Fukumura, D.; Jain, R.K. Photodynamic therapy for cancer. *Nature reviews. Cancer* **2003**, *3*, 380-387, doi:10.1038/nrc1071.
18. Frochot, C.; Mordon, S. Update of the situation of clinical photodynamic therapy in Europe in the 2003–2018 period. *Journal of Porphyrins and Phthalocyanines* **2019**, *23*, 347-357, doi:10.1142/s1088424619300027.
19. Monro, S.; Colón, K.L.; Yin, H.; Roque, J.; Konda, P.; Gujar, S.; Thummel, R.P.; Lilge, L.; Cameron, C.G.; McFarland, S.A. Transition Metal Complexes and Photodynamic Therapy from a Tumor-Centered Approach: Challenges, Opportunities, and Highlights from the Development of TLD1433. *Chemical Reviews* **2019**, *119*, 797-828, doi:10.1021/acs.chemrev.8b00211.
20. Chibazakura, T.; Toriyabe, Y.; Fujii, H.; Takahashi, K.; Kawakami, M.; Kuwamura, H.; Haga, H.; Ogura, S.; Abe, F.; Nakajima, M., et al. 5-Aminolevulinic acid enhances cell death under thermal stress in certain cancer cell lines. *Bioscience, biotechnology, and biochemistry* **2015**, *79*, 422-431, doi:10.1080/09168451.2014.975186.
21. Kennedy, J.C.; Pottier, R.H.; Pross, D.C. Photodynamic therapy with endogenous protoporphyrin IX: basic principles and present clinical experience. *Journal of photochemistry and photobiology. B, Biology* **1990**, *6*, 143-148, doi:10.1016/1011-1344(90)85083-9.
22. Kaspler, P.; Lazic, S.; Forward, S.; Arenas, Y.; Mandel, A.; Lilge, L. A ruthenium(ii) based photosensitizer and transferrin complexes enhance photo-physical properties, cell uptake, and photodynamic therapy safety and efficacy. *Photochemical & photobiological sciences: Official journal of the European Photochemistry Association and the European Society for*

Photobiology **2016**, *15*, 481-495, doi:10.1039/c5pp00450k.

23. Molpus, K.L.; Kato, D.; Hamblin, M.R.; Lilge, L.; Bamberg, M.; Hasan, T. Intraperitoneal photodynamic therapy of human epithelial ovarian carcinomatosis in a xenograft murine model. *Cancer Res* **1996**, *56*, 1075-1082.
24. Elliott, J.T.; Samkoe, K.S.; Gunn, J.R.; Stewart, E.E.; Gardner, T.B.; Tichauer, K.M.; Lee, T.Y.; Hoopes, P.J.; Pereira, S.P.; Hasan, T., et al. Perfusion CT estimates photosensitizer uptake and biodistribution in a rabbit orthotopic pancreatic cancer model: a pilot study. *Academic radiology* **2015**, *22*, 572-579, doi:10.1016/j.acra.2014.12.014.
25. Engbrecht, B.W.; Menon, C.; Kachur, A.V.; Hahn, S.M.; Fraker, D.L. Photofrin-mediated photodynamic therapy induces vascular occlusion and apoptosis in a human sarcoma xenograft model. *Cancer Res* **1999**, *59*, 4334-4342.
26. McFarland, S.A.; Mandel, A.; Dumoulin-White, R.; Gasser, G. Metal-based photosensitizers for photodynamic therapy: the future of multimodal oncology? *Curr Opin Chem Biol* **2019**, *56*, 23-27, doi:10.1016/j.cbpa.2019.10.004.
27. Ramu, V.; Aute, S.; Taye, N.; Guha, R.; Walker, M.G.; Mogare, D.; Parulekar, A.; Thomas, J.A.; Chattopadhyay, S.; Das, A. Photo-induced cytotoxicity and anti-metastatic activity of ruthenium(ii)-polypyridyl complexes functionalized with tyrosine or tryptophan. *Dalton transactions (Cambridge, England : 2003)* **2017**, *46*, 6634-6644, doi:10.1039/c7dt00670e.
28. Heinemann, F.; Karges, J.; Gasser, G. Critical Overview of the Use of Ru(II) Polypyridyl Complexes as Photosensitizers in One-Photon and Two-Photon Photodynamic Therapy. *Accounts of chemical research* **2017**, *50*, 2727-2736, doi:10.1021/acs.accounts.7b00180.
29. Fong, J.; Kasimova, K.; Arenas, Y.; Kaspler, P.; Lazic, S.; Mandel, A.; Lilge, L. A novel class of ruthenium-based photosensitizers effectively kills in vitro cancer cells and in vivo tumors. *Photochemical & photobiological sciences : Official journal of the European Photochemistry Association and the European Society for Photobiology* **2015**, *14*, 2014-2023, doi:10.1039/c4pp00438h.
30. Liu, S.; Leach, S.D. Zebrafish models for cancer. *Annual review of pathology* **2011**, *6*, 71-93, doi:10.1146/annurev-pathol-011110-130330.
31. Goessling, W.; North, T.E.; Zon, L.I. New waves of discovery: modeling cancer in zebrafish. *Journal of clinical oncology : official journal of the American Society of Clinical Oncology* **2007**, *25*, 2473-2479, doi:10.1200/jco.2006.08.9821.
32. Howe, K.; Clark, M.D.; Torroja, C.F.; Tarrance, J.; Berthelot, C.; Muffato, M.; Collins, J.E.; Humphray, S.; McLaren, K.; Matthews, L., et al. The zebrafish reference genome sequence and its relationship to the human genome. *Nature* **2013**, *496*, 498-503, doi:10.1038/nature12111.
33. Amatruda, J.F.; Shepard, J.L.; Stern, H.M.; Zon, L.I. Zebrafish as a cancer model system. *Cancer cell* **2002**, *1*, 229-231, doi:10.1016/s1535-6108(02)00052-1.
34. Lam, S.H.; Chua, H.L.; Gong, Z.; Lam, T.J.; Sin, Y.M. Development and maturation of the immune system in zebrafish, *Danio rerio*: a gene expression profiling, in situ hybridization and immunological study. *Developmental and comparative immunology* **2004**, *28*, 9-28, doi:10.1016/s0145-305x(03)00103-4.
35. Zon, L.I.; Peterson, R.T. In vivo drug discovery in the zebrafish. *Nat Rev Drug Discov* **2005**, *4*, 35-44, doi:10.1038/nrd1606.
36. Lawson, N.D.; Weinstein, B.M. In vivo imaging of embryonic vascular development using transgenic zebrafish. *Dev Biol* **2002**, *248*, 307-318, doi:10.1006/dbio.2002.0711.
37. Renshaw, S.A.; Loynes, C.A.; Trushell, D.M.; Elworthy, S.; Ingham, P.W.; Whyte, M.K. A transgenic zebrafish model of neutrophilic inflammation. *Blood* **2006**, *108*, 3976-3978,

doi:10.1182/blood-2006-05-024075.

38. Manghnani, P.N.; Wu, W.; Xu, S.; Hu, F.; Teh, C.; Liu, B. Visualizing Photodynamic Therapy in Transgenic Zebrafish Using Organic Nanoparticles with Aggregation-Induced Emission. *Nano-micro letters* **2018**, *10*, 61, doi:10.1007/s40820-018-0214-4.
39. Wang, C.; Qian, Y. A water soluble carbazolyl-BODIPY photosensitizer with an orthogonal D-A structure for photodynamic therapy in living cells and zebrafish. *Biomaterials science* **2019**, 10.1039/c9bm01709g, doi:10.1039/c9bm01709g.
40. Hanson, K.; Robinson, S.D.; Al-Yousuf, K.; Hendry, A.E.; Sexton, D.W.; Sherwood, V.; Wheeler, G.N. The anti-rheumatic drug, leflunomide, synergizes with MEK inhibition to suppress melanoma growth. *Oncotarget* **2018**, *9*, 3815-3829, doi:10.18632/oncotarget.23378.
41. van der Ent, W.; Burrello, C.; Teunisse, A.F.; Ksander, B.R.; van der Velden, P.A.; Jager, M.J.; Jochemsen, A.G.; Snaar-Jagalska, B.E. Modeling of human uveal melanoma in zebrafish xenograft embryos. *Invest Ophthalmol Vis Sci* **2014**, *55*, 6612-6622, doi:10.1167/iops.14-15202.
42. He, S.; Lamers, G.E.; Beenakker, J.W.; Cui, C.; Ghotra, V.P.; Danen, E.H.; Meijer, A.H.; Spaink, H.P.; Snaar-Jagalska, B.E. Neutrophil-mediated experimental metastasis is enhanced by VEGFR inhibition in a zebrafish xenograft model. *J Pathol* **2012**, *227*, 431-445, doi:10.1002/path.4013.
43. Chapman, A.; Fernandez del Ama, L.; Ferguson, J.; Kamarashev, J.; Wellbrock, C.; Hurlstone, A. Heterogeneous tumor subpopulations cooperate to drive invasion. *Cell Rep* **2014**, *8*, 688-695, doi:10.1016/j.celrep.2014.06.045.
44. Nicoli, S.; Ribatti, D.; Cotelli, F.; Presta, M. Mammalian tumor xenografts induce neovascularization in zebrafish embryos. *Cancer Res* **2007**, *67*, 2927-2931, doi:10.1158/0008-5472.CAN-06-4268.
45. Wang, J.; Cao, Z.; Zhang, X.M.; Nakamura, M.; Sun, M.; Hartman, J.; Harris, R.A.; Sun, Y.; Cao, Y. Novel mechanism of macrophage-mediated metastasis revealed in a zebrafish model of tumor development. *Cancer Res* **2015**, *75*, 306-315, doi:10.1158/0008-5472.CAN-14-2819.
46. Wehmas, L.C.; Tanguay, R.L.; Punnoose, A.; Greenwood, J.A. Developing a Novel Embryo-Larval Zebrafish Xenograft Assay to Prioritize Human Glioblastoma Therapeutics. *Zebrafish* **2016**, *13*, 317-329, doi:10.1089/zeb.2015.1170.
47. Hopkins, S.L.; Siewert, B.; Askes, S.H.C.; Veldhuizen, P.; Zwier, R.; Heger, M.; Bonnet, S. An in vitro cell irradiation protocol for testing photopharmaceuticals and the effect of blue, green, and red light on human cancer cell lines. *Photochemical & photobiological sciences : Official journal of the European Photochemistry Association and the European Society for Photobiology* **2016**, *15*, 644-653, doi:10.1039/c5pp00424a.
48. Cuello-Garibo, J.-A.; Meijer, M.S.; Bonnet, S. To cage or to be caged? The cytotoxic species in ruthenium-based photoactivated chemotherapy is not always the metal. *Chem Commun (Camb)* **2017**, *53*, 6768-6771, doi:10.1039/c7cc03469e.
49. Monro, S.; Colon, K.L.; Yin, H.; Roque, J., 3rd; Konda, P.; Gujar, S.; Thummel, R.P.; Lilge, L.; Cameron, C.G.; McFarland, S.A. Transition Metal Complexes and Photodynamic Therapy from a Tumor-Centered Approach: Challenges, Opportunities, and Highlights from the Development of TLD1433. *Chem Rev* **2019**, *119*, 797-828, doi:10.1021/acs.chemrev.8b00211.
50. Galluzzi, L.; Vitale, I.; Aaronson, S.A.; Abrams, J.M.; Adam, D.; Agostinis, P.; Alnemri, E.S.; Altucci, L.; Amelio, I.; Andrews, D.W., et al. Molecular mechanisms of cell death: recommendations of the Nomenclature Committee on Cell Death 2018. *Cell Death Differ* **2018**, *25*, 486-541, doi:10.1038/s41418-017-0012-4.
51. Mishra, R.R.; Kneitz, S.; Scharl, M. Comparative analysis of melanoma deregulated miRNAs

- in the medaka and Xiphophorus pigment cell cancer models. *Comparative biochemistry and physiology. Toxicology & pharmacology : CBP* **2014**, *163*, 64-76, doi:10.1016/j.cbpc.2014.01.002.
52. Li, H.; Qian, Z.M. Transferrin/transferrin receptor-mediated drug delivery. *Medicinal research reviews* **2002**, *22*, 225-250, doi:10.1002/med.10008.
 53. Qian, Z.M.; Li, H.; Sun, H.; Ho, K. Targeted drug delivery via the transferrin receptor-mediated endocytosis pathway. *Pharmacological reviews* **2002**, *54*, 561-587, doi:10.1124/pr.54.4.561.
 54. Johnsen, K.B.; Burkhart, A.; Thomsen, L.B.; Andresen, T.L.; Moos, T. Targeting the transferrin receptor for brain drug delivery. *Progress in neurobiology* **2019**, *181*, 101665, doi:10.1016/j.pneurobio.2019.101665.
 55. Nareyeck, G.; Wuestemeyer, H.; von der Haar, D.; Anastassiou, G. Establishment of two cell lines derived from conjunctival melanomas. *Experimental eye research* **2005**, *81*, 361-362, doi:10.1016/j.exer.2005.04.018.
 56. Keijser, S.; Maat, W.; Missotten, G.S.; de Keizer, R.J. A new cell line from a recurrent conjunctival melanoma. *The British journal of ophthalmology* **2007**, *91*, 1566-1567, doi:10.1136/bjo.2006.110841.
 57. Luyten, G.P.; Naus, N.C.; Mooy, C.M.; Hagemeyer, A.; Kan-Mitchell, J.; Van Drunen, E.; Vuzevski, V.; De Jong, P.T.; Luiders, T.M. Establishment and characterization of primary and metastatic uveal melanoma cell lines. *Int J Cancer* **1996**, *66*, 380-387, doi:10.1002/(sici)1097-0215(19960503)66:3<380::aid-ijc19>3.0.co;2-f.
 58. Chen, P.W.; Murray, T.G.; Uno, T.; Salgaller, M.L.; Reddy, R.; Ksander, B.R. Expression of MAGE genes in ocular melanoma during progression from primary to metastatic disease. *Clinical & experimental metastasis* **1997**, *15*, 509-518, doi:10.1023/a:1018479011340.
 59. Carlotti, F.; Bazuine, M.; Kekarainen, T.; Seppen, J.; Pognonec, P.; Maassen, J.A.; Hoeben, R.C. Lentiviral vectors efficiently transduce quiescent mature 3T3-L1 adipocytes. *Molecular therapy : the journal of the American Society of Gene Therapy* **2004**, *9*, 209-217, doi:10.1016/j.ymthe.2003.11.021.
 60. Hopkins, S.L.; Siewert, B.; Askes, S.H.; Veldhuizen, P.; Zwier, R.; Heger, M.; Bonnet, S. An in vitro cell irradiation protocol for testing photopharmaceuticals and the effect of blue, green, and red light on human cancer cell lines. *Photochemical & photobiological sciences : Official journal of the European Photochemistry Association and the European Society for Photobiology* **2016**, *15*, 644-653, doi:10.1039/c5pp00424a.

Chapter 4

Photosubstitution in a new trisheteroleptic ruthenium complex inhibits conjunctival melanoma growth in a zebrafish orthotopic xenograft model

Quanchi Chen ^{1#}, Jordi-Amat Cuello-Garibo ^{2#}, Vadde Ramu ², Yasmin Aydar ¹, Yevhen Batsuin, ² Sharon Bronkhorst ², Nataliia Beztsinna ², Lanpeng Chen ¹, Xue-Quan Zhou ², Claudia Schmidt ³, Ingo Ott ³, Martine J. Jager ⁴, B. Ewa Snaar-Jagalska ^{1*}, Sylvestre Bonnet ^{2*}

¹ Institute of Biology, Leiden University, Leiden, The Netherlands

² Leiden Institute of Chemistry, Leiden University, P.O. Box 9502, 2300 RA Leiden, The Netherlands

³ Institute of Medicinal and Pharmaceutical Chemistry, Technische Universität Braunschweig, Beethovenstrasse 55, D-38106 Braunschweig, Germany

⁴ Department of Ophthalmology, Leiden University Medical Center, Leiden, The Netherlands

These authors contributed equally to the paper

* Correspondence: b.e.snaar-jagalska@biology.leidenuniv.nl; Tel.: +31-71-527-4980 (E.S.J.) and bonnet@chem.leidenuniv.nl; Tel : +31-71-527-4260 (S.B.);

Manuscript ready for submission to Chemical science

Keywords: Eye, conjunctival melanoma, chemotherapy, photoactivation, zebrafish

Abstract

In vivo data are very rare for ruthenium-based photoactivated chemotherapy (PACT) compounds, a new family of phototherapeutic drugs that are activated *via* ligand photosubstitution. Here a novel trisheteroleptic ruthenium complex ($[2](PF_6)_2$) was generated and its light-activated anticancer properties were validated *in vitro* and in embryonic zebrafish cancer models. The dark toxicity of $[2](PF_6)_2$ was optimized by combining three different ligands with different hydrophobicities, each bound in a bidentate fashion to the metal centre. Upon green light irradiation, one of these ligands, 2-methylthiomethylpyridine (mtmp), was selectively photosubstituted by solvent molecules, thereby releasing the phototoxicity of the heavy metal photoproduct. Fifteen minutes of green light irradiation ($21 \text{ mW}\cdot\text{cm}^{-2}$, $19 \text{ J}\cdot\text{cm}^{-2}$, 520 nm) led to high phototherapeutic indexes (PI) for this compound, in particular in prostate cancer cells (PC3Pro4) and conjunctival melanoma cells (CRMM1 and CRMM2). The therapeutic potential of $[2](PF_6)_2$ was further evaluated in zebrafish ectopic and orthotopic tumour models of these cell lines. The ectopic model consisted of fluorescent PC3Pro4-, CRMM1-, or CRMM2-mCherry cells, injected intravenously (IV) into zebrafish, that formed perivascular metastatic lesions within four days at the posterior ventral end of caudal hematopoietic tissue (CHT). By contrast, in the orthotopic model, CRMM1- and CRMM2-mCherry cells were injected behind the eye where they developed metastatic lesions. After 24 hours, the engrafted embryos were treated at the maximally-tolerated dose of $[2](PF_6)_2$, which was determined for three different modes of administration: i) incubating the fish in drug-containing water (WA); ii) injecting the compound intravenously (IV) into the fish; or iii) injecting the compound retro-orbitally (RO) into the fish. Optimally, four consecutive PACT treatments were performed on engrafted embryos using 60 min drug-to-light intervals and 90 min green light irradiation ($21 \text{ mW}\cdot\text{cm}^{-2}$, $114 \text{ J}\cdot\text{cm}^{-2}$, 520 nm). Most importantly, this PACT protocol was not toxic to the zebrafish. In all three ectopic tumour models, $[2](PF_6)_2$ did not significantly diminish the formation of metastatic lesions. However, in both conjunctival melanoma orthotopic tumour models, retro-orbitally administered $[2](PF_6)_2$ significantly inhibited growth of the engrafted cells. Overall, this study represents the first demonstration in zebrafish cancer models of the clinical potential of ruthenium-based photoactivated chemotherapy against conjunctival melanoma.

Introduction

Cisplatin was the first metal-based chemotherapy drug approved by the Food & Drug Administration for the treatment of testicular tumours and ovarian adenocarcinoma, and with the development of carboplatin and oxaliplatin (two derivatives of cisplatin) the use of platinum-based drugs has expanded to the treatment of many different malignancies [1-3]. Although the exact mechanism of action of platinum(II) (Pt) complexes is still debated, it is generally accepted that the ultimate event that induces apoptosis in cancer cells is the binding of the heavy metal centre to DNA after hydrolysis of one or two labile ligand(s) of the metal complex [4]. DNA binding to Pt inhibits DNA replication and transcription, ultimately leading to cell death [5-7]. Spontaneous activation of the drug before it reaches the tumour,

leads to severe side effects in patients treated with platinum drugs, for example hepato- and nephrotoxicity, which limits the clinical efficacy of these compounds and the patients' quality of life [8-10]. Therefore, other metal-based compounds have been considered as anticancer chemotherapy candidates, including those based on ruthenium(II) (Ru) [11]. Although several of these compounds have reached the stage of clinical trials, the general toxicity of metal-based compounds, due to spontaneous activation of a metal-ligand bond before the drug reaches the tumour, remains an issue.

Ruthenium-based PhotoActivated ChemoTherapy (PACT) is a new anticancer phototherapy modality that uses visible light irradiation as an external trigger [12,13]. PACT primarily aims at limiting the biological action of the anticancer drug to the location of the tumour by localized, light-induced activation at the tumour site [14]. Unlike photodynamic therapy (PDT), a clinically-approved anticancer phototherapy method based on the photochemical activation of dioxygen by an excited photosensitizer, PACT relies on an oxygen-independent photochemical bond cleavage reaction. This process generates a molecular species that is more cytotoxic than the (non-activated) prodrug kept in the dark [15-17]. Many examples of PACT agents have been reported in the literature, among which are molecules based on ruthenium [18-20]. Ru-based PACT compounds make use of the versatile and well-understood photochemistry of polypyridyl ruthenium compounds, which, next to energy transfer and electron transfer, comprises light-induced photosubstitution reactions [21]. When photosubstitution occurs, one of the organic ligands bound to the metal is replaced by loosely-bound solvent molecules. In the dark, the ligand to be photosubstituted serves as a protecting group towards the coordination of biomolecules present in cells. After light irradiation, photosubstitution produces an "uncaged" metal compound that, by analogy with cisplatin, acts as an activated drug, as it can bind to biomolecules and induce cell death (Figure 1) [22-24]. For example, blue light-induced photosubstitution of the non-toxic ligand 2-methylthiomethylpyridine (mtmp) in compounds $[\text{Ru}(\text{dpp})_2(\text{mtmp})]^{2+}$ (**[1]**²⁺, dpp = 4,7-diphenyl-1,10-phenanthroline) and $[\text{Ru}(\text{bpy})_2(\text{mtmp})]^{2+}$ (**[3]**²⁺, bpy = 2,2'-bipyridine), has recently been demonstrated [25]. These two compounds belong to a wide family of complexes $[\text{Ru}(\text{N-N})_2(\text{L-L})]^{2+}$, where N-N are non-photocleavable "spectator" polypyridyl ligands, and L-L is a photocleavable chelate [25-29]. Although the photochemistry of this type of complexes is relatively well-understood, two major challenges in their development are on the one hand minimizing the difference between dark and light toxicity, and on the other hand, understanding how the molecular structure relates to the dark toxicity *in vivo*, i.e. the toxicity before photosubstitution takes place. In **[1]**²⁺ and **[3]**²⁺, both challenges are not met: **[1]**²⁺ bears two very hydrophobic dpp chelates that make the complex taken up by cells in large amounts and generate high cytotoxicity before light activation, while **[3]**²⁺ bears the much less hydrophobic bpy spectator ligands, as a result of which this compound is too hydrophilic to penetrate significantly into cancer cells, which prevents this compound to show any toxicity even after light activation [24].

We set out to resolve both challenges. First, we designed a new ruthenium complex, $[\text{Ru}(\text{dpp})(\text{bpy})(\text{mtmp})]^{2+}$ (**[2]**²⁺, Fig. 1), as a compromise between **[1]**²⁺ and **[3]**²⁺. A single dpp chelate is

expected to alleviate the excessive hydrophobicity and dark toxicity of $[1]^{2+}$, while it should increase the cellular uptake and photoinduced anticancer activity of $[3]^{2+}$. Second, after demonstration of the excellent phototherapeutic properties of $[2]^{2+}$ *in vitro*, this compound was subjected for the first time to *in vivo* efficacy testing and determination of the maximum tolerated dose using zebrafish ectopic and orthotopic tumour models. Zebrafish tumour models are advantageous for anticancer compound development as they allow for fast compound screening *in vivo* with low amounts of compound, compared to rodents, and with better statistics [30-33]. As zebrafish are transparent it is especially easy to activate a phototherapeutic compound by light in the whole body of the animal by simply shining light onto the aqueous solution containing the embryos [34-40]. The transparency of the embryo makes it easy to quantify the relative tumour burden, using engraftment of human cancer cells which stably express red fluorescent protein (RFP). This property has been used for studying PDT [41], as well as photoswitchable inhibitors, allowing analysis before and after light activation [37]. Zebrafish provide a particularly useful animal model for assessing drug toxicity: acute and chronic toxic effects of metal nanoparticles have been measured, with special focus on immunotoxicity, developmental toxicity, neurotoxicity, reproductive toxicity, cardiovascular toxicity, or hepatotoxicity [42,43]. Systemic drug toxicity to zebrafish embryos has been well described [44-46]. The zebrafish model allowed us to investigate for the first time the toxicity of photosubstitutionally active ruthenium compounds in different *in vivo* models of cancer while respecting the 3Rs principles (Reduction, Refinement, Replacement). As zebrafish embryo had not been used for PACT yet, we tested different protocols of compound administration, to find a mode of administration to test anti-cancer efficacy and toxicity. Critically, this work highlights that similarly high efficacies of a PACT compound *in vitro* do not necessarily translate into similarly high efficacies *in vivo*, where the mode of administration of the compound must be carefully optimized for each particular disease model.

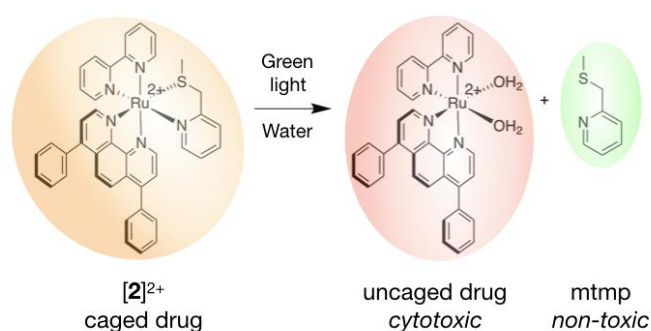


Fig. 1 Activation mechanism of the ruthenium-based PACT compound $[2]^{2+}$. Upon green light irradiation, the protecting, non-toxic mtmp ligand is photosubstituted by solvent molecules, which recovers the biomolecule-binding ability of the heavy metal centre, ultimately leading to toxicity and cell death.

Method and Materials

Synthesis

General: the ligands 2,2'-bipyridine (bpy) and 4,7-diphenyl-1,10-phenanthroline (dpp), and the precursor *cis*-[Ru(DMSO)₄Cl₂], were purchased from Sigma-Aldrich. Potassium hexafluorophosphate (KPF₆) was purchased from Alfa-Aesar. All reactants and solvents were used without further purification. The synthesis of [1]Cl₂ was described previously [47]. The ligand 2-(methylthiomethyl)pyridine (mtmp) was prepared according to the literature [48]. Electrospray mass spectra (ES MS) were recorded by using a Thermoquest Finnagen AQA Spectrometer and a MSQ Plus Spectrometer. All ¹H NMR spectra were recorded on a Bruker DPX-300 or DMX-400 spectrometers. Chemical shifts are indicated in ppm relative to the residual solvent peak.

[Ru(dpp)(DMSO)₂Cl₂] [4]: *cis*-[Ru(DMSO)₄Cl₂] (500 mg, 1.03 mmol) and bathophenanthroline (343 mg, 1.03 mmol) were heated at reflux in ethanol (35 mL) for 2 h. The reaction was then cooled to room temperature and the solvent volume reduced to ca. 10 mL in vacuo. The precipitate that formed upon cooling was filtered, washed with minimal cold ethanol and copious amounts of hexane/diethyl ether, and dried under vacuum. Yield: light-brown solid, 347 mg (0.52 mmol, 51%). ¹H NMR (400 MHz, CDCl₃) δ 10.19 (d, J = 5.4, 0.9 Hz, 1 H), 10.00 (d, J = 5.6, 0.9 Hz, 1 H), 8.03 (dd, 2 H), 7.89 (d, J = 5.5, 0.9 Hz, 1 H), 7.72 (d, J = 5.6, 0.9 Hz, 1 H), 7.65 – 7.51 (m, 10 H), 3.67 (s, 3 H, 1), 3.62 (s, 3 H, 2), 3.27 (s, 3 H), 2.70 (s, 3 H). ¹³C NMR (101 MHz, CDCl₃) δ 155.72, 152.34, 149.95, 148.98, 135.93, 135.79, 129.81, 129.68, 129.13, 128.73, 128.27, 125.49, 125.36, 125.30, 125.23, 47.15, 46.52, 45.49, 44.37.

[Ru(dpp)(ox)(mtmp)] [5]: [4] (300 mg, 0.45 mmol) and sodium oxalate (84.5 mg, 0.65 mmol) were heated at reflux in water (15 mL) for 1 h. The reaction was then cooled to room temperature and added to a hot (60 °C) solution of 2-[(methylthio)methyl]pyridine (63 mg, 0.45 mmol) in ethylene glycol (15 mL). The resulting mixture was heated at reflux for 3 h, cooled to room temperature and then added dropwise to 50 mL of stirring water. After 30 minutes, the precipitate was filtered through a 1 μm Micropore membrane. The solids were washed with copious amounts of water and minimal acetone before drying thoroughly under vacuum. Mixture of isomers was separated in silica column (R_f = 0.3) in DCM/ CH₃OH (2-20% CH₃OH). Only one isomer was isolated. Yield: dark red powder, 144 mg (0.21 mmol, 71%). ¹H NMR (400 MHz, CDCl₃) δ 9.63 (d, J = 5.6, 0.9 Hz, 1H), 9.34 (d, J = 5.4, 0.9 Hz, 1H), 8.08 (dd, J = 9.4, 0.9 Hz, 2H), 7.81 (d, J = 5.3 Hz, 1H), 7.64 – 7.47 (m, 11H), 7.43 – 7.36 (m, 2H), 6.81 (d, 1H), 6.59 (t, J = 6.1, 2.4 Hz, 1H), 4.66 (dd, 2H), 2.45 (s, 3H). ¹³C NMR (101 MHz, CDCl₃) δ 168.86, 167.83, 163.08, 153.42, 152.04, 151.05, 149.48, 148.15, 145.53, 136.37, 136.29, 134.29, 129.96, 129.78, 129.53, 129.35, 129.21, 129.17, 129.03, 128.39, 125.91, 125.48, 124.44, 123.14, 122.34, 45.79, 16.12. Anal. Calcd for C₃₃H₂₅N₃O₄RuS·3H₂O: C, 55.45; H, 4.37; N, 5.88 Found: C, 56.08; H, 4.56; N, 5.46.

[Ru(dpp)(bpy)(mtmp)](PF₆)₂ [2](PF₆)₂: [5] (140 mg, 0.211 mmol) was suspended in acetonitrile (3 mL) and then perchloric acid 1 M (3 mL) was added. After refluxing for 1 h, a red-brown solution of the Ru-

solvate was obtained and after cooling it was poured on 15 mL stirring water. The solid that precipitated was filtered and dried to yield the crude orange $[\text{Ru}(\text{dpp})(\text{mtmp})(\text{CH}_3\text{CN})_2](\text{ClO}_4)_2$ complex. The intermediate was dissolved in an ethylene glycol solution (15 mL) containing the bpy ligand (33 mg, 0.211 mmol) and heated at 100 °C for 6 h. The deep red mixture was cooled to room temperature and poured on stirring aqueous potassium hexafluorophosphate to precipitate the crude complex as the hexafluorophosphate salt. Configurational isomers were resolved by column chromatography on silica DCM/CH₃OH 95:5. Three fractions were obtained from a long orange band ($R_f \sim 0.5$), from which only the last fraction contained a pure isomer (3.2 mg, 1.5%) (Isomer B, **[2b]**(PF₆)₂). A mixture of isomers A/B in a ratio 0.23:1 has been used for photochemical analysis and biological testing, further referred to as **[2]**(PF₆)₂ (60 mg, 28%). ¹H NMR (400 MHz, CD₃CN) δ 9.63 (d, $J = 5.5$ Hz, 1HB), 9.39 (d, $J = 5.7$ Hz, 1HA), 8.61 (d, $J = 8.2$ Hz, 1HB), 8.58 – 8.51 (m, 2HA), 8.43 (d, $J = 8.1$ Hz, 1HB), 8.31 (dd, $J = 8.0, 1.5$ Hz, 1HB), 8.29 – 8.23 (m, 1HB + 1HA), 8.22 – 8.14 (m, 2HB + 2HA), 8.14 – 8.03 (m, 3HA), 8.02 (d, $J = 5.5$ Hz, 1HB), 7.99 (d, $J = 5.5$ Hz, 1HB), 7.93 (ddd, $J = 7.8, 6.5, 1.5$ Hz, 1HB), 7.86 (td, $J = 7.8, 1.6$ Hz, 1HA), 7.81 – 7.51 (m, 15HB + 15HA), 7.48 (dd, $J = 5.9, 1.5$ Hz, 1HA), 7.32 (ddd, $J = 7.1, 5.6, 1.3$ Hz, 1HA), 7.24 (d, $J = 5.5$ Hz, 1HB), 7.17 (td, $J = 7.2, 5.6, 1.4$ Hz, 1HB + 1HA), 6.98 (ddd, $J = 7.7, 5.8, 1.6$ Hz, 1HB), 4.82 (d, $J = 16.5$ Hz, 1HB), 4.74 (d, $J = 16.7$ Hz, 1HA), 4.28 (dd, $J = 16.6, 4.8$ Hz, 1HB + 1HA), 1.59 (s, 3HB), 1.32 (s, 3HA). ¹³C NMR (101 MHz, CD₃CN) δ 162.96, 162.63, 158.56, 157.73, 153.51, 153.33, 153.09, 152.90, 151.98, 150.77, 150.61, 150.05, 149.66, 148.72, 139.46, 138.67, 138.55, 136.62, 136.53, 130.79, 130.70, 130.13, 130.06, 129.20, 127.78, 127.26, 127.19, 127.12, 126.92, 125.86, 125.59, 125.55, 124.93, 45.36, 17.04. High Resolution ES MS m/z (calcd): 364.57519 (364.57446, **[2]**2+). Anal. Calcd for C₄₁H₃₃F₁₂N₅P₂RuS: C, 48.34; H, 3.26; N, 6.87 Found: C, 48.21; H, 3.41; N, 6.82.

Photochemistry: determination of the photosubstitution and singlet oxygen generation quantum yields

When monitoring photoreactions with UV-vis and mass spectrometry, a Cary 50 Varian spectrometer equipped with temperature control set to 298 K and a LED light source ($\lambda_{\text{ex}} = 521$ nm, with a Full Width at Half Maximum of 33 nm) with a photon flux of $6.21 \cdot 10^{-8}$ mol \cdot s⁻¹ was used. The irradiation experiments were performed in a quartz cuvette containing 3 mL of solution. A stock solution of the desired complex was prepared in CH₃CN, which was then diluted in the cuvette to a working solution concentration (36 μ M). The sample was deaerated 15 min by gentle bubbling of dinitrogen and the atmosphere was kept inert during the experiment by a gentle flow of dinitrogen on top of the cuvette. A UV-vis spectrum was measured every 30 s for the first 10 min, every 1 min for the next 10 min, and eventually every 10 min until the end of the experiment. Data were analysed with Microsoft Excel and Glotaran as follows: Upon light irradiation, a complex RuL converts into a complex RuY by photosubstitution of a ligand (L) by a solvent molecule (Y). Considering that both metal complexes are thermally stable, the quantum yield of the photosubstitution reaction Φ_{PR} can be calculated by monitoring the photoreaction with UV-vis spectroscopy. As explained in detail by Bahreman and Bonnet

[49], when the irradiation is performed at a wavelength that is not an isosbestic point, the Φ_{PR} can be obtained from the slope of a plot of the number of mol of RuL (n_{RuL}) vs. the total number of mol of photons absorbed by RuL from t_0 till t_i (Q_i). Q_i is calculated according to Equation 1:

$$Q_i(t) = \sum_{t=0}^i q_i \quad \text{Equation 1}$$

where q_i is the moles of photons absorbed by RuL between two consecutive UV-vis measurements at t_{i+1} and t_i ($\Delta t = t_{i+1} - t_i$). q_i is calculated according to Equation 2:

$$q_i = \left(\frac{(A_{RuL})_{ave}}{(A_e)_{ave}} \right)_i \cdot (1 - 10^{-3 \cdot (A_e)_{ave}}) \cdot \phi \cdot \Delta t \quad \text{Equation 1}$$

where $(A_{RuL})_{ave}$ is the average of the absorbance due to RuL between two consecutive UV-vis measurements, $(A_e)_{ave}$ is the average of the absorbance of the solution at the irradiation wavelength between two consecutive UV-vis measurements, $(1 - 10^{-3 \cdot (A_e)_{ave}})$ is the probability of absorption of a photon when the irradiation comes from the top of the quartz cuvette and goes through 3 cm pathlength, while all absorbances are measured perpendicularly through a 1 cm pathlength, and ϕ is the photon flux of the irradiation source at the irradiation wavelength.

The value of $(A_{RuL})_{ave}$, and by extension n_{RuL} , was calculated by modelling the evolution of the UV-vis spectra vs. time using the Glotaran software. We fitted hence the time-dependent evolution of the UV-vis spectroscopy data to a kinetic model based on first-order laws, obtaining two output data sets that can be used for the calculation of Φ_{PR} . The first dataset is a collection of globally fitted absorption spectra of the starting complex and the photoproduct, which makes possible the calculation of the molar extinction coefficient of all the species from that of the starting reagent (Fig. S1a). The second dataset is the modelled evolution of the relative fractions of the two ruthenium species vs. irradiation time, here as well according to global fitting (Fig. S1b). From the time evolution of these fractions and the molar absorption coefficient of all species, the time evolution of n_{RuL} can be calculated, as well as Q_i . The slope of the plot of n_{RuL} vs. Q_i (Fig. S1c) gives the quantum yield of the reaction.

Singlet oxygen quantum yield measurements were performed by direct spectroscopic detection of the 1275 nm emission, as described by Meijer *et al* [25].

Attached cell culture

Human conjunctival malignant melanoma cell lines CRMM1 and CRMM2, isolated by Nareyeck *et al* [50], were cultured in F12 Kaighn's modified medium (Hyclone, cat# SH30526.01) supplemented with 10% fetal bovine serum (FBS; Gibco). CM2005.1 established by Keijser *et al* [51] was cultured in RPMI 1640, Dutch Modified (Life Technologies, cat# 22409-015), supplemented with 10% fetal bovine serum (FBS; Gibco), 3 mM L-glutamine (1%, Life Technologies cat# 35050-038). Human uveal melanoma cell lines OMM1 (provided by Prof. Dr. G.P.M Luyten) [52], OMM2.5, and MEL270 (provided by Dr. B.R. Ksander) [53] were cultured in Ham's F12 medium (Sigma-Aldrich, cat# N3790) supplemented with 10%

FCS. Stable fluorescent CRMM1 and CRMM2 cell lines were generated using lentivirus expressing both tandem dimer (td)Tomato and Blasticidin-S, as previously described [54]. PC3Pro4 (provided by Dr. Gabriel van der Pluijm) was cultured in DMEM (Sigma-Aldrich, cat# 32160801) supplemented with 10% FCS. Human lung carcinoma A549 was distributed by the European Collection of Cell Cultures (ECACC), and purchased from Sigma Aldrich, cultured in DMEM (Sigma-Aldrich, cat# 32160801) supplemented with 10% FCS. Cells were cultured in either 25 cm² or 75 cm² flasks and split at 70-80% confluence. The flasks were incubated in a normoxic incubator at 37 °C at 5.0% CO₂ in a PHCbi O₂/CO₂ incubator, MCO-170M). The medium was refreshed twice a week. Cells used in all biological experiments were cultured for not more than eight weeks. Trypsin and Opti-MEM® (without phenol red) were purchased from Gibco® Life Technologies. Trypan blue (0.4% in 0.81% sodium chloride and 0.06% potassium phosphate dibasic solution) was purchased from Bio-Rad. Plastic disposable flasks and 96-well plates were obtained from Sarstedt. Cells were counted using a Bio-Rad TC10 automated cell counter with Bio-Rad Cell Counting Slides.

Spheroids cell culture and CellTiter-Glo 3D cell viability assay

A549 (500 cells/well) within 100 µL OptiMEM (Gibco® Life Technologies, cat# 11058021) were seeded in the low-attachment 96 well plates (Corning Spheroid microplate 4515) and incubated in normoxia (21% O₂). After 24 h, 100 µL/well of diluted [2](PF₆)₂ with six different concentrations in OptiMEM or OptiMEM for control was added into each well and the cells were further incubated for another 24 h (drug-to-light interval). 100 µL of medium was pipetted out from each well and 100 µL/well of new OptiMEM was added. Then, the plates for [2](PF₆)₂ treatment with light activation and vehicle with light activation groups were irradiated with green light (21 mW.cm⁻², 15 min, 19 J.cm⁻², 520 nm) and the plates for [2](PF₆)₂ treatment with no light activation and vehicle with no light activation groups were put in the dark box. After treatment, all plates were put back in the incubator for 48 h. Before the CellTiter-Glo 3D cell viability assay, the plates were taken out from the incubator and left out for 20 min to reach the room temperature. 100 µL medium was taken out from each plate and 100 µL of CellTiter Glo 3D was added per well. The plates were put on the shaker for 5 min and left the plates at room temperature without shaking for 25 min. The luminescence of the plates was read by Tecan reader.

Cellular uptake

Cell uptake studies for complexes [1]Cl₂ and [2](PF₆)₂ were conducted on A549 lung cancer cells. 1.6·10⁶ cells were seeded at t = 0 h in Opti-MEM complete (10 mL) in a 75 cm² T-flask. At t = 24 h the media was aspirated and cells were treated with solutions of [1]Cl₂, [2](PF₆)₂ to give a final concentration at the EC₅₀ in the dark (3.4 and 65µM, respectively) in a total volume of 10 mL. After 24 h of drug incubation at 37 °C and 21% O₂, the medium was aspirated and the cells were washed twice with PBS (5 mL). Then, the cells were trypsinized (2 mL), suspended with Opti-MEM (8 mL), and centrifuged (1200

rpm, 4 min). After aspiration of the supernatant, the cells were re-suspended in PBS (1 mL) and counted. After a second centrifugation, the supernatant was discarded. For metal and protein quantification, the pellets were resuspended in demineralized water (250 μ L) and lysed for 30 min by ultrasonication. The protein content of lysates was determined by the Bradford method, and the ruthenium content was determined by Atomic Absorption Spectroscopy.

A contrAA 700 high-resolution continuum-source atomic absorption spectrometer (Analytik Jena AG) was used. Pure samples of the respective complex were used as standard and calibration was done in a matrix-matched manner (meaning all samples and standards were adjusted to the same cellular protein concentration of 1.0 mg/mL by dilution with distilled water if necessary). Triton-X 100 (1%, 10 μ L) as well as nitric acid (13%, 10 μ L), were added to each standard sample (100 μ L). Samples were injected (25 μ L) into coated standard graphite tubes (Analytik Jena AG) and thermally processed as previously described by Schatzschneider et al.[55] Drying steps were adjusted and the atomization temperature set to 2400 °C. Ruthenium was quantified at a wavelength of 349.90 nm. The mean integrated absorbances of double injections were used throughout the measurements. The data from two independent biological replications were used to obtain the uptake values shown in Table 2.

Cell irradiation setup

The cell irradiation system consisted of a Ditabis thermostat (980923001) fitted with two flat-bottomed microplate thermoblocks (800010600) and a 96-LED array fitted to a standard 96-well plate. The $\lambda=520$ nm LED (OVL3324), fans (40 mm, 24 V DC, 9714839), and power supply (EA PS 2042-06B) were obtained from Farnell as reported in our previous publication [56].

Cytotoxicity assay

At day 0, cells were detached using 1 mL of trypsin, resuspended in 4 mL of media and transferred to a 15 mL corning falcon tube. Cells were counted using trypan blue and BioRad® TC20™ automated cell counter (Figure 11). Dilutions of 6000 (CRMM1), 6000 (CRMM2), 8000 (CM2005.1), 6000 (OMM1), 6000 (OMM2.5), 6000 (MEL270) 6000 (A549), and 6000 (PC3Pro4) cells/well were calculated from each cell suspension at a final volume of 6 mL. The cell suspensions were transferred to a 50 mL reservoir and 100 μ L of each cell line was seeded at the aforementioned cell densities in triplicate in six 96-well plates. Boarder wells were intentionally filled with PBS media to avoid boarder effects. After 24 h, the cells were treated with [2](PF₆)₂ with six different concentrations. After 24 h of post treatment the cells were exposed to the green light for 15 min (21 mW/cm², 19 J.cm⁻², 520 nm). The dark control plate was kept under dark conditions. Then cells were incubated for another 48 h before fixing them with trichloroacetic acid (10% w/w) solution. The fixed cells were kept at 4°C for 48h, when TCA was washed

out with distilled water before adding the sulphorhodamin B (SRB) (0.6 % SRB) dye. The SRB dye was washed out after 30 minutes and plates were air dried overnight. Next day, the dye was dissolved using Tri-base (0.25%) and absorbance of SRB at 510 nm was recorded from each well using a Tecan plate reader. The SRB absorbance data was used to calculate the fraction of viable cells in each well (Excel and GraphPad Prism software). The absorbance data were averaged from triplicate wells per concentration. Relative cell viabilities were calculated by dividing the average absorbance of the treated wells by the average absorbance of the untreated wells. Three independent biological replicates were completed for each cell line (three different passage numbers per cell line). The average cell viability of the three biological replicates was plotted versus log(concentration) [μM], with the SD error of each point. By using the dose–response curve for each cell line under dark- and irradiated conditions, the effective concentration (EC50) was calculated by fitting the curves to a non-linear regression function with a fixed maximum (100 %) and minimum (0 %) (relative cell viability) and a variable Hill slope [57].

Flow Cytometry

CRMM1 (10000/well) cells were seeded into an 8-well chamber in Opti-MEM™ (Gibco, Reduced Serum Medium, no phenol red) with 2.5% FBS (Gibco). After 24 h incubation, 4.3 μM of [2](PF₆)₂ was added into the medium. 24h later, wells were washed and new drug-free medium was added. The cells were exposed to green light (21 mW/cm², 19 J.cm⁻², 520 nm) for 15 min and incubated for 48 h. Medium of all wells was collected and wells were washed with PBS and lysed by 500 μL trypsin for 3 min. Collected medium was added to the wells with lysed cells, mixed and centrifuged for 2000 rpm, 3 min. After washing, cells were resuspended in 200 μL of 1X binding buffer. Next, 5 μL of Annexin-V-FITC and 5 μL of Propidium Iodide were added to each well and left for 15 min at room temperature. 200 μL of each sample was added to a well in a 96-well plate, and used for FACS measurement.

Zebrafish maintenance, tumour cells implantation and tumour analysis

Zebrafish lines were kept in compliance with the local animal welfare regulations and European directives. The study was approved by the local animal welfare committee (DEC) of Leiden University (Project: “Anticancer compound and target discovery in zebrafish xenograft model”. License number: AVD1060020172410). The Zebrafish Tg(fli1: GFP/Casper) [58] were handled in compliance with local animal welfare regulations and maintained according to standard protocols (www.ZFIN.org).

For cancer cell injection, two days post-fertilization (dpf), dechorionated zebrafish embryos were anaesthetized with 0.003% tricaine (Sigma) and plated on a 10cm Petri dish covered with 1.5% of solidified agarose. PC3Pro4, CRMM1 and CRMM2 cells were suspended in PBS containing 2% polyvinylpyrrolidone (PVP; Sigma-Aldrich) with a concentration of 50,000 cells/ μl and loaded into borosilicate glass capillary needles (1 mm O.D. × 0.78 mm I.D.; Harvard Apparatus). In the ectopic model, 200 mCherry fluorescent PC3Pro4 or (td)Tomato fluorescent CM cells were injected into the

Duct of Cuvier at 2 dpf, which led to dissemination through the blood circulation and outgrowth in the head and tail. In orthotopic tumour model, 100 (td)Tomato fluorescent CRMM1 or CRMM2 cells were injected retro-orbitally in 2 dpf embryos using a Pneumatic Picopump and a manipulator (WPI). After injection, the embryos were incubated in a 34 °C incubator. Images were acquired at 1-, 2-, 4- and 6-days post injection (dpi) with a Leica M165 FC stereo fluorescence microscope. Tumour growth was quantified by calculating the total fluorescence intensity and area with the ZF4 pixel counting program (Leiden). Each experiment was performed at least 3 times with a group size of >30 embryos.

Maximum tolerated dose (MTD) for wild-type zebrafish and tumour cell-injected zebrafish

For determining the MTD of the water administration (WA) of the [2](PF₆)₂ solution in wild type zebrafish, solutions of 0.1 μM, 0.25 μM, 0.5 μM, 1 μM, 2 μM were made before the experiment. At 2.5, 3.5, 4.5, 5.5 dpf, [2](PF₆)₂ was added to the fish water and maintained for 12 h. At 3, 4, 5, 6 dpf, the fish water was refreshed and after 1 h, embryos were exposed to green light for 90 min (21 mW.cm⁻², 114 J.cm⁻², 520 nm). For the IV and RO administration, [2](PF₆)₂ solution (50 μM, 100 μM, 200 μM, 300 μM, 500 μM) was made before the experiment. At 3, 4, 5, 6 dpf, 1nl of [2](PF₆)₂ was injected via the dorsal vein or the RO site and maintained for 1 h. Embryos were exposed to green light for 90 min (21 mW.cm⁻², 114 J.cm⁻², 520 nm). The images of treated and wild type embryos at 6dpf were taken using a DFC420C camera coupled to a Leica MZ16FA fluorescence microscope. In order to determine the MTD of tumour cell-bearing zebrafish, 90 min green light activation (21 mW.cm⁻², 114 J.cm⁻², 520 nm) was performed according to the same procedure, after [2](PF₆)₂ was delivered by WA, IV and RA administration as described above for the wild type embryos.

The antitumour efficacy of [2](PF₆)₂ by WA, IV and RO in zebrafish ectopic and orthotopic tumour models

Fluorescent PC3Pro4 cells were injected at 2 dpf into the Duct of Cuvier (ectopic model) and [2](PF₆)₂ was delivered by WA and IV administration with or without light treatment as described in 5.9. Fluorescent CRMM1 or CRMM2 cells were injected at 2 dpf into the Duct of Cuvier (ectopic model) and behind the eye (orthotopic model) and [2](PF₆)₂ was delivered by WA IV and RO administration with or without light treatment as described in 5.9. For the WA administration, the 0.5 μM [2](PF₆)₂ solution was added to the tumour cells-injected zebrafish at 2.5, 3.5, 4.5, 5.5 dpf and maintained for 12 h. At 3, 4, 5, 6 dpf, the fish water was refreshed, and after 1 h, embryos were exposed to green light for 90 min (21 mW.cm⁻², 114 J.cm⁻², 520 nm). For the IV and RO administration, 1 nL of 200 μM [2](PF₆)₂ solution was injected via the dorsal vein or the RO site at 3, 4, 5, 6 dpf. After 1 h interval, the embryos were exposed to green light for 90 min (21 mW.cm⁻², 114 J.cm⁻², 520 nm). After treatment, the embryo images were acquired with a Leica M165 FC stereo fluorescence microscope. Tumour growth was

quantified by calculating the total fluorescence intensity and area with the ZF4 pixel counting program (Leiden). Each experiment was performed at least 3 times with a group size of >30 embryos.

TUNEL assay

The zebrafish larvae were fixed overnight with 4% PFA at 4 °C. Embryos were washed in PBST for five minutes and dehydrated by a graded methanol series until reaching 100% methanol. Embryos were stored at -20 °C for further use. Embryos were gradually rehydrated in PBST (25%, 50%, 75%), washed twice for 10 minutes with PBST and digested by proteinase K (Roche) solution in PBST (10 µg/ml) at 37 °C for 40 minutes. After two washes in PBST, embryos were post-fixed in 4% PFA for 20 minutes. After washing them again twice in PBST for 10 minutes, 50 µl of TdT reaction mix (Roche) was added to the embryos. Embryos were overnight incubated with the TdT at 37 °C (in the dark). The reaction was stopped by three 15 min washes with PBST at room temperature and embryos were used for high-resolution imaging. Embryos were placed on glass-bottom petri dishes and covered with 1% low melting agarose containing 0.003% tricaine (Sigma). Imaging was performed using the Leica SP8 confocal microscope. The images were processed with ImageJ software. Each experiment was performed 3 times with a group size of 10 embryos.

Statistical analysis

Determination of the EC₅₀ concentrations in vitro was based on a non-linear regression analysis performed using GraphPad Prism Software. Results are presented as means ± SD from three independent experiments. Significant differences were detected by one-way ANOVA followed by Dunnett's multiple comparisons test implemented by Prism 8 (GraphPad Software, La Jolla, CA, USA). A p-value < 0.05 was considered statistically significant, *: p < 0.05, **: p < 0.01, ***: p < 0.001.

Results and discussion

Synthesis and photoreactivity

The synthesis of **[2]**²⁺ is more challenging than that of complexes such as **[1]**²⁺ or **[3]**²⁺ because **[2]**²⁺ is a tris-heteroleptic compound, i.e. it bears three different bidentate ligands that need to be coordinated to the metal in a controlled fashion (Fig. 2). With most generic synthetic routes, ligand scrambling occurred, i.e. **[2]**²⁺ was obtained with traces of [Ru(dpp)(mtmp)₂]²⁺, [Ru(bpy)(mtmp)₂]²⁺, **[1]**²⁺, or **[3]**²⁺, that were very difficult to remove. The synthesis of **[2]**(PF₆)₂ was hence adapted from a novel method developed by Keyes *et al* [59] that involved the sequential coordination, in this order, of dpp, mtmp, and bpy. The novelty of this method relies on the use of an intermediate oxalate ligand (ox²⁻) during the coordination of the second (mtmp) chelate. This negatively-charged chelate prevents the formation of species where two identical ligands coordinate to the metal even when one equivalent of mtmp is

used. After purification of the $[\text{Ru}(\text{dpp})(\text{mtmp})(\text{ox})]$ (**[5]**) intermediate complex, oxalate was removed selectively by HClO_4 treatment in acetonitrile, after which the last chelate (bpy) was reacted to afford, after counter anion metathesis, $[\mathbf{2}](\text{PF}_6)_2$. Due to the dissymmetry of mtmp and the tri-heteroleptic nature of the final complex, two configurational isomers are expected: one having the sulfur donor atom *trans* to bpy and another having the sulfur donor atom *trans* to dpp. These isomers were detected by ^1H NMR and initially separated by column chromatography. Isomer **[2a]** $(\text{PF}_6)_2$ was slightly contaminated with $[\text{Ru}(\text{dpp})(\text{bpy})_2](\text{PF}_6)_2$, while isomer **[2b]** $(\text{PF}_6)_2$ was pure according to ^1H NMR but obtained in a low yield (<2%). Later on, as no difference in reactivity could be observed between both isomers, mixtures of **[2a]** $(\text{PF}_6)_2$ and **[2b]** $(\text{PF}_6)_2$ deprived of any other impurities were prepared and further used in biological studies; it is designated below as **[2]** $(\text{PF}_6)_2$.

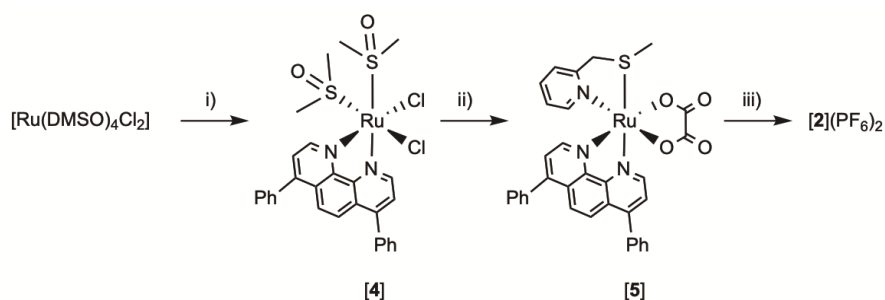


Figure 2 Synthesis of tris-heteroleptic compound $[\text{Ru}(\text{dpp})(\text{bpy})(\text{mtmp})](\text{PF}_6)_2$ (**[2]** $(\text{PF}_6)_2$). Conditions: i) 1.0 eq. dpp, EtOH, reflux 2 h, Y = 51%. ii) a) 1.5 eq. $\text{Na}_2\text{C}_2\text{O}_4$; water, reflux 1 h; b) 1.0 eq. mtmp, ethylene glycol, reflux 3 h; c) water; Y = 71%. iii) a) 1 M $\text{HClO}_{4(\text{aq})}/\text{CH}_3\text{CN}$ 1:1, reflux 1 h, b) 1.0 eq. bpy, ethylene glycol, 100 °C, 6 h; 3) aqueous KPF_6 ; Y = 28%.

The photoreactivity of **[2]** $(\text{PF}_6)_2$ was studied by UV-vis spectroscopy in CH_3CN . The spectrum of a solution of **[2]** $(\text{PF}_6)_2$ irradiated for 20 minutes with green light (521 nm, 14 $\text{mW}\cdot\text{cm}^{-2}$) showed an increase of the intensity of the metal-to-ligand charge-transfer (MLCT) band between 400-430 nm, and a decrease in the valley at 344 nm with clear isosbestic points at 363 and 440 nm (Fig. 3). After 15 minutes, when the reaction reached the steady state, mass spectrometry showed peaks at $m/z = 140.3$ and 336.3, corresponding to the free caging ligand $\{\text{mtmp}+\text{H}\}^+$ (calcd $m/z = 140.1$) and $[\text{Ru}(\text{bpy})(\text{Ph}_2\text{hen})(\text{CH}_3\text{CN})_2]^{2+}$ (calcd $m/z = 336.1$). No traces of bpy, dpp, or of any ruthenium complex resulting from the photosubstitution of one of the two bis-imine ligands, was observed by mass spectrometry. There was also no trace of the starting complex **[2]** $^{2+}$, confirming the selective and complete photosubstitution of mtmp upon light irradiation in deaerated CH_3CN , to produce $[\text{Ru}(\text{dpp})(\text{bpy})(\text{MeCN})_2]^{2+}$ as sole photosubstitution product. The photosubstitution quantum yield, measured by UV-vis spectroscopy was found to be 0.111 in these conditions (Fig. S1). The excited states of **[2]** $^{2+}$ do not necessarily deactivate only via photosubstitution and non-radiative decay; reaction with ground state oxygen to produce singlet oxygen ($^1\text{O}_2$) may happen, too, as described in PDT type II [60-62]. Hence, the quantum yield for the generation of $^1\text{O}_2$ (Φ_Δ) was experimentally determined by direct detection of the 1274 nm near-infrared phosphorescence of $^1\text{O}_2$ in an air-equilibrated CD_3OD solution

of $[2](PF_6)_2$. Under blue light irradiation (450 nm) using $[Ru(bpy)_3]Cl_2$ as reference ($\Phi_{\Delta} = 0.73$) [63], a Φ_{Δ} value of 0.096 was found for $[2]^{2+}$, which is slightly higher than for $[1]^{2+}$ ($\Phi_{\Delta} = 0.020$ in the same conditions), but much lower than PDT sensitizers such as Photofrin (0.90) [64], Foscan (0.43) [65], or TLD-1433 (1.0) [66]. Overall, the low Φ_{Δ} value and a rather high photosubstitution quantum yield make of $[2]^{2+}$ a promising PACT agent, provided it can enter cancer cells before light irradiation take place.

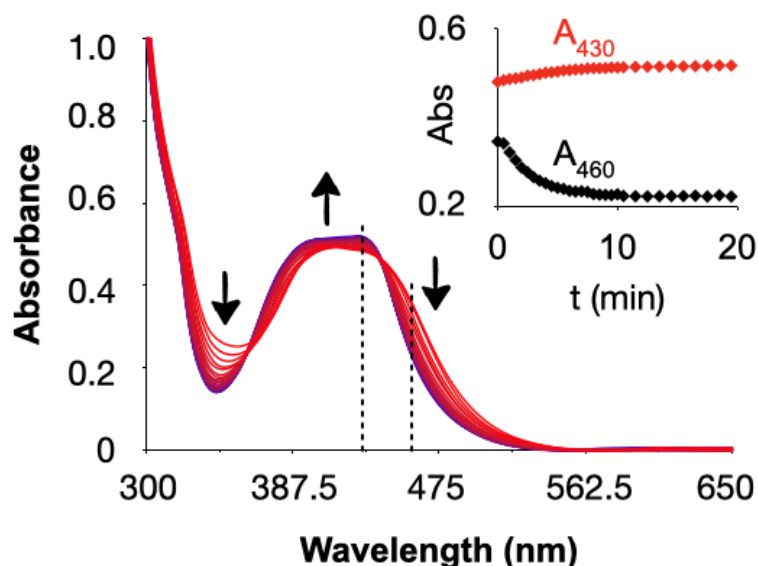


Figure 3 Evolution of the UV-vis spectrum of an acetonitrile solution of $[2](PF_6)_2$ (36 μM) upon green light irradiation (521 nm, 14 $mW \cdot cm^{-2}$, photon flux $6.2 \times 10^{-8} mol \cdot s^{-1}$) under inert atmosphere. Insert: black and red dots represent the evolution of the absorbance at 460 nm and 430 nm, respectively (dashed lines in the spectrum), vs. irradiation time.

Cellular uptake and cytotoxicity *in vitro*

Considering the good photosubstitution properties of $[2]^{2+}$, its cytotoxicity was first tested in the dark and upon green light activation in a human lung cancer cell line (A549) where the two known analogues $[1]^{2+}$ and $[3]^{2+}$ had already been evaluated [47]. The protocol is detailed in Hopkins *et al.* [67]. The effective concentrations (EC_{50}), defined as the compound concentration (in μM) that reduces cell viability by 50% compared to untreated cells, are shown in Table 1. In the dark, the EC_{50} value was 59 μM for $[2]^{2+}$, which is intermediate between that found, in the same conditions, for $[1]^{2+}$ (3.4 μM) and for $[3]^{2+}$ (>100 μM) [14]. After 15 minutes green light irradiation (520 nm, 21 $mW \cdot cm^{-2}$, 19 $J \cdot cm^{-2}$), the EC_{50} value decreased to 6.5 μM for $[2]^{2+}$, respectively, which is also intermediate between the 0.62 μM and >150 found for $[1]^{2+}$ and $[3]^{2+}$, respectively (Fig. 4). As suggested by Lameijer *et al.*, validating a compound as either a PACT agent or a PDT agent requires comparing the photoindexes (PI), rather than the EC_{50} values [68]. The photoindexes (PI) value for $[2]^{2+}$ (9.1) was twice higher than for $[3]^{2+}$ (5.5), which suggested that the compound design was successful. Qualitatively, cytotoxicity is closely related to cellular uptake and subcellular localization, which are in turn closely related to the lipophilicity of the

prodrug [69]. Typically, the presence of more phenyl groups results in an increase of lipophilicity [70]. The intermediate lipophilicity of [2]²⁺ obtained by balancing the number of dpp and bpy ligands, significantly decreased its dark toxicity, compared to [1]²⁺, while keeping its cytotoxicity after light activation much higher than for [3]²⁺. To verify quantitatively that this effect was related to drug uptake, A549 cells were treated for 24 h with [1]Cl₂ and [2](PF₆)₂ at their EC₅₀ concentrations (3.4 and 65 μM, respectively), counted, lysed, after which the ruthenium content was measured using ICP-MS (Table 1). In such conditions, the cellular uptake of [2]²⁺ was found almost equal to that of [1]²⁺, although the concentration used for treatment was 20 times higher. Similar experiments with [3]²⁺ had demonstrated that this compound was not taken up by A549 cells because of its too high hydrophilicity [14]. Thus, the intermediate lipophilicity of [2]²⁺, between that of [1]²⁺ and [3]²⁺, indeed allowed for moderating cellular uptake, which kept the dark toxicity low while not jeopardizing the toxicity after light activation (Table 2). Such balanced lipophilicity also allowed the compound to penetrate 3D multicellular tumour spheroids of the same cell line (A549). In such conditions, the activity of [2]²⁺ remained significantly improved upon light irradiation, with EC₅₀ values in the dark and after light irradiation (520 nm, 21 mW.cm⁻², 19 J.cm⁻²) of 172.9 and 70.9 μM, respectively. Most importantly, the viability of the tumour spheroid was almost eradicated at 300 μM upon light irradiation, which highlights the excellent phototoxicity of this compound also in a 3D environment.

Table 1 Cytotoxicity expressed as cell growth inhibition effective concentrations (EC₅₀ with 95% confidence intervals, in μM) of [1]Cl₂, [2](PF₆)₂ and in lung (A549) and prostate (PC3Pro4) cancer cell lines, in the dark and upon green light irradiation (21 mW.cm⁻², 15 min, 19 J.cm⁻², 520 nm).

Cell line	Light dose (J.cm ⁻²)	[1]Cl ₂			[2](PF ₆) ₂			[3]Cl ₂		
		EC ₅₀	95%CI	PI	EC ₅₀	95%CI	PI	EC ₅₀	95%CI	PI
A549	0	3.4	-0.76 0.97		59	-13 17		>150	-	-
	19	0.62	-0.11 0.14	5.5	6.5	-1.8 2.4	9.1	>150	-	-
PC3Pro4	0	4.7	-0.30 0.32		142	-52 83		>150	-	-
	19	0.79	-0.027 0.028	6.0	3.2	-0.54 0.65	45	>150	-	-

Table 2 Cellular uptake of [1]Cl₂ and [2](PF₆)₂ in A549 cells upon treatment near the dark EC₅₀ value.

	[1]Cl ₂	[2](PF ₆) ₂
Treatment concentration (μM)	3.4	65
Cellular uptake (nmol Ru/mg of cell protein)	2.11 ± 0.12	2.12 ± 0.33

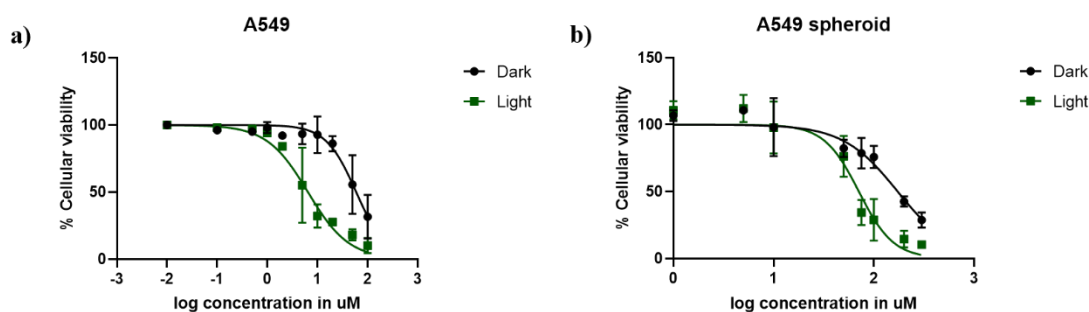


Figure 4 Dose-response curves for A549 cells treated with **[2](PF₆)₂**, and irradiated with green light (520 nm, 15 min, 21 mW.cm⁻², 19 J.cm⁻²) 24 h after treatment (green data points) or left in the dark (black data points). a) A549 cells were cultured in 2D cell monolayers. SRB assay was carried out at t=96 h. The absorbance of Sulforhodamine B in solution was measured at 520 nm. b) A549 cells were cultured as 3D multicellular tumour spheroids in ultra-low attachment flask. The spheroids were treated with **[2](PF₆)₂** at day 4, irradiated at day 5 (520 nm, 15 min, 21 mW.cm⁻², 19 J.cm⁻²), and their viability assayed at day 7 by a CellTiter-Glo 3D cell viability assay. Results are presented as means ± SD from three independent experiments with 95% confidence intervals.

Encouraged by these results, the cytotoxicity of **[2](PF₆)₂** was further assayed in a wider range of 2D cell monolayer models, i.e. using the PC3Pro4, CRMM1, CRMM2, CM2005.1, OMM1, OMM2.5 and MEL270 human cancer cell lines (Fig. S2). PC3Pro4 is a cancer cell line derived from a bone metastasis obtained after injection of PC3 human prostate cancer cells into nude mice [71], while CRMM1, CRMM2 and CM2005.1 are conjunctival melanoma cell lines and OMM1, OMM2.5 and MEL270 are uveal melanoma cell lines. The EC₅₀ values are listed in Table 2 and 3. Interestingly, **[2](PF₆)₂** exhibited higher toxicity in PC3Pro4, CRMM1 and CRMM2 cells upon light irradiation, and less toxicity in the dark, resulting in very high PI values of 45, >47, and >59, respectively (Table 3). In order to investigate the cytotoxic mechanism induced by light activated **[2](PF₆)₂**, CRMM1 cells were treated with 4.3 μM for 24 h, stained with Annexin V and propidium iodide, and analysed by fluorescence-activated cell-sorting (FACS). While the fraction of early apoptotic vs. necrotic cells in the cells treated with **[2](PF₆)₂** but not irradiated were almost identical to that of the vehicle control, almost half of the cells treated with **[2](PF₆)₂** and activated by light were found to be either necrotic (PI+, Annexin-) or in the late apoptotic/dead cell quadrant, while the number of early apoptotic cells decreased to almost zero (Fig. S3). These results come in strong contrast with the almost exclusively apoptotic cell death mode observed with another ruthenium-based PACT compound, [Ru(bapbpy)(dmsO)Cl]Cl, showing that the cell death mode with such compounds highly depends on the structure of the complex [72]. Overall, the excellent *in vitro* results observed in PC3Pro4, CRMM1, and CRMM2 cells, led us to selecting these cells for further testing of **[2](PF₆)₂** in zebrafish tumour models.

Table 3 Cytotoxicity expressed as effective concentrations (EC₅₀ with 95% confidence intervals, in μM) of [2](PF₆)₂ in conjunctival melanoma (CRMM1, CRMM2, CM2005.1) and uveal melanoma (OMM1, OMM2.5, MEL270) cell lines, in the dark and upon green light irradiation (21 mW.cm⁻², 15 min, 19 J.cm⁻², 520 nm).

Cell line	Light dose (J.cm ⁻²)	[2](PF ₆) ₂		
		EC ₅₀	95%CI	PI
CRMM1	0	>200		
	19	4.3	-0.89 1.1	>47
CRMM2	0	>200		
	19	3.4	-0.88 1.2	>59
CM2005.1	0	>200		
	19	15	-3.2 4.7	>13
OMM1	0	150	-20 30	
	19	24	-4.5 7.6	6.3
OMM2.5	0	100	-8.4 9.2	
	19	14	-1 1.2	7.1
MEL270	0	140	-20 27	
	19	13	-1.3 1.5	11

Maximum tolerated dose of [2](PF₆)₂ in zebrafish ectopic and orthotopic cancer models

To investigate the *in vivo* anti-cancer efficacy of [2](PF₆)₂, we utilized prostate (cell line PC3Pro4) and eye (CRMM1, CRMM2, CM2005.1) zebrafish embryonic cancer models, previously established in our group [73,74]. For prostate, androgen-independent osteotropic red-emitting PC3Pro4-mCherry cells (100-400 cells) were intravenously injected into the Duct of Cuvier (DoC) of Tg(Fli:GFP) endothelial reporter transgenic zebrafish line with green fluorescent vasculature (GFP) at 2 days post fertilization (dpf) (Fig. 5). The DoC is an open blood circulation channel connecting the heart and the trunk vasculature of the embryo [75]. Immediately after injection, cells haematogenously disseminated through the whole circulation. Most of the circulating cells regressed without extravasation or initiating tumour growth. However, within 1 day, some cells were able to extravasate exclusively at the posterior ventral end of caudal hematopoietic tissue (CHT), and invade into the tail fin where they developed perivascular metastatic lesions within 4 dpf (Fig. 5). CHT is an intermediate site of haematopoiesis

during zebrafish embryogenesis and is the functional analogue of the foetal liver during mammalian development [76]. Metastatic tumours grew around CHT at 6dpf, as detected by red fluorescence (excitation: 587 nm, emission: 610 nm) that can be quantified, either in terms of emission intensity, or by the relative tumour area in microscopy images; both quantifications are referred below as “relative tumour burden”. This tumour model is called “ectopic” as the CHT site does not represent the organ of origin of these cancer cells. For conjunctive melanoma (CM), we used an orthotopic model recently developed in our group for PDT treatment [57,77]. In short, the CM tumours were generated by injection of 200 CRMM1-mCherry or CRMM2-mCherry cells into the retro-orbital site of the embryo at 2 dpf (Fig. 6). From 2 to 6 dpf, the CRMM1 or CRMM2 cells formed local lesions at the injection site behind the eye. This tumour model is called “orthotopic” as the site for tumour growth, i.e. the eye, does represent the organ of origin of these cancer cells.

Table 4 The maximum tolerated dose (MTD) of [2](PF₆)₂ in wild type zebrafish embryos and in the ectopic and orthotopic CM tumour models.

[2](PF ₆) ₂	Maximum tolerated concentration	
	Wild Type Embryos	Tumour cells engrafted Embryos Ectopic and Orthotopic Model
Water Administration	1 µM	0.5 µM
Intravenous Administration	300 µM	200 µM
Retro-orbital Administration ^a	300 µM ^a	200 µM ^a

^a for CRMM1 and CRMM2 xenografts only.

In terms of drug treatment modalities, the embryos were subjected to three different protocols (Fig. 5 and 6). For the ectopic model, treatment with [2](PF₆)₂ was performed either by water administration (WA) or by intravenous injection (IV), while for the orthotopic model, treatment was performed either by WA, IV, or retro-orbital (RO) injections. Before testing the anti-tumour efficacy, it was necessary to evaluate the toxicity of the phototherapy treatment. The toxicity of green light alone (520 nm) was recently reported [57]. At an intensity of 21 mW.cm⁻², the zebrafish embryos could tolerate light irradiation until 6 h without any toxicity or visible developmental defects [57]. The toxicity of [2](PF₆)₂ was then evaluated by measuring its maximum tolerated dose (MTD) for the different administration modes, both for tumour-free embryos and tumour cell-injected embryos (Table 4 and Fig. S4). For treatment *via* water administration, different concentrations (0, 0.1 0.25, 0.5, 1, 2 µM) of [2](PF₆)₂ were added to the egg water (i.e., the water in which the zebrafish embryo were swimming) at 2.5, 3.5, 4.5 and 5.5 dpf, and incubation was continued overnight for a drug-to-light interval of 12 h. At 3, 4, 5, 6 dpf, excess [2](PF₆)₂ was washed by drug-free water and the embryos were further irradiated with green light (21 mW.cm⁻², 90 min, 114 J.cm⁻², 520 nm). In such conditions, an MTD of 0.5 µM for embryos engrafted with PC-Pro4-mCherry tumours, and of 1 µM for tumour-cell free embryos, was obtained. For treatment *via* intravenous or retro-orbital administration, 1 nL with different concentrations (0, 50, 100, 200, 300, 500 µM) of [2](PF₆)₂ was injected into the dorsal vein or retro-orbital site of zebrafish at 3, 4,

5, 6 dpf. After a shorter drug-light interval of 1 h, the zebrafish embryos were irradiated with the same dose of green light (21 mW.cm⁻², 90 min, 114 J.cm⁻², 520 nm). The lethality, aberrant morphology and fish length were measured at 6 dpf. Zebrafish embryos tolerated, without any effect on mortality, malformation and fish length, injection of [2](PF₆)₂, followed by light activation, at a MTD of 200 μM for embryos engrafted with PC-Pro4-mCherry, CRMM1, CRMM2 cells and of 300 μM for tumour-free embryos (see Fig. S4). These MTD values of 0.5 μM (WA) and 200 μM (IV and RO) were further used for assessing the anti-tumour efficacy in the zebrafish tumour models.

Effect of [2](PF₆)₂ on PC3Pro4 tumour growth by water and intravenous administration in zebrafish ectopic prostate cancer model

In the PC3Pro4-mCherry zebrafish ectopic model, both WA (0.5 μM) and IV administration (1 nL, 200 μM) of [2](PF₆)₂ were tested using the previously determined MTD. At 6 dpf, images of the PC3Pro4-mCherry tumours were taken using a stereo microscope. Quantification of the relative tumour burden was performed by measuring either the relative fluorescence intensity or the relative tumour area (Fig. 5). Using a 12 h (WA) or 1 h (IV) drug-to-light interval, green light activation (21 mW.cm⁻², 90 min, 114 J.cm⁻², 520 nm) did not change the tumour burden, compared to the dark groups, even when the treatment on each embryo was repeated 4 times (Fig. 4). Usually, WA in zebrafish is acknowledged to mimic the oral route in human patients. Indeed, the compound will first go into the enterohepatic circulation and then disseminate through the blood circulation. The fact that no anti-tumour activity was observed for [2](PF₆)₂ administered by WA in the prostate cancer zebrafish model, while it showed excellent activity in PC3Pro4 cell monolayers *in vitro* (Table 2), suggested that in the embryo, the compound may simply not be taken up into the blood circulation. Another possibility is that it was excreted within the 90 min irradiation time. In contrast, IV injection delivers the compound directly into the blood circulation, but this had no effect either. However, compound [2](PF₆)₂ may distribute anywhere in the embryo during the 1 h drug-to-light interval, or be excreted. To obtain anti-tumour efficacy upon light activation requires that the prodrug reaches the tumour in sufficiently high concentrations, which clearly did not happen here. Alternatively, engrafted prostate cancer cells might have gained chemotherapy resistance *in vivo*, which they did not have *in vitro* [78]. Overall, these results most probably suggest that more specific targeting strategies would be needed to achieve proper efficacy of this compound in ectopic prostate cancer models.

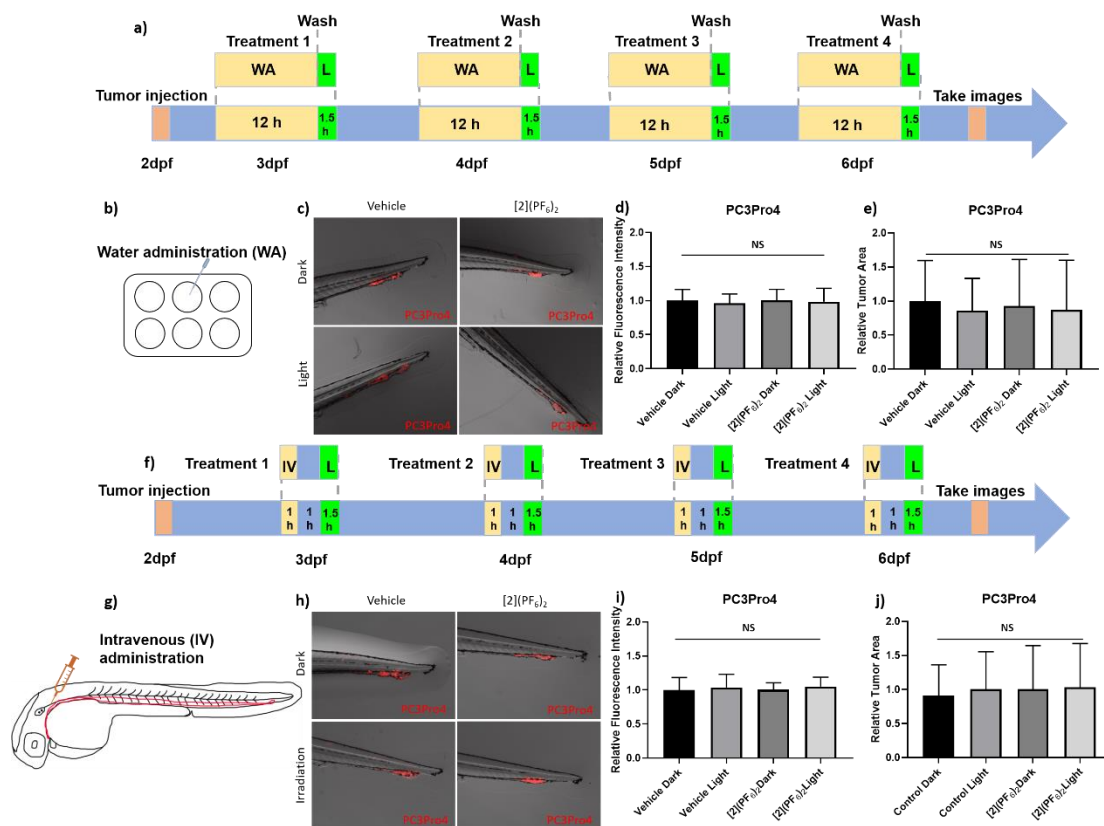


Fig. 5 Efficacy of $[2](PF_6)_2$ in PC3Pro4 prostate cancer zebrafish ectopic model. a) Schedule of tumour cells injection and treatment with $[2](PF_6)_2$ by water administration (WA). Around 300 PC3Pro4 cells were injected into Duct of Cuvier at 2dpf. $0.5 \mu M$ of $[2](PF_6)_2$ was added into water at 2.5, 3.5, 4.5, 5.5 dpf. At 3, 4, 5, 6 dpf, the compound was washed away, the embryos were irradiated with green light ($21 \text{ mW}\cdot\text{cm}^{-2}$, $114 \text{ J}\cdot\text{cm}^{-2}$, 520 nm) for 1.5 h. b) Water administration of $[2](PF_6)_2$ into 6-well plates containing engrafted embryos. c) The images of PC3Pro4 tumour burden at CHT site at 6 dpf. d) The relative fluorescence intensity of PC3Pro4 tumour burden at 6 dpf. e) The relative tumour area of PC3Pro4 tumour burden at 6 dpf. f) Schedule of tumour cells injections and treatment with $200 \mu M$ of $[2](PF_6)_2$ by intravenous administration. g) The injection site of intravenous administration (IV). h) The images of PC3Pro4 tumour burden at CHT site at 6 dpf. i) The relative fluorescence intensity of PC3Pro4 tumour burden at 6 dpf. j) The relative tumour area of PC3Pro4 tumour burden at 6 dpf. Results are presented as means \pm SD from three independent experiments.

$[2](PF_6)_2$ effect on CRMM1 and CRMM2 tumour growth by retro-orbital administration in the zebrafish orthotopic conjunctival melanoma model

When both the tumour cells and the prodrug are injected into the general blood circulation of the embryo, it should not be taken for granted that the drug properly biodistributes to reach the inside of a tumour at a sufficiently high concentration. One way to address this issue is to use a model where the prodrug is injected near the tumour. The efficacy of $[2](PF_6)_2$ was hence examined in the orthotopic model of conjunctival melanoma (CM) described above and in [57]. In this model, the tumour develops

in the back of the eye, near the location of the cancer cell injection, and the prodrug is also injected at the same place. A shorter drug-to-light interval is used (1 h) to avoid prodrug diffusion away from the tumour prior to light activation. In a sense, this model may better mimic local PDT treatments performed in human cancer patients. Following our treatment strategy as developed for the PDT sensitizer TLD-1433 [57], the MTD of [2](PF₆)₂ (1 nL, 200 μM) was injected retro-orbitally at 3, 4, 5, 6 dpf. After 1 h drug-to-light interval, the embryos in both light-irradiated groups (vehicle, [2](PF₆)₂) were irradiated with green light (520 nm, 90 min, 21 mW.cm⁻², 114 J.cm⁻²), while the two dark groups (vehicle, [2](PF₆)₂) were kept in the dark. During the experiment, the egg water of engrafted embryos was refreshed before injection and after irradiation. At 6 dpf and 4 consecutive treatments, quantification of the CRMM1 and CRMM2 relative tumour burden was performed by measuring either the relative fluorescence intensity or the relative tumour area using a stereo microscope (Fig. 6). In the group treated with [2](PF₆)₂ and green light (21 mW.cm⁻², 114 J.cm⁻², 520 nm), the CRMM1 tumour burden was significantly inhibited by 57% (fluorescent intensity) and 78% (tumour area) compared with the dark group, while the CRMM2 tumour burden was inhibited by 52% (fluorescence intensity) and 88% (tumour area), compared with the dark group. When comparing these excellent results with the absence of efficacy of the same compound in the ectopic model for prostate cancer, we envision that local RO administration of [2](PF₆)₂ generates a higher concentration of the inactive compound in the proximity of the tumour, and therefore that green light activation generates sufficient amounts of the activated ruthenium molecules, to attenuate localized CM development in the light-irradiated group (Fig. 6c-h). These results represent the first experimental demonstration that ruthenium-based PACT treatment can inhibit CM growth in an animal tumour model. They also suggest that compound [2](PF₆)₂ should be further investigated in pre-clinical rodent models.

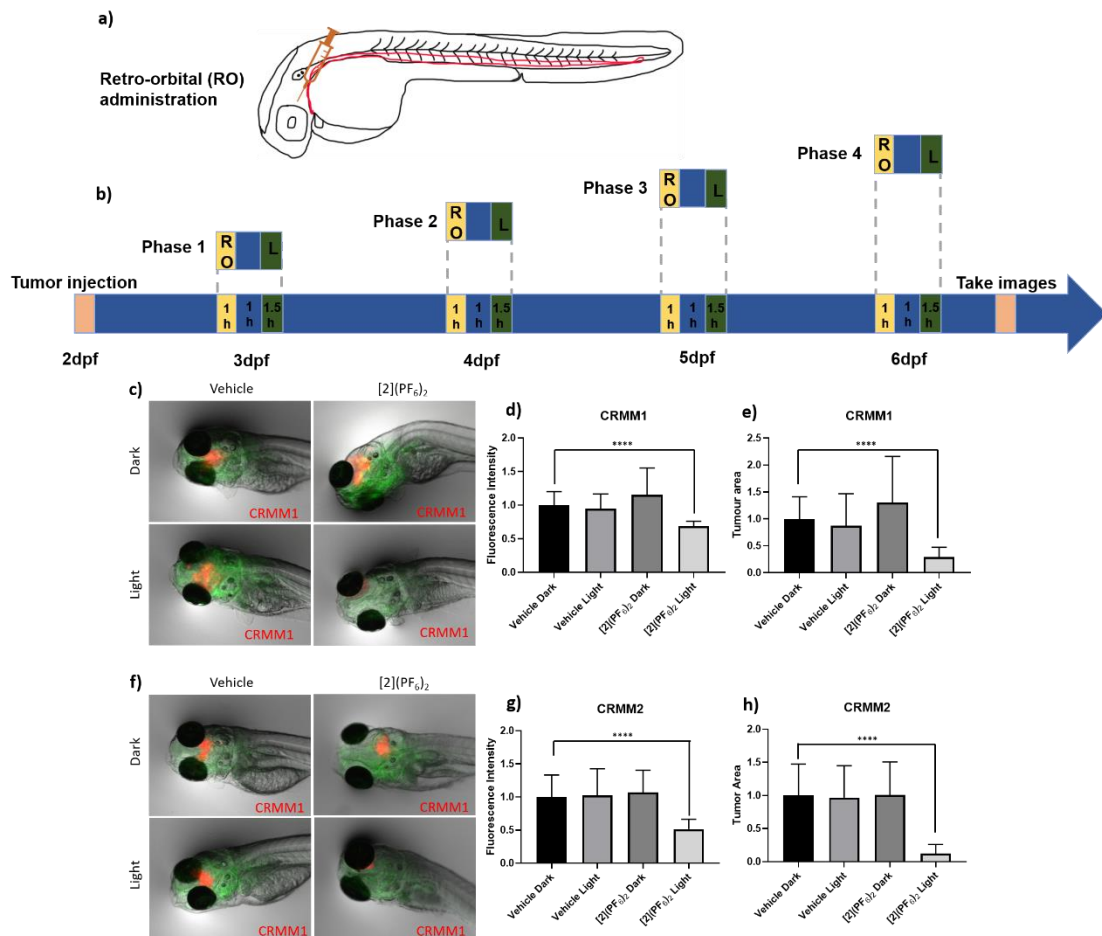


Fig. 6 Efficacy of the PACT compound [2](PF₆)₂ in the Tg(Fli:GFP/casper) zebrafish orthotopic model of conjunctival melanoma (CRMM1 and CRMM2 cell lines) by retro-orbital administration (RO). a) Scheme showing the injection site of retro-orbital administration. b) Time flow of [2](PF₆)₂ treatment with RO administration. Around 200 CRMM1 or CRMM2 cells were injected into the RO site of zebrafish embryos at 2 dpf. [2](PF₆)₂ was injected into RO site at 3, 4, 5, 6 dpf, and after 1 h drug-light interval, the embryos were irradiated with green light (520 nm, 21 mW.cm⁻², 90 min, 114 J.cm⁻²). c) The images of CRMM1 or CRMM2 tumour burden (in red) at CHT site at 6 dpf. Green represents vessels in zebrafish embryos. d, g) The relative red fluorescence (excitation: 554 nm, emission: 581 nm) intensity of CRMM1 or CRMM2 tumour burden at 6 dpf. e, h) The relative tumour area (pixel²) of CRMM1 or CRMM2 tumour burden at 6 dpf. Results are presented as means ± SD from three independent experiments. ****: P < 0.0001.

[2](PF₆)₂ induces CRMM1 cell apoptosis in the zebrafish orthotopic model

To monitor whether the observed inhibition of CM growth in the zebrafish orthotopic model by [2](PF₆)₂ was occurring *via* apoptosis, an *in situ* TUNEL assay was conducted on fixed embryos bearing CRMM1 tumours at 4 dpi (days post injection), which were either kept in the dark or irradiated with green light (520 nm, 90 min, 21 mW.cm⁻², 114 J.cm⁻²), and treated by RO injection at the MTD (1 nL, 200 μM) either with vehicle control or [2](PF₆)₂ (Fig. 6 and 7). In the TUNNEL assay, the DNA strand breaks in apoptotic tumour cells were stained with fluorescein and visualized as a green signal in microscopy images. In the

dark vehicle group, light vehicle group, and group treated with [2](PF₆)₂ but not irradiated, no positive green signal was detected (Fig. 7a). Only in the group treated with [2](PF₆)₂ and irradiated with green light (520 nm, 21 mW.cm⁻², 90 min, 114 J.cm⁻²), a significant number of cancer cells (Fig. 7b) stained positive for apoptotic signal and turned green, which co-localized with red signal of CRMM1 cells (yellow in overlay, Fig. 7a). This result indicated that the anti-tumour efficacy of [2](PF₆)₂ in this PACT regime was at least partially apoptosis-dependent, which significantly differs from the FACS analysis *in vitro*. It should also be noted that there was no apoptotic signal detected in the tissue surrounding the tumours, pointing out that light activated [2](PF₆)₂ attacked CM tumours but not healthy tissues, which is essential for minimizing side effects.

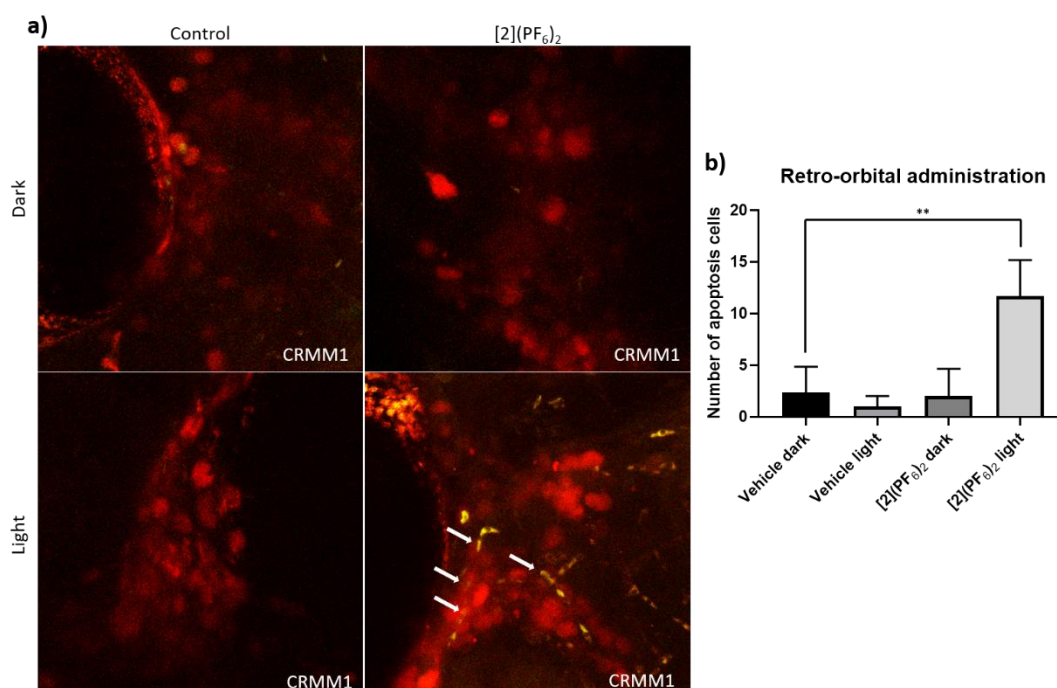


Figure 7 TUNEL assay in the CRMM1 orthotopic tumour model after RO injection of [2](PF₆)₂. a) Red fluorescent CRMM1 cells were injected behind the eye of the embryo at 2dpf, and the embryos were divided into four groups for drug treatment. RO administration of vehicle control and [2](PF₆)₂ was performed as described in Fig. 6. After dark or light exposure, embryos were fixed and TUNEL staining was performed. a) Representative overlay images of embryos are shown. In the group treated with [2](PF₆)₂ and light, nuclear DNA fragmentation in nucleases is detected by co-localization of green (DNA fragments) and red (CM tumour cell) signal, depicted on the overlay as yellow signal marked by white arrows. In the dark control group, light control group, and group treated with [2](PF₆)₂ and left in the dark, there were no positive green apoptotic tumour cells. The background green signal in the [2](PF₆)₂ light groups did not co-localize with cytosolic red signal, which is diminished in degraded cells and TUNEL stains only the DNA breaks in these CM apoptotic cells. b) Quantification of the number of apoptotic tumour cells (yellow dots). Experiment was performed 3 times with a group size of 10 embryos. **: P < 0.01.

Conclusions

In conclusion, we have synthesized the new tris-heteroleptic ruthenium-based PACT prodrug [2](PF₆)₂ which is characterized by a well-balanced hydrophobicity in the dark. The toxicity of this chemical is obtained by green light activation, which triggers photosubstitution of the non-toxic mtmp ligand and liberates a ruthenium-based activated photoproduct. This activated photoproduct can bind to many biomolecules, which ultimately leads to cell death. Of course, [2](PF₆)₂ has not been designed for specific targets in tumour cells, which may be seen as a potential sources of side-effects. On the other hand, this lack of specificity ensures that single mutations in cancer cells would not quench the cytotoxic activity of the light-activated compound, as confirmed by the large range of unrelated cancer cell lines (lung, prostate, eye) in which [2](PF₆)₂ remained photoactive. Still, differences in photoindexes existed between cell lines, which pointed at PC3Pro4, CRMM1, and CRMM2 cell lines, for further *in vivo* evaluation. We do not know why the uveal melanoma cell lines did not show a better response to the treatment with [2](PF₆)₂, but we decided to use the conjunctival cell lines when we saw how much more sensitive these were. Zebrafish embryos allowed us to demonstrate the efficacy of ruthenium-based PACT in conjunctival melanoma xenografts *in vivo* [48]; this provided the first MTD values for a photosubstitutionally active ruthenium compound administered either *via* water, intravenous injection, or retro-orbital injection. More than this, our results also highlight the difference between ectopic and orthotopic *in vivo* models for photoactivated drugs: while the photoindexes *in vitro* were high both in prostate cancer cells (PC3Pro4) and conjunctival melanoma cells (CRMM1, CRMM2), *in vivo* there was no activity in the ectopic model of prostate cancer, while activity was excellent in the orthotopic model of conjunctival melanoma. Such a difference underscores the interaction between the type of tumour model as well as the mode of compound administration in tumour xenografts, which cannot be modelled *in vitro* but dramatically influence both (pro)drug biodistribution, drug uptake by the tumour, and hence the final anti-tumour efficacy of the treatment. Overall, the present validation of the anti-tumour efficacy of retro-orbitally administered ruthenium compound [2](PF₆)₂ in zebrafish conjunctival melanoma orthotopic models suggests that further pre-clinical development of this new PACT drug should be considered in larger models (rodents) for conjunctival melanoma, where light irradiation can be limited to the tumour.

Conflict of interest

There are no conflicts of interest to declare.

Acknowledgements

The European Research Council is kindly acknowledged for a Starting Grant (RuProLight) and a Proof-of-Concept grant (Ru4EYE) to S.B. The Chinese Scholarship Council is kindly acknowledged for a PhD grants to Q.C.

References

1. Dilruba, S.; Kalayda, G.V. Platinum-based drugs: past, present and future. *Cancer chemotherapy and pharmacology* **2016**, *77*, 1103-1124, doi:10.1007/s00280-016-2976-z.
2. Galanski, M. Recent developments in the field of anticancer platinum complexes. *Recent patents on anti-cancer drug discovery* **2006**, *1*, 285-295, doi:10.2174/157489206777442287.
3. Lebwohl, D.; Canetta, R. Clinical development of platinum complexes in cancer therapy: an historical perspective and an update. *European journal of cancer (Oxford, England : 1990)* **1998**, *34*, 1522-1534, doi:10.1016/s0959-8049(98)00224-x.
4. Pouysségur, J.; Dayan, F.; Mazure, N.M. Hypoxia signalling in cancer and approaches to enforce tumour regression. *Nature* **2006**, *441*, 437-443, doi:10.1038/nature04871.
5. Jamieson, E.R.; Lippard, S.J. Structure, Recognition, and Processing of Cisplatin-DNA Adducts. *Chemical reviews* **1999**, *99*, 2467-2498, doi:10.1021/cr980421n.
6. Fraval, H.N.; Rawlings, C.J.; Roberts, J.J. Increased sensitivity of UV-repair-deficient human cells to DNA bound platinum products which unlike thymine dimers are not recognized by an endonuclease extracted from *Micrococcus luteus*. *Mutation research* **1978**, *51*, 121-132, doi:10.1016/0027-5107(78)90014-3.
7. Dasari, S.; Tchounwou, P.B. Cisplatin in cancer therapy: molecular mechanisms of action. *European journal of pharmacology* **2014**, *740*, 364-378, doi:10.1016/j.ejphar.2014.07.025.
8. Karasawa, T.; Steyger, P.S. An integrated view of cisplatin-induced nephrotoxicity and ototoxicity. *Toxicology letters* **2015**, *237*, 219-227, doi:10.1016/j.toxlet.2015.06.012.
9. Cersosimo, R.J. Hepatotoxicity associated with cisplatin chemotherapy. *The Annals of pharmacotherapy* **1993**, *27*, 438-441, doi:10.1177/106002809302700408.
10. Martins, N.M.; Santos, N.A.; Curti, C.; Bianchi, M.L.; Santos, A.C. Cisplatin induces mitochondrial oxidative stress with resultant energetic metabolism impairment, membrane rigidification and apoptosis in rat liver. *Journal of applied toxicology : JAT* **2008**, *28*, 337-344, doi:10.1002/jat.1284.
11. Kenny, R.G.; Marmion, C.J. Toward Multi-Targeted Platinum and Ruthenium Drugs-A New Paradigm in Cancer Drug Treatment Regimens? *Chemical reviews* **2019**, *119*, 1058-1137, doi:10.1021/acs.chemrev.8b00271.
12. Garner, R.N.; Gallucci, J.C.; Dunbar, K.R.; Turro, C. [Ru(bpy)₂(5-cyanouracil)₂]²⁺ as a potential light-activated dual-action therapeutic agent. *Inorganic chemistry* **2011**, *50*, 9213-9215, doi:10.1021/ic201615u.
13. Respondek, T.; Garner, R.N.; Herroon, M.K.; Podgorski, I.; Turro, C.; Kodanko, J.J. Light activation of a cysteine protease inhibitor: caging of a peptidomimetic nitrile with Ru(II)(bpy)₂. *Journal of the American Chemical Society* **2011**, *133*, 17164-17167, doi:10.1021/ja208084s.
14. Cuello-Garibo, J.-A.; Meijer, M.S.; Bonnet, S. To cage or to be caged? The cytotoxic species in ruthenium-based photoactivated chemotherapy is not always the metal. *Chem Commun (Camb)* **2017**, *53*, 6768-6771, doi:10.1039/c7cc03469e.
15. Wilson, W.R.; Hay, M.P. Targeting hypoxia in cancer therapy. *Nat Rev Cancer* **2011**, *11*, 393-410, doi:10.1038/nrc3064.
16. Lameijer, L.N.; Ernst, D.; Hopkins, S.L.; Meijer, M.S.; Askes, S.H.C.; Le Dévédec, S.E.; Bonnet, S. A Red-Light-Activated Ruthenium-Caged NAMPT Inhibitor Remains Phototoxic in Hypoxic Cancer Cells. *Angew Chem Int Ed Engl* **2017**, *56*, 11549-11553, doi:10.1002/anie.201703890.
17. Bonnet, S. Why develop photoactivated chemotherapy? *Dalton transactions (Cambridge, England : 2003)* **2018**, *47*, 10330-10343, doi:10.1039/c8dt01585f.
18. Mari, C.; Gasser, G. Lightning up Ruthenium Complexes to Fight Cancer? *Chimia (Aarau)* **2015**, *69*, 176-181, doi:10.2533/chimia.2015.176.
19. Farrer, N.J.; Salassa, L.; Sadler, P.J. Photoactivated chemotherapy (PACT): the potential of excited-state d-block metals in medicine. *Dalton transactions (Cambridge, England : 2003)* **2009**, 10.1039/b917753a, 10690-10701, doi:10.1039/b917753a.
20. Arora, K.; Herroon, M.; Al-Afyouni, M.H.; Toupin, N.P.; Rohrabough, T.N., Jr.; Loftus, L.M.; Podgorski, I.; Turro, C.; Kodanko, J.J. Catch and Release Photosensitizers: Combining Dual-Action Ruthenium Complexes with Protease Inactivation for Targeting Invasive Cancers. *Journal of the American Chemical Society* **2018**, *140*, 14367-14380,

- doi:10.1021/jacs.8b08853.
21. Zhou, Q.-X.; Lei, W.-H.; Chen, J.-R.; Li, C.; Hou, Y.-J.; Wang, X.-S.; Zhang, B.-W. A new heteroleptic ruthenium(II) polypyridyl complex with long-wavelength absorption and high singlet-oxygen quantum yield. *Chemistry* **2010**, *16*, 3157-3165, doi:10.1002/chem.200902563.
 22. Sainuddin, T.; Pinto, M.; Yin, H.; Hetu, M.; Colpitts, J.; McFarland, S.A. Strained ruthenium metal–organic dyads as photocisplatin agents with dual action. *Journal of Inorganic Biochemistry* **2016**, *158*, 45-54, doi:<https://doi.org/10.1016/j.jinorgbio.2016.01.009>.
 23. Hufziger, K.T.; Thowfeik, F.S.; Charboneau, D.J.; Nieto, I.; Dougherty, W.G.; Kassel, W.S.; Dudley, T.J.; Merino, E.J.; Papish, E.T.; Paul, J.J. Ruthenium dihydroxybipyridine complexes are tumor activated prodrugs due to low pH and blue light induced ligand release. *Journal of Inorganic Biochemistry* **2014**, *130*, 103-111, doi:<http://dx.doi.org/10.1016/j.jinorgbio.2013.10.008>.
 24. Howerton, B.S.; Heidary, D.K.; Glazer, E.C. Strained ruthenium complexes are potent light-activated anticancer agents. *Journal of the American Chemical Society* **2012**, *134*, 8324-8327, doi:10.1021/ja3009677.
 25. Meijer, M.S.; Bonnet, S. Diastereoselective Synthesis and Two-Step Photocleavage of Ruthenium Polypyridyl Complexes Bearing a Bis(thioether) Ligand. *Inorganic chemistry* **2019**, *58*, 11689-11698, doi:10.1021/acs.inorgchem.9b01669.
 26. Wachter, E.; Heidary, D.K.; Howerton, B.S.; Parkin, S.; Glazer, E.C. Light-activated ruthenium complexes photobind DNA and are cytotoxic in the photodynamic therapy window. *Chem Commun (Camb)* **2012**, *48*, 9649-9651, doi:10.1039/c2cc33359g.
 27. Roque, J., 3rd; Havrylyuk, D.; Barrett, P.C.; Sainuddin, T.; McCain, J.; Colón, K.; Sparks, W.T.; Bradner, E.; Monro, S.; Heidary, D., et al. Strained, Photoejecting Ru(II) Complexes that are Cytotoxic Under Hypoxic Conditions. *Photochemistry and photobiology* **2020**, *96*, 327-339, doi:10.1111/php.13174.
 28. Albani, B.A.; Peña, B.; Dunbar, K.R.; Turro, C. New cyclometallated Ru(II) complex for potential application in photochemotherapy? *Photochemical & photobiological sciences : Official journal of the European Photochemistry Association and the European Society for Photobiology* **2014**, *13*, 272-280, doi:10.1039/c3pp50327e.
 29. Hufziger, K.T.; Thowfeik, F.S.; Charboneau, D.J.; Nieto, I.; Dougherty, W.G.; Kassel, W.S.; Dudley, T.J.; Merino, E.J.; Papish, E.T.; Paul, J.J. Ruthenium dihydroxybipyridine complexes are tumor activated prodrugs due to low pH and blue light induced ligand release. *Journal of inorganic biochemistry* **2014**, *130*, 103-111, doi:10.1016/j.jinorgbio.2013.10.008.
 30. Letrado, P.; de Miguel, I.; Lamberto, I.; Díez-Martínez, R.; Oyarzabal, J. Zebrafish: Speeding Up the Cancer Drug Discovery Process. *Cancer Res* **2018**, *78*, 6048-6058, doi:10.1158/0008-5472.CAN-18-1029.
 31. Kucinska, M.; Murias, M.; Nowak-Sliwiska, P. Beyond mouse cancer models: Three-dimensional human-relevant in vitro and non-mammalian in vivo models for photodynamic therapy. *Mutation research* **2017**, *773*, 242-262, doi:10.1016/j.mrrev.2016.09.002.
 32. Letrado, P.; de Miguel, I.; Lamberto, I.; Díez-Martínez, R.; Oyarzabal, J. Zebrafish: Speeding Up the Cancer Drug Discovery Process. *Cancer Res* **2018**, *78*, 6048-6058, doi:10.1158/0008-5472.can-18-1029.
 33. Xiao, J.; Glasgow, E.; Agarwal, S. Zebrafish Xenografts for Drug Discovery and Personalized Medicine. *Trends in cancer* **2020**, 10.1016/j.trecan.2020.03.012, doi:10.1016/j.trecan.2020.03.012.
 34. Amatruda, J.F.; Shepard, J.L.; Stern, H.M.; Zon, L.I. Zebrafish as a cancer model system. *Cancer Cell* **2002**, *1*, 229-231, doi:10.1016/s1535-6108(02)00052-1.
 35. Zhang, X.; de Boer, L.; Heiligers, L.; Man-Bovenkerk, S.; Selbo, P.K.; Drijfhout, J.W.; Høgset, A.; Zaat, S.A.J. Photochemical internalization enhances cytosolic release of antibiotic and increases its efficacy against staphylococcal infection. *Journal of controlled release : official journal of the Controlled Release Society* **2018**, *283*, 214-222, doi:10.1016/j.jconrel.2018.06.004.
 36. Mauriello Jimenez, C.; Aggad, D.; Croissant, J.G.; Tresfield, K.; Laurencin, D.; Berthomieu, D.; Cubedo, N.; Rossel, M.; Alsaïari, S.; Anjum, D.H., et al. Porous Porphyrin-Based Organosilica Nanoparticles for NIR Two-Photon Photodynamic Therapy and Gene Delivery in Zebrafish. *Advanced Functional Materials* **2018**, *28*, 1800235, doi:10.1002/adfm.201800235.

37. Matera, C.; Gomila, A.M.J.; Camarero, N.; Libergoli, M.; Soler, C.; Gorostiza, P. Photoswitchable Antimetabolite for Targeted Photoactivated Chemotherapy. *Journal of the American Chemical Society* **2018**, *140*, 15764-15773, doi:10.1021/jacs.8b08249.
38. Bouchaala, R.; Anton, N.; Anton, H.; Vandamme, T.; Vermot, J.; Smail, D.; Mély, Y.; Klymchenko, A.S. Light-triggered release from dye-loaded fluorescent lipid nanocarriers in vitro and in vivo. *Colloids and surfaces. B, Biointerfaces* **2017**, *156*, 414-421, doi:10.1016/j.colsurfb.2017.05.035.
39. He, J.; Wang, Y.; Missinato, M.A.; Onuoha, E.; Perkins, L.A.; Watkins, S.C.; St Croix, C.M.; Tsang, M.; Bruchez, M.P. A genetically targetable near-infrared photosensitizer. *Nature methods* **2016**, *13*, 263-268, doi:10.1038/nmeth.3735.
40. Li, S.P.; Lau, C.T.; Louie, M.W.; Lam, Y.W.; Cheng, S.H.; Lo, K.K. Mitochondria-targeting cyclometalated iridium(III)-PEG complexes with tunable photodynamic activity. *Biomaterials* **2013**, *34*, 7519-7532, doi:10.1016/j.biomaterials.2013.06.028.
41. Manghnani, P.N.; Wu, W.; Xu, S.; Hu, F.; Teh, C.; Liu, B. Visualizing Photodynamic Therapy in Transgenic Zebrafish Using Organic Nanoparticles with Aggregation-Induced Emission. *Nano-micro letters* **2018**, *10*, 61, doi:10.1007/s40820-018-0214-4.
42. Bai, C.; Tang, M. Toxicological study of metal and metal oxide nanoparticles in zebrafish. *Journal of applied toxicology : JAT* **2020**, *40*, 37-63, doi:10.1002/jat.3910.
43. Wehmas, L.C.; Anders, C.; Chess, J.; Punnoose, A.; Pereira, C.B.; Greenwood, J.A.; Tanguay, R.L. Comparative Metal Oxide Nanoparticle Toxicity Using Embryonic Zebrafish. *Toxicology reports* **2015**, *2*, 702-715, doi:10.1016/j.toxrep.2015.03.015.
44. Gutiérrez-Lovera, C.; Martínez-Val, J.; Cabezas-Sainz, P.; López, R.; Rubiolo, J.A.; Sánchez, L. In vivo toxicity assays in zebrafish embryos: a pre-requisite for xenograft preclinical studies. *Toxicology mechanisms and methods* **2019**, *29*, 478-487, doi:10.1080/15376516.2019.1611980.
45. Das, B.C.; McCormick, L.; Thapa, P.; Karki, R.; Evans, T. Use of zebrafish in chemical biology and drug discovery. *Future medicinal chemistry* **2013**, *5*, 2103-2116, doi:10.4155/fmc.13.170.
46. Zon, L.I.; Peterson, R.T. In vivo drug discovery in the zebrafish. *Nature reviews. Drug discovery* **2005**, *4*, 35-44, doi:10.1038/nrd1606.
47. Cuello-Garibo, J.A.; Meijer, M.S.; Bonnet, S. To cage or to be caged? The cytotoxic species in ruthenium-based photoactivated chemotherapy is not always the metal. *Chem Commun (Camb)* **2017**, *53*, 6768-6771, doi:10.1039/c7cc03469e.
48. Reisner, E.; Abikoff, T.C.; Lippard, S.J. Influence of steric hindrance on the core geometry and sulfoxidation chemistry of carboxylate-rich diiron(II) complexes. *Inorganic chemistry* **2007**, *46*, 10229-10240, doi:10.1021/ic7014176.
49. Bahreman, A.; Cuello-Garibo, J.A.; Bonnet, S. Yellow-light sensitization of a ligand photosubstitution reaction in a ruthenium polypyridyl complex covalently bound to a rhodamine dye. *Dalton transactions (Cambridge, England : 2003)* **2014**, *43*, 4494-4505, doi:10.1039/c3dt52643g.
50. Nareyeck, G.; Wuestemeyer, H.; von der Haar, D.; Anastassiou, G. Establishment of two cell lines derived from conjunctival melanomas. *Experimental eye research* **2005**, *81*, 361-362, doi:10.1016/j.exer.2005.04.018.
51. Keijser, S.; Maat, W.; Missotten, G.S.; de Keizer, R.J. A new cell line from a recurrent conjunctival melanoma. *The British journal of ophthalmology* **2007**, *91*, 1566-1567, doi:10.1136/bjo.2006.110841.
52. Luyten, G.P.; Naus, N.C.; Mooy, C.M.; Hagemeyer, A.; Kan-Mitchell, J.; Van Drunen, E.; Vuzevski, V.; De Jong, P.T.; Luiders, T.M. Establishment and characterization of primary and metastatic uveal melanoma cell lines. *International journal of cancer* **1996**, *66*, 380-387, doi:10.1002/(sici)1097-0215(19960503)66:3<380::aid-ijc19>3.0.co;2-f.
53. Chen, P.W.; Murray, T.G.; Uno, T.; Salgaller, M.L.; Reddy, R.; Ksander, B.R. Expression of MAGE genes in ocular melanoma during progression from primary to metastatic disease. *Clinical & experimental metastasis* **1997**, *15*, 509-518, doi:10.1023/a:1018479011340.
54. Carlotti, F.; Bazuine, M.; Kekarainen, T.; Seppen, J.; Pognonec, P.; Maassen, J.A.; Hoeben, R.C. Lentiviral vectors efficiently transduce quiescent mature 3T3-L1 adipocytes. *Molecular therapy : the journal of the American Society of Gene Therapy* **2004**, *9*, 209-217, doi:10.1016/j.ymthe.2003.11.021.

55. Schatzschneider, U.; Niesel, J.; Ott, I.; Gust, R.; Alborzina, H.; Wölfl, S. Cellular Uptake, Cytotoxicity, and Metabolic Profiling of Human Cancer Cells Treated with Ruthenium(II) Polypyridyl Complexes [Ru(bpy)₂(N N)]Cl₂ with N N=bpy, phen, dpq, dppz, and dppn. *ChemMedChem* **2008**, *3*, 1104-1109, doi:10.1002/cmdc.200800039.
56. Hopkins, S.L.; Siewert, B.; Askes, S.H.; Veldhuizen, P.; Zwier, R.; Heger, M.; Bonnet, S. An in vitro cell irradiation protocol for testing photopharmaceuticals and the effect of blue, green, and red light on human cancer cell lines. *Photochemical & photobiological sciences : Official journal of the European Photochemistry Association and the European Society for Photobiology* **2016**, *15*, 644-653, doi:10.1039/c5pp00424a.
57. Chen, Q.; Ramu, V.; Aydar, Y.; Groenewoud, A.; Zhou, X.Q.; Jager, M.J.; Cole, H.; Cameron, C.G.; McFarland, S.A.; Bonnet, S., et al. TLD1433 Photosensitizer Inhibits Conjunctival Melanoma Cells in Zebrafish Ectopic and Orthotopic Tumour Models. *Cancers* **2020**, *12*, doi:10.3390/cancers12030587.
58. Lawson, N.D.; Weinstein, B.M. In vivo imaging of embryonic vascular development using transgenic zebrafish. *Dev Biol* **2002**, *248*, 307-318, doi:10.1006/dbio.2002.0711.
59. Burke, C.S.; Keyes, T.E. An efficient route to asymmetrically dicationic tris(heteroleptic) complexes of Ru(II). *RSC Advances* **2016**, *6*, 40869-40877, doi:10.1039/C6RA06086B.
60. Mari, C.; Pierroz, V.; Rubbiani, R.; Patra, M.; Hess, J.; Spingler, B.; Oehninger, L.; Schur, J.; Ott, I.; Salassa, L., et al. DNA Intercalating Ru(II) Polypyridyl Complexes as Effective Photosensitizers in Photodynamic Therapy. *Chemistry-a European Journal* **2014**, *20*, 14421-14436, doi:10.1002/chem.201402796.
61. Frei, A.; Rubbiani, R.; Tubafard, S.; Blacque, O.; Anstaett, P.; Felgentrager, A.; Maisch, T.; Spiccia, L.; Gasser, G. Synthesis, Characterization, and Biological Evaluation of New Ru(II) Polypyridyl Photosensitizers for Photodynamic Therapy. *Journal of Medicinal Chemistry* **2014**, *57*, 7280-7292, doi:10.1021/jm500566f.
62. Shi, G.; Monro, S.; Hennigar, R.; Colpitts, J.; Fong, J.; Kasimova, K.; Yin, H.; DeCoste, R.; Spencer, C.; Chamberlain, L., et al. Ru(II) dyads derived from α -oligothiophenes: A new class of potent and versatile photosensitizers for PDT. *Coordination Chemistry Reviews* **2015**, *282-283*, 127-138, doi:<http://dx.doi.org/10.1016/j.ccr.2014.04.012>.
63. Garcia-Fresnadillo, D.; Georgiadou, Y.; Orellana, G.; Braun, A.M.; Oliveros, E. Singlet-Oxygen (¹Δg) Production by Ruthenium(II) complexes containing polyazaheterocyclic ligands in methanol and in water. *Helvetica Chimica Acta* **1996**, *79*, 1222-1238, doi:10.1002/hlca.19960790428.
64. Moan, J.; Sommer, S. Oxygen dependence of the photosensitizing effect of hematoporphyrin derivative in NHIK 3025 cells. *Cancer Res* **1985**, *45*, 1608-1610.
65. Bonnett, R. *Studies on 5,10,15,20-tetrakis(m-hydroxyphenyl)chlorin, mTHPC (Temoporfin)*; SPIE: 1995; Vol. 2371.
66. Arenas, Y.; Monro, S.; Shi, G.; Mandel, A.; McFarland, S.; Lilge, L. Photodynamic inactivation of Staphylococcus aureus and methicillin-resistant Staphylococcus aureus with Ru(II)-based type I/type II photosensitizers. *Photodiagnosis and photodynamic therapy* **2013**, *10*, 615-625, doi:10.1016/j.pdpdt.2013.07.001.
67. Hopkins, S.L.; Siewert, B.; Askes, S.H.C.; Veldhuizen, P.; Zwier, R.; Heger, M.; Bonnet, S. An in vitro cell irradiation protocol for testing photopharmaceuticals and the effect of blue, green, and red light on human cancer cell lines. *Photochemical & Photobiological Sciences* **2016**, *15*, 644-653, doi:10.1039/C5PP00424A.
68. Lameijer, L.N.; Ernst, D.; Hopkins, S.L.; Meijer, M.S.; Askes, S.H.C.; Le Dévédec, S.E.; Bonnet, S. A Red-Light-Activated Ruthenium-Caged NAMPT Inhibitor Remains Phototoxic in Hypoxic Cancer Cells. *Angewandte Chemie International Edition* **2017**, *56*, 11549-11553, doi:10.1002/anie.201703890.
69. Horobin, R.W.; Stockert, J.C.; Rashid-Doubell, F. Fluorescent cationic probes for nuclei of living cells: why are they selective? A quantitative structure-activity relations analysis. *Histochemistry and Cell Biology* **2006**, *126*, 165-175, doi:10.1007/s00418-006-0156-7.
70. Puckett, C.A.; Barton, J.K. Methods to Explore Cellular Uptake of Ruthenium Complexes. *Journal of the American Chemical Society* **2007**, *129*, 46-47, doi:10.1021/ja0677564.
71. Pettaway, C.A.; Pathak, S.; Greene, G.; Ramirez, E.; Wilson, M.R.; Killion, J.J.; Fidler, I.J. Selection of highly metastatic variants of different human prostatic carcinomas using orthotopic implantation in nude mice. *Clinical Cancer Research* **1996**, *2*, 1627-1636.

72. van Rixel, V.H.S.; Siewert, B.; Hopkins, S.L.; Askes, S.H.C.; Busemann, A.; Siegler, M.A.; Bonnet, S. Green light-induced apoptosis in cancer cells by a tetrapyridyl ruthenium prodrug offering two trans coordination sites. *Chemical science* **2016**, *7*, 4922-4929, doi:10.1039/c6sc00167j.
73. Hill, D.; Chen, L.; Snaar-Jagalska, E.; Chaudhry, B. Embryonic zebrafish xenograft assay of human cancer metastasis. *F1000Research* **2018**, *7*, 1682, doi:10.12688/f1000research.16659.2.
74. van der Ent, W.; Burrello, C.; Teunisse, A.F.; Ksander, B.R.; van der Velden, P.A.; Jager, M.J.; Jochemsen, A.G.; Snaar-Jagalska, B.E. Modeling of human uveal melanoma in zebrafish xenograft embryos. *Investigative ophthalmology & visual science* **2014**, *55*, 6612-6622, doi:10.1167/iovs.14-15202.
75. Drabsch, Y.; He, S.; Zhang, L.; Snaar-Jagalska, B.E.; ten Dijke, P. Transforming growth factor- β signalling controls human breast cancer metastasis in a zebrafish xenograft model. *Breast Cancer Res* **2013**, *15*, R106-R106, doi:10.1186/bcr3573.
76. Murayama, E.; Kissa, K.; Zapata, A.; Mordelet, E.; Briolat, V.; Lin, H.-F.; Handin, R.I.; Herbomel, P. Tracing hematopoietic precursor migration to successive hematopoietic organs during zebrafish development. *Immunity* **2006**, *25*, 963-975, doi:10.1016/j.immuni.2006.10.015.
77. Monro, S.; Colón, K.L.; Yin, H.; Roque, J., 3rd; Konda, P.; Gujar, S.; Thummel, R.P.; Lilge, L.; Cameron, C.G.; McFarland, S.A. Transition Metal Complexes and Photodynamic Therapy from a Tumor-Centered Approach: Challenges, Opportunities, and Highlights from the Development of TLD1433. *Chemical reviews* **2019**, *119*, 797-828, doi:10.1021/acs.chemrev.8b00211.
78. Wang, G.; Zhao, D.; Spring, D.J.; DePinho, R.A. Genetics and biology of prostate cancer. *Genes Dev* **2018**, *32*, 1105-1140, doi:10.1101/gad.315739.118.

Supporting information for

Photosubstitution in a new trisheteroleptic ruthenium complex inhibits conjunctival melanoma growth in zebrafish orthotopic xenograft model

Quanchi Chen ^{1#}, Jordi-Amat Cuello-Garibo ^{2#}, Vadde Ramu ², Yasmin Aydar ¹, Yevhen Batsuin,² Sharon Bronkhorst ², Nataliia Beztsinna ², Lanpeng Chen ¹, Xue-Quan Zhou ², Claudia Schmidt ³, Ingo Ott ³, Martine J. Jager ⁴, B. Ewa Snaar-Jagalska ^{1*}, Sylvestre Bonnet ^{2*}

¹ Institute of Biology, Leiden University, Leiden, The Netherlands

² Leiden Institute of Chemistry, Leiden University, P.O. Box 9502, 2300 RA Leiden, The Netherlands

³ Institute of Medicinal and Pharmaceutical Chemistry, Technische Universität Braunschweig, Beethovenstrasse 55, D-38106 Braunschweig, Germany

⁴ Department of Ophthalmology, Leiden University Medical Center, Leiden, The Netherlands

These authors contributed equally to the paper

* Correspondence: b.e.snaar-jagalska@biology.leidenuniv.nl ; Tel.: +31-71-527-4980 (E.S.J.); bonnet@chem.leidenuniv.nl ; Tel : +31-71-527-4260 (S.B.);

QUANTUM YIELD DETERMINATION

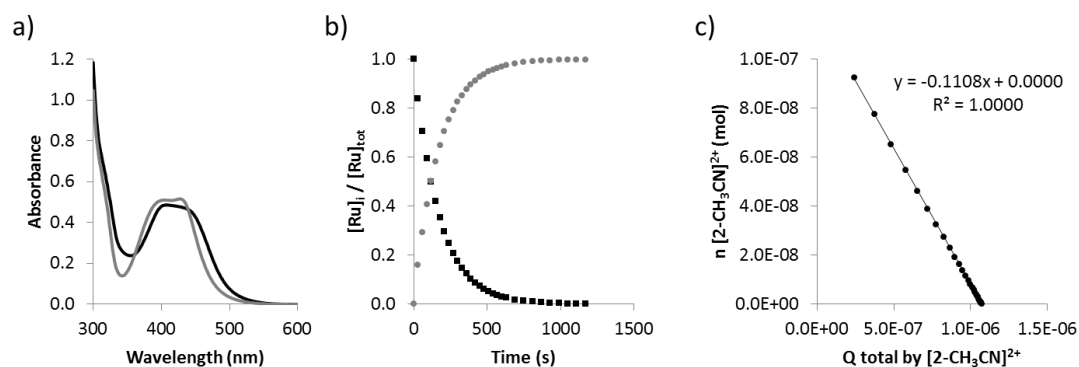


Figure S1 Kinetic data for the second step of the photosubstitution of $[2](PF_6)_2$ in CH_3CN under N_2 . a) Globally fitted absorption spectra of the mono-aqua intermediate $[Ru(dpp)(bpy)(\eta^1\text{-mtmp})(CH_3CN)]$ ($[2-CH_3CN]$, black) and $[Ru(dpp)_2(CH_3CN)_2]^{2+}$ (grey) according to modeling using the Glotaran software. b) Modeled evolution of the relative concentrations of $[2-CH_3CN]^{2+}$ (squares) and $[Ru(dpp)_2(CH_3CN)_2]^{2+}$ (circles) vs. irradiation time according to global fitting using Glotaran. c) Plot of the amount of $[2-CH_3CN]^{2+}$ (mol) vs. total amount of photons absorbed by $[2-CH_3CN]^{2+}$ (mol). The slope of the obtained line is the opposite of the quantum yield of the formation of the bis-aqua complex. Conditions: 0.036 mM solution of $[2](PF_6)_2$ in CH_3CN irradiated at 298 K under N_2 using a 521 nm LED at $6.21 \cdot 10^{-8} \text{ mol} \cdot \text{s}^{-1}$.

DOSE-RESPONSE CURVES IN CONJUNCTIVE MELANOMA, UVEAL MELANOMA AND PROSTATE CANCER CELL LINES

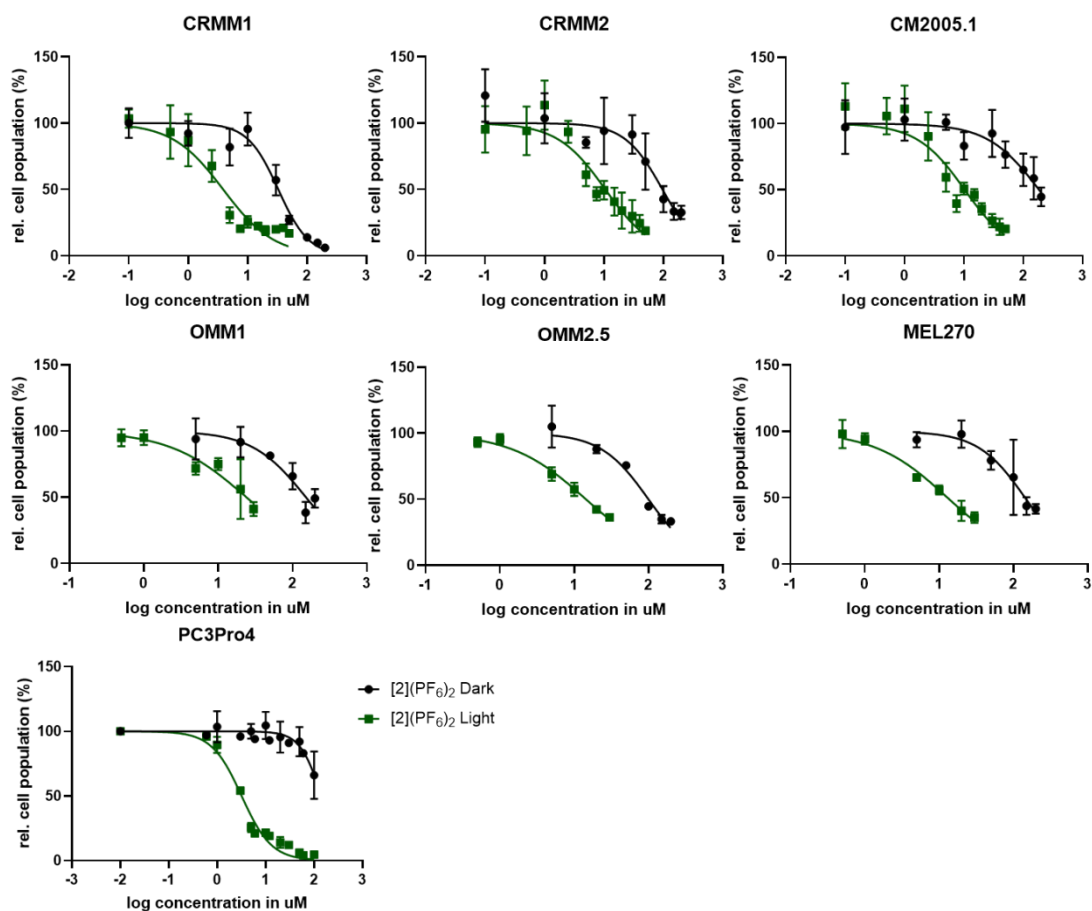


Figure S2 Dose-response curves for CRMM1, CRMM2, CM2005.1, OMM1, OMM2.5, MEL270 and PC3Pro4 cells treated with [2](PF₆)₂ and irradiated with green light (520 nm, 21 mW/cm², 19 J.cm⁻²) 24 h after treatment (green data points) or left in the dark (black data points). SRB assay was carried out at t=96 h. The absorbance of Sulforhodamine B in solution was measured at 520 nm. Results are presented as means ± SD from three independent experiments.

ANNEXIN V-PI ASSAY

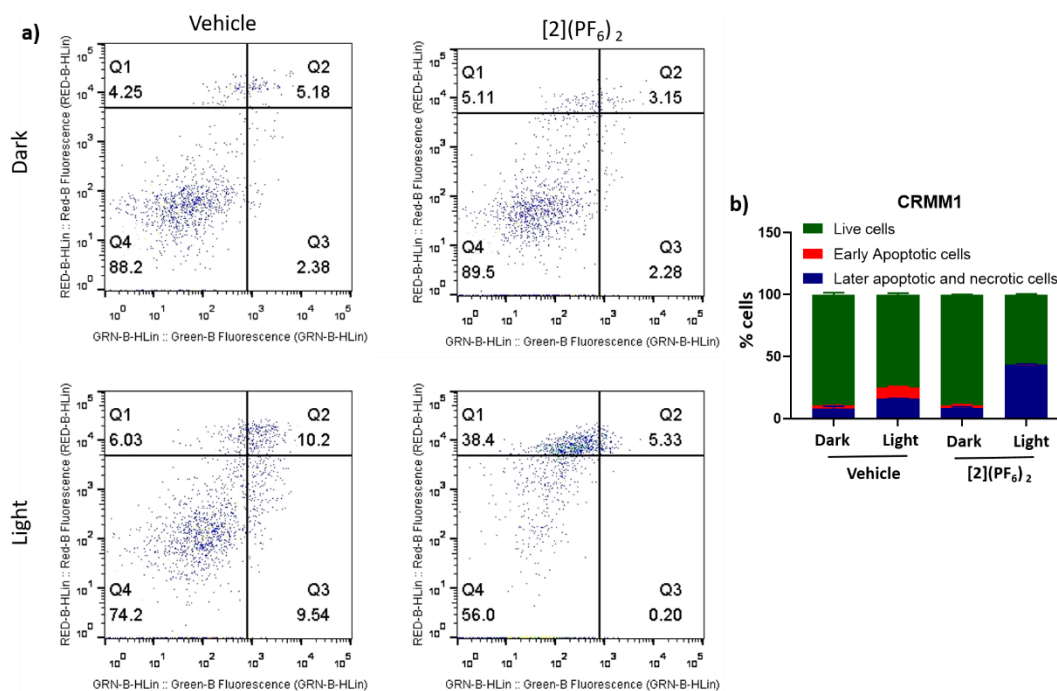


Figure S3 Green light irradiation of [2](PF₆)₂ induces apoptosis and necrosis in CRMM1 cells. 4.3 μM of [2](PF₆)₂ was added into the medium of CRMM1 cells. After 24 h, [2](PF₆)₂ was washed by new free-drug medium and 15 min of green light (21 mW/cm², 19 J.cm⁻², 520 nm) was performed. After treatment, the cells were incubated for another 48 h. **a)** CRMM1 cells were stained with Annexin-V-FITC and Propidium Iodide. **b)** The percentages of live, early apoptotic, later apoptotic and necrotic cells in CRMM1 were counted by FACS. Results are presented as means ± SD from three independent experiments.

MAXIMUM TOLERATED DOSE DETERMINATION

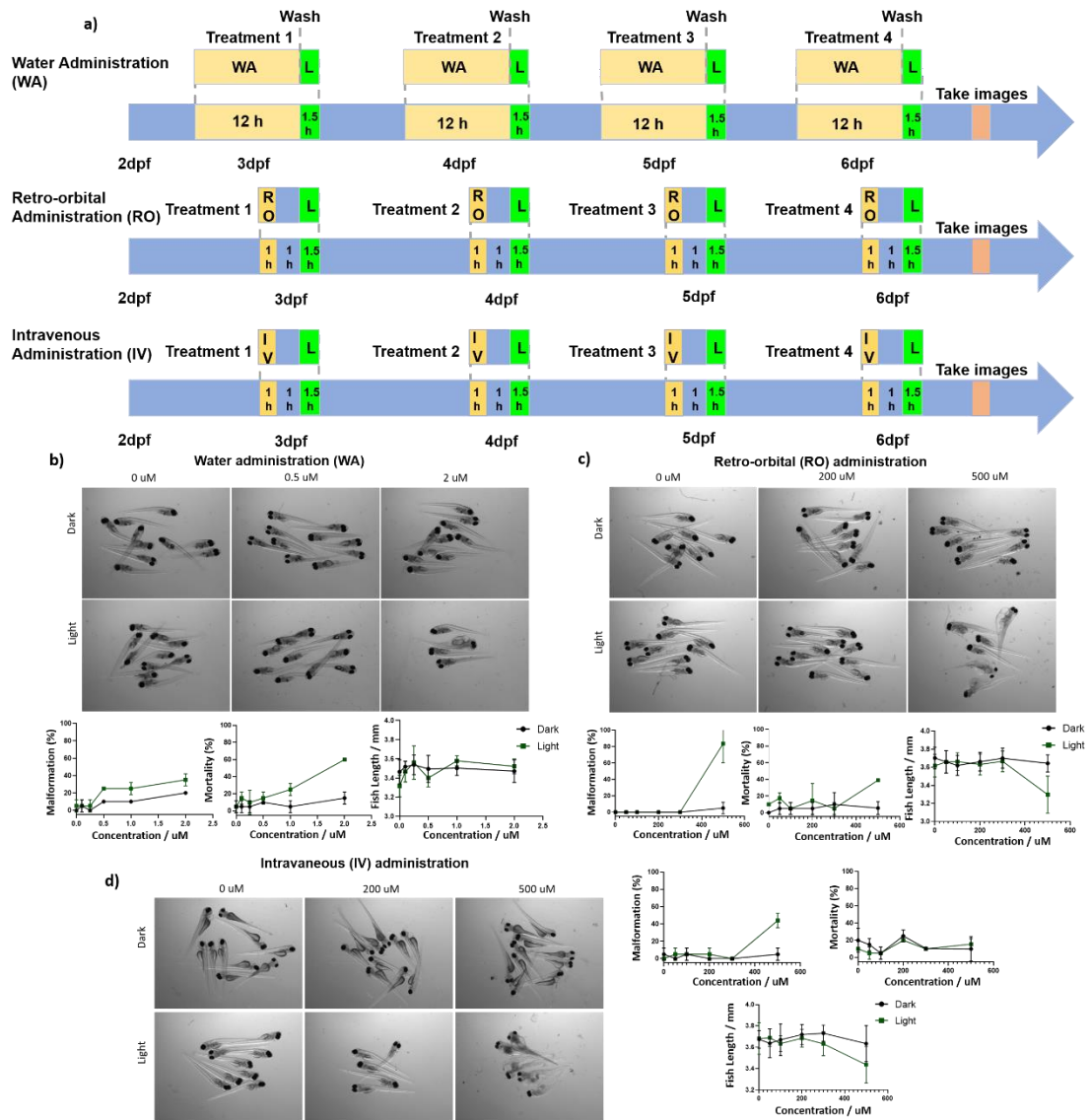


Figure S4 The maximum tolerated dose of $[2](PF_6)_2$ in wild type zebrafish embryos administered through three different routes. **a)** Schedule of $[2](PF_6)_2$ treatment in wild type zebrafish. Water administration (WA): $[2](PF_6)_2$ (0 μ M, 0.1 μ M, 0.25 μ M, 0.5 μ M, 1 μ M, 2 μ M) were added to the water containing 10 embryos per well at 2.5, 3.5, 4.5, 5.5 dpf, for 12h (yellow box). After these treatments, the drug was removed and replaced by egg water followed by 90 min green light irradiation (21 mW/cm², 114 J.cm⁻², 520 nm), depicted as a green lightning bolt. Intravenous injection (IV) or retro-orbital injection (RO): 1 nL of $[2](PF_6)_2$ (0 μ M, 50 μ M, 100 μ M, 200 μ M, 300 μ M, 500 μ M) were injected into the embryos at 3 dpf to 6 dpf every morning, followed by 60 min drug-to-light interval (yellow box) and 90 min green light irradiation (21 mW/cm², 114 J.cm⁻², 520 nm), depicted as a green lightning bolt. **b)** WA, **c)** RO, **d)** IV. **b-d)** Images were made of irradiated (light) and non-irradiated (dark) embryos (n=30) at 6dpf and the percentages of mortality, malformation and fish length were calculated (shown as means \pm SD from three independent experiments). Representative images of embryos under dark and light conditions are shown.

Chapter 5

Light triggered, cancer cell-specific targeting and liposomal drug delivery in a zebrafish xenograft model

Li Kong¹⊥, Quanchi Chen²⊥, Frederick Campbell¹, Ewa Snaar-Jagalska^{2*} and Alexander Kros^{1*}

⊥ **Authors contributed equally**

¹Supramolecular and Biomaterials Chemistry, Leiden Institute of Chemistry, Leiden University, Einsteinweg 55, 2333 CC Leiden, The Netherlands

²Institute of Biology, Leiden University, Leiden 2311 EZ, The Netherlands

E-mail: a.kros@chem.leidenuniv.nl, b.e.snaar-jagalska@biology.leidenuniv.nl

Published in: Advanced Healthcare Materials 2020, 9, 1901489; doi: 10.1002

Keywords: cancer nanomedicine, liposomes, light activation, *in vivo*, embryonic zebrafish

Abstract

Cell-specific drug delivery remains a major unmet challenge for cancer nanomedicines. Here, we demonstrate light-triggered, cell-specific delivery of liposome-encapsulated doxorubicin to xenograft human cancer cells in live zebrafish embryos. Our method relies on light triggered dePEGylation of liposome surfaces to reveal underlying targeting functionality. To demonstrate general applicability of our method, we show light triggered, MDA-MB-231 breast cancer cell specific targeting *in vivo* (embryonic zebrafish) using both clinically relevant, folate-liposomes, as well as an experimental liposome-cell fusion system. In the case of liposome-cell fusion, delivery of liposomal doxorubicin direct to the cytosol of target cancer cells resulted in enhanced cytotoxicity, compared to doxorubicin delivery *via* either folate-liposomes or free doxorubicin, as well as a significant reduction in xenograft cancer cell burden within the embryonic fish.

Introduction

The majority (5 of 7) of clinically approved, *targeted* nanomedicines are liposomal formulations used to treat various human cancers [1,2]. All function through passive targeting of solid tumors *via* the enhanced permeability and retention (EPR) effect – a phenomenon characterized by the ill-defined (“leaky”) vasculature and poor lymphatic drainage of select solid tumors [3,4]. To maximize passive targeting to solid tumors, PEGylation of nanoparticle surfaces is a long-standing strategy to reduce serum protein absorption, limit nanoparticle recognition and clearance by the reticulo-endothelial system (RES) in the liver and spleen, and prolong circulation lifetimes [5,6]. Once passively accumulated within the target tumor, however, drugs must be released from a nanoparticle at effective therapeutic concentrations (typically cytotoxic concentrations). In the case of Doxil® (PEGylated liposomal doxorubicin) – the first clinically approved, targeted cancer nanomedicine – extracellular drug release relies on passive diffusion of doxorubicin across the liposome membrane. To maximise free drug concentrations within targeted tumors, methods to actively load very high concentrations of doxorubicin within liposomes have been developed [7]. Despite this, the superiority of clinically approved liposomal doxorubicin formulations, over administered free doxorubicin, remains contentious. It is now generally accepted that improved toxicological profiles, rather than improved efficacy, constitute the main pharmacological benefit of liposomal-doxorubicin formulations (over administration of the free drug).

A potentially more effective strategy to treat cancer is to promote cellular uptake of drug-filled nanomedicines within cancer cells. This is most commonly attempted through the display of active targeting moieties (e.g. RGD, folate) from a nanoparticle surface [8,9]. However, active targeting strategies to promote cellular uptake of nanoparticles typically conflict with strategies employed to prolong circulation lifetimes. Most notably, the extremely limited cellular uptake of PEGylated nanoparticles hinders efficient intracellular drug delivery to cancer cells [10]. To overcome this PEG

dilemma, stimuli-responsive dePEGylation of nanoparticles within the target tumor has been investigated [11,12]. In the majority of cases, dePEGylation is triggered by an endogenous stimuli (low pH [13], matrix metalloproteinases [14]), exploiting pathophysiological differences between healthy and tumor tissues. However, suboptimal cleavage conditions/rates – common pH-sensitive groups (*e.g.* hydrazones, acetals and benzoic imines) are optimally sensitive at pH <6, whereas the tumor microenvironment is generally pH >6.5 [15]– typically lead to inefficient drug release profiles. Alternatively, dePEGylation of a nanoparticle can be triggered by an external stimuli, *e.g.* light [12]. In this way, nanoparticle activation can be localized with very high spatiotemporal resolution, including deep within tissue. Two photon excitation sources, for example, can be used to focus light within femtoliter (fL) volumes at tissue depths of up to 1 cm [16,17], while deeper tissues/pathologies can be accessed using fibre optic LEDs or injectable microLEDs [18-20]. Although the use of light to dePEGylate nanomedicines has mainly been used to trigger *extracellular* drug release from a nanocarrier [21-26], enhanced tumor targeting and active cellular uptake of dual responsive polymersomes following light activation has recently been reported [27]. In this case, near-infrared (NIR) light was used in combination with upconverting nanoparticles (UCNPs) to achieve efficient nanoparticle dePEGylation deep within a murine xenograft tumor.

Herein, we show light-triggered and cell specific targeting of doxorubicin-filled liposomes to xenograft breast cancer cells in live embryonic zebrafish. Our method relies on responsive dePEGylation of a liposome surface, *in situ* and *in vivo*, to reveal underlying, active targeting functionality tethered to the liposome surface. To demonstrate the general applicability of this approach, we show light-triggered targeting of liposomal-doxorubicin formulations to cancer cells using both clinically relevant, folate-decorated liposomes (F-liposomes, targeting the overexpressed folate receptor on xenograft MDA-MB-231 cells [28,29]), as well as an experimental, two component (peptide E and K) fusion system that promotes direct fusion of liposome and cell membranes, with concurrent cytosolic delivery of encapsulated liposomal content (**Figure 1**) [30]. For the fusion system, liposome-cell interactions rely on the recognition and binding of two coiled-coil forming peptides – peptide E (*amino acid sequence*: (EIAALEK)_n) and peptide K (*amino acid sequence*: (KIAALKE)_n) – tethered to opposing lipid membranes [31]. For this system to work, target cancer cell membranes must, therefore, first be enriched with the synthetic lipopeptide CPK (cholesterol-PEG₄-peptide K, see **Scheme S1** for chemical structure) to form K-functionalised cells. Once engrafted *in vivo*, these cells can recognize, bind to and fuse with circulating liposomes whose membranes are enriched with the complementary lipopeptide, CPE (cholesterol-PEG₄-peptide E, see **Scheme S1** for chemical structure). Crucially, prior to light-triggered dePEGylation, both PEGylated E- and PEGylated F-liposomes freely circulated throughout the vasculature of the embryonic fish and did not interact either with xenograft cancer cells or key RES cell types of the embryo.

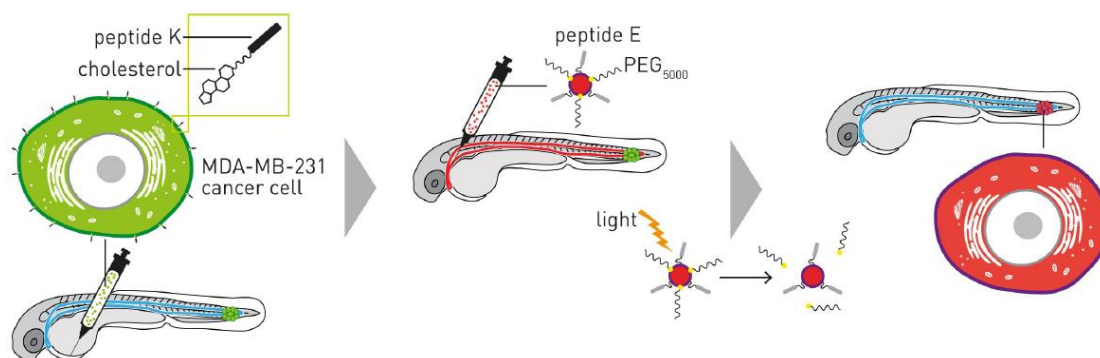


Figure 1 Light-triggered, cancer-cell specific liposome-cell fusion in xenograft zebrafish embryos. Human cancer cells are first pre-functionalised with cholesterol-peptide K4 in vitro. Functionalised cancer cells are then injected into the circulation (via the Duct of Cuvier) of 2-day old zebrafish embryos. Xenograft cancer cells quickly accumulate within the caudal hematopoietic tissue (CHT) of the embryo. One hour after cancer cell injection, EPEG-liposomes are injected into circulation via the posterior caudal vein (PCV). Prior to light triggered dePEGylation, liposomes are confined to the vasculature of the fish and freely circulate. Following UV irradiation and in situ dePEGylation, liposomes rapidly and selectively bind to and fuse with xenograft cancer cells. This interaction is mediated through the recognition of fusogenic peptides E and K displayed from opposing lipid membranes. Liposome-encapsulated cargos (eg. cytotoxic drugs) are delivered directly to the cytosol of the recipient cell.

Materials

1,2-dioleoyl-sn-glycero-3-phosphocholine (DOPC), 1,2-dioleoyl-sn-glycero-3-phosphoethanolamine (DOPE), 1,2-dioleoyl-sn-glycero-3-phosphoethanolamine-N-(7-nitro-2-1,3-benzoxadiazol-4-yl) (DOPE-NBD), 1,2-dioleoyl-sn-glycero-3-phosphoethanolamine-N-(lissamine rhodamine B sulfonyl) (DOPE-LR), 1,2-dipalmitoyl-sn-glycero-3-phosphoethanolamine-N-(6-((folate)amino)hexanoyl) (DPPE-FolateCap) and 1,2-distearoyl-sn-glycero-3-phosphoethanolamine-N-[methoxy(polyethylene glycol)-5000] (ammonium salt) (DSPE-PEG₅₀₀₀) were purchased from Avanti Polar Lipids. 1,2-Dioleoyl-sn-glycero-3-phosphoethanolamine-Atto633 was purchased from ATTO-TEC GmbH (Germany). Cholesterol, doxorubicin hydrochloride (DOX), propidium iodide (PI) and all other chemical reagents were purchased at the highest grade available from Sigma Aldrich and used without further purification. All solvents were purchased from Biosolve Ltd. Phosphate buffered saline (PBS): 5 mM KH₂PO₄, 15 mM K₂HPO₄, 150 mM NaCl, pH 7.4. Lipopeptide constructs – E₄ and K₄ – were synthesized as previously reported [30]. Photolabile cholesterol-PEG constructs – PEG₂₀₀₀ and PEG₅₀₀₀ – were synthesized as previously reported [32].

Light source

A 375-nm LED (Maximum measured wavelength = 370 nm, FWHM = 13.4 nm; H2A1-H375-S, Roithner Lasertechnik, Vienna, Austria), driven by a custom-built LED driver (I = 350 mA), was used as UV light source in all cases except for Figure S2. Irradiation setups, timings, power densities (as determined by

light actinometry) and light doses (for cell and zebrafish experiments) are reported for individual experiments. For monitoring the photolysis of E_{PEG}-liposomes (Figure S2), UV lamp (SUNON lamp SF9225AT; 56.8 W, 50-60 Hz) was used as UV light source.

Liposome formulation and biophysical characterisation

Phospholipids (DOPC:DOPE:cholesterol; 2:1:1), as a stock solution (10 mM) in chloroform, and either lipopeptide E₄ or K₄, as a stock solution (100 μM) in chloroform:methanol (1:1), or DPPE-Folate as a stock solution (100 μM) in chloroform, were mixed to the desired molar ratios and dried to a film, first under a stream of N₂ and then >1h under vacuum. The lipid film was then re-hydrated in PBS and sonicated (Branson 2510 Ultrasonic Cleaner) for 5 min at 55°C to yield E-liposomes, K-liposomes or F-liposomes respectively (1 mol% E/K/folate in all cases).

Post-modification of E- and F-liposomes with photolabile cholesterol-PEG constructs was carried out as previously described [32]. Briefly, for lipid mixing experiments involving E-liposomes, hydrated and sonicated solutions of cholesterol-PEG (2-20 μM) in PBS were added in equal volumes to E-liposomes (200 μM total [lipid]) in PBS and incubated for 30 min to yield E-liposomes (100 μM total [lipid]) with varying mol% cholesterol-PEG displayed from the outer membrane leaflet. For lipid mixing experiments, fluorescent lipid probes (DOPE-NBD and DOPE-LR, 0.5 mol% each) were included within E-liposome formulations.

Hydrodynamic diameters of all liposomes, as measured by dynamic light scattering (DLS; Zetasizer Nano ZS, Malvern Instruments, UK) were approx. 100 nm and polydispersities <0.2. DLS measurements were made at room temperature and at a total lipid concentration of 100μM. For zeta potential measurements (Zetasizer Nano ZS, Malvern Instruments, UK), liposomes were formulated in ddH₂O and diluted in salt (NaCl) solution. Zeta potentials were measured at room temperature, at 500 μM total lipid concentration and 10mM NaCl concentration. All reported DLS measurements and zeta potentials are the average of three measurements. For DLS and zeta potential experiments monitoring changes following light activation, liposomes were irradiated (370 ± 7 nm, 202 mW/cm²) for 15 mins in quartz cuvettes with the LED mounted 1 cm from the sample.

For transmission electron microscopy (TEM) images of EPEG-liposomes and FPEG-liposomes, a drop of liposome solution (1 mM) was placed on a lacey carbon covered TEM copper grid for 3 mins before dabbing dry through the underside of the grid with a tissue. The sample was then washed three times with ddH₂O, Finally, a drop of phosphotungstic acid (TPA, 1% w/v) in H₂O was added and the sample left to dry in the dark. Images were obtained at an accelerating voltage of 100 kV (TEM JEOL 1230 instrument).

Propidium iodide encapsulation within E-liposomes

Propidium iodide (PI) was loaded into E-liposomes *via* passive encapsulation. Briefly, lipid films (1 mM total lipids) were hydrated in PBS containing 15 mM PI and sonicated for 2–3 min in a sonication bath at 55 °C. Un-encapsulated PI was removed through size exclusion chromatography (illustra™ NAP™ Sephadex™ G-25, GE-Healthcare, USA) according to the manufacturer's guidelines. *Final concentration for cell experiments*: liposomes (400 μM total lipids); encapsulated PI (75 μM).

Doxorubicin encapsulation within E- and F-liposomes

Active loading of doxorubicin hydrochloride (DOX) was carried out as previously reported [7]. Briefly, liposomes (10mM total lipid) were formulated (sonication) in sodium citrate buffer (pH 3.5) before being passed through a size exclusion column (illustra™ NAP™ Sephadex™ G-25, GE Healthcare, USA) using PBS buffer (pH 7.4) as eluent to set up a pH gradient across the liposome membrane. Next, DOX (powder) was added to the liposomal solution at a final concentration of 1 mg/mL and incubated overnight at 4 °C. Finally, free DOX was removed by size exclusion chromatography (illustra™ NAP™ Sephadex™ G-25, GE Healthcare, USA). The entrapment efficiency (EE) and drug loading content (DL) of DOX was determined using UV–vis spectrophotometry (Cary 300 UV-Vis, Agilent). Briefly, liposomes were solubilized by addition of Triton X-100 (0.5% v/v), absorption measured at 480nm, and [DOX] calculated against a predetermined DOX calibration curve (free DOX in PBS containing Triton X-100 (0.5% v/v)). The loading efficiency was calculated according to the following equation:

$$EE = \frac{C_{DOX \text{ in liposomes}}}{C_{total}} * 100\%$$

$$DL = \frac{\text{Weight of DOX}}{\text{Weight of liposomes}} * 100\%$$

Where $C_{DOX \text{ in liposomes}}$ is the concentration of DOX determined in the liposomes, C_{total} is the total added concentration of DOX, 'Weight of DOX' is the weight of DOX encapsulated in the liposomes and 'Weight of liposomes' is the weight of liposomes. Unfortunately, active loading of DOX, in this case, did not yield the high reported encapsulation efficiencies (typically >85%) as expected. After final size exclusion column chromatography, E_{PEG}-liposomes (4 mM total lipid concentration) contained 200 μM DOX (5% EE, 4.02% DL), whereas F_{PEG}-liposomes (4 mM total lipid concentration) contained 195 μM DOX (4.8% EE, 3.92% DL).

DOX concentrations for WST in vitro experiments: liposomal-DOX formulations either diluted or concentrated (spin column) to desired [DOX] – ie. 200 μM DOX = 4 mM total lipids; 50 μM DOX = 1mM total lipids.

NOTE: For F-liposomes, total lipid concentrations (and therefore [folate]) are 2.5% higher than for E-liposomes (and [peptide E]) at identical [DOX] to compensate for the slight variation in EE between E- and F-liposomes.

NOTE: where [DOX] <25 μ M and [total lipid] <500 μ M, the concentration of peptide E (1mol%, displayed from the liposome surface) is less than the concentration of peptide K (5 μ M, displayed from the cell membrane).

Final DOX concentrations for in vivo (zebrafish embryo xenograft) experiments: 200 μ M DOX; 4 mM total lipids (40 μ M peptide E).

In vitro DOX release

To monitor the release of DOX from liposomes, 1 mL of DOX loaded liposomes (200 μ M DOX; 4 mM E_{PEG} liposomes or 4.1 mM F_{PEG} liposomes) in PBS were placed in dialysis tubing (MWCO: 3.5 KDa) and dialyzed against 20 mL PBS at 37°C. At various time intervals, 3.0 mL of dialysis buffer was removed and replaced with fresh buffer. The amount of released DOX was quantified by fluorescence emission at 595 nm (Ex = 480 nm) against a predetermined calibration curve (DOX in PBS). The cumulative release was calculated according to the following equation:

$$\text{Cumulative release (\%)} = \frac{C_{\text{cumulative release}}}{C_{\text{total}}} \times 100$$

where $C_{\text{cumulative release}}$ is the cumulative released concentration of DOX in dialysis buffer and C_{total} is the total added concentration of DOX. At each successive timepoint, $C_{\text{cumulative release}}$ was corrected to account for the removed and replaced dialysis buffer of previous timepoints (eg. $C_{\text{cumulative release}}$ (at the 4th time point) = $3(C_{\text{DOX}}$ at the 1st time point + C_{DOX} at the 2nd time point + C_{DOX} at the 3rd time point) + $20(C_{\text{DOX}}$ at the 4th time point)). To monitor light activated release of DOX, liposomes were irradiated (370 ± 7 nm, 202 mW/cm²) for 15 mins in quartz cuvettes, with the LED mounted 1 cm from the sample, before adding to the dialysis tube.

Photolysis of E_{PEG}-liposomes

A solution of E_{PEG}-liposomes (total lipid = 5 mM, 4 mol% PEG₅₀₀₀, 1 mol% of lipopeptide E₄) in PBS was irradiated under the UV lamp (SUNON UV lamp SF9225AT; 56.8 W, 50-60 Hz), for 5 min, followed immediately by acquisition of the UV-visible absorption spectra. The same sample was then re-irradiated and this cycle repeated for cumulative irradiation time points of 10, 20, 30, 40 and 60 min.

Lipid mixing assay

For lipid mixing assays, NBD fluorescence (excitation: 465 nm emission: 530 nm) was measured upon mixing fluorescent E_{PEG}-liposomes and non-fluorescent K-liposomes every 20 s for 3500 s (TECAN Plate Reader Infinite M1000). The 0% value was determined by measuring NBD emission of E_{PEG}-liposomes

to which an equal amount of PBS (in place of K-liposomes) was added. The 100% value was determined using liposomes containing half the fluorescent probe (DOPE-NBD and DOPE-LR) concentrations i.e. 0.25 mol%. The percentage of lipid mixing (%F(t)) was calculated as:

$$\%F(t) = \frac{F(t) - F_0}{F_{\max} - F_0}$$

where F(t) is the fluorescence intensity measured, F₀ is the 0% fluorescence intensity and F_{max} is the 100% fluorescence intensity. For measuring the effects of UV irradiation on the rate of lipid mixing, E_{PEG}-liposomes were irradiated (370 ± 7 nm, 202 mW/cm²) for 15 mins with the LED mounted at a distance of 1 cm from the sample, prior to the addition of K-liposomes.

Cell culture, WST and *in vitro* assays

HeLa cells and MDA-MB-231 breast cancer cells (ATCC), stably expressing GFP (Plasmid #106172; Addgene.org) were cultured in Dulbecco's Modified Eagle's Medium (DMEM)/F12, supplemented with 10% fetal calf serum (FCS, iron supplied), 2% L-glutamine. Cells were cultured in an atmosphere of 5% CO₂ at 37°C. Medium was refreshed every two days and cells passaged at 70% confluence by treatment with trypsin-EDTA (0.05% trypsin).

For *in vitro* assays (Figure 2b), HeLa cells (1x10⁵ mL⁻¹) were transferred to 8-well cell culture plates (300 µL, µ-Slide 8 Well, Ibidi GmbH) and cultured for a further 24 h. A solution of lipopeptide K₄ (5 µM in DMEM + 10% FCS; prepared by sonication, 5 min, 55°C, Branson 2510 Ultrasonic Cleaner), was added (300 µL) to cells and incubated for 2 h at 37 °C. The lipopeptide K₄ solution was carefully removed and cells washed (3 x PBS). E_{PEG}-liposomes (300 µL, 400 µM, 8 mol% PEG₂₀₀₀ or 4 mol% PEG₅₀₀₀, 1 mol% DOPE-NBD) in PBS, with encapsulated PI (75 µM), were then added to cells and incubated at 37 °C for 20 min. Cells were then washed (3 x DMEM+FCS) and immediately imaged by confocal microscopy (Leica TCS SP8, Solms, Germany; *wavelengths*: NBD-DOPE: Ex/Em: 455/530 nm (Ex laser: 488 nm), propidium iodide: Ex/Em: 535/617 nm (Ex laser: 543 nm). For light triggered membrane fusion, E_{PEG}-liposomes (300 µL, 400 mM, 4 mol% PEG₅₀₀₀) were added to cells and irradiated (15 mins, 370 ± 7 nm, 50.6 mW/cm², *light dose* = 45.5 J/cm²) from directly above (2cm) the well plate. Following irradiation, cells were incubated for a further 20 min, washed (3 x DMEM+FCS) and imaged. To demonstrate spatial control over liposome-cell membrane fusion, E_{PEG}-liposomes (300 µL, 400 µM, 4 mol% PEG₅₀₀₀) were added cells, the well plate half covered with aluminum foil and irradiation applied as above. Following incubation at 37 °C for 20 min, cells were carefully washed (3 x DMEM+FCS) and confocal imaging performed across the boundary of the (now removed) aluminium foil.

For WST cell proliferation assays, MDA-MB-231 cells were seeded in 96-well plates (10,000 cells per well) and incubated overnight. For E-liposome experiments, lipopeptide-K solution (5 µM, 100 µL,

DMEM+FCS) was added to cells, incubated for 2 h and washed away (3 x PBS). For F-liposomes, cells were simply washed with PBS prior to addition of liposomes. To the cells were then added either solutions of free DOX (100 μ L, varying concentrations in 1:1 PBS:DMEM+FCS), E_{PEG}-liposomes or F_{PEG}-liposomes, both containing DOX (100 μ L varying liposome/DOX concentrations in 1:1 PBS:DMEM+FCS) and incubated for 2 h. For the '+UV' liposome samples, cells were irradiated (15 mins, 370 \pm 7 nm, 50.6 mW/cm², *light dose* = 45.5 J/cm²) immediately after sample addition to cells. Following incubation, cells were washed (3 x DMEM+FCS), re-suspended in DMEM+FCS and incubated for a further 24 h. Cell media was then removed and 100 μ L Cell Proliferation Reagent, WST-1 (Sigma) added to each well. Cells were incubated for a further 3 h, according to the supplier guidelines. To determine cell viability, absorbance at 450 nm was measured. All experiments were carried out in quadruplicate.

Zebrafish experiments

Zebrafish (*Danio rerio*, strain AB/TL) were maintained and handled according to the guidelines from the Zebrafish Model Organism Database (<http://zfin.org>) and in compliance with the directives of the local animal welfare committee of Leiden University. Fertilization was performed by natural spawning at the beginning of the light period, and eggs were raised at 28.5 °C in egg water (60 μ g/mL Instant Ocean sea salts). At 24 hours post-fertilization (hpf), 0.2 mM N-phenylthiourea was added to the egg water to prevent malanization. At 2 days post-fertilisation (dpf), embryos were anaesthetized with 0.01% tricaine and embedded in 0.4% agarose containing tricaine prior to microinjection. In addition to WT embryos, the established zebrafish line *Tg(kdrl:GFP/mpeg1:GAL4^{el24}/UAS-E1b:nfsB-mCherryⁱ¹⁴⁹)* [33] was also used (Figure 3a).

For biodistribution studies in zebrafish embryos, MDA-MB-231 cells (2 x 10⁶) were suspended in (PBS/EDTA), pelleted (5 min, 1200 rpm), washed (PBS), pelleted again and finally re-suspended in 2% PVP in PBS (10 μ L) ready for injection. Suspended cells were loaded in a glass capillary needle, prepared using a Flaming/Brown micropipette puller (model P-99, HEAT=496, PULL=95, VEL.=60, TIME=90, Sutter Instrument Co.) Forceps were used to cut the end of the needles and the exposure time and gas pressure were adjusted in order to inject around 300 cells. Cells were engrafted into the circulation of a 2-day old embryo, *via* the Duct of Cuvier. In the case of E-liposome experiments, MDA-MB 231 cells were pretreated with lipopeptide-K, as for *in vitro* assays. One hour after engraftment, E_{PEG}- or F_{PEG}-liposomes (1 mM, 3 nL, 4mol% PEG₅₀₀₀, 1mol% DOPE-LR) in PBS were injected into circulation *via* the posterior cardinal vein. Embryos were kept at 34 °C. For *in situ* UV irradiation (15 mins, 370 \pm 7 nm, 13.5 mW/cm², *light dose* = 0.45 J/embryo), the LED light source was positioned directly above (3 cm) the embryo in agarose. Images were taken 45 min after liposome injection using either a Leica MZ16FA fluorescent microscope coupled to a DFC420C camera or Leica TCS SPE confocal microscope. Wavelength settings for GFP Ex: 488 nm, Em: 500-550 nm and for rhodamine Ex laser: 552 nm, Ex laser: 570-650 nm. Images were processed and quantified using the Fiji distribution of ImageJ [34].

For doxorubicin delivery in zebrafish embryos, 3 nL doxorubicin-filled E_{PEG}-liposomes (4 mM total lipids, 4 mol% PEG₅₀₀₀, 200 μM DOX) in PBS were injected into the circulation of 2-day old xenograft zebrafish embryos (K-functionalised MDA-MB-231 cells, generated as described above) *via* the posterior cardinal vein. Embryos were kept at 34 °C throughout the course of the experiment. Where applicable, UV irradiation (15 mins, 370 ± 7 nm, 13.5 mW/cm², *light dose* = 0.45 J/embryo) was performed immediately following liposomes injection. The LED light source was positioned directly above (3 cm) the embryo in agarose. Four days post-injection (4 dpi), fluorescent images were obtained, using a Leica MZ16FA fluorescent microscope coupled to a DFC420C camera and Leica TCS SPE confocal microscope, and cancer cell mass, within the tail invasive site, quantified based on the green fluorescent signal of xenograft MDA-MB-231 cells (Image analysis software: ImageJ 1.51n, National Institutes of Health, USA). One-way ANOVA tests were performed to compare means of the three groups of data.

Statistical Analysis

Data presented as mean values ± SD. No pre-processing of data was performed. Data was analysed by one-way ANOVA (non-parametric and mixed) statistical test using GraphPad Prism 8.0.1. Significance is shown as P value (****, $p < 0.0001$; NS, not significant). Sample sizes for each statistical analysis are individually reported and no statistical methods were used to predetermine sample size.

Results and Discussion

We have previously shown the interaction between fusogenic peptides E and K, displayed from opposing membranes, can be sterically shielded through PEGylation of E-functionalized liposomes (E_{PEG}-liposomes) [35]. Furthermore, through incorporation of a photocleavable linker, we have shown precise spatiotemporal control of liposome-liposome fusion and liposome-cell docking through light triggered dePEGylation of E_{PEG}-liposomes *in vitro* [32]. In this case, PEG₂₀₀₀ was sufficient in length to sterically shield the interaction between complementary, three heptad (21 amino acid) E and K peptides (E₃ and K₃). However, to achieve full fusion of liposome and cell membranes, E and K peptides must be extended to four heptad repeats (E₄/K₄, 28 amino acids) [30].

To assess the optimal PEG length necessary to sterically shield the E₄/K₄ peptide interaction, lipid mixing experiments between E₄- and K₄-liposomes were, therefore, first performed *in vitro* (**Figure 2a**). For this, photolabile cholesterol-*o*-nitrobenzyl-PEG constructs (PEG₂₀₀₀ and PEG₅₀₀₀, see **Scheme S1** for chemical structure) were incorporated (*via* post-modification), at varying mol% (0-10 mol%) within E₄-liposome formulations (see Supporting Information for size and zeta potentials of all liposomes, **Figure S1** for TEM images of E_{PEG}- and F_{PEG}-liposomes). As photocleavable functionality, methoxy-functionalised *o*-nitrobenzyl groups were selected as: 1) they have been successfully used as photocage of a variety of bioactive compounds and biomolecules in complex biological solutions, 2) they have rapid photolysis kinetics, and 3), as the methyl substituted variant (at the benzylic position), the evolved nitroso photolytic by-products are less toxic than unsubstituted nitroso variants [36]. Now with larger,

tetrameric E₄ and K₄ peptides displayed from liposome surface, PEG₂₀₀₀ was shown ineffective at shielding the interaction between complementary peptides, as evidenced by significant lipid mixing of E- and K-liposome membranes even at high incorporated mol% of PEG. In contrast, >2 mol% cholesterol-PEG₅₀₀₀ incorporated within the E-liposome membrane was sufficient to completely shield the E₄/K₄ interaction. Furthermore, upon UV irradiation (15 mins, 370 ± 7 nm, 202 mW/cm², see **Figure S2** for dePEGylation efficiency) of an equimolar solution of K-liposomes and E_{PEG}-liposomes (4 mol% photolabile cholesterol-PEG₅₀₀₀), complete restoration of lipid mixing of K- and E-liposome membranes (**Figure 2a**) and a concomitant increase in liposome size, due to the fusion of two or more distinct liposomes (**Figure S3**), was observed. Given the significantly smaller molecular size of folate, we assumed 4 mol% PEG₅₀₀₀ would be amply sufficient to sterically mask displayed folate functionality from the F-liposome surface. E_{PEG}-liposomes (containing 4 mol% photolabile cholesterol-PEG₅₀₀₀) were stable in aqueous media (+ 10% serum) for at least 20h at room temperature (**Figure S4**).

Next, light induced liposome-cell interactions, mediated through E/K complexation, were assessed *in vitro* (**Figure 2b-d**). For these experiments, HeLa cells were pre-functionalised with lipopeptide K₄ constructs (to form K-functionalised cells), as previously described [37]. E_{PEG}-liposomes (400 μM, 4 mol% PEG₂₀₀₀ or PEG₅₀₀₀) – containing a fluorescent lipid probe (1 mol% DOPE-NBD, green) and encapsulated propidium iodide (PI, a turn-on intercalator, 75 μM, red) – were incubated with K-functionalised cells, washed and imaged, both before and after UV irradiation (15 mins, 370 ± 7 nm, 50.6 mW/cm², *light dose* = 45.5 J/cm²). Under analogous irradiation conditions and experimental setups, no photocytotoxicity was observed [24]. Supporting lipid mixing experiments, E_{PEG}-liposomes (PEG₂₀₀₀, 4 mol%), prior to light irradiation, interacted with K-functionalised HeLa cells (**Figure 2b**), confirming PEG₂₀₀₀ is an insufficient steric shield in blocking E₄/K₄ interactions in both liposome-liposome and liposome-cell fusion experiments. In contrast, prior to light triggered dePEGylation, E_{PEG}-liposomes (PEG₅₀₀₀, 4 mol%) showed no interaction with cells nor intracellular PI delivery (**Figure 2c**). However, subsequent *in situ* UV irradiation (15 mins, 370 ± 7 nm, 50.6 mW/cm², *light dose* = 45.5 J/cm²) resulted in HeLa cell membranes homogeneously labelled with liposome-associated lipid probes (DOPE-NBD) and PI clearly dispersed within the cell cytosol (**Figure 2d**). Analogous localization and homogenous dispersion of lipid probes throughout target plasma cell membranes (rather than punctae within cells, indicative of endosomal uptake) was previously observed in E₄/K₄ mediated liposome-cell fusion experiments, including in the presence of various endocytosis inhibitors [30]. From these experiments, 4 mol% PEG₅₀₀₀ displayed on the surface of E₄-liposomes was deemed sufficient to inhibit putative E₄/K₄ mediated liposome-cell fusion and, by using photolabile lipid-PEG constructs, precise spatiotemporal control over liposome-cell membrane fusion could be achieved (**Figure S5**).

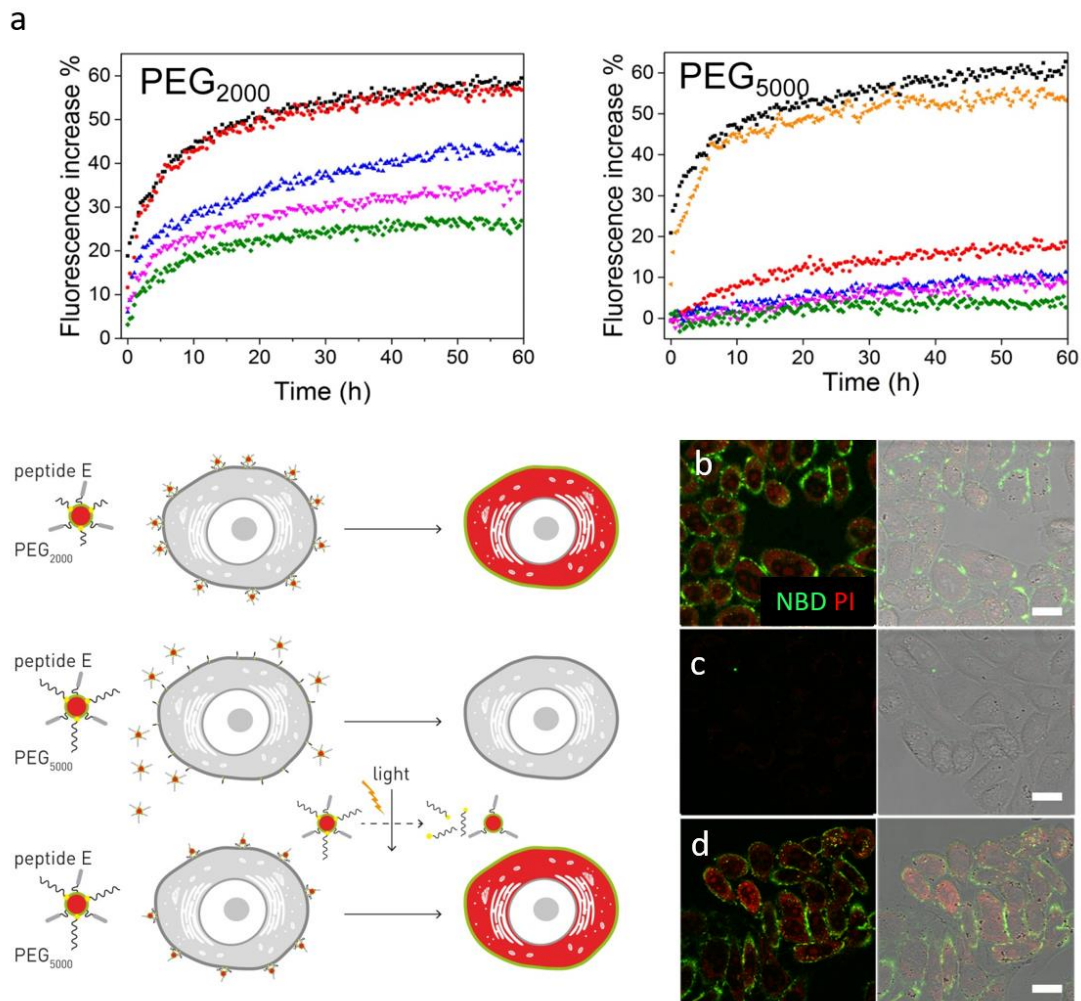


Figure 2 Optimisation of required PEG length. A. Lipid mixing experiments of E- and K-liposomes incorporating varying mol% cholesterol-nitrobenzyl-PEG₂₀₀₀ (left) or cholesterol-nitrobenzyl-PEG₅₀₀₀ (right) within E-liposome formulations. 0 mol% (black), 2 mol% (red), 4 mol% (blue), 8 mol% (pink) and 10 mol% (green), 4mol% following UV irradiation (15min, 370 ± 7 nm, 202 mW/cm²) (orange). Liposome-cell fusion of E_{PEG}-liposomes (4 mol% PEG₂₀₀₀, – before UV, (B); 4 mol% PEG₅₀₀₀ before (C) and after (D) applied UV light (15 mins, 370 ± 7 nm, 50.6 mW/cm², *light dose* = 45.5 J/cm²). E_{PEG}-liposomes contained 1 mol% DOPE-NBD (lipid probe, green) and encapsulated PI (75 μM, turn-on intercalator, red), scale bars = 30 μm.

Next, light triggered, active targeting of liposomes to xenograft MDA-MB-231 breast cancer cells was assessed within live embryonic zebrafish (Figure 3). Both F-liposomes, targeting the overexpressed folate receptor on MDA-MB-231 cells [28,29], and E-liposomes, targeting K-functionalised MDA-MB-231 cells, were independently tested. Zebrafish embryos are small (2-3 mm in length) and transparent enabling fluorescence imaging of specific biological events across entire living organisms in real time [38]. Zebrafish are increasingly used as model organisms to study fundamental processes such as embryogenesis, cell migration, sleep and disease pathogenesis [39,40]. This includes the development of embryonic zebrafish xenograft models to study the pathogenesis of human cancers [41-43], including human breast cancers [44,45]. Here, MDA-MB-231 breast cancer cells, stably expressing GFP, were

microinjected into the circulation of 2-day old zebrafish larvae *via* the duct of Cuvier and quickly accumulated (<1 hours post injection (hpi)) within the caudal hematopoietic tissue (CHT) [46]. One hour after injection of cancer cells, either fluorescently labelled E_{PEG-} or F_{PEG-}-liposomes (4 mol% PEG₅₀₀₀, 1 mol% DOPE-LR probe) were injected (1 mM, 3 nL) into circulation *via* the posterior cardinal vein (PCV). Prior to UV irradiation, both E_{PEG-} and F_{PEG-}-liposomes freely circulated, were confined within the vasculature of the embryo, and no co-localization of liposomes with either xenograft cancer cells or key RES cell types of the embryonic zebrafish (*e.g.* scavenging endothelial cells (SECs) or blood resident macrophages) [47], was observed (**Figure 3**).

Following *in situ* UV irradiation (15 mins, 370 ± 7 nm, 13.5 mW/cm², *light dose* = 0.45 J/embryo) of the embryonic fish, however, both E- and F-liposomes rapidly and selectively co-localised with xenograft cancer cells (<30 min, *i.e.* prior to first image acquisition) (**Figure 3**). Under these irradiation conditions, embryos continued to develop normally (up to 6 days post-fertilisation (dpf)) and no phenotypic abnormalities were observed (**Figure S6**). Under identical conditions, the biodistribution of F_{PEG-}-liposomes containing non-cleavable PEG₅₀₀₀ (DSPE-PEG₅₀₀₀, Avanti) remained unchanged before and after *in situ* light irradiation, demonstrating the targeting requirement of both liposomes containing photocleavable PEG as well as UV light (**Figure S7**). In the case of E-liposomes, E/K specificity was confirmed by repeating the experiment in the absence of peptide K (displayed from xenografted cancer cells). In this case, no E-liposome accumulation with cancer cells was observed following UV irradiation, confirming the requirement and selectivity of E₄/K₄ recognition and complexation for cell specific targeting (**Figure S8**).

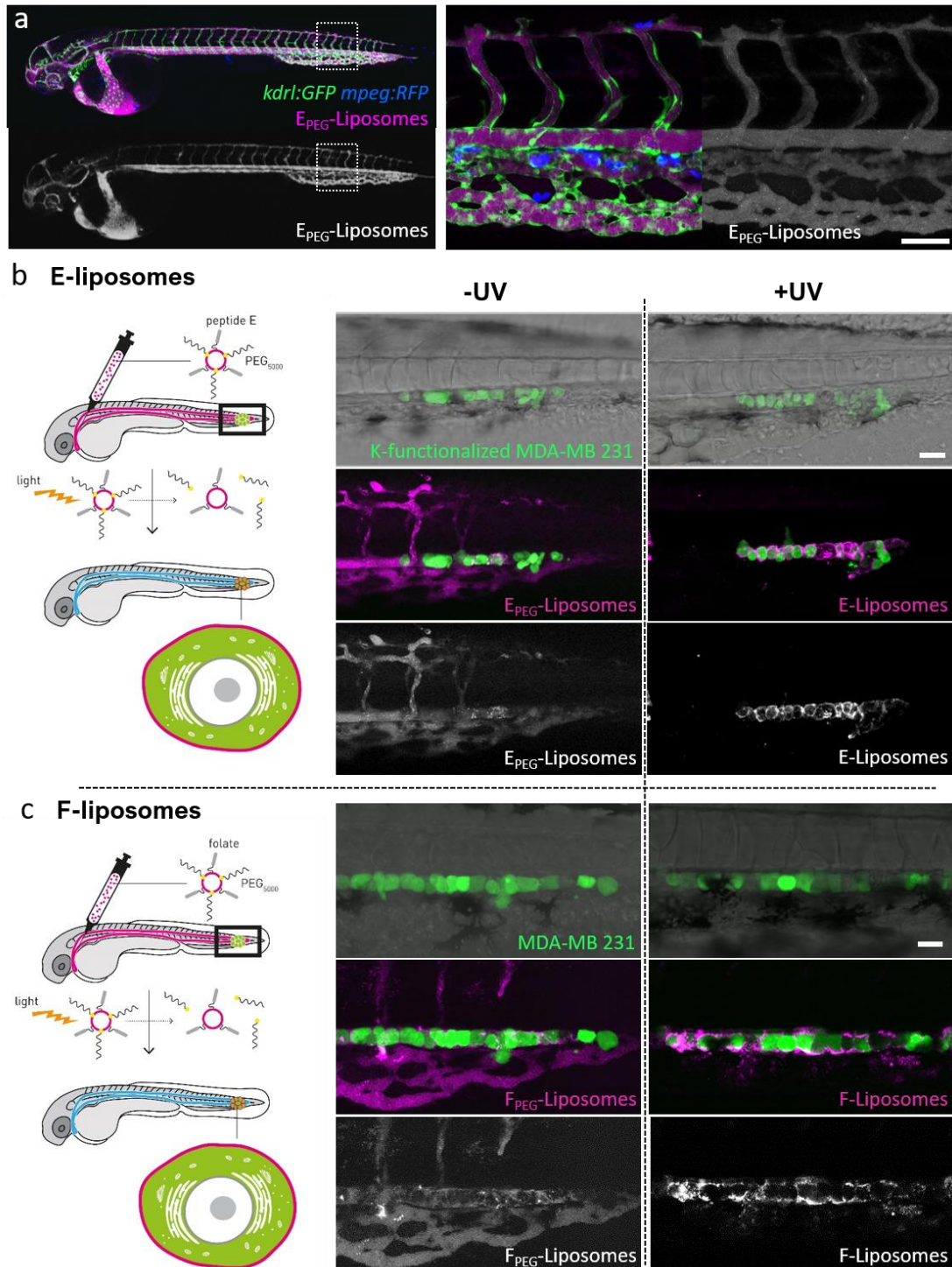


Figure 3 Cancer cell-specific, light triggered liposome-cell interactions *in vivo*. A. Biodistribution of E_{PEG}-liposomes (1 mM, 4 mol% PEG₅₀₀₀, containing 1 mol% DOPE-Atto 633, far red) in *Tg(kdr1:GFP/mpeg:RFP)* zebrafish embryos (2 dpf), following i.v. injection. Liposomes are confined within the vasculature of the embryo and freely circulate. No liposome co-localisation with either endothelial cells (green) or (blood resident) macrophages (blue) is observed indicative of the ability of E_{PEG}-liposomes to evade key RES cell types. Confocal z-stacks acquired at 1hpi. B,C. MDA-MB-231 human breast cancer cells, stably expressing GFP, were injected into the circulation of a 2-day old zebrafish embryo and quickly accumulated in the caudal hematopoietic tissue (CHT). In the case of E-liposomes, cells were pre-treated with lipopeptide K. Into this xenograft model, either E_{PEG}- or F_{PEG}-liposomes (1 mM, 4 mol% PEG₅₀₀₀,

containing 1 mol% DOPE-LR, red) were injected into circulation. Prior to UV irradiation, both E_{PEG}- or F_{PEG}-liposomes were freely circulating, confined within the vasculature of the fish (left image panels). Following UV irradiation (15 mins, 370 ± 7 nm, 13.5 mW/cm², *light dose* = 0.45 J/embryo) and photolytic dePEGylation, both E- and F-liposomes selectively bound to xenograft cancer cells within the CHT (right image panels). Data are representative of three independent experiments (each n=5). Field of view = boxed region in embryo cartoon. Scale bars = 100 µm.

Extending our approach to liposome mediated, intracellular drug delivery, we first measured the *in vitro* cytotoxicity (MDA-MB 231 cells, WST assay) of doxorubicin-filled E_{PEG}- and F_{PEG}-liposomes (4 mol% PEG₅₀₀₀), before and after light activation, and compared this to the toxicity of free doxorubicin (**Figure 4a**). Again, for experiments involving E_{PEG}-liposomes, cells were first pretreated with lipopeptide K. For both E_{PEG}- and F_{PEG}-liposomes, cell viability was unaffected in the absence of applied UV light, and, in the case of E_{PEG}-liposomes, no intracellular DOX delivery was observed (**Figure 4b**, F_{PEG}-liposomes were not analyzed under the fluorescence microscope). Upon light triggered dePEGylation, however, both E- and F-liposome mediated delivery of doxorubicin led to enhanced cytotoxicity (IC₅₀ approx. 100 µM and 200 µM, respectively for E- and F-lipo-DOX) compared to free DOX (IC₅₀ approx. 300 µM). Interestingly, under these experimental conditions, the most potent cytotoxicity was observed for E/K mediated liposomal delivery of DOX. This suggests DOX delivery direct to the cell cytosol, following liposome-cell membrane fusion, is a potentially potent method of drug delivery. Importantly, freshly prepared DOX-loaded liposomes used in all cases, as significant DOX leakage (30-40%) from the liposome core was observed for all formulations during prolonged storage and would affect the efficiency of liposomal DOX delivery over time (**Figure S9**).

Next, doxorubicin-filled E_{PEG}-liposomes (4 mol% PEG₅₀₀₀, 250 µM doxorubicin) were intravenously microinjected into embryonic zebrafish xenografts (K-functionalised MDA-MB-231 breast cancer cells) (**Figure 4c**) and the efficacy in reducing tumor burdens assessed (**Figure 4d and 4e**). For this, relative cancer cell proliferation was quantified by measuring total GFP fluorescence of xenograft cancer cells. Here, significantly (p<0.0001) reduced cancer cell proliferation (46.9% reduction) was only observed in the '+UV' group. In the absence of light, tumor proliferation was unaffected and no significant difference in cancer cell numbers was measured compared to the untreated controls. Again, using cancer cells unfunctionalized with peptide K, no reduction in cancer cell proliferation was observed (**Figure S10**), further emphasising the essential requirement and selectivity of E₄/K₄ recognition and complexation.

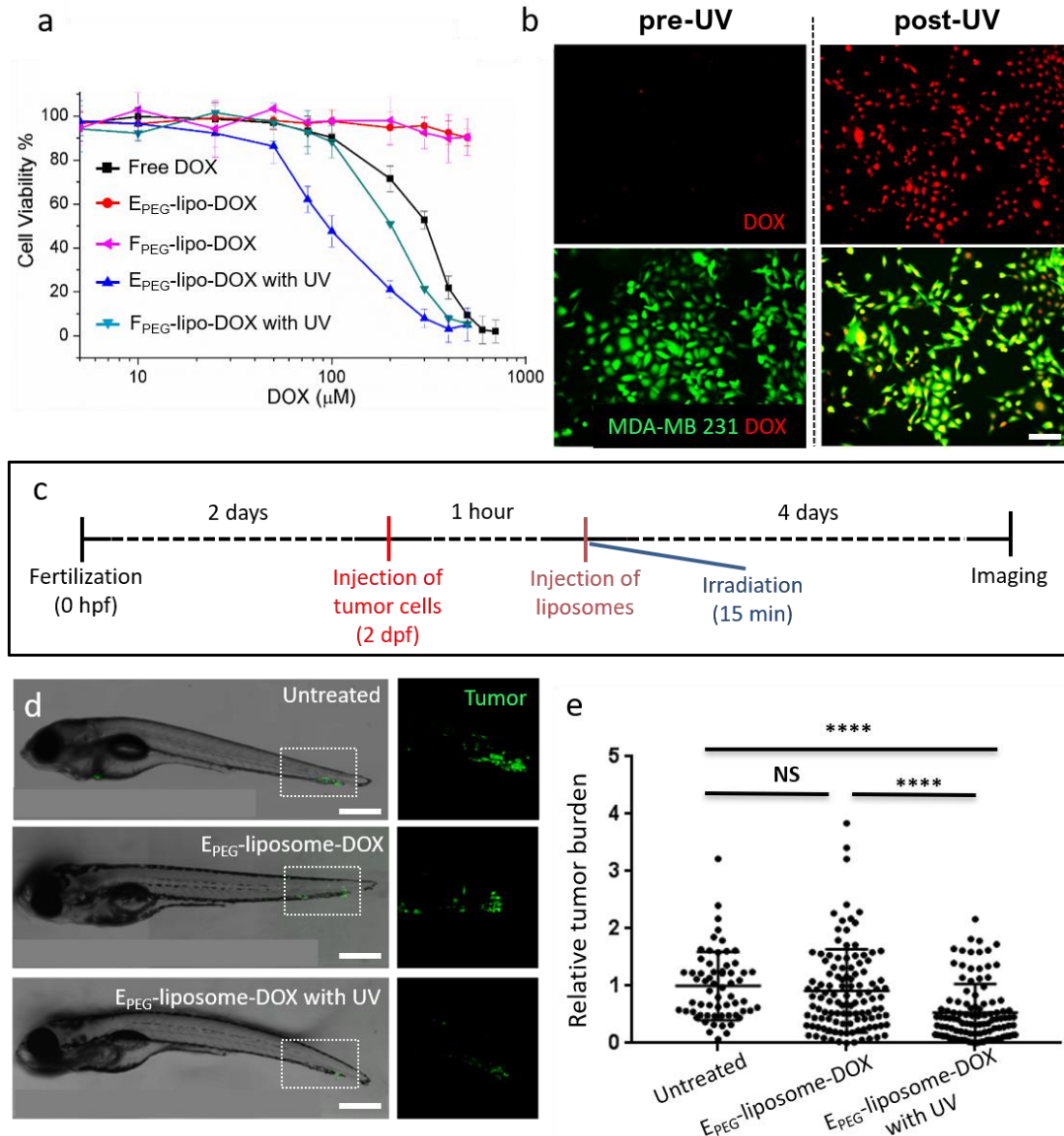


Figure 4 Delivery of liposome-encapsulated doxorubicin to MDA-MB 231 cells both *in vitro* and *in vivo*. **a**. MDA-MB-231 breast cancer cell viability *in vitro* (measured by WST assay) following 2 h incubation with either DOX-filled E_{PEG}-liposomes (4 mol% PEG₅₀₀₀), before (red) and after (blue) UV activation (15 mins, 370 ± 7 nm, 50.6 mW/cm², *light dose* = 45.5 J/cm²); F_{PEG}-liposomes (4 mol% PEG₅₀₀₀), before (pink) and after (cyan) UV activation; or free doxorubicin (black) without UV irradiation. For +UV samples, liposomes were added to cells and immediately irradiated. 2 h incubation time includes 15 min irradiation time. In the absence of light, both E_{PEG}- and F_{PEG}-lipo-DOX formulations were non-toxic. Following light activation, liposome mediated delivery of doxorubicin resulted in enhanced cytotoxicity (F-liposomes, IC₅₀ = approx. 200 μM; E-liposomes, IC₅₀ = approx. 100 μM) compared to free doxorubicin (IC₅₀ = approx. 300 μM). In all cases, freshly prepared DOX-filled liposomes were used to minimize the effects of DOX leakage over time. **b**. Intracellular DOX delivery by E_{PEG}-liposomes (200 μM encapsulated DOX, red) and K-functionalised MDA-MB-231 breast cancer cells, stably expressing GFP, green, before (left) and after (right) UV irradiation (15 mins, 370 ± 7 nm, 50.6 mW/cm², *light dose* = 45.5 J/cm²). Scale bars=100 μm. **c**. Timeline of zebrafish development, MDA-MB-231 cell injection, liposome injection and quantification in the zebrafish embryo. At 2 dpf, MDA-MB-231 cells (approx. 300 cells) were injected into circulation *via* the duct of Cuvier. One hour after 124

engraftment, DOX-filled, E_{PEG}-liposomes (3nl, 4mM total lipid; 200 μM encapsulated doxorubicin) were injected into circulation *via* the posterior cardinal vein. UV irradiation (15 mins, 370 ± 7 nm, 13.5 mW/cm², *light dose* = 0.45 J/embryo), where appropriate, was performed immediately after the injection of liposomes. Tumor burden analysed at 4 dpi. **d,e.** Visualisation and quantification of cancer proliferation in the zebrafish embryo. Significant (P<0.0001) reduction in tumor volume was only observed for DOX-filled, E_{PEG}-liposomes, following in situ light activation. In the absence of light activation, tumor progression/burden was unaffected as for untreated controls. Data is presented as mean values ± SD, each point on the scatter plots represents one larva. Brackets indicate significantly different values (****, p < 0.0001; NS, not significant) based on one-way ANOVA statistical testing. n = 61 individually injected embryos (untreated group). n = 114 (without UV group) and n = 108 (with UV group). Scale bars = 500 μm.

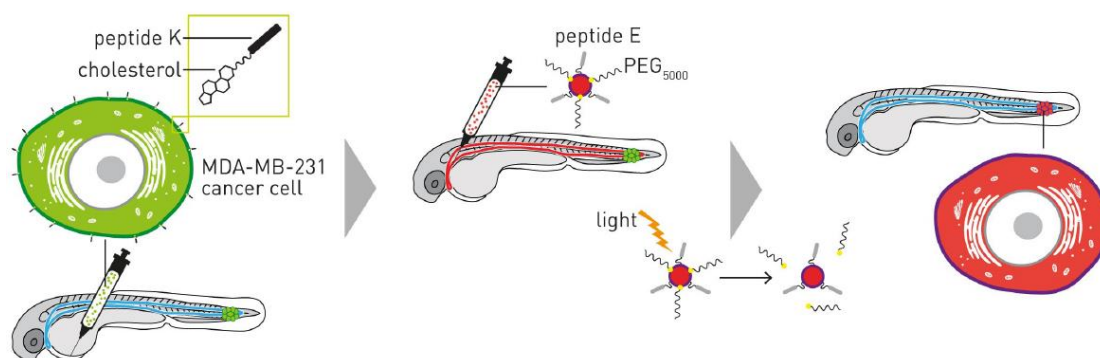
Conclusion

Here, we successfully demonstrate light triggered targeting of liposomes to xenograft cancer cells *in vivo*. Our approach relies on the light triggered dePEGylation of liposome surfaces, revealing underlying targeting functionality. General applicability of this approach was demonstrated using both an experimental two component fusion system (peptides E and K) as well as clinically relevant folate-decorated liposomes. Both E_{PEG}- and F_{PEG}-liposomes, prior to light triggered activation, freely circulated throughout the vasculature of the embryonic zebrafish, and showed no significant interactions with either target cancer cells or key RES cell types (scavenging endothelial cells or blood resident macrophages) within the fish [47]. In mammals, analogous RES cell types, namely liver sinusoidal endothelial cells (LSECs), Kupffer cells (hepatic, blood resident macrophages) and splenic macrophages, are responsible for the clearance of the majority of *i.v.* administered nanoparticles from the body [48]. While there is currently no established model for the EPR effect in embryonic zebrafish, the implications of our findings are that both E_{PEG}- and clinically relevant F_{PEG}-liposomes, prior to light activation, would likely evade RES clearance in mammals, prolonging circulation lifetimes and the potential for liposome accumulation in pathological tissues with enhanced permeability.

In the case of E-liposome targeting, prior modification of cancer cell membranes with complementary peptide K is a pre-requisite. While this system provides us with a fundamental tool to probe alternative liposomal drug delivery routes (*i.e.* fusion vs. endocytosis), as well as a highly selective handle for targeting as is shown in this study, the necessity for components displayed from both liposome and target cell membranes is a major limitation to further *in vivo* application. Similarly, the use of UV light as a trigger raises valid concerns over applicability in larger, non-transparent mammals, including humans. To some extent, these concerns relate to the poor tissue penetration of UV light (approx. 100-200 μm). As a result, the clinical use of UV light is restricted to the topical treatment of cosmetic skin disorders, including psoriasis, acne and eczema [49]. However, these limitations are increasingly being overcome, as fundamental advances in fiber optic [18] and wireless LED technologies [19,20] facilitate the localized delivery of UV light deep within patients. Alternatively, extended exposure to UV light is known to pose a significant health risk, with the potential to cause DNA damage, cytotoxicity and cancer

[50]. In this study, applied UV-A (370 ± 7 nm) light doses to zebrafish embryos (12.1 J/cm^2) are well below recommended (skin) exposure limits ($32 \text{ J/cm}^2 @ 375 \text{ nm}$). Furthermore, while single photon UV-A (370 nm) light is optimal for the photolysis of *o*-nitrobenzyl functionalities, the use of 2-photon excitation sources [51,52] or photolabile chemistries sensitive to longer wavelength, visible light [53,54], offer options for light activation both deep in tissue and with reduced photocytotoxicity.

Finally, this study highlights the unique opportunities offered by the embryonic zebrafish model in the design and optimization of nanomedicines. In this study, we were able to 1) generate our desired xenograft cancer model without the need for immunosuppression (the adaptive immune system is not yet developed zebrafish embryos), 2) directly visualize the changing pharmacokinetics of stimuli-responsive nanoparticles *in situ*, *in vivo* and in real time and 3) set-up and perform efficacy studies, involving several hundred animals, within 1 week. The combined level of detailed assessment, low cost and experimental speed, afforded by the embryonic zebrafish model, is simply not achievable using conventional animal models (eg. mice and rats). As to the predictive potential of the embryonic zebrafish, we, and others, have recently shown both pharmacokinetic parameters and key cellular interactions of nanomedicines are highly conserved between the embryonic zebrafish and mice [47,55].



Cancer cell-specific drug delivery remains a major unmet challenge for nanomedicines. In this work, we use light to 'turn on' the targeting of nanomedicines, *in situ* and *in vivo*, enabling on demand cancer cell specific drug delivery in live zebrafish embryos.

Acknowledgements This work was funded through Chinese Scholarship Council grants (LK, QC) and the Netherlands Organization for Scientific Research (NWO-Vici-project nr. 724.014.001; FC, AK). Arwin Groenewoud (Institute of Biology, Leiden University) is thanked for the kind gift of Plasmid #106172 (Addgene.org). Infographics were developed by Joost Bakker (www.scicomvisuals.com).

References

1. Ventola, C.L. Progress in Nanomedicine: Approved and Investigational Nanodrugs. *P & T: a peer-reviewed journal for formulary management* **2017**, *42*, 742-755.
2. Shi, J.; Kantoff, P.W.; Wooster, R.; Farokhzad, O.C. Cancer nanomedicine: progress,

- challenges and opportunities. *Nat Rev Cancer* **2017**, *17*, 20-37, doi:10.1038/nrc.2016.108.
3. Maeda, H.; Wu, J.; Sawa, T.; Matsumura, Y.; Hori, K. Tumor vascular permeability and the EPR effect in macromolecular therapeutics: a review. *Journal of controlled release : official journal of the Controlled Release Society* **2000**, *65*, 271-284, doi:10.1016/s0168-3659(99)00248-5.
 4. Maeda, H.; Nakamura, H.; Fang, J. The EPR effect for macromolecular drug delivery to solid tumors: Improvement of tumor uptake, lowering of systemic toxicity, and distinct tumor imaging in vivo. *Advanced drug delivery reviews* **2013**, *65*, 71-79, doi:10.1016/j.addr.2012.10.002.
 5. Immordino, M.L.; Dosio, F.; Cattel, L. Stealth liposomes: review of the basic science, rationale, and clinical applications, existing and potential. *International journal of nanomedicine* **2006**, *1*, 297-315.
 6. Suk, J.S.; Xu, Q.; Kim, N.; Hanes, J.; Ensign, L.M. PEGylation as a strategy for improving nanoparticle-based drug and gene delivery. *Advanced drug delivery reviews* **2016**, *99*, 28-51, doi:10.1016/j.addr.2015.09.012.
 7. Fritze, A.; Hens, F.; Kimpfler, A.; Schubert, R.; Peschka-Süss, R. Remote loading of doxorubicin into liposomes driven by a transmembrane phosphate gradient. *Biochimica et biophysica acta* **2006**, *1758*, 1633-1640, doi:10.1016/j.bbamem.2006.05.028.
 8. Byrne, J.D.; Betancourt, T.; Brannon-Peppas, L. Active targeting schemes for nanoparticle systems in cancer therapeutics. *Advanced drug delivery reviews* **2008**, *60*, 1615-1626, doi:10.1016/j.addr.2008.08.005.
 9. Bazak, R.; Houri, M.; El Achy, S.; Kamel, S.; Refaat, T. Cancer active targeting by nanoparticles: a comprehensive review of literature. *Journal of cancer research and clinical oncology* **2015**, *141*, 769-784, doi:10.1007/s00432-014-1767-3.
 10. Mishra, S.; Webster, P.; Davis, M.E. PEGylation significantly affects cellular uptake and intracellular trafficking of non-viral gene delivery particles. *European journal of cell biology* **2004**, *83*, 97-111, doi:10.1078/0171-9335-00363.
 11. Fang, Y.; Xue, J.; Gao, S.; Lu, A.; Yang, D.; Jiang, H.; He, Y.; Shi, K. Cleavable PEGylation: a strategy for overcoming the "PEG dilemma" in efficient drug delivery. *Drug delivery* **2017**, *24*, 22-32, doi:10.1080/10717544.2017.1388451.
 12. Kong, L.; Campbell, F.; Kros, A. DePEGylation strategies to increase cancer nanomedicine efficacy. *Nanoscale horizons* **2019**, *4*, 378-387, doi:10.1039/c8nh00417j.
 13. Webb, B.A.; Chimenti, M.; Jacobson, M.P.; Barber, D.L. Dysregulated pH: a perfect storm for cancer progression. *Nat Rev Cancer* **2011**, *11*, 671-677, doi:10.1038/nrc3110.
 14. Mehner, C.; Hockla, A.; Miller, E.; Ran, S.; Radisky, D.C.; Radisky, E.S. Tumor cell-produced matrix metalloproteinase 9 (MMP-9) drives malignant progression and metastasis of basal-like triple negative breast cancer. *Oncotarget* **2014**, *5*, 2736-2749, doi:10.18632/oncotarget.1932.
 15. Vaupel, P.; Kallinowski, F.; Okunieff, P. Blood flow, oxygen and nutrient supply, and metabolic microenvironment of human tumors: a review. *Cancer Res* **1989**, *49*, 6449-6465.
 16. Karotki, A.; Khurana, M.; Lepock, J.R.; Wilson, B.C. Simultaneous two-photon excitation of photofrin in relation to photodynamic therapy. *Photochemistry and photobiology* **2006**, *82*, 443-452, doi:10.1562/2005-08-24-ra-657.
 17. Bolze, F.; Jenni, S.; Sour, A.; Heitz, V. Molecular photosensitisers for two-photon photodynamic therapy. *Chem Commun (Camb)* **2017**, *53*, 12857-12877, doi:10.1039/c7cc06133a.
 18. Yun, S.H.; Kwok, S.J.J. Light in diagnosis, therapy and surgery. *Nature biomedical engineering* **2017**, *1*, doi:10.1038/s41551-016-0008.
 19. Kim, T.I.; McCall, J.G.; Jung, Y.H.; Huang, X.; Siuda, E.R.; Li, Y.; Song, J.; Song, Y.M.; Pao, H.A.; Kim, R.H., et al. Injectable, cellular-scale optoelectronics with applications for wireless optogenetics. *Science (New York, N.Y.)* **2013**, *340*, 211-216, doi:10.1126/science.1232437.
 20. Bansal, A.; Yang, F.; Xi, T.; Zhang, Y.; Ho, J.S. In vivo wireless photonic photodynamic therapy. *Proceedings of the National Academy of Sciences of the United States of America* **2018**, *115*, 1469-1474, doi:10.1073/pnas.1717552115.
 21. Wang, J.; Ouyang, Y.; Li, S.; Wang, X.; He, Y. Photocleavable amphiphilic diblock copolymer with an azobenzene linkage. *RSC Advances* **2016**, *6*, 57227-57231, doi:10.1039/C6RA12129B.

22. Saravanakumar, G.; Park, H.; Kim, J.; Park, D.; Pramanick, S.; Kim, D.H.; Kim, W.J. Miktoarm Amphiphilic Block Copolymer with Singlet Oxygen-Labile Stereospecific β -Aminoacrylate Junction: Synthesis, Self-Assembly, and Photodynamically Triggered Drug Release. *Biomacromolecules* **2018**, *19*, 2202-2213, doi:10.1021/acs.biomac.8b00290.
23. Jin, Q.; Cai, T.; Han, H.; Wang, H.; Wang, Y.; Ji, J. Light and pH dual-degradable triblock copolymer micelles for controlled intracellular drug release. *Macromolecular rapid communications* **2014**, *35*, 1372-1378, doi:10.1002/marc.201400171.
24. Kong, L.; Poulcharidis, D.; Schneider, G.F.; Campbell, F.; Kros, A. Spatiotemporal Control of Doxorubicin Delivery from "Stealth-Like" Prodrug Micelles. *International journal of molecular sciences* **2017**, *18*, doi:10.3390/ijms18102033.
25. Zhou, D.; Guo, J.; Kim, G.B.; Li, J.; Chen, X.; Yang, J.; Huang, Y. Simultaneously Photo-Cleavable and Activatable Prodrug-Backboned Block Copolymer Micelles for Precise Anticancer Drug Delivery. *Advanced healthcare materials* **2016**, *5*, 2493-2499, doi:10.1002/adhm.201600470.
26. Kalva, N.; Parekh, N.; Ambade, A.V. Controlled micellar disassembly of photo- and pH-cleavable linear-dendritic block copolymers. *Polymer Chemistry* **2015**, *6*, 6826-6835, doi:10.1039/C5PY00792E.
27. Zhou, M.; Huang, H.; Wang, D.; Lu, H.; Chen, J.; Chai, Z.; Yao, S.Q.; Hu, Y. Light-Triggered PEGylation/dePEGylation of the Nanocarriers for Enhanced Tumor Penetration. *Nano letters* **2019**, *19*, 3671-3675, doi:10.1021/acs.nanolett.9b00737.
28. Hartmann, L.C.; Keeney, G.L.; Lingle, W.L.; Christianson, T.J.; Varghese, B.; Hillman, D.; Oberg, A.L.; Low, P.S. Folate receptor overexpression is associated with poor outcome in breast cancer. *International journal of cancer* **2007**, *121*, 938-942, doi:10.1002/ijc.22811.
29. Meier, R.; Henning, T.D.; Boddington, S.; Tavri, S.; Arora, S.; Piontek, G.; Rudelius, M.; Corot, C.; Daldrup-Link, H.E. Breast cancers: MR imaging of folate-receptor expression with the folate-specific nanoparticle P1133. *Radiology* **2010**, *255*, 527-535, doi:10.1148/radiol.10090050.
30. Yang, J.; Bahreman, A.; Daudey, G.; Bussmann, J.; Olsthoorn, R.C.; Kros, A. Drug Delivery via Cell Membrane Fusion Using Lipopeptide Modified Liposomes. *ACS central science* **2016**, *2*, 621-630, doi:10.1021/acscentsci.6b00172.
31. Robson Marsden, H.; Elbers, N.A.; Bomans, P.H.; Sommerdijk, N.A.; Kros, A. A reduced SNARE model for membrane fusion. *Angewandte Chemie (International ed. in English)* **2009**, *48*, 2330-2333, doi:10.1002/anie.200804493.
32. Kong, L.; Askes, S.H.; Bonnet, S.; Kros, A.; Campbell, F. Temporal Control of Membrane Fusion through Photolabile PEGylation of Liposome Membranes. *Angewandte Chemie (International ed. in English)* **2016**, *55*, 1396-1400, doi:10.1002/anie.201509673.
33. Ellett, F.; Pase, L.; Hayman, J.W.; Andrianopoulos, A.; Lieschke, G.J. mpeg1 promoter transgenes direct macrophage-lineage expression in zebrafish. *Blood* **2011**, *117*, e49-56, doi:10.1182/blood-2010-10-314120.
34. Schindelin, J.; Arganda-Carreras, I.; Frise, E.; Kaynig, V.; Longair, M.; Pietzsch, T.; Preibisch, S.; Rueden, C.; Saalfeld, S.; Schmid, B., et al. Fiji: an open-source platform for biological-image analysis. *Nature methods* **2012**, *9*, 676-682, doi:10.1038/nmeth.2019.
35. Tomatsu, I.; Marsden, H.R.; Rabe, M.; Versluis, F.; Zheng, T.; Zope, H.; Kros, A. Influence of pegylation on peptide-mediated liposome fusion. *Journal of Materials Chemistry* **2011**, *21*, 18927-18933, doi:10.1039/C1JM11722J.
36. Klán, P.; Šolomek, T.; Bochet, C.G.; Blanc, A.; Givens, R.; Rubina, M.; Popik, V.; Kostikov, A.; Wirz, J. Photoremovable protecting groups in chemistry and biology: reaction mechanisms and efficacy. *Chemical reviews* **2013**, *113*, 119-191, doi:10.1021/cr300177k.
37. Zope, H.R.; Versluis, F.; Ordas, A.; Voskuhl, J.; Spaink, H.P.; Kros, A. In vitro and in vivo supramolecular modification of biomembranes using a lipidated coiled-coil motif. *Angewandte Chemie (International ed. in English)* **2013**, *52*, 14247-14251, doi:10.1002/anie.201306033.
38. Sieber, S.; Grossen, P.; Bussmann, J.; Campbell, F.; Kros, A.; Witzigmann, D.; Huwyler, J. Zebrafish as a preclinical in vivo screening model for nanomedicines. *Advanced drug delivery reviews* **2019**, *151-152*, 152-168, doi:10.1016/j.addr.2019.01.001.
39. Santoriello, C.; Zon, L.I. Hooked! Modeling human disease in zebrafish. *The Journal of clinical investigation* **2012**, *122*, 2337-2343, doi:10.1172/jci60434.

40. Cronan, M.R.; Tobin, D.M. Fit for consumption: zebrafish as a model for tuberculosis. *Disease models & mechanisms* **2014**, *7*, 777-784, doi:10.1242/dmm.016089.
41. Grabher, C.; Look, A.T. Fishing for cancer models. *Nature biotechnology* **2006**, *24*, 45-46, doi:10.1038/nbt0106-45.
42. Konantz, M.; Balci, T.B.; Hartwig, U.F.; Dellaire, G.; André, M.C.; Berman, J.N.; Lengerke, C. Zebrafish xenografts as a tool for in vivo studies on human cancer. *Annals of the New York Academy of Sciences* **2012**, *1266*, 124-137, doi:10.1111/j.1749-6632.2012.06575.x.
43. Drabsch, Y.; Snaar-Jagalska, B.E.; Ten Dijke, P. Fish tales: The use of zebrafish xenograft human cancer cell models. *Histology and histopathology* **2017**, *32*, 673-686, doi:10.14670/hh-11-853.
44. Tulotta, C.; Stefanescu, C.; Beletkaia, E.; Bussmann, J.; Tarbashevich, K.; Schmidt, T.; Snaar-Jagalska, B.E. Inhibition of signaling between human CXCR4 and zebrafish ligands by the small molecule IT1t impairs the formation of triple-negative breast cancer early metastases in a zebrafish xenograft model. *Disease models & mechanisms* **2016**, *9*, 141-153, doi:10.1242/dmm.023275.
45. Drabsch, Y.; He, S.; Zhang, L.; Snaar-Jagalska, B.E.; ten Dijke, P. Transforming growth factor- β signalling controls human breast cancer metastasis in a zebrafish xenograft model. *Breast Cancer Res* **2013**, *15*, R106, doi:10.1186/bcr3573.
46. de Boeck, M.; Cui, C.; Mulder, A.A.; Jost, C.R.; Ikeno, S.; Ten Dijke, P. Smad6 determines BMP-regulated invasive behaviour of breast cancer cells in a zebrafish xenograft model. *Scientific reports* **2016**, *6*, 24968, doi:10.1038/srep24968.
47. Campbell, F.; Bos, F.L.; Sieber, S.; Arias-Alpizar, G.; Koch, B.E.; Huwyler, J.; Kros, A.; Bussmann, J. Directing Nanoparticle Biodistribution through Evasion and Exploitation of Stab2-Dependent Nanoparticle Uptake. *ACS nano* **2018**, *12*, 2138-2150, doi:10.1021/acsnano.7b06995.
48. Zhang, Y.N.; Poon, W.; Tavares, A.J.; McGilvray, I.D.; Chan, W.C.W. Nanoparticle-liver interactions: Cellular uptake and hepatobiliary elimination. *Journal of controlled release : official journal of the Controlled Release Society* **2016**, *240*, 332-348, doi:10.1016/j.jconrel.2016.01.020.
49. Vangipuram, R.; Feldman, S.R. Ultraviolet phototherapy for cutaneous diseases: a concise review. *Oral diseases* **2016**, *22*, 253-259, doi:10.1111/odi.12366.
50. Narayanan, D.L.; Saladi, R.N.; Fox, J.L. Ultraviolet radiation and skin cancer. *International journal of dermatology* **2010**, *49*, 978-986, doi:10.1111/j.1365-4632.2010.04474.x.
51. Furuta, T.; Wang, S.S.; Dantzker, J.L.; Dore, T.M.; Bybee, W.J.; Callaway, E.M.; Denk, W.; Tsien, R.Y. Brominated 7-hydroxycoumarin-4-ylmethyls: photolabile protecting groups with biologically useful cross-sections for two photon photolysis. *Proceedings of the National Academy of Sciences of the United States of America* **1999**, *96*, 1193-1200, doi:10.1073/pnas.96.4.1193.
52. Peng, K.; Tomatsu, I.; Korobko, A.V.; Kros, A. Cyclodextrin-dextran based in situ hydrogel formation: a carrier for hydrophobic drugs. *Soft Matter* **2010**, *6*, 85-87, doi:10.1039/B914166A.
53. Shanmugam, V.; Selvakumar, S.; Yeh, C.S. Near-infrared light-responsive nanomaterials in cancer therapeutics. *Chemical Society reviews* **2014**, *43*, 6254-6287, doi:10.1039/c4cs00011k.
54. Aujard, I.; Benbrahim, C.; Gouget, M.; Ruel, O.; Baudin, J.B.; Neveu, P.; Jullien, L. o-nitrobenzyl photolabile protecting groups with red-shifted absorption: syntheses and uncaging cross-sections for one- and two-photon excitation. *Chemistry* **2006**, *12*, 6865-6879, doi:10.1002/chem.200501393.
55. Sieber, S.; Grossen, P.; Detampel, P.; Siegfried, S.; Witzigmann, D.; Huwyler, J. Zebrafish as an early stage screening tool to study the systemic circulation of nanoparticulate drug delivery systems in vivo. *Journal of controlled release : official journal of the Controlled Release Society* **2017**, *264*, 180-191, doi:10.1016/j.jconrel.2017.08.023.

Supporting information for

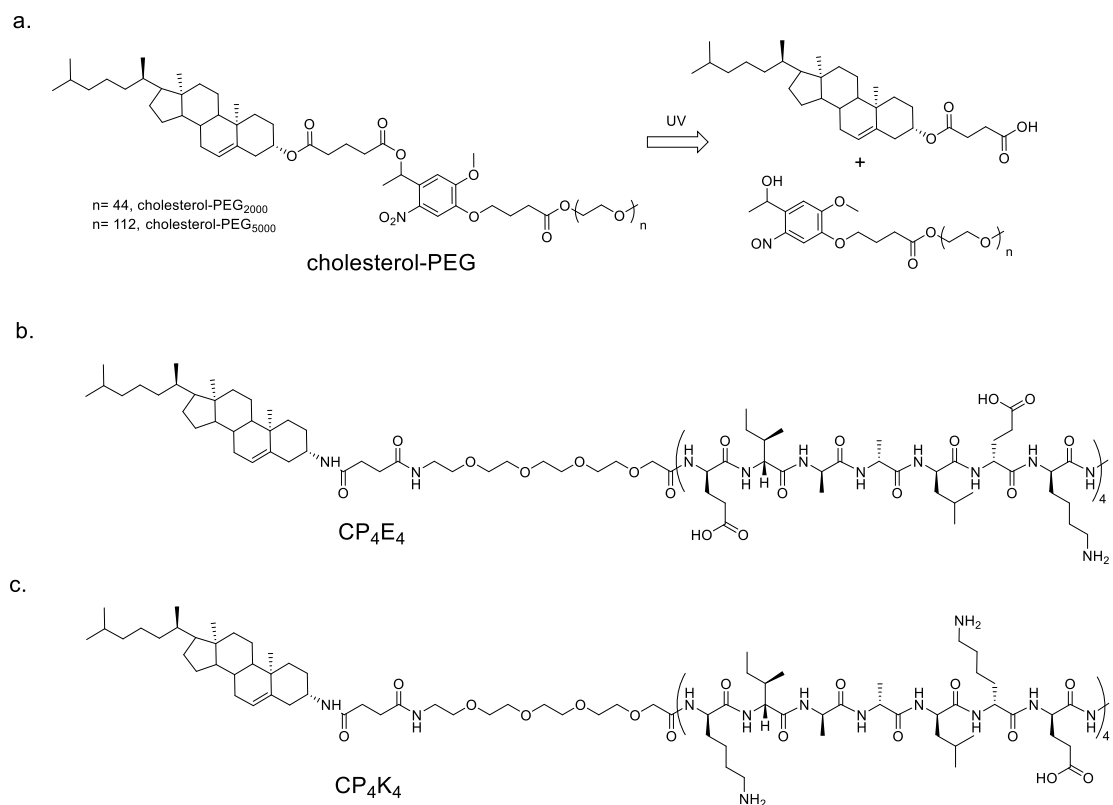
Light triggered, cancer cell-specific targeting and liposomal drug delivery in a zebrafish xenograft model

Li Kong¹⊥, Quanchi Chen²⊥, Frederick Campbell¹, Ewa Snaar-Jagalska^{2*} and Alexander Kros^{1*}

¹Supramolecular and Biomaterials Chemistry, Leiden Institute of Chemistry, Leiden University, Einsteinweg 55, 2333 CC Leiden, The Netherlands

²Institute of Biology, Leiden University, Leiden 2311 EZ, The Netherlands

E-mail: a.kros@chem.leidenuniv.nl; b.e.snaar-jagalska@biology.leidenuniv.nl



Scheme S1a. Chemical structures of cholesterol-PEG and photolysis products, **b.** Chemical structure of lipopeptide-E (CP₄E₄), **c.** Chemical structure of lipopeptide-K (CP₄K₄).

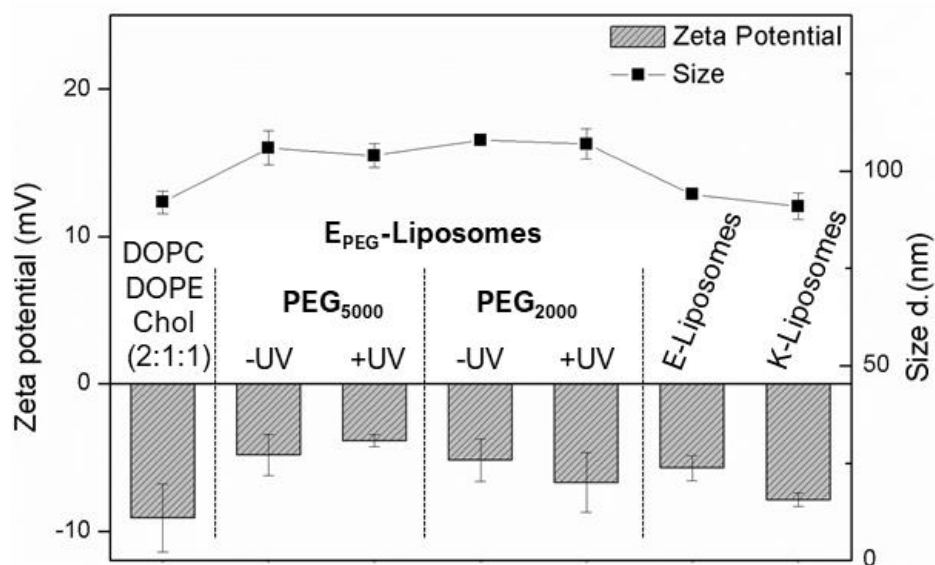


Table S1 Size and zeta potentials of E/K liposomes (containing 1mol% E or K lipopeptide). E_{PEG}-liposomes contain 4 mol% cholesterol-*o*-nitrobenzyl-PEG. Base liposome formulation (DOPC:DOPE:Chol; 2:1:1) contains neither lipopetide or PEG. No significant differences in size were observed for E_{PEG}-liposomes containing 2, 6, 8 or 10mol% PEG (data not shown). Light irradiation (15 mins, 370 ± 7 nm, 202 mW/cm²)

F _{PEG} -liposomes (1mol% DPPE-Folate, 4mol% PEG ₅₀₀₀)	Size d. (nm)	PDI	Zeta potential (mV)
-UV	91.3	0.10	-7.9
+UV	92.1	0.13	-6.2

Table S2 Size and zeta potentials of F_{PEG}-liposomes before and after light irradiation (15 mins, 370 ± 7 nm, 202 mW/cm²)

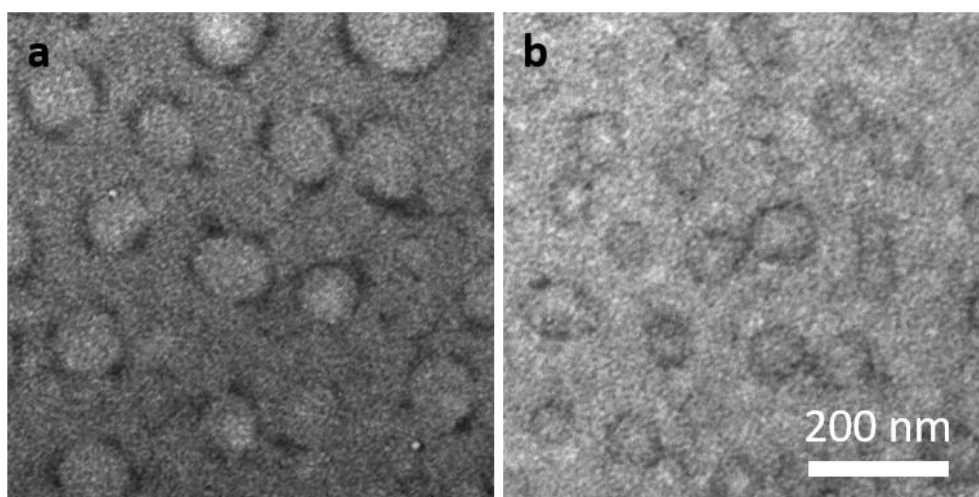


Figure S1 TEM images (TPA stained) of E_{PEG} -liposomes (a) and F_{PEG} -liposomes (b) (total lipid = 1 mM, 4 mol% PEG₅₀₀₀, 1 mol% lipopeptide E₄ or DPPE-Folate). Average size of E_{PEG} -liposomes and F_{PEG} -liposomes is 98 nm and 82 nm respectively.

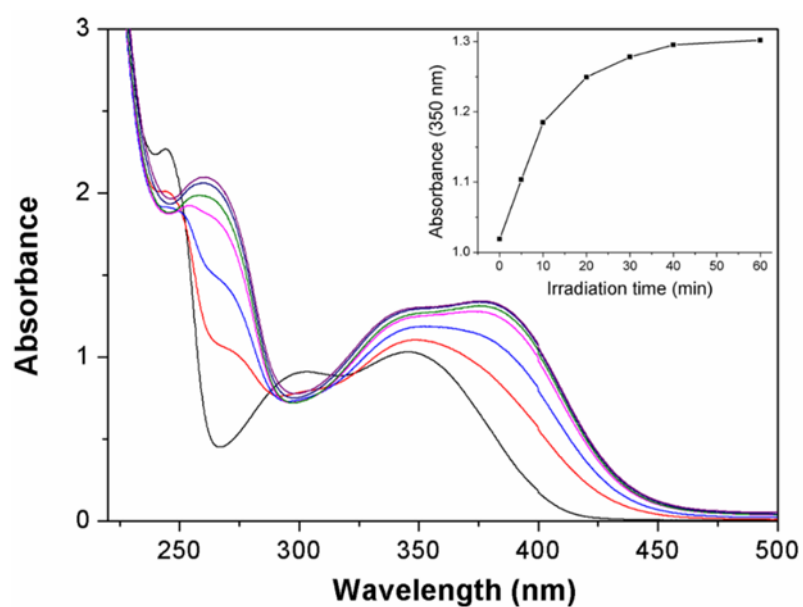


Figure S2 UV-Vis spectra of the photolysis of a solution of E_{PEG} -Liposomes (total lipid = 5 mM, 4 mol% PEG₅₀₀₀, 1 mol% lipopeptide E₄). *Inset*: Reaction profile over time as a function of UV absorption at 350 nm. Irradiation times: 0 (black), 5 (red), 10 (blue), 20 (pink), 30 (green), 40 (navy) and 60 min (violet). The isobestic points appeared at 250 nm, 287 nm and 322 nm.

Note: UV light source used for this experiment was less intense than the LED used in all other experiments.

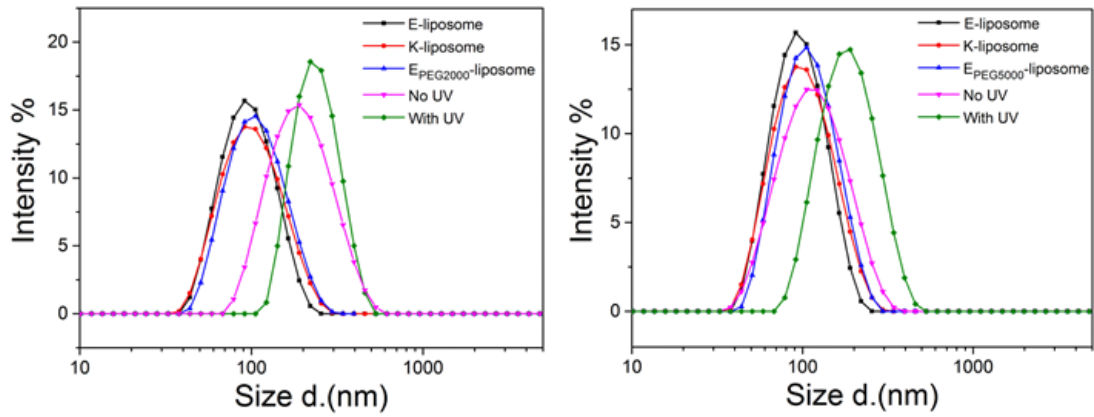


Figure S3 DLS data accompanying liposome-liposome lipid mixing experiments. For E_{PEG2000}-liposomes (left, 4 mol% PEG₂₀₀₀) an increase in liposome hydrodynamic diameter was observed *in the absence* of UV irradiation/PEG photolysis. This indicates PEG₂₀₀₀ is not sufficiently long enough to shield E₄/K₄ recognition and binding. For E_{PEG5000}-liposomes (right, 4 mol% PEG₅₀₀₀), an increase in liposome size is only observed following UV irradiation (15 mins, 370 ± 7 nm, 202 mW/cm^2), loss of PEG and restoration of the interaction between peptide E and K.

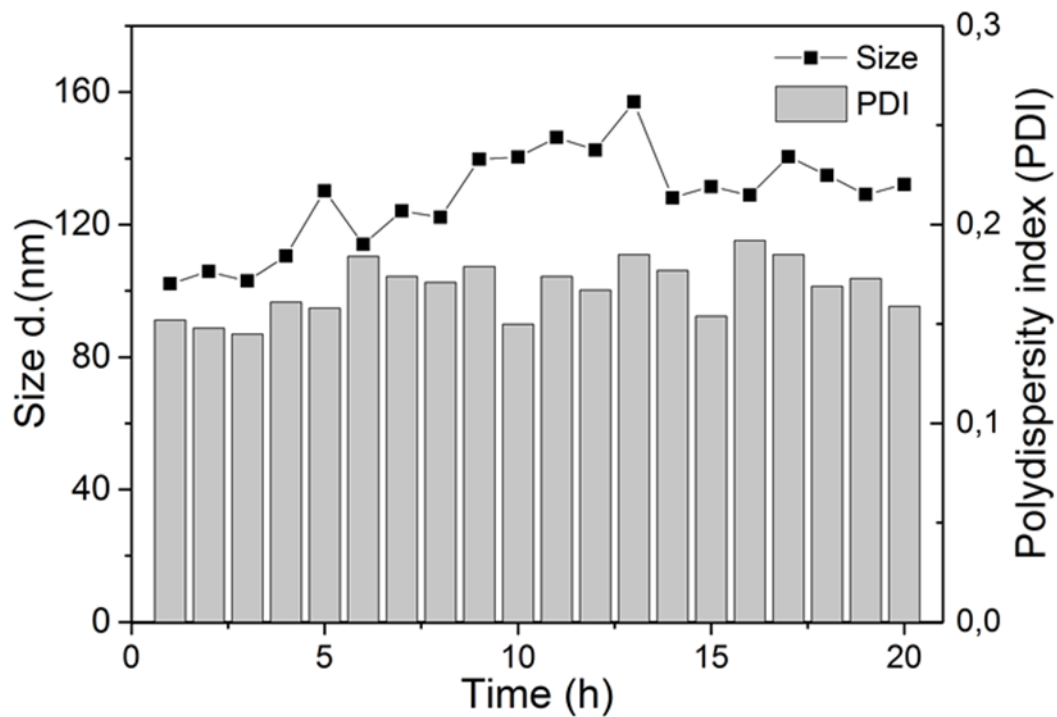


Figure S4 Stability of E_{PEG}-liposomes (4mol% PEG₅₀₀₀) in media + 10% FCS over time

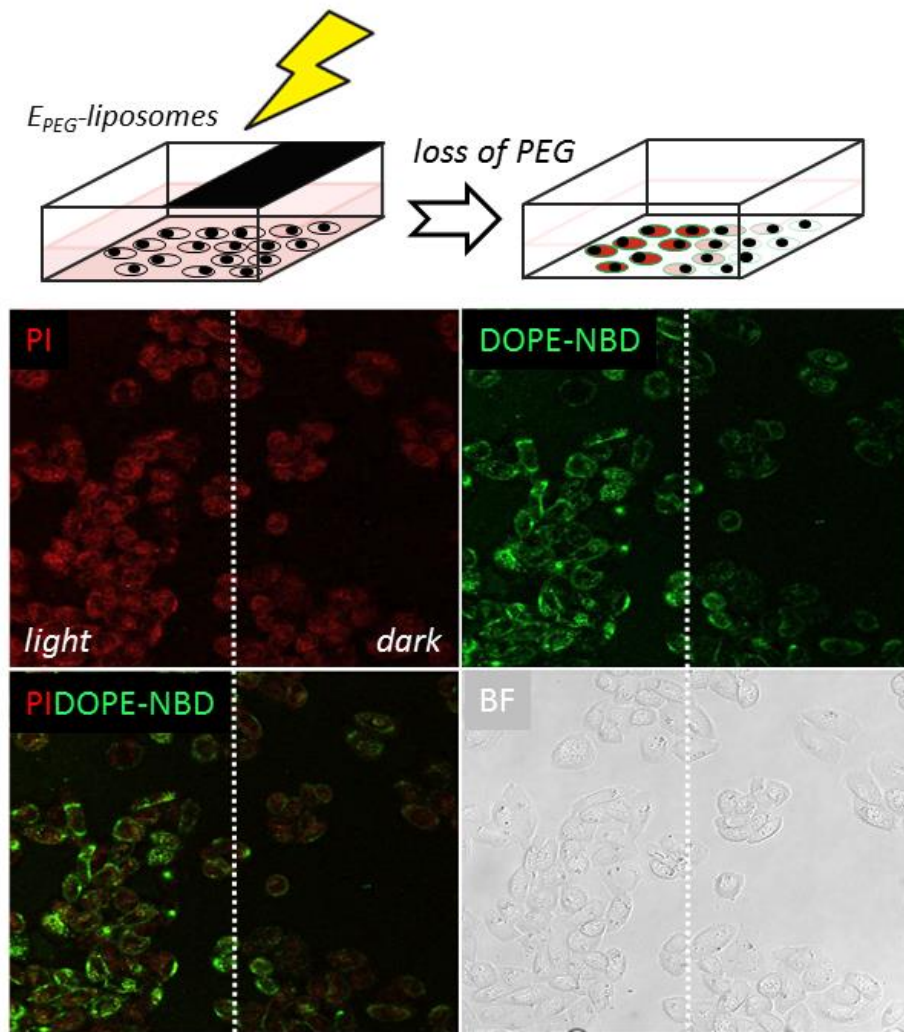


Figure S5 Light templated liposome-cell fusion and concomitant cargo delivery *in vitro*. Following localized UV irradiation (15 mins, 370 ± 7 nm, 50.6 mW/cm², *light dose* = 45.5 J/cm²), E_{PEG} -liposomes (400 μ M total lipids, 1 mol % DOPE-NBD, green lipid probe, 75 μ M encapsulated PI, red) fuse with K-functionalized HeLa cell membranes with concomitant delivery of PI to the cell cytosol. In the absence of UV irradiation, but within the same experimental well, cells show significantly less liposome-associated fluorescence.

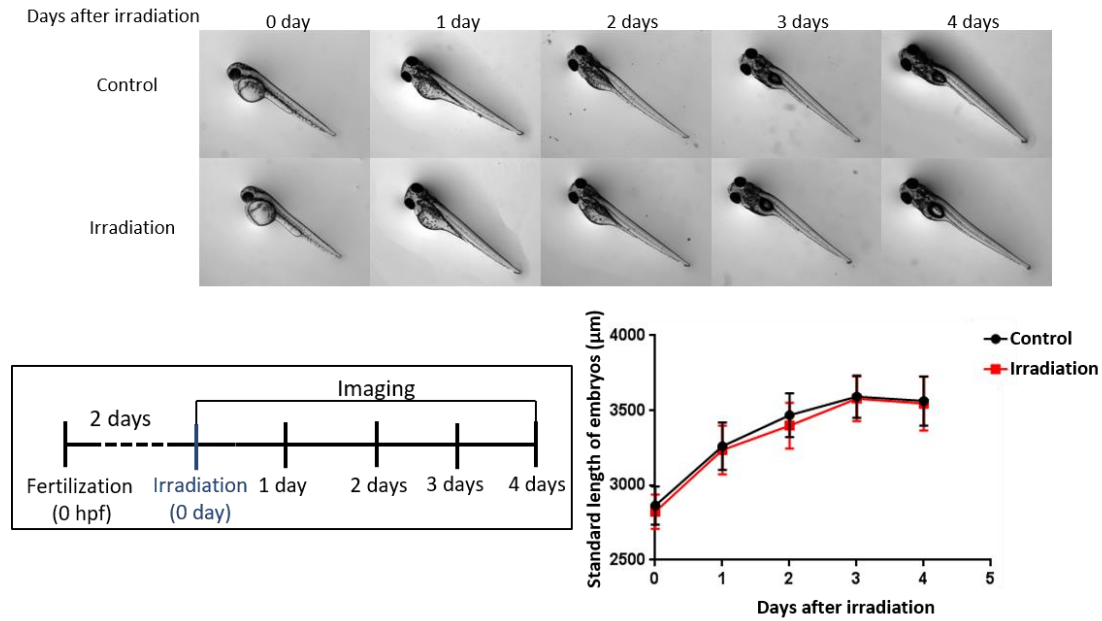


Figure S6 UV-A phototoxicity in zebrafish embryos. UV-A phototoxicity in zebrafish embryos. For irradiated embryos, a single dose of UV-A light (15 mins, 370 ± 7 nm, 13.5 mW/cm², *light dose* = 0.45 J/embryo) was applied to zebrafish embryos (2 dpf). Images were taken 0, 1, 2, 3, 4 days (2-6 dpf) after irradiation using a Leica MZ16FA fluorescent microscope (BF mode) coupled to a DFC420C camera. The standard length of embryos was measured from the eye to the end of the tail (ImageJ 1.51n). Under these irradiation conditions, embryos developed normally and no phenotypic abnormalities were observed. Data presented as mean \pm SD. *Sample sizes*: Control group (d0: n = 20; d1: n = 20; d2: n = 20; d3: n = 20; d4: n = 19) Irradiation group (d0: n = 20; d1: n = 19; d2: n = 18; d3: n = 18; d4: n = 16).

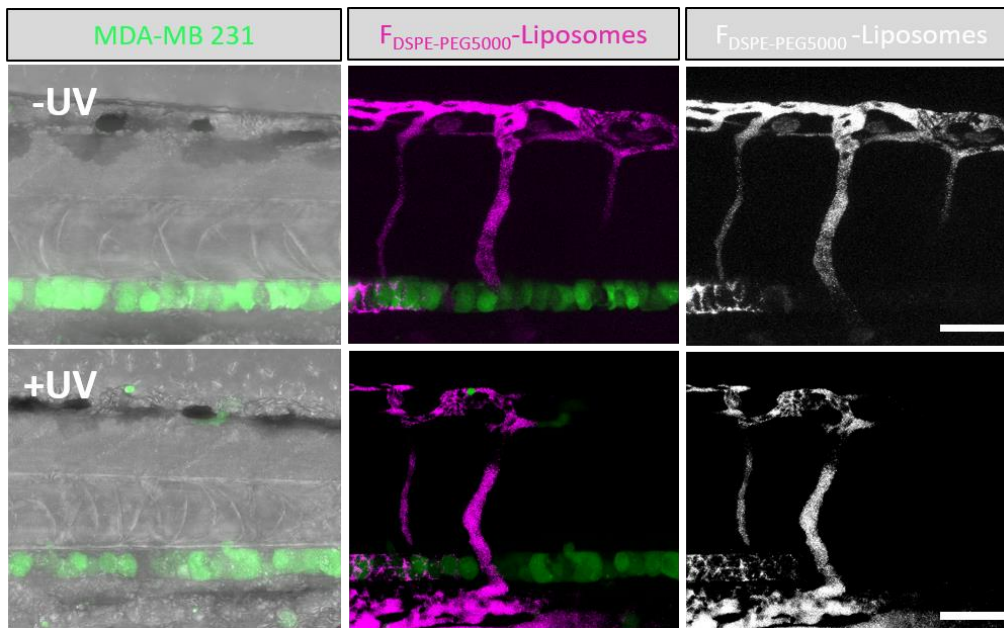


Figure S7 (Control for) Cell-specific, light triggered liposome-cell interactions *in vivo*. MDA-MB-231 human breast cancer cells, stably expressing GFP were injected into the circulation of a 2-day old zebrafish embryo and quickly accumulated in the caudal hematopoietic tissue (CHT). $F_{DSPE-PEG5000}$ -liposomes (1 mM, 4 mol% DSPE-PEG₅₀₀₀, containing 1 mol% DOPE-LR, red) were injected into circulation. In this case, both before and after UV irradiation (15 mins, 370 ± 7 nm, 13.5 mW/cm², *light dose* = 0.45 J/embryo), liposomes remained freely circulating, confined to the vasculature of the embryo. Scale bars = 100 μ m

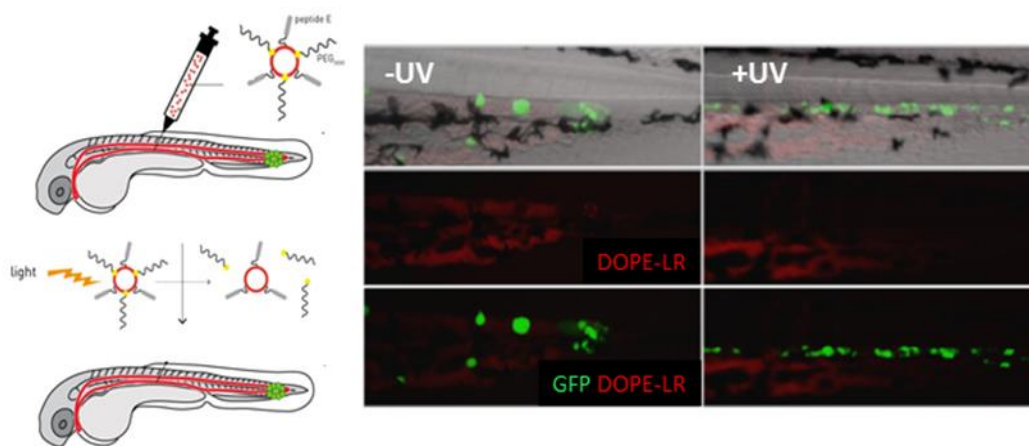


Figure S8 (Control for) Cell-specific, light triggered liposome-cell interactions *in vivo*. MDA-MB-231 human breast cancer cells, stably expressing GFP were injected into the circulation of a 2-day old zebrafish embryo and quickly accumulated in the caudal hematopoietic tissue (CHT). These cells had not been prior functionalized with lipopeptide K. E_{PEG} -liposomes (1 mM, 4 mol% PEG₅₀₀₀, containing 1 mol% DOPE-LR, red) were injected into circulation. In this case, both before and after UV irradiation (15 mins, 370 ± 7 nm, 13.5 mW/cm², *light dose* = 0.45 J/embryo), liposomes remained freely circulating, confined to the vasculature of the embryo.

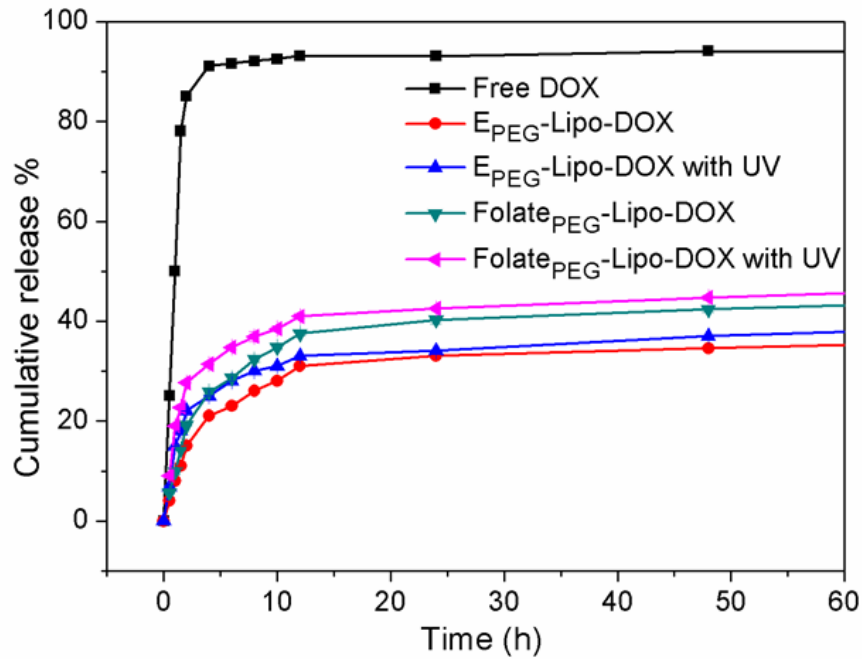


Figure S9 Doxorubicin release curves for E_{PEG}- and F_{PEG}-lipo-DOX formulations, before and after UV (15 mins, 370 ± 7 nm, 202 mW/cm²) irradiation.

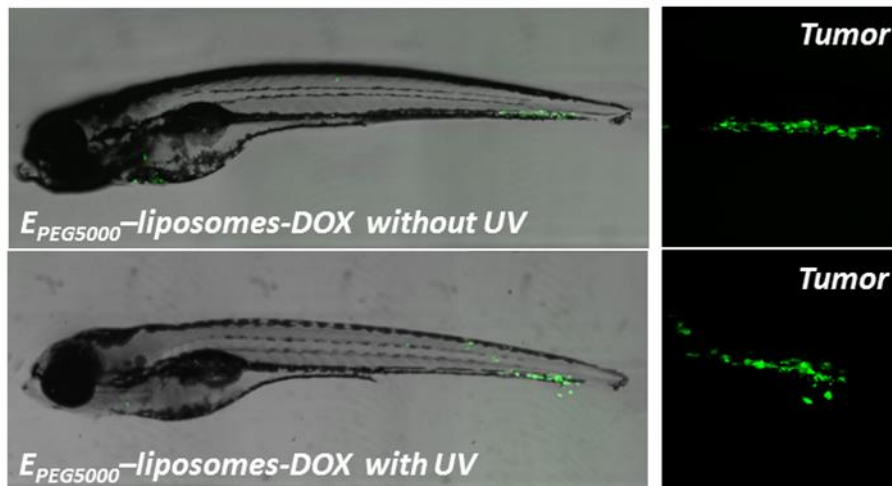


Figure S10 (Control for) Cell-specific doxorubicin delivery to xenograft cancer cells *in vivo*. MDA-MB-231 human breast cancer cells, stably expressing GFP were injected into the circulation of a 2-day old zebrafish embryo. These cells had not been prior functionalized with lipopeptide K. No reduction in tumor volume was observed following injection of doxorubicin-filled (200 μM doxorubicin) E_{PEG}-liposomes, both before (top) and after (bottom) *in situ* UV irradiation (15 mins, 370 ± 7 nm, 13.5 mW/cm², *light dose* = 0.45 J/embryo).

Chapter 6

Summary

Cancer is still a leading cause of death worldwide. Chemotherapy is often the treatment of choice to treat cancer, although side effects alter normal cell physiology and may affect the patient's quality of life. Progress in biomedical research has shown that pharmacological targeting of cancer cells is not the only therapeutic option. Interactions between tumour cells and their surrounding stroma may support cancer cell survival and spreading, and offer a potential new treatment strategy. In addition, the application of new inducible photosensitizers and specific drug delivery carriers can improve selectivity of anti-cancer treatments. Zebrafish models have increasingly been applied to cancer research and drug discovery. In this thesis, a zebrafish embryonic cancer model is presented as an innovative model organism to study the role of macrophages in tumour angiogenesis. In addition, we successfully demonstrated that zebrafish provide a fast-vertebrate cancer model to test the administration regimen of drugs, conditions of light irradiation, host toxicity and anti-cancer efficacy of photodynamic therapy and photoactivated therapy drugs. Finally, we observed that light-triggered, cell-specific delivery of liposome-encapsulated doxorubicin reduced cancer cell burden without enhanced cytotoxicity in live zebrafish embryos.

In **chapter 2**, we explored the function of zebrafish macrophages in tumour xenografts. He et al had shown that transient depletion of macrophages by Pu.1 morpholino treatment blocked tumour angiogenesis at the primary site of metastatic onset [1]. Here, we used metronidazole to chemically deplete macrophages in *Tg* zebrafish (*Mpeg:GAL4:UAS:NTR:mCherry*) engrafted with cutaneous melanoma cells and observed that after macrophages depletion, tumour angiogenesis was impaired. The macrophages were attracted into tumour sites and promoted tumour vessel formation. Emerging evidence suggests that lactic acid as a product of glycolysis can attract macrophages and induce angiogenesis targeting highly glycolytic cancer cells [2]. To test this, a macrophage attraction assay was performed by injecting lactic acid into the zebrafish hindbrain. By counting the number of macrophages, we observed that lactic acid indeed attracted zebrafish macrophages. Chemical inhibition of tumour cell glycolysis by 2-Deoxyglucose (2DG) blocked the lactate secretion. Engraftment of these cells into zebrafish embryos reduced attraction of macrophages and impaired tumour angiogenesis suggesting that macrophages provided specific cytokines to support angiogenesis.

In **chapter 3**, we validated a photodynamic therapy (PDT) compound, TLD1433, in zebrafish ectopic and orthotopic models. Importantly, this ruthenium-based photosensitizer has passed a phase I clinical trial

for PDT treatment of bladder cancer. In our study we investigated a possible repurposing of this drug for treatment of conjunctival melanoma (CM). Firstly, the therapeutic potential of light activated TLD1433 was tested on several cell lines derived from conjunctival melanoma (CRMM1, CRMM2 and CM2005), uveal melanoma (OMM1, OMM2.5, MEL270), epidermoid carcinoma (A431) and cutaneous melanoma (A375). The best responding cell lines, CRMM1 and CRMM2 were selected for *in vivo* testing of this PDT compound. The maximally-tolerated dose of TLD1433 was determined in wild type embryos and embryos engrafted with CM cells by applying three drug-administration routes (water administration, intravenous and retro-orbital administration). The zebrafish embryos engrafted with CM cells tolerated less TLD1433 compared with wild type embryos. Using the maximally-tolerated dose of TLD1433, we observed that TLD1433 sensitizer inhibited tumour growth in the CM ectopic model after intravenous (IV) and retro-orbital (RO) administrations, and in the CM orthotopic model after RO administration. These results clearly illustrate that the zebrafish embryonic cancer models can be utilized to optimise the route of administration and the dose for photoactivated chemotherapy compounds.

In **chapter 4**, the light-activated anticancer properties of a novel trisheteroleptic ruthenium complex **[2]**(PF₆)₂ were validated *in vitro* and in an embryonic zebrafish CM model. The metal complex **[2]**²⁺ was designed based on previous work in order to increase cellular uptake, its photoinduced anticancer activity with a low dark toxicity. This photoactivated chemotherapy (PACT) compound can be light-activated via an oxygen-independent photosubstitution reaction. It is for the first time that the toxicity and efficacy of such a ruthenium-based complex was tested in the zebrafish embryonic cancer model. Different concentrations and administration methods of this drug were examined to find an optimal balance between toxicity and a therapeutic effect. Our results revealed a higher efficacy of this ruthenium compound in the *in vivo* orthotopic CM model than in the ectopic CM model, indicating that this novel compound should be further explored in the local treatment of conjunctival melanoma in more advance preclinical models.

In **chapter 5**, we demonstrated that light-triggered and cell-specific targeting of doxorubicin-filled liposomes diminished growth of xenografted breast cancer cells in a zebrafish embryonic model. Light-induced dePEGylation was used to shield the E₄/K₄ peptide interaction. The liposome-cell interactions depend on the recognition and binding of two coiled-coil forming peptides – peptide E on liposomes and peptide K on cancer cells. Light-triggered dePEGylation improved cancer cell-liposome fusion and allowed specific delivery of liposomal doxorubicin to target cancer cells. In addition, folate-decorated liposomes (F-liposomes) targeted the overexpressed folate receptor on xenograft MDA-MB-231 cells and also promoted direct fusion of liposome and cell membranes. The experimental component fusion systems (peptides E and K) and tumour-cell specific receptor folate-decorated liposomes both delivered doxorubicin to tumour cells to induce tumour cell death. As the liposomes and tumour cells expressed fluorescence, they were easily detected in the zebrafish embryos, allowing measurements of

fluorescence areas and intensity. This work illustrates that the zebrafish embryonic cancer model can serve as an efficient platform for optimization of nanomedicine toxicity, biodistribution, stability and anti-cancer efficiency.

In conclusion, we started out to use the zebrafish embryonic tumour model to investigate the interaction between host macrophages with their tumour microenvironment. The lactic acid secreted by tumour cells could attract macrophages and then induced tumour angiogenesis. Secondly, we used zebrafish embryonic cancer models for PDT and PACT compound testing. The PDT compound TLD1433, and PACT compound [2](PF₆)₂ showed a selective anti-cancer efficacy. Finally, in order to increase the cellular uptake of compounds, cell-specific targeting of liposomes was introduced. Liposome-encapsulated doxorubicin was delivered into tumour cells upon light-activation and reduced tumour burden.

Collectively, in this thesis we demonstrated that zebrafish embryonic cancer models are excellent for the discovery of new drugs and their use has the potential to speed up development of novel anti-cancer treatments with translational potential.

References

1. He, S.; Lamers, G.E.; Beenakker, J.W.; Cui, C.; Ghotra, V.P.; Danen, E.H.; Meijer, A.H.; Spink, H.P.; Snaar-Jagalska, B.E. Neutrophil-mediated experimental metastasis is enhanced by VEGFR inhibition in a zebrafish xenograft model. *The Journal of pathology* **2012**, *227*, 431-445, doi:10.1002/path.4013.
2. Colegio, O.R.; Chu, N.Q.; Szabo, A.L.; Chu, T.; Rhebergen, A.M.; Jairam, V.; Cyrus, N.; Brokowski, C.E.; Eisenbarth, S.C.; Phillips, G.M., et al. Functional polarization of tumour-associated macrophages by tumour-derived lactic acid. *Nature* **2014**, *513*, 559-563, doi:10.1038/nature13490.

Nederlandse Samenvatting

Kanker is nog altijd een van de grootste doodsoorzaken wereldwijd. Chemotherapie is vaak de eerste keuze voor de behandeling van kanker, maar de bijwerkingen hiervan veranderen de normale fysiologie van cellen en hebben grote gevolgen voor kwaliteit van leven van patiënten. Vooruitgang in biomedisch onderzoek heeft laten zien dat er ook andere therapeutische mogelijkheden zijn. De overleving en verspreiding van tumorcellen kan bevorderd worden door interacties met het omliggende weefsel. Ingrijpen op dit proces is een mogelijke nieuwe behandelingsstrategie. Daarnaast zou de selectiviteit van behandelingen tegen kanker verbeterd kunnen worden door medicijnen lichtgevoelig te maken (met fotosensitizers) en door de ontwikkeling van dragers (bijvoorbeeld liposomen) die zorgen voor een specifieke medicijnafgifte. De zebrafish wordt in toenemende mate toegepast als modelorganisme bij kanker- en geneesmiddelenonderzoek. In dit proefschrift worden zebrafishembryo's gepresenteerd als een innovatief modelsysteem om de rol van macrofagen bij bloedvatontwikkeling (angiogenese) in tumoren te bestuderen. Bovendien laten wij zien dat de zebrafish een geschikt kankermodel is voor het testen van de toedieningswijze van geneesmiddelen, de condities voor activering van lichtgevoelige verbindingen, de toxiciteit voor het organisme en de effectiviteit van foto-dynamische en foto-actieve therapieën. Ten slotte hebben wij aangetoond dat licht-geïnduceerde, cel-specifieke aflevering van een in liposomen verpakt geneesmiddel (doxorubicine) de groei van humane kankercellen in de zebrafish kan remmen zonder cytotoxische bijwerkingen.

In **hoofdstuk 2** hebben we de functie van macrofagen van de zebrafish bij de xenotransplantatie van humane tumorcellen onderzocht. Eerder onderzoek van onze groep had laten zien dat tijdelijke onderdrukking van de ontwikkeling van macrofagen (door uitschakeling van de transcriptiefactor Pu.1) de angiogenese van tumoren blokkeert op de primaire locatie waar metastasering begint. In dit hoofdstuk hebben wij metronidazole gebruikt voor chemische ablatie van macrofagen in transgene zebrafishes (*Mpeg:GAL4:UAS:NTR:mCherry*) waarin huidmelanoomcellen waren getransplanteerd. We zagen dat de tumor-angiogenese was verstoord in de afwezigheid van macrofagen, terwijl in de controlegroep de macrofagen werden aangetrokken naar plaatsen van tumorgroei en daar de vorming van bloedvaten bevorderden. Er is toenemend bewijs dat lactaat als product van de glycolyse macrofagen kan aantrekken en angiogenese induceren bij sterk glycolytisch actieve kankercellen. Om deze mogelijkheid te onderzoeken hebben wij lactaat geïnjecteerd in een hersenventrikel van de zebrafish en konden aantonen dat deze stof de aantrekking van macrofagen verhoogt. Chemische remming van de glycolyse van tumorcellen met 2-Deoxyglucose (2DG) blokkeerde de uitscheiding van lactaat. Wanneer deze cellen werden getransplanteerd in zebrafishembryo's was de tumor-angiogenese verminderd, wat suggereert dat de macrofagen die door lactaat worden aangetrokken, specifieke cytokinen produceren die de angiogenese bevorderen.

In **hoofdstuk 3** valideren wij een chemische verbinding (TLD1433) voor foto-dynamische therapie (PDT)

in ectopische en orthotopische zebrawismodellen voor conjunctivaal melanoom. Eerst werd TLD1433 getest op verschillende cellijnen afgeleid van conjunctivaal melanoom (CRMM1, CRMM2, CM2005), uveaal melanoom (OMM1, OMM2.5, MEL270), epidermoïde carcinoom (A431) and cutaan melanoom (A375). De beste kandidaten (cellijnen CRMM1 en CRMM2) werden geselecteerd om de PDT-verbinding *in vivo* te testen. De maximaal getolereerde dosis van TLD1433 werd bepaald in zowel wildtype embryo's als in embryo's waarin conjunctivaal melanoomcellen (CM) getransplanteerd waren. TLD1433 werd vervolgens toegediend aan de embryo's via drie routes (in het water, intraveneus en retro-orbitaal). De CM-getransplanteerde embryo's tolereerden minder TLD1433 dan wildtype embryo's. TLD1433 remde tumorgroei in het ectopische CM-model na intraveneuze en retro-orbitale toediening en in het orthotopische CM-model na retro-orbitale toediening. Deze resultaten illustreren duidelijk dat ons zebrawis-kankermodel kan worden toegepast om de toedieningsroute en de dosis van licht-geactiveerde, chemotherapeutische verbindingen te optimaliseren.

In **hoofdstuk 4** hebben wij ons gericht op een foto-activeerbare therapie (PACT) en daarbij de anti-kanker eigenschappen van een nieuw trisheteroleptisch rutheniumcomplex ($[2](PF_6)_2$) gevalideerd *in vitro* en in een zebrawisembryomodel voor CM. Het metaalcomplex $[2]^{2+}$ was op basis van eerder onderzoek ontworpen om de cellulaire opname en de licht-geïnduceerde anti-kanker activiteit te vergroten en daarbij een lage toxiciteit in het donker te behouden. De familie van rutheniumverbindingen kan door licht geactiveerd worden via een zuurstof-onafhankelijke fotosubstitutiereactie. Dit is de eerste keer dat de toxiciteit en effectiviteit van zo'n ruthenium-gebaseerd complex is getest in het zebrawiskankermodel. Verschillende toedieningswijzen werden onderzocht om een optimale balans te vinden tussen toxiciteit en therapeutisch effect. Wij vonden een hogere effectiviteit van de rutheniumverbinding in het *in vivo* orthotopische CM-model dan in het ectopische CM-model. Deze resultaten vormen een goede basis voor verder onderzoek naar de toepassing van deze nieuwe verbinding voor de lokale behandeling van CM in meer geavanceerde preklinische modellen.

In **hoofdstuk 5** hebben wij aangetoond dat de groei van getransplanteerde borstkankercellen in zebrawisembryo's geremd kan worden via een licht-geïnduceerde en cel-specifieke therapie met doxorubicine-bevattende liposomen. Wij hebben hierbij een licht-induceerbare verwijderingsmethode van het polyethyleenglycol van de liposomen onderzocht door de interactie te reguleren tussen twee peptiden (E op liposomen en K op tumorcellen) die nodig zijn voor de fusie van liposomen met celmembranen van tumorcellen en specifieke afgifte van medicijnen. Wij konden een directe fusie tussen liposomen en celmembranen van tumorcellen bewerkstelligen met het experimentele twee-componenten-systeem (fusie van peptiden E en K) evenals met een systeem van folaat-omhulde liposomen (F-liposomen) die gericht zijn op de folaatreceptor die tot overexpressie komt op getransplanteerde MDA-MB-231-cellen. Beide systemen leverden voldoende doxorubicine aan tumorcellen om tumorceldood te induceren. Omdat de liposomen en tumorcellen fluorescerend waren,

konden zij makkelijk gedetecteerd worden in de zebraisembryo's en was het mogelijk om oppervlakte en intensiteit te kwantificeren. Dit onderzoek illustreert dat het zebraiskankermodel dienst kan doen als een efficiënt platform voor optimalisatie van de toxische eigenschappen, biodistributie, stabiliteit en anti-kanker werkzaamheid van nanomedicijnen.

Concluderend, wij hebben kankermodellen gebaseerd op zebraisembryo's succesvol gebruikt om de rol van macrofagen in de micro-omgeving van getransplanteerde tumorcellen te onderzoeken. Het lactaat dat door tumorcellen wordt uitgescheiden bleek macrofagen te kunnen aantrekken en vervolgens tumor-angiogenese te induceren. Daarnaast hebben we deze zebraiskankermodellen gebruikt om PDT- en PACT-strategieën te testen. De PDT-verbinding TLD1433 en de PACT-verbinding **[2]**(PF₆)₂ vertoonden een selectieve anti-kanker werkzaamheid. Ten slotte hebben we een cel-specifieke therapie getest waarbij liposomen worden gebruikt om de cellulaire opname van anti-kanker verbindingen te vergroten. Hierbij zijn wij erin geslaagd om doxorubicine in liposomen te verpakken en af te leveren aan tumorcellen na foto-activatie.

Bij elkaar genomen toont dit proefschrift aan dat zebraiskankermodellen uitstekend geschikt zijn voor de ontdekking van nieuwe geneesmiddelen en de potentie hebben om de ontwikkeling van nieuwe anti-kanker therapieën te versnellen.

Abbreviations

BBB	blood brain barrier
BM	bone marrow
CAFs	cancer-associated fibroblasts
CHT	caudal haematopoietic tissue
CM	conjunctival melanoma
CSC	cancer stem cell
CSF-1	colony-stimulating factor
DHFR	dihydrofolate reductase
DLI	drug-to-light interval
DMC	disseminated melanoma cells
DMEM	dulbecco's minimal essential medium
DOC	duct of cuvier
DOPC	1,2-dioleoyl-sn-glycero-3-phosphocholine
DOPE	1,2-dioleoyl-sn-glycero-3-phosphoethanolamine
DOX	doxorubicin hydrochloride
Dpf	days post fertilization
ECCC	european collection of cell cultures
ECM	extracellular matrix
EE	entrapment efficiency
EMT	epithelial-to-mesenchymal transition
EPR	enhanced permeability and retention
FACS	fluorescence-activated cell sorting
FCS	fetal calf serum
FOV	field of view
GBM	glioblastoma multiforme
GM	glutamine-S
HIF-1 α	hypoxia-inducible factor 1 α
Hpi	hours post injection
IDH1	isocitrate dehydrogenase 1
IFN γ	interferon gamma
IV	intravenous administration
LSECs	liver sinusoidal endothelial cells
MMPs	matrix metalloproteinases
MTD	maximum tolerated dose
Mtmp	methylthiomethylpyridine
MTZ	metronidazole

NSCLC	non-small-cell lung cancer
NTR	nitroreductase
OXPPOS	oxidative phosphorylation
P/S	penicillin/streptomycin
PACT	photoactivated chemotherapy
PBS	phosphate-buffered saline
PCV	posterior caudal vein
PDT	photodynamic therapy
PDX	patient-derived xenografts
PET	positron emission tomography
PI	phototherapeutic index
PIGF	placental growth factor
PpIX	protoporphyrin IX
PSs	photosensitizers
Pt	platinum
RES	reticulo-endothelial system
RFP	red fluorescent protein
RGP	radial growth phase
RO	retro-orbital administration
ROS	reactive oxygen species
Ru	ruthenium
SECs	scavenger endothelial cells
SIV	sub-intestinal vein
SRB	sulforhodamine B
TAA _s	tumor-associated-antigens
TAM	tumour-associated macrophages
TCA	trichloroacetic acid
2DG	2-deoxy-d-glucose
2HG	2-hydroglutarate
5-ALA	5-aminolevulinic acid
TEM	transmission electron microscopy
TLRs	toll-like receptors
TME	tumour microenvironmet
TNF- α	tumour necrosis factor alpha

TSA	tumour-specific-antigens
UCNPs	upconverting nanoparticles
UVR	ultra-violet radiation
VEGF	vascular endothelial growth factor
VGP	vertical growth phase
WA	water administration
zPDX	patient-derived xenografts in zebrafish

Publication List

1. C. Tulotta, C. Stefanescu, **Q. Chen**, V. Torraca, A. H. Meijer & B. E. Snaar-Jagalska. CXCR4 signaling regulates metastatic onset by controlling neutrophil motility and response to malignant cells. *Scientific Reports*. 2019, 9, 2399
2. Li Kong#, **Quanchi Chen**#, Frederick Campbell, Ewa Snaar-Jagalska, Alexander Kros. Light triggered, cancer cell-specific targeting and liposomal drug delivery in a zebrafish xenograft model. *Advanced healthcare materials*. 2020, e1901489
3. **Quanchi Chen**, Vadde Ramu, Yasmin Aydar, Arwin Groenewoud, Xue-Quan Zhou, Martine J. Jager, Houston Cole, Colin G. Cameron, Sherri A. McFarland, Sylvestre Bonnet, and B. Ewa Snaar-Jagalska. TLD1433 photosensitizer inhibits conjunctival melanoma cells in zebrafish ectopic and orthotopic tumour models. *Cancers*. 2020, 12, 587; doi:10.3390
4. **Quanchi Chen**, Li Kong, Frederick Campbell, Ewa Snaar-Jagalska, Alexander Kros. Effects of PEGylation on the in vivo biodistribution of differently charged liposomes. Manuscript in preparation
5. **Quanchi Chen**, Vadde Ramu, Yasmin Aydar, Xue-Quan Zhou, B. Ewa Snaar-Jagalska, Sylvestre Bonnet. New ruthenium-based photoactivated chemotherapy compound is cytotoxic for various tumour cells in culture and conjunctival melanoma cells in zebrafish orthotopic xenograft model. Manuscript in preparation

Curriculum vitae

Quanchi Chen was born on the 2nd of October 1990 in Yancheng, Jiangsu, China. In 2008, he started his bachelor studies in clinical medicine at Nanjing Medical University. In 2013 he continued his master research in Shanghai Tenth People's Hospital. After obtaining his master degree in 2015, he was awarded a research scholarship from the Chinese Scholarship Council. With this scholarship, he moved to the Netherlands and joined the group headed by Prof. B. Ewa Snaar-Jagalska in the Institute of Biology Leiden at Leiden University and performed his PhD research project entitled "Development of novel anti-cancer strategies utilizing the zebrafish xenograft model". In this project, he utilized the zebrafish embryonic tumour models to investigate how macrophages modified by the tumour microenvironment promote tumour angiogenesis formation. In collaboration with Prof. Alexander Kros and Prof. Sylvestre Bonnet from the Leiden Institute of Chemistry at Leiden University he developed and utilized zebrafish cancer models to optimize the light-triggered liposome system to deliver doxorubicin specifically to cancer cells and tested anti-cancer efficacy of novel PDT and PACT compounds to attenuate ocular melanoma. He presented his research at international conferences and supervised four MSc students.